Three dimensional Pickup Ion velocity distribution functions observed at 1 AU with STEREO/PLASTIC: Anisotropic features and density enhancements in pitch angle distributions as tools to investigate transport effects

Dissertation zur Erlangung des Doktorgrades
.der Mathematisch-Naturwissenschaftlichen-Fakultät
der Christian-Albrechts-Universität zu Kiel

vorgelegt von
Duncan Keilbach

2023-06-29

Three dimensional Pickup Ion velocity distribution functions observed at 1 AU with STEREO/PLASTIC: Anisotropic features and density enhancements in pitch angle distributions as tools to investigate transport effects

Duncan Keilbach, 2023
Institut für Experimentelle und Angewandte Physik
Mathematisch Naturwissenschaftliche Fakultät
Christian Albrechts Universität zu Kiel

Dissertation zur Erlangung des Doktorgrades der Mathematisch-Naturwissenschaftlichen-Fakultät der Christian-Albrechts-Universität zu Kiel
Druckreife Fassung

Betreuer: Prof. Dr. Robert F. Wimmer Schweingruber, Institut für Experimentelle und Angewandte Physik, CAU Kiel

Datum der Disputation: 3.4.2023

Erstgutachter: Prof. Dr. Robert F. Wimmer Schweingruber, Institut für Experimentelle und Angewandte Physik, CAU Kiel

Zweitgutachter: Prof. Dr. Sebastian Wolf, Institut für Theoretische und Astrophysik, CAU Kiel

Veröffentlicht auf dem Open Access Server MACAU der CAU Kiel unter der Lizenz **CC-BY-ND 4.0**.
URN: urn:nbn:de:gbv:8:3-2023-00455-9

Abstract

The solar wind (SW) is a magnetized plasma which emerges from the Sun [Biermann [1951], Parker [1958]] and is embedded into a bubble of interstellar plasma, the Local Interstellar Medium (LISM) (e.g. Spitzer [1942], Axford et al. [1963], Frisch et al. [2011]). The SW is a different magnetized plasma than the LISM. An interface between both plasmas is formed and the volume filled by the SW is called the Heliosphere (e.g. Axford et al. [1963]). Pickup Ions (PUIs) are charged particles embedded into the SW, but not necessarily of solar origin (e.g. Axford [1972]). A PUI is produced if a neutral particle is ionized in the SW. After ionization, the newly created ion is subjected to Lorentz-Force and gyrates around the magnetic field which is carried by the SW. Hence, the former neutrals are transported by the SW. Apart from inner-heliospheric sources such as planetary atmospheres, comets or interplanetary dust (e.g. Geiss et al. [1995a], Gloeckler and Geiss [1998], Quinn et al. [2018]), neutral particles from the LISM are a source of PUIs. Other than charged particles from the LISM, they enter the Heliosphere and become ionized. This way, PUIs of interstellar origin provide information about the LISM which can be gained from in-situ observations of particles within the Heliosphere. This work focuses on these interstellar PUIs which in the following are referenced to as just PUIs.

Since their first direct observation by Möbius et al. [1985], models for the transport of PUIs and their Velocity Distribution Function (VDF) have undergone many iterations. Initially, the VDF of PUIs resembles a torus in velocity space. However, during transport in the SW the VDF is modified. Initially, the consensus was, that PUIs are swiftly scattered in velocity space by wave fields, so that the VDF at observation becomes isotropic (e.g. Jokipii [1966], Axford [1972], Vasyliunas and Siscoe [1976]). Later, more anisotropic features were discovered in the VDF. PUI observations of Moebius et al. [1995], Gloeckler and Geiss [1998] concluded that the scattering is less efficient than previously assumed which lead to the hemispherical model of Isenberg [1997]. Here, velocity space is divided into two hemispheres and different transport characteristics are assumed for both.

To that point, only one dimensional observations of PUI VDFs were commenced.[Drews et al. [2015]] employed the PLAsma and SupraThermal Ion Composition (PLASTIC) instrument onboard of the Solar TErrestrial RElations Observatory (STEREO) for two dimensional observations of the VDF of He^+ PUIs and found direct traces of a torus distribution. Parameters of the LISM can be derived from PUIs (e.g. Moebius et al. [1995], Drews et al. [2012], Möbius et al. [2015], Taut et al. [2018]). So accurate models of PUI transport are required for a meaningful and precise derivation of the LISM's parameters. Recently, Berger [2018] and Fischer et al. [2021] employed data from the Solar Wind Ion Composition Spectrometer (SWICS) instruments aboard Ulysses and the Advanced Composition Explorer (ACE) to observe 3d PUI VDFs, but required averages over long time periods for that. Analogously, this work aims to employ STEREO/PLASTIC observations to derive three dimensional (3d) PUI VDFs. Other than SWICS, PLASTIC is theoretically capable of observing particles from almost all azimuthal directions of incident at once, which is promising to enable observations of shorter-term VDFs. In this work, a new calibration of STEREO A/PLASTIC pulse height analysis (PHA) data is performed to obtain observations of He^+ PUIs and their 3d velocity vectors. Focus is put on instrumental limitations and errors. This way, an asymmetric and nonlinear response of the instrument to particles from different angles of incident is found. After an initial analysis of the instrumental data of all sections, it is found that data from the Wide Angle Partition of PLASTIC is not sufficiently reliable. So the focus for this work is put on data from the Solar

Duncan Keilbach- Three dimensional Pickup Ion velocity distribution functions observed at 1 AU with STEREO/PLASTIC: Anisotropic features and density enhancements in pitch angle distributions as tools to investigate transport effects

Wind Sector of PLASTIC. With 3d histograms of He^+ PUIs' velocities, observations of PUI VDFs are made. The PUI events are sorted by the direction of the magnetic and the histograms are divided by histograms averaged over all magnetic field directions. From that, anisotropic features of the VDFs are found with a preference of the anisotropic signatures for magnetic field azimuthal angles of $\pm 90°$ to the radial direction. Similar features are found in pitch angle distributions. For pitch angle distributions, instrumental limitations for the range of observable pitch angles as a function of the magnetic field direction are discussed. The observed pitch angle distributions are also sorted by SW conditions and coordinates where they were observed to find systematic influences to the transport of PUIs in the SW. Also, PUI pitch angle distributions are observed as a function of the relative velocity of a PUI w.r.t. the SW bulk velocity and it is found that anisotropic features can partly be linked to PUIs of velocities which correspond to freshly created PUIs. For the observations, limitations resulting from the limited field of view of the solar wind section of PLASTIC are discussed.

With the methods and limitations found for the observation of 3d PUI VDFs, not only new insights into the transport of PUIs can be found which may provide new constraints for the modelling of PUI transport. Also, PLASTIC is in its observation principle similar to the Heavy Ion Sensor onboard of Solar Orbiter, so that the insights and methods of this work can be applied to new data of Solar Orbiter.

Zusammenfassung

Der Sonnenwind (SW) ist ein magnetisiertes Plasma, welches von der Sonne kontinuierlich ausgestoßen wird [Biermann [1951], Parker [1958]] und eingebettet ist in eine Wolke aus interstellarem Plasma, dem Lokalen Interstellaren Medium (LISM) (z.B. Spitzer [1942], Axford et al. [1963], Frisch et al. [2011]). Der SW und das LISM sind unterschiedliche magnetisierte Plasmen. Daher bildet sich eine Grenzschicht zwischen den beiden und das Volumen, welches vom SW ausgefüllt wird, wird die Heliosphäre genannt (z.B. Axford et al. [1963]). Pickup Ionen (PUIn) sind geladene Teilchen, welche in den SW eingebettet worden sind, aber nicht notwendigerweise von solarem Ursprung sind (z.B. Axford [1972]). Ein PUI wird produziert, wenn ein Neutralteilchen im SW ionisiert wird. Nach der Ionisation ist das neu erzeugte Ion der Lorentzkraft unterworfen und gyriert um das Magnetfeld herum und dieses wird vom SW getragen. Daher werden die vormaligen Neutralteilchen nun vom SW transportiert. Neben Quellen von innerhalb der Heliosphäre, wie z.B. planetare Atmosphären, Kometen oder interplanetaren Staub (z.B. Geiss et al. [1995a], Gloeckler and Geiss [1998], Quinn et al. [2018]), sind Neutralteilchen aus dem LISM eine Quelle für PUIn. Im Gegensatz zu geladenen Teilchen aus dem LISM, können sie in die Heliosphäre eindringen und dort ionisiert werden. Auf diese Weise können mittels PUIn von interstellarem Ursprung Einblicke in das LISM gewonnen werden und zwar mittels in-situ Teilchenbeobachtungen innerhalb der Heliosphäre. Da sich diese Arbeit auf diese PUIn aus interstellaren Quellen fokussiert, werden diese im Folgenden direkt als PUIn bezeichnet.

Seitdem Möbius et al. [1985] erstmals PUIn direkt beobachtet hat, sind die Modelle für den Transport der PUIn und für ihre Geschwindigkeitsverteilungsfunktion (VDF) häufig modifiziert worden. Anfänglich ähnelt die VDF der PUIn einem Torus im Geschwindigkeitsraum. Allerdings wird die VDF während des Transports im SW modifiziert. Der ursprüngliche Konsenz dazu war, dass PUIn durch wellenartige Felder schnell im Geschwindigkeitsraum gestreut werden, sodass die letztlich beobachtete VDF isotrop wird (z.B. Jokipii [1966], Axford [1972], Vasyliunas and Siscoe [1976]. Später worden anisotropere Merkmale in der VDF entdeckt. Durch Beobachtungen kamen Moebius et al. [1995], Gloeckler and Geiss [1998] zu dem Schluss, dass die Streuung weniger effizient ist als bisher angenommen und dies führte zum hemisphärischen Modell von Isenberg [1997]. Darin wird der Geschwindigkeitsraum in zwei Hemisphären aufgeteilt, wobei für beide unterschiedliche Transportcharakteristiken angenommen werden.

Bis dahin gab es lediglich eindimensionale Beobachtungen der PUI VDFn. Drews et al. [2015] nutzte das PLAsma and SupraThermal Ion Composition (PLASTIC) Instrument der Solar TErrestrial RElations Observatory (STEREO) Raumsonde for zweidimensionale Beobachtungen der VDF von He^+ PUIn und beobachtete direkte Spuren einer Torusverteilung. Parameter aus dem LISM können von PUI Beobachtungen gewonnen werden (z.B. Moebius et al. [1995], Drews et al. [2015], Möbius et al. [2015], Taut et al. [2018]), also sind akkurate Modelle des Transports von PUIn eine Voraussetzung für eine aussagekräftige und präzise Bestimmung der Parameter des LISM. Kürzlich nutzten Berger [2018] und Fischer et al. [2021] Daten der Solar Wind Ion Composition Spectrometer (SWICS) Instrumente der Ulysses und Advanced Composition Explorer (ACE) Raumsonden, um dreidimensionale PUI VDFn zu beobachten. Allerdings benötigten sie hierzu Mittelungen über lange Zeiträume. Analog dazu, ist es das Ziel dieser Arbeit, STEREO/PLASTIC Beobachtungen zu nutzen, um dreidimensionale (3d) PUI VDFn zu beobachten. Anders als SWICS ist PLASTIC theoretisch in der Lage, Teilchen aus fast allen azimuthalen Eintrittsrichtungen auf einmal zu beobachten und das ist dafür vielversprechend, VDFn auch über kürzere Zeiträume mitteln zu können.

Duncan Keilbach- Three dimensional Pickup Ion velocity distribution functions observed at 1 AU with STEREO/PLASTIC: Anisotropic features and density enhancements in pitch angle distributions as tools to investigate transport effects

In dieser Arbeit wird eine Neukalibration von STEREO A/PLASTIC Pulshöhenanalyse- (PHA-) Daten durchgeführt, um He^+ PUIn und ihre 3d Geschwindigkeitsvektoren zu beobachten. Hierbei wird der Fokus auf instrumentelle Fehlerquellen gesetzt. So wurde festgestellt, dass das Instrument asymmetrisch und nichtlinear auf Teilchen aus unterschiedlichen Eintrittsrichtungen reagiert. Nach ersten Analyse der instrumentellen Daten aller Sektionen ist festgestellt worden, dass Daten der Wide Angle Partition von PLASTIC nicht ausreichend zuverlässig sind. Also wird in dieser Arbeit der Fokus auf den Sonnenwindsektor von PLASTIC gesetzt. Mittels 3d Histogrammen von He^+ PUI Geschwindigkeitsvektoren, sind Beobachtungen der VDFn entstanden. Die einzeln gemessenen PUI Teilchen wurden außerdem nach der Richtung des Magnetfeldes sortiert und die Histogramme durch Histogramme, welche als Mittelung über alle Magnetfeldrichtungen entstanden sind, dividiert. Daraus ließen sich anisotrope Merkmale in den VDFn finden. Diese Signaturen haben eine Präferenz, bei azimuthalen Mangetfeldwinkeln von $\pm 90°$ relativ zur Radialen gefunden zu werden. Ähnliche Signaturen wurden auch in Pitchwinkelverteilungen gefunden. Für Pitchwinkelverteilungen, wurden instrumentelle Limitationen im Sinne der Spanne an Beobachtbaren Pitchwinkeln als Funktion der Ausrichtung des Magnetfeldes diskutiert. Die beobachteten Pitchwinkelverteilungen wurden darüber hinaus nach Bedingungen im SW und den Koordinaten, wo sie beobachtet worden sind, sortiert, um systematische Einflüsse auf den Transport der PUIn im SW zu finden. Auch wurden PUI Pitchwinkelverteilungen als Funktion der Geschwindigkeit der PUIn relativ zur mittleren Geschwindigkeit der Hauptkomponente des SWs eingeordnet und so wurde herausgefunden, dass einige anisotrope Signaturen mit PUIn in Verbindung gebracht werden können, deren relative Geschwindigkeit zu der von frisch erzeugten PUIn passt. Für diese Beobachtungen wurden Limitationen, die sich aus dem Sichtfeld des Sonnenwindsektors von PLASTIC ergeben, diskutiert.

Mittels der Methoden und Einschränkungen bzw. Limitationen für die Beobachtung von 3D PUIn VDFn können nicht nur neue Einsichten für den Transport der PUIn gewonnen werden, sondern auch könnte die Beobachtungsart dieser Arbeit genutzt werden, um neue Randbedingungen für die Modellierung des PUI Tranports zu finden. Auch ist das Messprinzip von PLASTIC dem des Heavy Ion Sensors von Solar Orbiter ähnlich, sodass die Einsichten und Methoden, die diese Arbeit ermittelt hat, auch für neue Daten von Solar Orbiter anwendbar sind.

Duncan Keilbach- Three dimensional Pickup Ion velocity distribution functions observed at 1 AU with STEREO/PLASTIC: Anisotropic features and density enhancements in pitch angle distributions as tools to investigate transport effects

Contents

1 **Introduction** 1

2 **Review of heliospheric physics specific to interstellar pickup ions** 7
- 2.1 The Sun, the Solar Wind, the Heliosphere and its local neighborhood . . . 8
  - 2.1.1 The Sun . . . 9
  - 2.1.2 Elemental composition and charge states in the solar wind . . . 10
  - 2.1.3 Magnetic field conditions and global properties of the Solar Wind . . . 12
  - 2.1.4 Solar wind classification . . . 14
  - 2.1.5 Medium to large scale structures in the solar wind . . . 17
  - 2.1.6 Wave phenomena in the Solar Wind . . . 18
  - 2.1.7 Wave particle interactions . . . 27
  - 2.1.8 Properties of the Solar Wind in velocity space . . . 35
  - 2.1.9 Formation of the Heliosphere . . . 38
- 2.2 Pickup Ions . . . 39
  - 2.2.1 Inner source pickup ions . . . 40
  - 2.2.2 The trajectory of interstellar neutrals . . . 40
  - 2.2.3 Ionization processes in the heliosphere . . . 42
  - 2.2.4 Features of the spatial distribution of PUIs . . . 43
  - 2.2.5 The velocity distribution function of PUIs . . . 47
  - 2.2.6 Theoretical PUI velocity distributions at 1 AU derived from test particle simulations . . . 54

3 **Instrumentation** 61
- 3.1 Time-of-flight mass spectrometers . . . 61
  - 3.1.1 Energy per charge separation . . . 63
  - 3.1.2 Time of flight measurement . . . 65
  - 3.1.3 Total Energy . . . 68
  - 3.1.4 Combining the measurements (Particle identification) . . . 68
  - 3.1.5 Onboard moments, matrix rates and Pulse Height Analysis (PHA) data . . . 69
  - 3.1.6 The instrumental entrance system and acceptance angles . . . 73
- 3.2 STEREO/PLASTIC . . . 73
  - 3.2.1 PLAsma and SupraThermal Ion Composition (PLASTIC) . . . 75
- 3.3 STEREO/MAG . . . 80

4 **Preparation of STEREO / PLASTIC and STEREO / MAG data** 85
- 4.1 Separation of He^+ pickup ions from STEREO / PLASTIC PHA events . . . 85
  - 4.1.1 Derivation of a mass separation scheme . . . 86
  - 4.1.2 Derivation of a mass per charge separation scheme . . . 88
- 4.2 Auxilliary data products . . . 94
  - 4.2.1 The heliospheric position of STEREO . . . 96
  - 4.2.2 Treatment of the magnetic field data . . . 96
  - 4.2.3 Combination with Maxwellian fits of Solar Wind Velocity Distribution Functions . . . 96
  - 4.2.4 Observations of ICMEs, SIRs and interplanetary shocks . . . 96
  - 4.2.5 Pre-filtered Fe PHA events . . . 96
  - 4.2.6 Derivation of the de-Hoffmann-Teller frame from STEREO / PLASTIC and STEREO / MAG observations . . . 97
- 4.3 Verification of data analysis methods and results of the instruments calibration . 99

4.3.1 Mapping of the instruments azimuthal position and quadrant bins 99
4.3.2 One dimensional transformed w spectra in the context of azimuthal position 104

5 Signatures of the He^+ pickup ion torus in three dimensional velocity distribution functions observed with STEREO / PLASTIC 109
5.1 Two dimensional projections of the He^+ pickup ion velocity distribution function 109
5.2 Probable causes for the unexpected behavior of the WAP pixels 110
5.3 Three dimensional He^+ pickup ion velocity distribution functions observed within the Solar Wind Sector 114
5.3.1 Theoretical considerations for histograms of w and φ in the special case of a radial reference velocity 115
5.3.2 Generalization of the histogram method for generalized reference velocity directions 117
5.3.3 Observed velocity distribution functions 119
5.3.4 Absolute velocity distribution functions 120
5.3.5 Differential velocity distribution functions 121
5.3.6 Differential velocity distribution functions in the context of different solar wind regimes 126
5.4 Azimuthal differences in the particle detection efficiency 138
5.4.1 Comparison of the solar wind sector's aperture halves over time 139
5.4.2 Azimuthally varying detection efficiencies as derived from SECCHI calibration rolls 140

6 Pitch angle distributions of He^+ pickup ions observed with STEREO / PLASTIC 154
6.1 Introductory discussion of instrumental limitations 154
6.2 Pitch angle distributions for selected magnetic field and solar wind conditions . . 161
6.2.1 Statistical considerations 162
6.2.2 Observed pitch angle distributions 169
6.2.3 Density enhancements at azimuthal magnetic field angles of $\pm 90°$ 172
6.2.4 Traces of fresh pickup ions and indications of transport as a function of the age of PUIs in the Focusing Cone region 173
6.2.5 Traces of fresh pickup ions and transport effects in different regions and solar wind conditions 176

7 Conclusions and Outlook 178

A Probability distribution of chance coincidences in case A 206

B Description of algorithms and computational schemes 208
B.1 Noise reduction 208
B.2 Normalizations and weights 209
B.2.1 Normalization to the occurrences of magnetic field directions 209
B.2.2 Normalization to the coverage of a particles gyro orbit within the aperture. 210

C Overview of moving averages of TCR counts in the Solar Wind Sector of STEREO A / PLASTIC for groups of azimuthal position bins 211

D Full overview of slices through the 3d He^+ PUI VDFs 211

1 Introduction

Interstellar Pickup Ions (PUIs) have been first directly observed in the solar wind (SW) by Möbius et al. [1985]. The SW is a continuous stream of charged particles emanating from the Sun [Biermann [1951], Parker [1958]] and forms a region called the heliosphere (e.g. Axford et al. [1963]), which is a bubble of plasma carved into the local interstellar medium [Spitzer [1942], Crutcher [1982], Lallement and Bertin [1992], Frisch et al. [2011]]. However, interstellar PUIs are neither of solar nor of heliospheric origin. They are created by ionization from interstellar neutrals (ISNs) which inflow into the heliosphere (e.g. Axford [1972]). As newly created ions they are picked up by the SW. An introductive review of the SW is provided in Chapter 2.1 and Chapter 2.2 discusses PUIs in further detail.

The predominant process of ionization depends on the particle species and the position of ionization in the heliosphere: The probability of photoionization by solar ultraviolet (UV) radiation scales with the flux of photons. Hence, this ionization process is more important at 1 AU than at the heliospheric boundary. In addition to photoionization, charge-exchange and electron-impact ionization with particles in the SW can ionize the ISNs. Here, the ionization probability is a function of the SW density (e.g. Axford [1972]). Since both the flux of photons and the SW density decline with increasing distance from the Sun, the ionization due to charge-exchange and electron-image ionization are also more probable close to the Sun than further outward.
Not only ISNs are ionized and picked up by the SW. Particles of heliospheric origin can also become PUIs. E.g. neutralized former ions from the SW can undergo similar ionization processes. Additionally, cometary or planetary material is sputtered by the SW, which also creates new ions. These PUIs of heliospheric origin are often referred to as inner-source PUIs and differ in their velocity characteristics significantly from PUIs of interstellar origin Gloeckler and Geiss [1998]. This work focuses on interstellar PUIs. So in the following, PUIs refers to interstellar PUIs only unless stated otherwise.

Observations of interstellar PUIs at 1 AU allow to infer parameters of the local interstellar medium which neighbors the heliosphere at a distance of at least 120 AU [Gurnett et al. [2013], Stone et al. [2013]], since the particles originate from ISNs and their characteristics are influenced by the characteristics of the former ISNs. Essentially, the PUIs provide a sample of elements found in the ISN (e.g. Axford [1972]). Yet, the parameters which can be inferred are not limited to a trace of the ISNs composition. From the spatial PUI density distribution the direction of the inflow of the local interstellar medium can be obtained [Moebius et al. [1995], Drews et al. [2012], Taut et al. [2018]]. Moreover, the observation of the PUI Velocity Distribution Function (VDF) as a function of spatial coordinates allows to infer not only the direction of the interstellar inflow, but the relative velocity between the heliosphere and the local interstellar medium [Möbius et al. [2015], Taut et al. [2018]].
Until direct observations of ISNs in the heliosphere were made with the interstellar boundary explorer (IBEX) [McComas et al. [2005]], PUIs were the primary method of observation of ISNs in the heliosphere. IBEX focused on the observation of energetic neutral atoms and revealed an unexpected feature: On maps, where densities were displayed as a function of viewing direction, a ribbon-like density enhancement is found [McComas et al. [2009]]. A complete understanding of the sources and mechanisms which create the ribbon is yet to be achieved. In some possible mechanisms for the creation PUIs are involved. For example, theoretical treatments which simulate outwardly transported PUIs and allow for re-neutralisation of the PUIs close to the heliospheric boundary, have been seen to reproduce the shape of the ribbon [Heerikhuisen

et al. [2010], McComas et al. [2014], Zirnstein et al. [2015]]. Such simulations rely on a good understanding of the transport of PUIs and knowledge about the PUI VDF. Moreover, an understanding of the processes which lead to the ribbon may also provide clues to the spatial structure of the heliosphere (e.g. Zirnstein et al. [2015, 2017]).

The pickup process creates a characteristic initial VDF for freshly created PUIs: Since the PUIs gyrate around the local magnetic field which is carried by the SW their motion is best described as a superposition of translation with the field which is carried by the SW and gyration around that field and a velocity contributed by the velocity of the former ISN. The initial velocity of gyration is the vectorial sum of the velocity which transports the field and the velocity of the former ISN at ionization (e.g. Axford [1972]). The velocity of the former ISN and the SW velocity from the transition from a resting frame into the SW frame therefore contribute to a field-parallel translation and the field-perpendicular fraction which adds to the velocity of gyration. In the following, the velocity component which carries the magnetic field is called the transport velocity. Under continuous ionization, the VDF is then a superposition of gyrations at different phases of the gyro orbit, but the same or similar gyration orbits. Hence, a torus is formed, which is centered in velocity space at the velocity which transports the magnetic field and is oriented perpendicular to the local magnetic field. Such a distribution is strongly anisotropic in pitch angle space.

Yet, transport processes modify the VDF and the pitch angle distribution. To describe the transport, the PUIs velocity $\vec{v}_{\mathrm{pui}}$ is related to the transport (or reference) velocity $\vec{v}_{\mathrm{ref}}$ and for simple comparison the quantity $w_{\mathrm{ref}} = |\vec{v}_{\mathrm{pui}}|/|\vec{v}_{\mathrm{ref}}|$ is obtained. For an injection at an angle of 90° between the magnetic field and $\vec{v}_{\mathrm{ref}}$ and at a phase of the PUIs gyration, for which the PUI velocity is parallel to $\vec{v}_{\mathrm{ref}}$, a value of $w_{\mathrm{ref}} = 2$ is found. Similarly, for an antiparallel velocity $w_{\mathrm{ref}} = 0$ is found, so that unaccelerated PUIs are found in the range of $0 \leq w_{\mathrm{ref}} \leq 2$. For w_{ref} the PUI velocities are related to a resting frame. However, since PUIs are transported by the SW, it is more convenient and natural to the PUI physics to convert the PUI velocity into the SW frame. This obtains $\varpi_{\mathrm{ref}} = |\vec{v}_{\mathrm{pui}} - \vec{v}_{\mathrm{ref}}|/|\vec{v}_{\mathrm{ref}}|$. In both the discussed cases which yield $w_{\mathrm{ref}} = 0$ or $w_{\mathrm{ref}} = 2$, $\varpi_{\mathrm{ref}} = 1$ is obtained. Therefore, the basic w_{ref} is a marker for the PUI velocity, which is independent of the gyration phase. However, for the vectorial difference required to compute ϖ_{ref}, not only the absolute velocities, but also the directions of both the PUI and the SW velocity are required. As is discussed in a following paragraph, this requirement is challenging for observation with a spacecraft.
For newly created PUIs, $\varpi_{\mathrm{ref}} = 1$ is expected. So, the ring-like distribution which is expected in velocity space is associated with a radius of $\varpi_{\mathrm{ref}} = 1$ around the transport velocity.
The previous theoretical treatment interaction of the particles with waves in the SW employs stochastic processes. From this the concept follows, that the pitch angle distribution is broadened swiftly compared to the time scale of transport from injection to 1 AU and lead to a more isotropic distribution in velocity space (e.g. Jokipii [1966], Vasyliunas and Siscoe [1976], Fisk et al. [1997], Saul et al. [2007]). These theoretical treatments of PUI transport therefore imply, that instead of an anisotropic ring distribution, because of scattering during transport a shell-like distribution is observed. Here, also a meaningful problem of PUI observation is seen, which is that instead of freshly created PUIs (the initial condition for transport), observed PUIs are to be considered as a mixture of only a small fraction of freshly created PUIs and of a large fraction PUIs which have undergone a considerable amount of transport. In addition to the discrepancy between theoretical expectations and PUI transport theory (i.e. the observation of anisotropic features at 1 AU) there is the caveat that the transport velocity and therefore also the PUIs velocity are not unambiguously defined. Commonly, the SW proton bulk velocity is employed

(e.g. Gloeckler and Geiss [1998]).
However, observed PUI VDFs in the solar wind frame are still a measure of the amount of scattering of pitch angles during transport. Indications that the scattering is less efficient than assumed, are observations of anisotropic features. Such observations were made by Moebius et al. [1995], Gloeckler and Geiss [1998], Oka et al. [2002] and initially led to the concept of a division of phase space into hemispheres where the efficiency of pitch angle scattering is different from hemisphere to hemisphere [Isenberg [1997]]. Different transport in and between hemispheres may explain anisotropic features in PUI VDFs. Yet, anisotropic features can also be tracers or remains of the initial torus distribution, especially if it is observed that their position in velocity space is a function of the magnetic field direction [Drews et al. [2015]].
In addition to pitch angles, also accelerations and decelerations in terms of ϖ_{ref} have been observed. Deceleration is expected to occur as a consequence of the SW's expansion: If the SW and the PUIs are modelled as an ideal gas, the expansion of the SW is adiabatic, so that as a consequence of the ideal gas law the PUIs are decelerated [Moebius et al. [1988]]. This also implies, that if this adiabatic cooling is considered as the only process of deceleration, values of $\varpi_{\mathrm{ref}} < 1$ refer to PUIs, which have undergone transport in contrast to freshly created PUIs with $\varpi_{\mathrm{ref}} = 1$. Furthermore, with this concept applied, ϖ_{ref} can be viewed as an estimation of the age of a PUI for values of $\varpi_{\mathrm{ref}} < 1$. Yet, this concept is based on an oversimplification and also any value of ϖ_{ref} can also be a combination of acceleration an deceleration effects, so that an inference of the PUIs age just from ϖ_{ref} is imprecise.
Concerning acceleration processes, acceleration from wave-particle interaction can be considered. Since the velocity of a charged particle in a magnetic wave field reacts nonlinearly to the wave (e.g. Keilbach et al. [2017a,b, 2018]). The nonlinear acceleration in wave fields of multiple waves with random phases has also been described by stochastic processes (e.g. Jokipii [1966]). The nonlinear acceleration can lead to suprathermal tails in the distribution of the PUIs absolute velocity. Similarly, discontinuities in the SW and compression regions are expected to significantly accelerate charged particles.Fittingly, compression regions were recently linked to suprathermal tails in the PUI VDF [Yang et al. [2020], Moebius et al. [2019], Bower et al. [2019]].
In addition, ϖ_{ref} as derived from observational data is dependent on the reference velocity employed for computation. If this velocity does not match the actual transport velocity, apparent accelerations and decelerations might occur. Commonly, the SW proton bulk velocity is employed (e.g. Gloeckler and Geiss [1998]). However, a different velocity may be more suitable. Recently, Němeček et al. [2020] presented a method to derive the de-Hoffmann-Teller (dHT) velocity. Since the dHT frame is a force-free frame, this velocity is an interesting candidate for a velocity to relate observed PUI VDFs to and ideally gain new insights into the transport of PUIs. For illustration, basic simulations of PUI transport are conducted with a test particle approach to visualize the apparent modifications in the PUI VDFs observed when an inadequate velocity frame for PUI transport is assumed. The simulation is presented as a closing chapter for the review of PUIs.

Up to Drews et al. [2015], studies limited the observations of PUI VDFs to one dimensional distributions. Such observations are challenging to obtain, especially since most of the instruments employed to observe PUIs either observe only a fraction of phase space or are not intended to resolve the velocities of incoming particles by direction or both. The Solar Wind Ion Composition Spectrometer SWICS instruments onboard Ulysses and the Advanced Composition Explorer have the capability to resolve particles by incoming direction, but with a coarse spatial resolution. Drews et al. [2015] employed observations of the PLAsma and SuptraThermal Ion Composition instrument on board the Solar TErrestrial RElations Observatory STEREO/PLASTIC to obtain two-dimensional PUI observations. The observations of Drews et al. [2015] also showed

anisotropic features in PUI VDFs, which resemble remnants or traces of an initial torus distribution. Since, as discussed in the following, the observation with STEREO/PLASTIC is affected by not yet completely described instrumental effects, the anisotropic signatures found by Drews et al. [2015] might also be caused by instrumental effects. Hence, this work also revisits STEREO/PLASTIC PUI VDFs with focus on instrumental effects and a discussion of the validity of anisotropic features in PUI VDFs.
To relate PUI velocities to the magnetic field, data from STEREO/PLASTIC and the Magnetometer MAG onboard of STEREO are employed. And since PLASTIC is theoretically capable to observe three dimensional (3d) particle velocities, this work aims to build on Drews et al. [2015] and obtain 3d PUI VDFs. Since PLASTIC is a time-of-flight mass spectrometer, the introduction to the instruments in Chapter 3 starts with a general review of time-of-flight mass spectrometers (Chapter 3.1). Then, details specific to PLASTIC are described in Chapter 3.2. Finally, Chapter 3.3 introduces STEREO/MAG.
The design concept of STEREO/PLASTIC aimed to enable the observation of charged particles with a lateral Field Of View (FOV) of almost 360° and in parts of the FOV with also latitudinal resolution, so that theoretically, the observation of 3d VDFs is feasible [Galvin et al. [2008]]. In practice, there are a plethora of challenges which hinder the derivation of 3d PUI VDFs from PLASTIC data, which in parts were already discussed by Drews et al. [2015], Taut et al. [2018]. Also, the Heavy Ion Sensor (HIS) [Owen et al. [2020]] aboard the 2020 launched Solar Orbiter [Müller et al. [2020]] utilizes a detection concept similar to PLASTIC. Hence, a method to derive 3d PUI VDFs and a detailed discussion of instrumental limitations and caveats is timely. In this thesis, a fist step to determine the 3d PUI VDFs is to analyze the data from PLASTIC's electrostatic deflection system to determine absolute velocities. This method is very unspecific to PLASTIC and can be applied to HIS, SWICS and other time-of-flight mass spectrometers. Similar to PLASTIC, the electrostatic deflection system of HIS is a section of a dome, wherein the actual azimuthal angle of incident is measured at the end of an ion's track through the instrument. The elevation angle is determined by an electrostatic deflection system at the entrance into the instrument. So, basically the vectorial velocity information is determined in spherical coordinates, which is analogous to how it is determined by PLASTIC. A robust method to determine 3d PUI VDFs from that information and a discussion of the method's limits and caveats can be directly related to HIS. Similar to PLASTIC, HIS measures the particles' time-of-flight and their total energy via a solid state detector (SSD). Since in this work, the position of Pulse Height Analysis (PHA) events in energy-per-charge vs. time-of-flight vs. total energy space is employed to identify the species of particles and separate He^+ from the rest of particles, also that method can directly be related to HIS. If the data of PLASTIC is analyzed in different sections of the instrument separately, for pitch angle distributions it has to be taken into account that the sections have a limited FOV. The respective implication also apply to HIS, since the FOV of HIS is approximately a quarter of PLASTIC's FOV.

Compared to SWICS, the construction of PLASTIC is more complicated. The aperture system of PLASTIC is divided into different parts. The solar wind sector, which has a latitudinal acceptance of 45° and the center of it points at the Sun. The other two parts of the aperture complete the almost 360° of the instrument's latitudinal FOV, but to a large part resolve the incident angles coarser than the solar wind sector. The angular resolution is managed by two different systems: A resistive anode which is located in the quadrant of the instrument in which also the solar wind sector is found and discrete anodes in the other quadrants. The discrete anodes divide the 90° of a quadrant into 8 bins and the resistive anode into 64 bins, wherein 48 bins fall into the solar wind sector.
Since, in contrast to earlier time-of-flight mass spectrometers, the design of PLASTIC aimed

at an almost full lateral coverage, the accommodation of the necessary parts which detect the particles is a challenge and some design choices for the instrument make it more challenging to process its data than e.g. for SWICS. Firstly, only two quadrants of the instrument are equipped with SSDs. SSDs measure the total energy of a particle. Secondly, latitudinal resolution which is achieved by electrostatic deflection is only available in the solar wind sector. Thirdly, in the lateral center of the solar wind sector a support structure is fitted at which particles are scattered. This introduces an ambiguity in the lateral position detection. Fourthly, since the particles in the solar wind sectors are guided to incident on the SSDs, the resistive anode is not triggered by particles themselves, but by secondary electrons which are released from the SSD when a particle impacts. Fifthly, since the aperture of the solar wind sector features electrostatic deflection, the geometry factor of the solar wind sector's aperture is different from the geometry factor from the different parts of the instrument (the wide angle partition). And finally, the particles' time-of-flight is measured by a two-point measurement for which a time-of-flight chamber is fitted in the instrument which requires a start and a stop signal to work. In PLASTIC the stop signal is triggered by different mechanisms in sections with SSDs than in sections without SSDs which makes PLASTIC more complex to analyze.
This may also be a probable partial reason why the count rates measured in the wide angle partition are inconsistent with those obtained in the solar wind sector. The count rates are systematically lower than in the solar wind sector and also differ unphysically from latitudinal position bin to position bin. The differences between the latitudinal position bins follow a seemingly random, but time stable pattern which is investigated and found to be independent of the local magnetic field direction.

In addition, long-term time series of counts in both halves of the solar wind sector are created for data from 2008 to 2019 to investigate a time dependency of the asymmetry and find traces of instrumental aging. During 2015 the spacecraft was located behind the Sun as seen from Earth. During that period the spacecraft performed a 180° roll. So, in data from 2015 on, it was expected that the long-term behavior of the ratio of count rates is inverted, if asymmetric detection efficiencies are discounted. Yet, the development of the count rate ratios after the roll is inconsistent with that expectation, but also with expectations arising only from asymmetric detection efficiencies before 2015.

In the light of the instrument's problems an approach to recalibrate the instrument based on PHA data with the goal to identify He^+ ions is presented in Chapter 4. Chapter 4 also describes auxiliarly data products employed for the following analysis.
Also, the method of Němeček et al. [2020] to derive the dHT velocity from observational data is adapted to STEREO / PLASTIC data, so that together with this work's derivation method of 3d He^+ future studies are enabled which investigate PUI VDFs with the aim to find a correct transport frame. Yet, such studies may be affected by instrumental limitations of STEREO/PLASTIC which are also discussed in this work.

In this work, only data from the solar wind sector STEREO A/PLASTIC is employed to derive 3d He^+ PUI VDFs and pitch angle distributions. Chapter 5 discusses 3d VDFs and Chapter 6 follows with pitch angle distributions and in both instrumental limitations to the results are discussed in detail.
In particular, it is found that the solar wind sector of the instrument detects particles with an asymmetric efficiency, so that in one half of the sector systematically more particles are detected than in the other half. The extent of these asymmetries is estimated by an investigation of data during time periods, when roll maneuvers were commenced which originally were intended to

calibrate the spacecraft's magnetometer. During these rolls which last 3 h, the spacecraft is rotated by 360° around the Sun-spacecraft axis. Efforts to quantify the asymmetries are discussed in Chapter 5.4.
Another instrumental effect, which needs to be considered if pitch angle distributions are observed, is that the measurement probability of a particle depends on the instrumental aperture's opening angles, the local magnetic field direction, the transport velocity, and the pitch angle. This is a consequence of the particles' gyration: In velocity space, parts of the gyro orbit can be located outside the areas which are covered by the instrument's aperture. This means that a particle must be at the right phase of its gyro orbit when close to the instrument in order to incident into the aperture. For PUIs, a uniform stochastic distribution can be assumed to describe their gyro phases. Then, the fraction of the gyro orbit covered by the aperture compared to the whole gyro orbit is a measure for the probability that a particle incidents into the aperture.
As an introduction into observations of pitch angle distributions, Chapter 6.1 derives a mathematical expression for that geometry based probability and demonstrates it by application to model distributions.Also, the geometry based probabilities are employed in the following as a reciprocal correction factor for derived pitch angle distributions.
Pitch angle distributions derived from STEREO/PLASTIC observations are presented in Chapter 6.2. The pitch angle distributions are ordered by the region where they were observed and the absolute velocity of the PUIs. It is found that the magnetic field directions and pitch angles at which anisotropic features are found approximately agree with expectations for freshly created PUIs for $\varpi_{\mathrm{SW}} \sim 1$. The similarity decreases if lower values of ϖ_{SW} are selected for analysis. This observation is a tracer of PUI transport processes and this applied method might help to estimate the time scale on which transport processes modify the pitch angle distributions.

If observations of an anisotropic structure in the PUI VDF persist, pitch angle scattering is weaker than initially assumed. However, the scattering may also be a function of the type of SW conditions that the PUIs have sampled. Due to a limited number of observations, studies which investigate the velocity characteristics of PUIs as a function of the SW type are, at the point of writing this work, just becoming feasible. The interesting nature of such studies are not only emphasized by this work, but also by e.g. Bower et al. [2019], who found observational hints to energization and scattering of PUIs in interplanetary shocks.
In addition, the combination of pitch angle and ϖ_{SW} distributions and the investigation, at which pitch angles anisotropic structures are found (if they are found) as compared to the direction of the interplanetary magnetic field as well as at which values of ϖ_{SW} these are found, also yields interesting constraints to the validity of common transport theories. E.g. if PUIs are preferentially found at pitch angles which accord to local production (pitch angles correlated to the magnetic field direction) for $\varpi_{\mathrm{SW}} \sim 1$, but not for smaller values, it could be interpreted as a trace of adiabatic cooling, since under the assumption of adiabatic cooling, smaller values of ϖ_{SW} correspond to older PUIs. Also, the values of ϖ_{SW}, at which anisotropic features are found, can also provide constraints for the heating and scattering of PUIs during transport.

2 Review of heliospheric physics specific to interstellar pickup ions

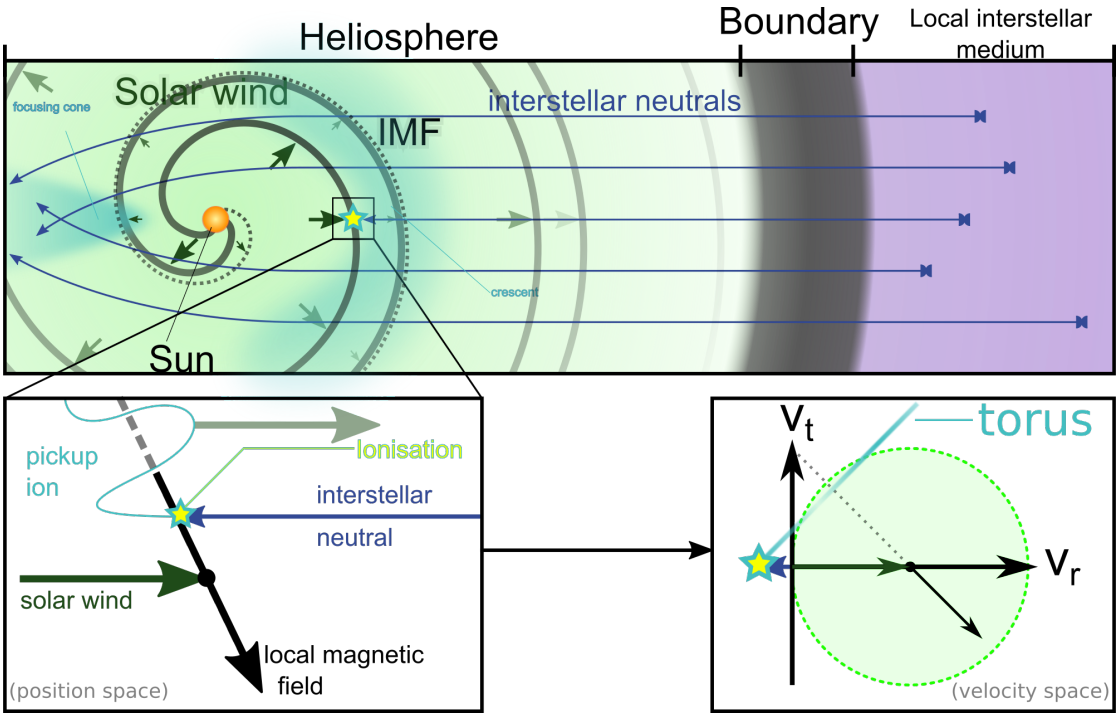

Figure 1: Schematic overview of the generation of pick-up from interstellar neutrals.

The physics of interstellar Pickup Ions (PUIs) is influenced by a variety of parameters of their surroundings. Hence, this chapter starts with a review of the PUIs surroundings, namely the Heliosphere. The Heliosphere is the region governed by and carved into the Sun's interstellar surroundings by the solar wind (SW) [Axford et al. [1963], Hundhausen [1968], Axford [1972]]. The SW is a stream of plasma, which emanates continuously from the Sun (e.g. Parker [1958], Prölss [2013]).

The first part of this chapter (chapter 2.1) is a review of a Heliosphere which begins with the SW's source, shifts its focus further away from the Sun by reviewing the physics of the SW in the order of small scales to larger scales. The largest scale structure formed by the SW is the Heliosphere and therefore the review ends with the Heliospheric boundary and the Heliosphere's surroundings.
Interstellar PUIs originate from the Heliosphere's surroundings (e.g. Axford [1972]), so it is convenient to continue in the second part of this chapter (chapter 2.2) with a review of interstellar PUIs.

2.1 The Sun, the Solar Wind, the Heliosphere and its local neighborhood

The SW is a continuous stream of charged particles emanating from the Sun. It is a magnetized plasma which expands from the Sun and passes Earth's orbit at average number densities of $\sim 5\,\mathrm{cm}^{-3}$. In comparison, an ultra high vacuum still ranges at number densities from $10^5 \mathrm{cm}^{-3}$ to $10^8 \mathrm{cm}^{-3}$ and air at normal pressure has a number density of $\sim 2.7 \cdot 10^{19} \mathrm{cm}^{-3}$ [ISO 3529-1:2019]. This means, that the physical properties of the SW are different from any artificially created plasma (on Earth). Especially the mean free path of particles in the SW is considerably longer than of particles in a laboratory plasma.

The first documented indicator of material being emitted from the Sun has been observed in 1859, when a sudden, localized increase in brightness of the Sun has been observed [Carrington [1859], Hodgson [1859]], which is a phenomenon now known to be connected to a coronal mass ejection.
Today it is known that such events are linked to geomagnetic storms occurring days later (e.g. Crooker [2000]). Thus, the influence of the Sun on human life on Earth goes beyond shedding light and heat on the planet: Eruptive events on the Sun like solar flares often emit X-Rays alongside energetic particles and thus cause disturbances to satellite communication and even enhancements of the electric ground level on Earth (e.g. Baker [1998], Crooker [2000]).
Apart from such bursts of high-energy particles from the Sun, the main component of particles emitted from the Sun is continuously emitted. Before the first direct observation of this component, the observation that comets have two tails has hinted at its existence: A tail is formed behind the comet (in opposite direction of motion) and another one seems to be pointing away from the Sun. While the first is related to neutral gas evaporating from the comet, the latter is peculiar, since it does not fit to the kinematics of the comet and an external force accelerates the particles of the second tail while not affecting the first tail. This led to the idea that the Sun emits a "wind" of charged particles which sputters charged particles from a comet and carries them outward [Biermann [1951, 1957], Parker [1958]]. In 1959 this SW was first directly observed by the Luna 1 spacecraft [Gringauz et al. [1960]] and later confirmed by many other spacecraft (e.g. Obridko and Vaisberg [2017]).

2.1.1 The Sun

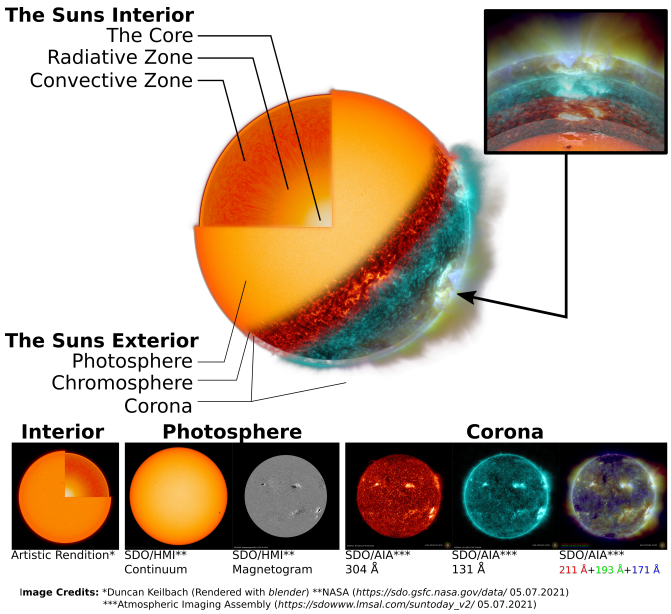

Figure 2: Depiction and overview of the Sun's layers. The central viewgraph shows a full disk observation of the Sun superimposed with its different layers analogous to different layers of an onion peel. The images, out of which this central viewgraph consists, are listed below the central viewgraph alongside the spacecraft and instrument. If applicable, also the wavelengths of the observations are listed there. The top right viewgraph is a superposition of the different layers' images rotated such, that a Sunspot is in the center of observation. The image credits are listed below the list of images.

Before the SW's properties are exhibited in further detail, the star it originated from is reviewed: The Sun is the only star which is close enough to Earth to be studied by humans as a three dimensional structure. It is also the only star close enough to Earth for direct observations of particles emitted from it. The study of the Sun also allows to draw conclusions about similar stars, especially other stars of the Sun's type, which is G2V (or G-type main-sequence) [Williams [2016a]]. However, a detailed description of all scientific aspects of the Sun, which provides a vast variety of interesting phenomena, would go beyond the scope of this work. The following provides a phenomenological overview of the Sun.

Given the high temperature of the Sun as well as the large mass of the Sun ($\sim 1.98 \cdot 10^{30}$ kg [Williams [2016a]]), to this date in-situ observations of the Suns interior are impossible to conduct. So far, the closest a spacecraft has approached to the Sun while remaining in operation is a distance of ~ 10 solar radii [Fox et al. [2016], JHU APL [2019]]. Therefore models of the Sun's internal structure are derived from conclusions based on what is seen from the outside. Since Wollaston [1802], Fraunhofer [1817] studied the H_α lines in the Sun's spectrum, the presence of hydrogen in the Sun is known. Further elements (e.g. Helium) have also been observed by spectroscopic measurement [Russell [1929], Asplund et al. [2009], Williams [2016a]].

In common theory (e.g. Weigert et al. [2012]), the Sun produces energy within its dense core (compare Fig. 2, from which heat is conducted by radiation and convection of hot plasma. Seen from inside to outside, first outward energy transport via radiation dominates (the radiative zone, Fig. 2), but as the radiation is absorbed by the Sun's material and thereby further heats it, convection dominates the heat transport (the convective zone, Fig. 2).

On the apparent (visible) surface of the Sun, the photosphere (compare Fig. 2), the convection is visible in form of structured cells (granules). Employing a black body reference spectrum, the photospheric effective temperature has been estimated as ~ 5772 K [Williams [2016a]]. Since the wavelengths emitted by the Sun make up the Earth's illumination by daylight, human eyes are naturally adapted to perceive the part of the main part of the spectrum which remains after

modification in the Earth's atmosphere (e.g. Meschede and Gerthsen [2015]). Therefore, the remote sensing observation of the photosphere is predominantly within the visual spectrum. The structuring of the photosphere can also be observed within magnetograms (e.g. Schou et al. [2012]). The observation of structures on the photosphere lead to the conclusion, that the photosphere rotates differentially about an axis tilted by several degrees w.r.t the Suns magnetic north pole. Hereby the rotation is faster at the equator ($\sim 25.6 days$) than at the Sun's poles ($\sim 33.5 days$) [Bartels [1934], Wilcox and Howard [1970], Snodgrass and Ulrich [1990]].
The plasma layer above the photosphere is the chromosphere (compare Fig. 2), which can be observed e.g. during solar eclipses together with another layer of the Sun which has due to its structuring during observation at solar eclipses been referred to as the crown of the Sun. This gives rise to the name solar corona [Prölss [2013]]. Particularly interesting about the corona is its temperature. Spectral lines observed within the corona hint towards temperatures in the magnitude of $\sim 10^6$ K (e.g. Brosius et al. [1996]). Under the assumption that the different layers of the corona follow a height dependent temperature profile, observations at different wave lengths allow to observe the Corona at different heights above the photosphere (e.g. Delaboudinière et al. [1995], Aschwanden [2006]).
The structure of the corona is mainly a tracer of the coronal magnetic field, so that the corona is a complex system of plasma flow, from which plasma escapes continuously: The SW (e.g. Parker [1958], Prölss [2013]).

2.1.2 Elemental composition and charge states in the solar wind

The SW consists of protons, electrons and heavy ions, wherein the elemental composition of the SW originates from the elemental composition of the photosphere, but interestingly does not match it. Elements with a low first ionization potential have been observed with enriched abundances and the elemental composition varies over time [Gloeckler and Geiss [1989], Zurbuchen et al. [2002]]. Apart from charged particles, also a small fraction of neutral atoms have been observed as part of the SW (e.g. Collier et al. [2001]). Of all positively charged particles in the SW, protons make up the largest fraction in terms of number density [Bame et al. [1975]], the remaining fractional density is shared by alpha particles and ions of elements with mass numbers of more than two [Bame et al. [1975]]. In the following, ions with mass numbers higher than two will be referred to as heavier ions. Of all ions except from protons, alpha particles are the most abundant [Bame et al. [1975]]. The exact elemental composition of the SW is challenging to obtain. Especially the ratio between heavier ions and protons is a seldomly observed parameter, since most instruments measure either heavy ions or protons. Since the flux of SW protons is considerably higher than the flux of heavier ions, the requirements for the observation of protons and helium ions differ from the requirements to observe heavier ions. With the PLASma and SupraThermal Ion Composition (PLASTIC) instrument aboard the Solar TErrestrial RElations Observatory (STEREO) it has been attempted to construct an instrument which observes protons, Helium and heavier ions (up to Fe) [Galvin et al. [2008]]. Also, since the elemental composition of the SW varies over time, any comparison of elemental abundances is to be seen as a momentary representation or as a long-term average. As a dramatic example for this, studies like von Steiger et al. [2000] and Zurbuchen et al. [2002] can be referred to, who employed data from the Ulysses spacecraft [Wenzel et al. [1989]]. Their findings indicated, that especially SW linked to coronal holes differs from the rest of the SW in elemental composition. They also noted a possible link between an element's first ionization potential and a density enhancement or depletion of the element w.r.t. their expectations.
Concerning a long-term average, the Genesis mission was designed to enable a detailed analysis of the constituents of the SW by returning samples of material to Earth, which have been ex-

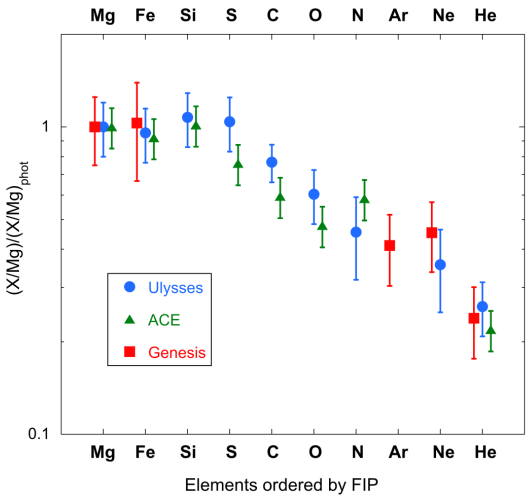

Figure 3: Elemental abundances of selected elements in the SW relative to photospheric abundances normalized to Mg. The figure has been taken from Reisenfeld et al. [2007]. The red plotted data belongs to Genesis observations [Burnett et al. [2003], Reisenfeld et al. [2007]]. The blue plotted data belongs to a study of Ulysses data from von Steiger et al. [2000] and the green data corresponds to ACE data. The elements in the plot have been sorted according to the first ionization potential. Interestingly, the relative abundance of elements in the SW is dependent of their first ionization potential.

posed to the SW [Burnett et al. [2003]]. The spacecraft contained a selection of flat discs made of different materials and exposed them to the SW once spaceborne, so that particles of the SW became embedded into the discs during the mission time lasting from 2001 to 2004. Even though the spacecraft crashed, since it failed to deploy its parachute on return to Earth, the returned samples have been retrieved. In following analyses (e.g. Reisenfeld et al. [2007], Vogel et al. [2011], Pepin et al. [2012]), the elemental and isotopic composition of the SW has been studied in detail. Parts of their studies results are shown in Fig. 3.

The charge states in the solar wind are dominated by processes in the lower Corona and the Photosphere: As the plasma expands outward with charge states reflecting a static equilibrium, the charge states freeze in [Hundhausen et al. [1968]]. In a simplified model, this is explained by comparison of the time scale for charge modification and the time scale for expansion. The first scales with the reciprocal of the electron density, which decreases in the Corona as the particles move away from the Sun (hence the time scale increases). The latter decreases within the Corona as the particles move away from the Sun. Hence, a point in the Corona exists, where charge modification is considerably slower than expansion [Hundhausen et al. [1968], Owocki et al. [1983], Aellig et al. [1997]].
The freezing in of charge states allows to infer the electron temperature in the Solar Corona from the SW's charge composition [Owocki et al. [1983]]. However, it should be noted, that depending on the geometry of the coronal magnetic field, the particles' trajectory in the Corona is more dynamic and complicated than a simple radial expansion. Also the assumption of an equilibrium state is unrealistic, since the Corona is highly dynamic. Another caveat to be considered, if the electron temperature is inferred from the SW's charge composition, assumptions about the electron Velocity distribution Functions (VDFs) shape need to be made. The assumption of a

model distribution possibly introduces a systematic error into the inferred temperatures.

2.1.3 Magnetic field conditions and global properties of the Solar Wind

In this chapter, global properties of the SW and the embedded magnetic field are reviewed. However, apart from the discussed models also medium scale structures (compare Chapter 2.1.5) and microphysical processes are found in the SW, which deviate from the global models. A review of the microphysical properties of the SW particles is provided in Chapter 2.1.8 and a brief and non exhaustive review of wave activity is provided in Chapter 2.1.6.
The solar sources of the SW have not been fully identified yet. It is known, that the SW emanates in different streams. Hereby, the field lines of the solar coronal magnetic field above coronal holes are open in radial direction and allow for outward plasma flow. Thus, observations point towards a magnetic connection between the coronal holes and some of the streams of SW [McComas et al. [2000]] . Yet, these observations only connect part of the different streams of SW to these source regions.
Also, the plasma's properties like the average velocity or elemental composition differ from stream to stream. The differences from stream to stream lead to the conception of different types of SW. We focus on different concepts to divide the streams into different types of SW in section 2.1.4.
The idea to categorize the SW streams is physically meaningful. One argument for this is, that the SW streams tentatively originating from coronal holes are similar to each other e.g. in the range of velocities, in which they are observed [McComas et al. [2000]]. Another more important argument is, that the different streams of SW do not mix with each other. This leads to the different streams in the SW forming a complex and partially interwoven strand structure often referred to as the magnetic carpet [Borovsky [2008]] (compare Chapter 2.1.5). However, first a more global model of the magnetic and flow structure of the SW is reviewed.

2.1.3.i The global heliospheric magnetic field: Parkers model On global scales, the motion of the SW is described by an adiabatic radial expansion [Parker [1958]]. Outside the corona, the hydrodynamic pressure exceeds the magnetic pressure and the magnetic field freezes in. This means, that the magnetic field is dominated by the motion of the plasma.
The global approximation of the resulting structure of the magnetic field in the ecliptic plane is described by the Parker-Model [Parker [1958]]. It assumes a single type, homogeneous SW which emanates from source regions on the photosphere and that the SW expands radially. Also, the source regions of the SW rotate with the photosphere and the rotation of the photosphere is assumed constant (not differential). Since the source region of a SW stream rotates with the photosphere, the SW stream is on global scales not shaped like a radial line like one would expect from a radial expansion. Rather, the streams shape is spooled by the rotation and a spiral structure is formed on global scales. Since the magnetic field is dominated by the kinetic properties of the SW, the magnetic field within the ecliptic plane is an Archimedian spiral on global scales [Parker [1958]].

Intuitively, the resulting steady-state magnetic field is best formalized in a spherical coordinate system with the radial component B_r, the ecliptic angular component B_θ and the azimuthal

angular component B_ϕ. In this coordinate system [Parker [1958]] states

$$B_r(r,\theta,\phi) = B(\theta,\phi_0)\cdot\left(\frac{b}{r}\right)^2, \quad (1)$$

$$B_\theta(r,\theta,\phi) = 0, \quad (2)$$

$$B_\phi(r,\theta,\phi) = B(\theta,\phi_0)\cdot\left(\frac{\omega_P}{u}\right)(r-b)\left(\frac{b}{r}\right)^2\sin(\theta)\ \text{, where} \quad (3)$$

ω_P is the angular frequency of the photospheric rotation and u is the average solar wind velocity. $B(\theta,\phi_0)$ and b normalize the model by providing a reference magnetic field $B(\theta,\phi_0)$ at the distance b from the Sun.
In this model, the angle between the SW velocity and the magnetic field vector increases with distance to the Sun. At 1 AU it is approximately at 45°. This angle can be seen as a guideline for global averages and will therefore be referred to as Parker angle.

2.1.3.ii Generalizations, Improvements and different approaches Obviously the model by Parker [1958] is an oversimplification, as it

- describes a steady-state magnetic field on global scales,
- assumes a single velocity of the SW,
- does not include the differential nature of the photospheric rotation
- does not include the complex structure of the photospheric magnetic field
- does not take into account temporal variations of the conditions at the Sun.

Adopting the general idea of Parkers model, Fisk [1996] proposed a model for the global magnetic field including the differential rotation of the photosphere modeled by moving footpoints of the magnetic field lines. For this model it is also assumed that a large, polar coronal hole exists which is aligned to an axis offset from the solar rotation axis and the axis rotates rigidly [Fisk [1996], Fisk et al. [1999]]. As a third assumption it is stated, that the SW from the polar coronal hole expands nonradially. This model was developed at the time of publication of findings of the Ulysses mission [Wenzel et al. [1989]], which observed the SW conditions at latitudes far from the in-ecliptic plane. One of these findings were deviations from the global structure of the Parker model (e.g. Balogh et al. [1995]). As a main result, the model produces a nonzero component of the magnetic field in the B_θ component [Fisk [1996], Fisk et al. [1999]] and excursions in latitude of the magnetic field, which have been observationally backed by e.g. Zurbuchen et al. [1997].
Yet, regions exist, where the model by Parker [1958] is more suited to approximate the magnetic field [Fisk et al. [1999]]. So a hybrid-model of both was conceived by Burger and Hitge [2004], which is referred to as the Fisk-Parker model in the following.

The models for the heliospheric magnetic field discussed to this point are global models and thus not made to describe the dynamic and medium to small scale behavior of the field. Models, which aim to reproduce a more detailed behavior of the magnetic field employ magnetogram images of the photosphere[1] as a boundary condition. The potential field source surface model (PFSS) assumes in approximation a net zero current in the SW, which enables the existence of

[1]For information about instrumentation for the observation of photospheric magnetic field, the interested reader may refer to e.g. the Helioseismic and Magnetic Imager [Schou et al. [2012], Scherrer et al. [2012]] onboard the Solar Dynamics Observatory [Pesnell et al. [2012]].

a scalar potential Φ describing the magnetic field via $\vec{B} = -\vec{\nabla}\Phi$. Since Maxwells equations state $\vec{\nabla} \cdot \vec{B} = 0$, the Laplace equation $\triangle\Phi = 0$ describes the scalar potential [Altschuler and Newkirk [1969]]. While these models are able to reproduce closed magnetic structures above e.g. sun spots, which can be observed in X-Ray images of the Sun's corona (e.g. Sams III et al. [1992]), they are not precise. Studies like Peleikis et al. [2017] and Kruse et al. [2021] attempted to trace different SW streams which have been observed in-situ at 1 AU, to magnetic field structures obtained from a PFSS model and obtained low rates of matching. Also PFSS models extrapolate the magnetic field only from the Photosphere up to a so called source surface, which is typically a sphere (although ellipsoids have also been suggested [Kruse et al. [2020]]) of several solar radii. Different approaches, which model the whole heliosphere, employ complex simulation software of the solar wind plasma[2]. Since these models are limited by the capacity of computational devices, they model the SW and its magnetic field with rough spatial resolution and require a set of simplifications. To describe the simulated modelling of the SW in full detail would go beyond the scope of this work.

2.1.4 Solar wind classification

As the foregoing section about models of the interplanetary magnetic field shows, the coronal magnetic field has a highly complex structure. As the SW is emanated from these, it is also governed by complex structures on varying scales (e.g. Borovsky [2008]). Therefore study of the spatial structure of the SW is an interesting field, since the SW exhibits interesting features from scales of a protons gyro-orbit up to the global scale of the heliosphere (e.g. Verscharen et al. [2019]). Of special interest for this work is the classification of the SW. The different streams the SW consists of not only differ from each other in terms of the elemental and charge state composition (e.g. Geiss et al. [1995b], Aellig et al. [1999]), but also in terms of their microphysical properties (e.g. Marsch et al. [1982], McComas et al. [2003], Borovsky [2008]).
Historically, it was a commonly used approach to divide the SW by average velocity v_{sw} into two to three categories (e.g. Feldman et al. [2005]), these have been compiled into Tab. 1. The exact velocity for the categorizations sometimes varies slightly. Hence Tab. 1 provides example values. Although the SW is highly dynamic and the distribution of velocities in the SW depends on solar variables (e.g. on larger time scales i.e. the solar cycle) [Kasper et al. [2007]], as a guideline for the reader, Fig. 4 depicts the distribution of average solar wind velocities as observed when the Genesis spacecraft collected samples from the SW. If the approach of classification by velocity is used, ejecta (products of coronal mass ejections and other eruptive events on the Sun), SIRs and CIRs should be explicitly excluded, since the physical properties of particle transport differ considerably in them (e.g. Jian et al. [2013], Xu and Borovsky [2015], Jian et al. [2018, 2019]).

2.1.4.i Coronal hole solar wind By definition, the SW originates at the Sun and the most intuitive way one would imagine the outflow of a SW stream from the Sun is a radial, ballistic flow from the Photosphere onwards like the model of Parker [1958] proposed it (compare Chapter 2.1.3.i). However, as described in chapter 2.1.3.ii the shape of the coronal magnetic field is considerably more complicated. So at least before the point of frozen-in magnetic fields the assumption of radial outflow does not hold true. Still, zones in the coronal magnetic field exist, which feature open[3], magnetic field lines. Since the larger of these zones appear dark in X-Ray and EUV, these regions are called coronal holes [Prölss [2013]].

[2]The interested reader may refer to Gombosi et al. [2018]

[3]Here, open means that the field lines do not close in proximity to the Sun. Rather, their shape is governed by the expansion of the SW. In theory, the field lines will become closed eventually on scales of several hundreds of AU in regions, where the SW encounters the local interstellar medium and the field lines reconnect.

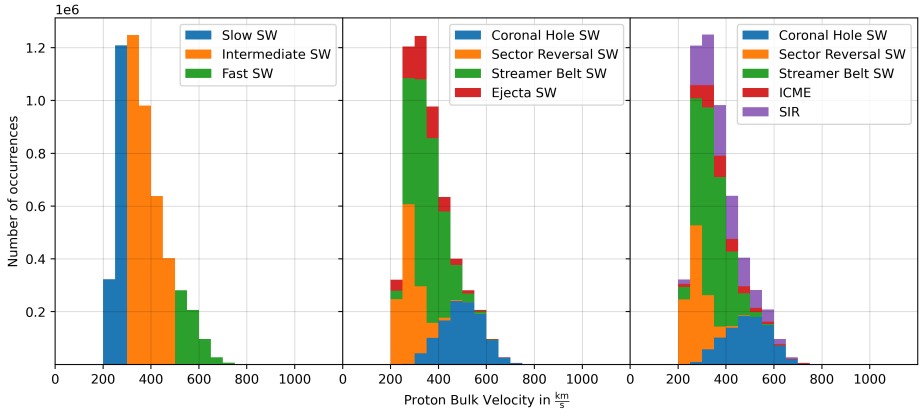

Figure 4: Distribution of average SW velocities as observed during the period of 2008 until 2019 by STEREO/PLASTIC. In all three panels a different way of characterizing the SW is employed. In the left panel, the SW is just classified by velocity and divided into three groups. For the center panel the classification scheme of Xu and Borovsky [2015] has been employed. The ejecta classification of this scheme has been observed to falsely classify parts of slow, dense and cold SW as ejecta. Hence, the right panel employs the same scheme with a modification: The ejecta classification is omitted. Instead, time periods indicated by the ICME and SIR lists of [Jian et al. [2013, 2018, 2019], Kucera [2022]] are accordingly classified.

Category	Requirement in a two type categorization	Requirement in a three type categorization
slow SW	$v_{sw} < 450 \frac{\text{km}}{\text{s}}$	$v_{sw} < 400 \frac{\text{km}}{\text{s}}$
intermediate SW	-	$400 \frac{\text{km}}{\text{s}} \leq v_{sw} < 500 \frac{\text{km}}{\text{s}}$
fast SW	$450 \frac{\text{km}}{\text{s}} \leq v_{sw}$	$500 \frac{\text{km}}{\text{s}} \leq v_{sw}$

Table 1: Commonly used classification to divide the SW into classes based on velocity. In the two type categorization, the intermediate SW category is not existent. It is noteworthy, that classification on velocity alone is generally neither a good representation of the detailed compositional and physical properties nor of the winds definitive solar origin (e.g. Xu and Borovsky [2015], Peleikis et al. [2017]).

Early observations showed a correlation between solar wind streams of high velocity and coronal holes as a projected source [Krieger et al. [1973]]. Later, combined observations of the mean SW velocity, magnetic field polarity (both in situ and out of the ecliptic plane) and coronograph images linked to in-situ observations of the SW at velocities roughly faster than $\sim$ 450 km/s from the Ulysses spacecraft [Wenzel et al. [1989]] to polar coronal holes by projection of the spacecraft's position [McComas et al. [2000]]. This lead to the general assumption, that the fast SW (compare table 1) originates from coronal holes. This, in turn opens the still unresolved question of the origin of the slower parts of the SW. The elemental and charge state composition of magnetic loops (i.e. above active regions of the Sun) resembles the composition of the slower SW. This lead to the assumption that these loops are part of the origin of the slower SW (e.g. Antiochos et al. [2011]). The problems with finding the origin of the slower SW may also hint at

a general problem of the classification of the SW by velocity: It is crude and prone to systematic error: A slower SW stream might be subject to acceleration processes from its origin to the point of observation. So, if classified by velocity alone, a SW stream may be wrongly classified with respect to the intended classification. Hence, the category of SW originating from coronal holes will be referred to as coronal hole wind instead of fast SW, so that its origin is reflected rather than its velocity characteristic. In Fig. 4 velocity histograms of SW protons are plotted. In the left panel, the histogrammed data is sorted by a classification algorithm based on velocity alone (according to Tab. 1). In the center panel, the histogrammed data is sorted by a classification scheme adapted from Xu and Borovsky [2015] (compare Chapter 2.1.4.iii). A comparison between both panels allows to compare the coronal hole wind with the velocity classification and while indeed most almost all of the fast SW of the left panel corresponds to coronal hole wind in the center panel, in the intermediate SW velocity range also coronal hole wind is found, but alongside other types of SW.

It also needs to be remarked that a full categorization scheme of the SW must include stream interaction regions (SIRs)/ corotating interaction regions (CIRs) and ejecta, since the former is a region of acceleration and the latter is material from eruptive events at the Sun (compare chapter 2.1.5).

2.1.4.ii Parameters for classification As the foregoing section showed, a classification of the SW by velocity only is unreliable in the separation of the SW into physically meaningful categories. The categorization by origin is a more promising approach, but coronal hole wind is the only category to haven been directly linked to source regions yet (e.g. McComas et al. [2000]). So, different approaches are worthwhile to examine.
Naturally, the set of parameters employed for classification is dependent of the intent of use of the classification scheme. Since the charge states of the SW ions freeze in, they are not only a tracer of the coronal temperature of their source region, but are also believed to remain almost constant during the expansion of a SW stream. Therefore, the ratio of O^{7+} density to O^{6+} density, C^{6+} to O^{5+} are common products employed to characterize SW streams.

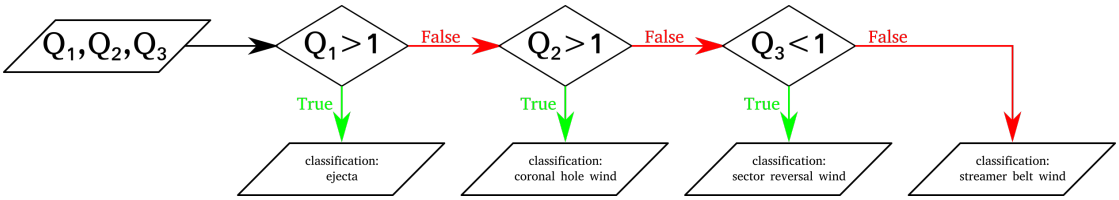

Figure 5: Flow diagram to classify SW according to the classification scheme of Xu and Borovsky [2015], which divides the SW up into four classes. The input quantities $Q1$, $Q2$ and $Q3$ are defined in Eqs. 4,5 and 6

2.1.4.iii The Xu-Borovsky Scheme The commonly used Xu-Borovsky [Xu and Borovsky [2015]] Scheme characterizes the SW into four groups based on three parameters. The quantities the scheme categorizes the SW streams by are

- the proton density n_p
- the average velocity of the proton core v_p

- the proton temperature T_p
- the absolute magnetic field B

From these the three quantities

$$Q_1 := 0.841 B n_p^{-0.315} T_p^{-0.222} v_p^{-0.171} \quad (4)$$

$$Q_2 := 0.877 \cdot 10^{-11} T_p B^{1.42} v_p^{3.44} n_p^{-2.12} \quad (5)$$

$$Q_3 := 0.0561 T_p B^{0.752} v_p^{0.445} n_p^{-1.14} \quad (6)$$

are computed to classify the SW into four categories employing the algorithm outlined in Fig. 5. The four classes of SW proposed by this scheme retain the coronal hole SW, but also include sector reversal and streamer belt winds as well as ejecta. The streamer belt SW can roughly be seen as the successor of the slow SW category from the classification by velocity outlined in table 1. The sector reversal SW originates most likely from the top of helmet streamers (where the polarity of encompassing open magnetic field lines reverses). It is likely to find more turbulent and wave phenomena in faster SW types (e.g. Bruno and Carbone [2013]). This underlines the importance of a separation of data into different types of SW.
The ejecta group may not accurately classify all ICMEs. Also stream interaction regions are not represented in this scheme. Hence, for this work the scheme is modified: The decision, whether wind is ejecta or not, is omitted, instead only the conditions dependent of Q_2 and Q_3 are evaluated. Afterwards, all wind is filtered for times, which occur within ICME and/or SIR lists (e.g. [Jian et al. [2013, 2018, 2019], Kucera [2022]]).
Although their categorization scheme has been developed for ACE/SWICS data, we adapt their approach to STEREO/PLASTIC data, as STEREO also orbits the Sun at $\sim$ 1 AU. Such an approach has also been employed by e.g. Kruse et al. [2021].

2.1.5 Medium to large scale structures in the solar wind

The different streams of SW outflowing from the Sun result in a structuring of the SW, which can also be observed at 1 AU as the ideas to classify the SW of the previous chapter demonstrated. The expansion of different SW streams into the Heliosphere is postulated to form a complex and intertwined structure of SW streams [Bartley et al. [1966], Bruno et al. [2001]], which is sometimes referred to as a magnetic carpet (e.g. Borovsky [2008]) and of multifractal nature (e.g. Verscharen et al. [2019]). Since all of these streams are fully magnetized plasma, they can not mix each other (magnetic field lines do not cross), which results in regions of interaction as well as particle acceleration within the Heliosphere (e.g. Prölss [2013]).

2.1.5.i Coronal mass ejections and ejecta Apart from the continuously outflowing component of the SW the Sun is known to emit bursts of matter in eruptive events [Carrington [1859], Hodgson [1859]]. The study of these events is a field of its own. To describe it in exhausting detail lies clearly beyond the scope of this work. However, the interested reader may refer to Webb and Howard [2012].
In short, coronal mass ejections (CMEs) emit a burst of magnetized plasma (ejecta) into the Heliosphere, which can not mix with the rest of the SW hence forming an outwards travelling bubble, which often drives a shock wave in front of it. Also, a distinct structure, called a magnetic cloud, is found in association with most CMEs. In general, CMEs can be seen as disturbed SW conditions and regions of particle acceleration. Therefore, observational lists of CMEs have been created (e.g Cane and Richardson [2003], Richardson and Cane [2010]).

2.1.5.ii Stream interactions and co-rotating interaction regions Stream interaction regions are a consequence of the simultaneous emission of different SW streams from the Sun and can be well explained with the SW model by Parker [1958]. The following description is well known to the extraterrestrial physics community and can be found in e.g. Jian et al. [2006]. Considering two streams of SW with two different velocities, the respective spiral structure of each stream is curved differently, since the curvature is a function of SW velocity. This gives rise to a point, where the less curved stream of the faster of both streams collides with the slower one. Being magnetized plasmas, both can not mix with each other. Hence, the faster SW is slowed, while the slower SW is accelerated. Since the SW is supersonic, the information of the acceleration/deceleration travels slower through the medium than the medium itself, so that on both sides of the stream interaction shocks are formed. Some SIRs in the SW remain stationary and locked to the 27-day rotational period of the Sun. In this case, they are called CIRs.

2.1.6 Wave phenomena in the Solar Wind

As a magnetized plasma, the SW can be perturbed by many different types of plasma waves (compare e.g. Bruno and Carbone [2013] for a broader overview). Since wave particle interaction can lead to significant acceleration processes (e.g. Jokipii [1966], Tsurutani and Lakhina [1997]), the VDF of not only the SW but also particles embedded into it (e.g. PUIs) can be modified by plasma waves. As a magnetized plasma, fluctuations or disturbances in the velocity of particles in the SW couple to modifications in the electric and magnetic fields which conversely influence the particles' motion (e.g. Alfvén [1942], Stix [1957, 1992], Baumjohann and Treumann [2012]). Also wave phenomena lead to resonant and, in parts, nonlinear effects. Depending on the particles involved in the oscillation, different wave modes and polarizations (or combinations thereof) are possible. Yet, a full coverage of wave types in the SW is clearly beyond the scope of this work and the interested reader may be referred to overview and textbook work, such as Stix [1992], Baumjohann and Treumann [2012], Bruno and Carbone [2013]. Pure electron waves are not treated in this work, since an electrons' gyration handedness is opposite to the gyration handedness of positively charged ions which makes electron specific wave modes less relevant for this work than proton and heavier ion specific waves.

Name	Symbol	Definition
sound velocity	c_s	$c_s = \sqrt{\frac{\gamma p_p}{m_p n_p}}$
Alfvénic velocity	v_A	$v_A = \frac{B_0}{\sqrt{\mu_0 m_p n_p}}$
magnetosonic velocity	c_{ms}	$c_{ms} = \sqrt{c_s^2 + v_A^2}$

Table 2: Definition of typical wave velocities in a single fluid magnetized proton plasma as it can be found in e.g. Baumjohann and Treumann [2012]. In the definitions the following quantities are employed: adiabatic index γ, kinetic proton plasma pressure p_p, proton mass m_p, proton density $n_{0,p}$, B_0 the magnitude of the background magnetic field, m_i the mass of an ion heavier than protons, n_i the density of that ion and μ_0 the vacuum permeability.

2.1.6.i Magnetohydrodynamic considerations This chapter reviews mangetohydrodynamic considerations, which lead to a description of many wave modes including the Alfvénic and the magnetosonic wave. The considerations of this chapter focus closely on the computations outlined in Baumjohann and Treumann [2012] and are held as a brief overview rather than a

concise mathematical treatment. The interested reader may refer to text books like Stix [1992], Baumjohann and Treumann [2012] for a more detailed computation.
In a single-fluid proton plasma which is initially stationary and homogenous, small time dependent fluctuations in density δn_p, velocity $\delta\vec{v}$, electric field $\delta\vec{E}$ and magnetic field $\delta\vec{B}$ are introduced. Hereby, small means, that the amplitude of the magnetic field's fluctuation is smaller than the stationary magnetic field $\vec{B}_0$, hence $|\delta\vec{B}| << \vec{B}_0$ applies. Then, a linearized approach for proton density n_p, velocity $\vec{v}$, electric field $\vec{E}$ and magnetic field $\vec{B}$ is justified. If the coordinate system is chosen such that the overall pressure is in equilibrium, the average electric fields and velocity vanish, then the linearized approach leads to

$$n_p = n_{0,p} + \delta n_p \tag{7}$$
$$\vec{v} = \delta\vec{v} \tag{8}$$
$$\vec{E} = \delta\vec{E} \tag{9}$$
$$\vec{B} = \vec{B}_0 + \delta\vec{B} \; . \tag{10}$$

Now, with the definitions in Tab. 2, the condition that the background magnetic field is aligned with the z-axis $\vec{B}_0 := B_0\hat{e}_z =: B_0\hat{e}_\parallel$ and the wave ansatz $\delta\vec{v} = \delta\vec{v}_0 \exp\left(i\vec{k}\cdot\vec{x} - i\omega t\right)$ are introduced where $\vec{k}$ is the wave vector, $\vec{x}$ the location, ω the circular wave frequency and t time. Since the wave propagation is coupled to the protons' motion and the protons' motion is governed by gyration around the local magnetic field, it is convenient to split the quantities into a field parallel component (indicated by the index $\parallel$, e.g. $k_\parallel$ which is a wavevector of parallel propagation) and a perpendicular component (indicated by the index $\perp$).
With these definitions, the continuity equation, the equation of momentum conservation and Faraday's induction law are employed to yield the condition

$$\left(\left(\omega^2 - k_\parallel^2 v_A^2\right)\hat{1} - c_{ms}^2\vec{k}\vec{k} + \left(\vec{k}\hat{e}_\parallel + \hat{e}_\parallel\vec{k}\right)k_\parallel v_A^2\right)\cdot\delta\vec{v} = 0 \; . \tag{11}$$

Since a nonzero velocity fluctuation is required for wave propagation, the first part of the product is of interest for the solution. To simplify that part of the equation, a coordinate system is chosen, where $\vec{k}_\perp \parallel \hat{e}_x$ applies, so that the wave vector is split into parallel and perpendicular components via $\vec{k} = k_\parallel\hat{e}_\parallel + k_\perp\hat{e}_x$. Then Eq. 11 transforms to

$$\begin{pmatrix} \omega^2 - v_A^2k_\parallel^2 - c_{ms}^2k_\perp^2 & 0 & -c_s^2k_\parallel k_\perp \\ 0 & \omega^2 - v_A^2k_\parallel^2 & 0 \\ -c_s^2k_\parallel k_\perp & 0 & \omega^2 - c_s^2k_\parallel^2 \end{pmatrix}\begin{pmatrix}\delta v_x \\ \delta v_y \\ \delta v_z\end{pmatrix} = 0 \tag{12}$$

and a solution is found if the matrix's determinant vanishes. Each of the equation's solutions yields a different wave mode. In this work, two of these solutions are reviewed:

- the Alfvénic wave with $\omega = \pm k_\parallel v_A$ (Chapter 2.1.6.ii) and
- the magnetosonic wave with $\omega^4 - \omega^2c_{ms}^2k^2 + c_s^2v_A^2k^2k_\parallel^2 = 0$ (Chapter 2.1.6.iv).

However, before these are reviewed, it must be acknowledged, that the SW not only consists of protons. Not only electrons contribute to the plethora of wave modes in the SW with their specific and hybrid modes (e.g. Stix [1992], Baumjohann and Treumann [2012]), but also the ions heavier than protons in the SW contribute to the collective behavior of the SW plasma. With the contribution of different ions new wave modes are introduced. In addition, the Alfvénic velocity is modified with contributions depending on the ions' mass density (compare Tab. 2) and the Alfvénic mode becomes the ion-cyclotron wave which is as well as the Alfvénic mode further reviewed in Chapter 2.1.6.ii.

2.1.6.ii Alfvénic waves in the Solar Wind The Alfvénic wave [Alfvén [1942]] is supported by fully magnetized plasmas and is a circularly polarized wave perturbing both the SW ion velocity as well as the magnetic field lines in unison. Especially because they are circularly polarized and within the gyro frequency range of many charged particles embedded into the SW, Alfvénic waves are considered an important type of waves for resonant wave-particle interaction. Generally, Alfvénic waves exist in frequency ranges below the proton cyclotron frequency and expand with a phase velocity of v_A as outlined in Tab. 2 which is commonly also called the Alfvénic velocity. However, this model strictly only holds true for a single ion plasma, since different ions have different cyclotron frequencies and are therefore differently susceptible to resonance with circularly polarized waves (e.g. Tsurutani and Lakhina [1997]). In the SW this means, that the single-fluid proton Alfvénic velocity is an approximation, since protons make up the majority of ions in the SW (compare Chapter 2.1.2). However, especially the contribution of α particles to the Alfvénic velocity is non negligible and correction terms need to be considered (e.g. Baumjohann and Treumann [2012]).
In addition, the inclusion of an ion species alongside the protons introduces a complication to the dispersion relation of the Alfvénic vecloity at frequencies, which are not considerably lower than the proton cyclotron frequency. In this frequency range, the wave mode transitions into an ion cyclotron wave [Stix [1957], Verscharen and Marsch [2011]]. Here, with increasing absolute wave vector value, the frequency asymptotically closes to the proton cyclotron frequency $\omega_{c,p}$, so that both the group and the phase velocity decrease gradually with increasing absolute wave vector. At and above the proton cyclotron frequency this wave mode does not exist. However, different wave types with different properties take its place (e.g. Stix [1992]).
In contrast to the dispersion relation of the single-fluid Alfvénic wave which is $\omega = \pm v_A k_\parallel$ which results in constant phase and group velocity, the ion cyclotron waves dispersion relation is given by

$$\omega = \omega_{c,p} \cdot \left((kl_p)^2 + \frac{1}{2}(kl_p)^4 - \frac{1}{2}(kl_p)^3 \sqrt{(kl_p)^2 + 4} \right)^{1/2} \quad \text{, where} \tag{13}$$

l_p is the proton inertial length (e.g. Verscharen and Marsch [2011]).

2.1.6.iii Identification of Alfvénic waves from HELIOS data The mission duration of the HELIOS spacecrafts lasted from 1974 to 1985 and the spacecrafts were launched onto elliptical orbits around the Sun which brought them towards minimum distances of 0.29 AU from the Sun. Both spacecraft were equipped with triaxial fluxgate magnetometers which had the capability to observe the magnetic field with a rate of 4 Hz. Employing data from that spacecraft, computational methods to identify Alfvénic waves within the magnetic field data are explored. The study outlined in the following, was presented by Keilbach et al. [2019].

2.1.6.iii.a Phenomenological identification and general issues The aim of the study was to study Alfvénic waves as a function of the distance from the Sun as well as providing patterns of measured Alfvénic waves as input data for simulation. To that end a wavelet-based algorithm was developed to identify Alfvénic cyclotron waves in time series of magnetic field vectors observed by HELIOS. For the algorithm the characteristics of a cycltron were employed, namely for a cyclotrons the following statements are true (e.g. Tsurutani and Lakhina [1997])

- A left-hand circulary polarized wave field is found, ideally superposed to a constant or very slowly (compared to the wave's frequency) varying background magentic field. However, in real data often the waves are superposed to or interacting with different wave types and waves at different frequencies.

- A cyclotron wave is incompressible.
- The turbulent part of the magnetic field is perpendicular to the SW bulk velocity.
- The turbulent field part is also perpendicular to the wavevector.
- The turbulent field part is also perpendicular to the background field.

A common quantity to these conditions is the background magnetic field which in measurement data is challenging to define and determine. The concept of a magnetic background field upon which waves perturbate may also be purely theoretical and not feasible to apply to actual data. If a mono frequent cyclotron wave is observed, in theory, the background field could be determined by an average of the magnetic field vectors of a time series over a whole wave period, which is a mathematical consequence of the circular polarization. However, not only is the frequency of observed waves in magnetic fields not known a priori, but also are mono frequent wave fields very scarce.

A different measure for an estimation of the magnetic background field is required. And as a first step, an empirical algorithm for the identification of large scale structures in the SW such as a flux tubes was implemented with the idea to average the magnetic field data over the duration of one flux tube. Then, the scale of averaging is different per flux tube that the spacecraft crosses. Hence, different frequency ranges can be observed per flux tube. Yet, this approach related the magnetic field data to a physically more meaningful quantity than e.g. instrumental constants (like a certain number of measurement cycles) or in this context arbitrary human defined measures of time (e.g. days, hours). Previous studies (e.g. Borovsky [2008]) have shown, that the identification of large scale structures based only on magnetic field data alone is less reliable than together with different quantities of the SW. Yet, the HELIOS observations of the SW velocity are with a time resolution which is 160 times slower in frequency than the 4 Hz magnetic field vectors. To avoid strong uncertanities which arise from the time interpolation and also to not loose time resolution of the magnetic field, it was decided not to synchronize the magnetic field data with the SW velocity time series and instead only rely on the magnetic field time series.

The method to determine large scale structures is outlined in Fig. 6. In summary, it aims to find boundaries in structures by a detection of abrupt changes in the magentic field. This is achieved by computation of a score of directional change and a score of change of the length of the vectors and a comparison of these to empirical threshold values.
From the resulting structure boundaries, time intervals are found, when the spacecraft roamed within the same structure in the SW. These are employed as time periods for averaging to obtain a measure for an unperturbed background magnetic field vector. For further analysis, the instantaneous magnetic field is obtained by a difference between the observed magnetic field vectors at 4 Hz and the averaged magnetic field. To investigate the instantaenous field's characteristics w.r.t. polarization and incompressibility, it is transformed into cylindrical coordinates, where the cylinders central axis is directed such, that it points in direction of the averaged background field. This way, a field-parallel part and a field-perpendicular part (w.r.t. the background field) of the instantaenous peturbations are obtained alongside a phase angle φ. For convenience, the angle ϑ is obtained, which is the angle between the instantaneous field and the average background field.
From these quantities, hodograms of time periods identified as similar are readily created. Such are displayed for an example timeseries for data of 09/27/1976 in Fig. 7. In particular, Fig. 7 displays hodograms for three selected time periods. In the left and the right hodogram, the magnetic field vectors align on a circle and the time evolution of the vectors' position hints towards a

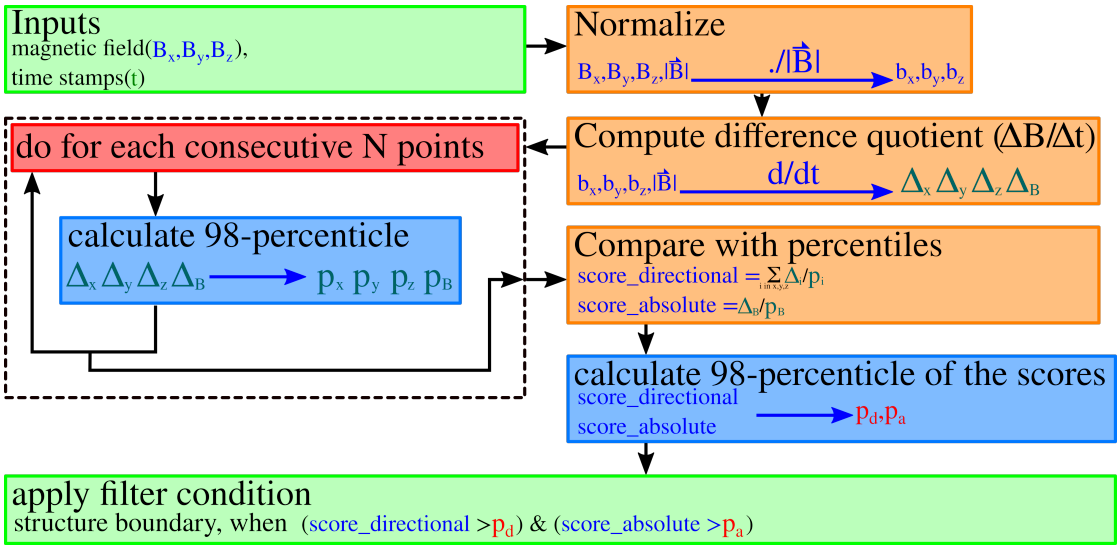

Figure 6: Float diagram of the algorithm to find boundaries of large scale structures in the SW from time series of HELIOS magnetic field observations. Firstly, the series of magnetic field vectors is normalized. Then, difference quotients between consecutive normalized magnetic field vectors are computed, where per pair of consecutive points three difference quotients are obtained from the difference quotients of the respective three components and one from the vectors' absolute values. Then, for each difference quotient the 98 percentiles of the $N-1$ difference quotients and itself are computed where N is an empirical input value. A time series of scores are then computed from the time series of percentiles by the fraction of difference quotients and respective percentiles. Threshold values of the scores are then found by the 98-percentiles of the scores (this time computed over the whole time series). Boundaries are then found, when the directional score as well as the absolute score exceed their respective threshold values.

rotation of the magnetic field which could point to Alfvénic wave activity. However, the parallel magnetic field changes also significantly during these times which hints towards compressible wave activity. This could either be superposed to the Alfvénic waves or actually a different wave type is seen in these plots. The central hodogram displays an example in which no clear rotation of the magnetic field could have been found as a contrasting example.

2.1.6.iii.b Identification by continuous wavelet transformation In addition, wavelet analysis can be employed to identify wave signatures. In contrast to the phenomenological method which employs hodograms, a wavelet transformation also yields the time variation of a wave's amplitude, which is helpful for a physically meaningful activation and deactivation of wave activity in a simulation.
In general, a wavelet transformation is similar to a fourier transformation. In a fourier transformation, the integrable function f is transformed from the time domain to the frequency domain via the scalar product of the vector space of functions with the unit vectors of the periodic

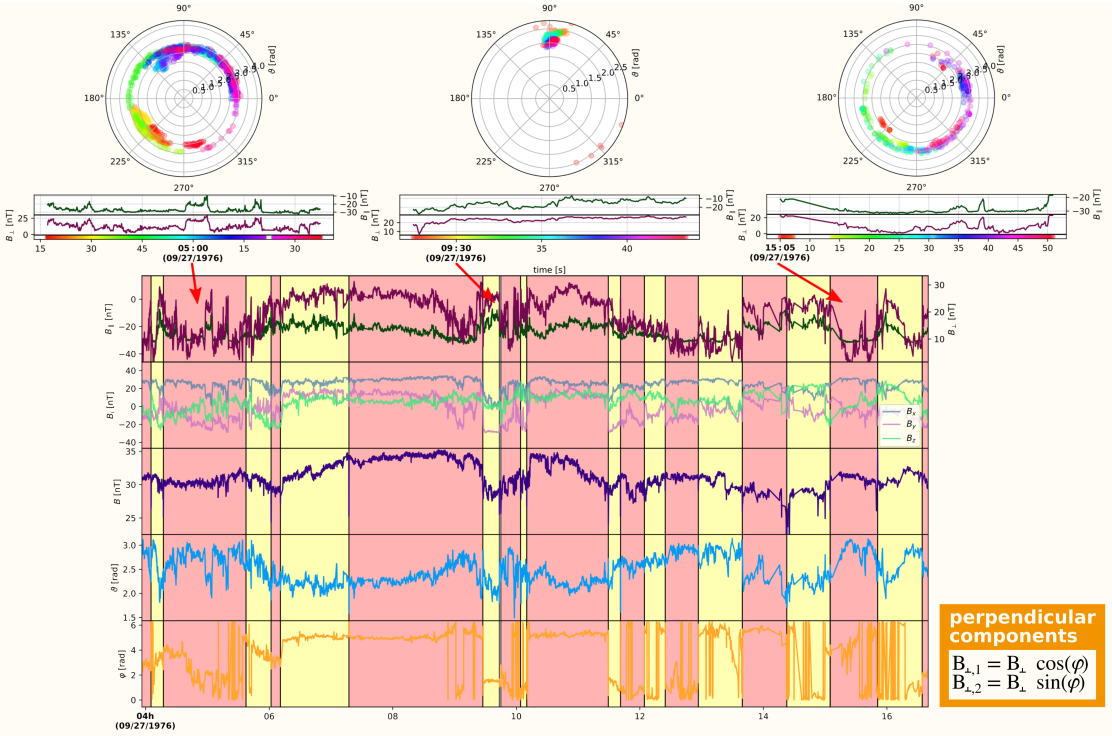

Figure 7: Bottom array of plots: Time series of HELIOS magnetic field observations. The x-axis displays time of the day 09/27/1976 in hours. Shaded alternatingly in pale red and pale yellow are the time intervals which were identified as within the same large scale structure in the SW. Plotted in the different panels are (from top to bottom) magnetic field parallel to the background magnetic field (left y-axis) and perpendicular to it (right y-axis), the $x-$,$y-$ and $z-$ components of the magnetic field in RTN-coordinates, the absolute magnetic field, the angle between background magnetic field and instantaneous magnetic field and the phase angle of the instantaenous magnetic field. In the three top plots, hodograms of three selected time periods are shown. The times to which they correspond are marked by red arrows, which point to the bottom plots.

Duncan Keilbach- Three dimensional Pickup Ion velocity distribution functions observed at 1 AU with STEREO/PLASTIC: Anisotropic features and density enhancements in pitch angle distributions as tools to investigate transport effects

function space. The resulting transformed function $\hat{f}$ (e.g. Butz [2009]) is obtained via

$$\hat{f}(\omega) = \int_{-\infty}^{\infty} f(t)e^{-i\omega t}dt, \forall\omega \in \mathbb{R} \ . \tag{14}$$

In Eq. 14 the expression $e^{-i\omega t}$ is a complex wave function at circular wave frequency ω. One might also denote it as $\psi_\omega(t) := e^{-i\omega t}$, so that Eq. 14 shortens to

$$\hat{f}(\omega) = \int_{-\infty}^{\infty} f(t)\psi_\omega(t)dt, \forall\omega \in \mathbb{R} \ . \tag{15}$$

While the wave functions $\psi_\omega(x)$ are constant in amplitude, a wavelet aims to model oscillations which are limited over time, so that a wavelet is only nonzero within a given distance from 0. This way, the prorotype of a wavelet (or the mother wavelet of a certain wavelet type) is defined as the time domained function $\psi(t)$ [Daubechies [1992]]. Similarly to a fourier transform, a wavelet transform is interested in convolving such a wavelet at different widths with an original function. Hence, the mother wavelet is scaled via $\psi_a(t) := (a)^{-1/2}(t/a)$ to obtain a scaled wavelet. The scaled wavelet not only operates at a different *pseudo*-frequency, but also has a different width for different values of a. Via a replacement of $\psi_\omega(t)$ with $\psi_a(t)$, a functionally similar integral to the fourier transformation is found, which reads

$$\tilde{f}(a) = \int_{-\infty}^{\infty} f(t)\psi_a(t)dt = \frac{1}{|a|^{1/2}} \int_{-\infty}^{\infty} f(t)\psi\left(\frac{t}{a}\right)dt, \forall a \in \mathbb{R} \ . \tag{16}$$

However, this equation does not yet yield meaningful results, since a wavelet is not nonzero at all values of t. A time offset also needs to be introduced. To offset the wavelet at different times, the time shift parameter b can be introduced and the function is time shifted like $\psi_{a,b}(t) := \psi_a(t-b)$. So, a two dimensional function is yielded as the wavelet transformed, which can be interpreted as the correlation between the function f and a wavelet at the pseudofrequency a and the time offset b. The wavelet transformation [Daubechies [1992]] then reads

$$\tilde{f}(a,b) = \frac{1}{|a|^{1/2}} \int_{-\infty}^{\infty} f(t)\psi\left(\frac{t-b}{a}\right)dt, \forall a,b \in \mathbb{R} \ . \tag{17}$$

It is important to state, that the pseudofrequency can not be exactly translated into the frequency spectrum of a fourier transform, since based on the mother wavelet itself may consist of a spectrum of different frequencies [Daubechies [1992]].
Fig. 8 displays continous wavelet transforms of the instantaenous magnetic field during the period which the left hodogram of Fig. 7 depicts. In that hodogram a rotation of the magnetic field with a period length of approximately 16 minutes is seen. This corresponds to increased activity in the corresponding pseudofrequency in Fig. 8. There, three components of the instantaneous magnetic field have been wavelet transformed for which the coordinate system is rotated such that the components mean either parallel or perpendicular directions to the background magnetic field. The two perpendicular components display in some frequency bands similar activity, especially in the pseudofrequency which fits to the observed rotations. A correlated wavelet transformed in a pseudofrequency band in both frequency bands hints at an elliptic or if amplitudes match to circularly polarized waves. So, an indication of cyclotron wave activity is found here. Yet,

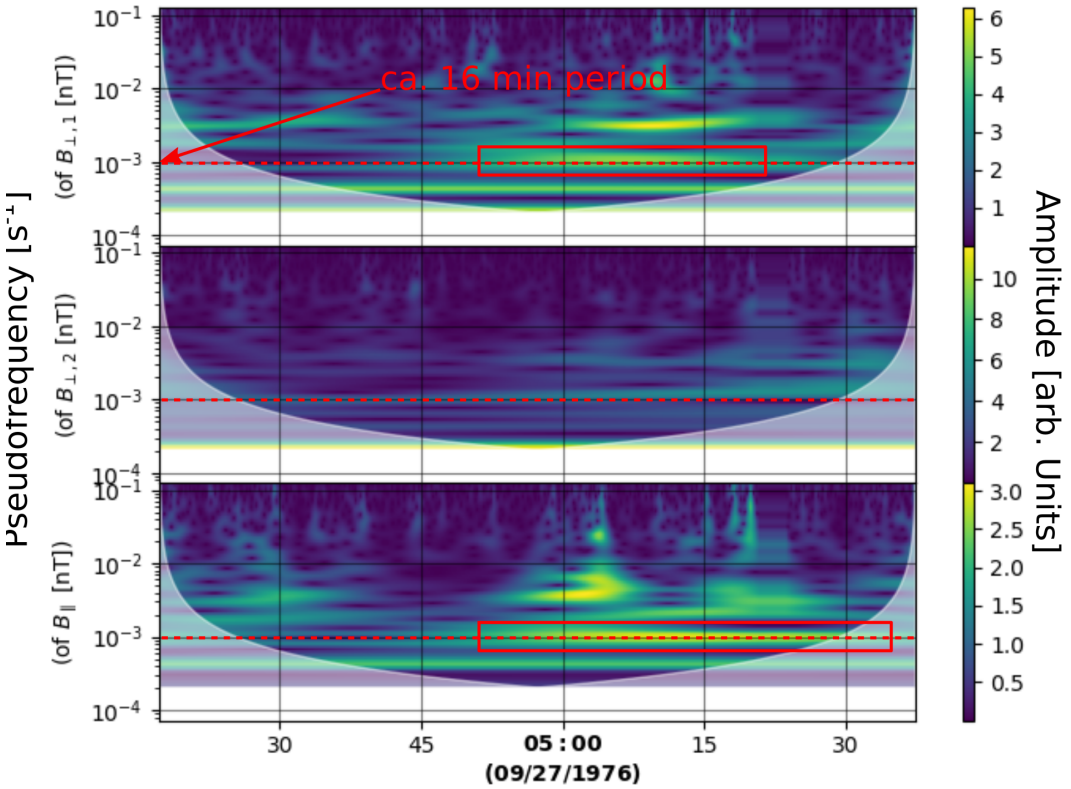

Figure 8: Continuous wavelet transform of the magnetic field observations of the left hodogram of Fig. 7. The different plots show transformations of different components of the instantaenous magnetic field. A period length of approximately 16 minutes is marked in all plots, since this is approximately the period length of the rotation of the magnetic field which was observed in the left hodogram of Fig. 7.

interestingly, also in the wavelet transformed of the parallel components increased activity is observed in the pseudofrequency of 16 minutes which hints at compressible wave activity.
The study displayed the potential of wavelet transformations to investigate wave activity in the SW. With a carefully selected coordinate systems, even the identification of cyclotron waves might be possible. Yet, the method still needs to be checked for reliability. Also the displayed example, even though it well presents a potential way to identify cyclotron wave activity, shows wave activity at a very slow frequency compared to the gyro frequency of protons in the SW: At a magnetic field of 5 nT the gyro period is $\sim$ 13 s. For a hodogram, the displayed time interval of data needs to be chosen at according scales. Else, as displayed in the example rotation of the magnetic field, larger scaled rotations hide these smaller waves. To correlation check the wavelet transforms of the two magnetic field components and also consider the results of an anticorellation check between the perpendicular components and the paralell component of the instantaneous magnetic field could be a more promising aproach [Köhler and Wimmer-Schweingruber [2010]].

2.1.6.iii.c Approaches to define enhanced quantities to identify cyclotron wave activity The proposed approach of the foregoing chapter to identify cyclotron wave activity by a correlation of perpendicular components of the instantaneous magnetic field still has the caveat, that the average magnetic field, which is employed for the transformation of the measured field in the spacecraft frame into the coordinate system which refers to the concept of a background magnetic field upon which wave activity propagates relies on the time scale of averaging. In the foregoing chapter for this time scale the largest amount of time between to discontinuities has been employed. Yet, one could argue that that time scale is not an optimal measure depending on the frequency spectrum of waves which is to be observed. If a mono frequent circularly polarized wave activity would be observed, the ideal averaging period would be integer multiples of the wave period, since then all wave-related direction changes of the magnetic field cancel each other out.
Based on that concept, as a follow up to the study presented by Keilbach et al. [2019], the idea was explored to expand the continuous wavelet transform by the introduction of a differently averaged background field for coordinate transformation for each pseudofrequency band of the wavelet transform. However, after testing it was found out, that a back transformation of such a modified wavelet transform is not possible, since firstly there are nonlinear cross terms between the fields of different time scales and secondly the integration constant for back transformation could not be defined.

Another problem to the wavelet transform as a method to investigate wave activity is the limitation of magnetic field observation by a single spacecraft, that only the time evolution of the wave activity at a single point in space is observed, but not the time and space evolution. For the initial goal to obtain pre-defined waves for test particle simulations, both wave frequency and wave vector are required to fully reconstruct an observed wave, but by the single-point measurement only a doppler shifted wave frequency is obtained at the spacecraft. If similar conditions are assumed within a few wavelengths, the theoretical dispersion relation could reconstruct the required parameter. In the future, it might be more fruitful to employ observations from multiple spacecraft. Recently, Jentsch [2021] studied the spatial and temporal evolution of interplanetary shocks with observations of multiple spacecraft. However for the study of wave processes, ongoing missions which feature multi spacecraft observations of magnetic fields, may not be able to obtain enough spatial resolution for an analysis detailed enough. Already for shock fronts, Jentsch [2021] remarked, that processes which happen within the observed structure while it travels in between the spacecraft still remain unknown.

2.1.6.iv Magnetosonic waves The solution $\omega^4 - \omega^2 c_{ms}^2 k^2 + c_s^2 v_A^2 k^2 k_\parallel^2 = 0$ of Eq. 12 leads to the magnetosonic wave mode. For the description of the magnetosonic wave in this chapter, Baumjohann and Treumann [2012] is referenced. From the roots of that equation, the dispersion relation

$$\omega^2 = \frac{k^2}{2} \cdot \left(c_{ms}^2 \pm \left((v_A^2 - c_s^2)^2 + 4 v_A^2 c_s^2 \frac{k_\perp^2}{k^2} \right)^{1/2} \right) \tag{18}$$

is found. In contrast to the Alfvénic wave the magnetosonic wave is compressible and the dispersion relation allows for different propagation directions propagation parallel to the local magnetic field. The different signs in Eq. 18 refer to the fast (positive sign) and the slow (negative sign) magnetosonic wave. Since Eq. 18 depends on the factor $k_\perp^2/k^2$, the dispersion relation is dependent on the angle between $\vec{k}$ and the local magnetic field. For perpendicular propagation

($k = k_\perp$), the dispersion relation becomes

$$\omega^2 = \frac{1}{2}k^2(c_{ms}^2 \pm c_{ms}^2) \quad \text{so, that} \tag{19}$$

the slow mode does not propagate and the fast mode propagates with a constant phase velocity in this case. For parallel propagation ($k = k_\parallel$) the dispersion relation becomes

$$\omega^2 = \frac{1}{2}k^2\left(c_s^2 + v_A^2 \pm (c_s^2 - v_A^2)\right) \ . \tag{20}$$

Magnetosonic waves are of special importance if disturbances are found in the SW, since the magnetosonic velocity determines the maximum velocity, with which the information about a pressure change can travel through the plasma. The SW is supersonic, so that in front of disturbances in the SW shocks can form.

2.1.7 Wave particle interactions

The presence of turbulent electric, magnetic and velocity fields as well as perturbations in the particle density can lead to strong acceleration of particles in the SW (e.g. Baumjohann and Treumann [2012]). Therefore, wave-particle interactions need to be considered when studying the SW or particles embedded therein, such as PUIs (compare chapter 2.2). For all interactions between the particles and the waves, resonances take a crucial part. These are further described in Chapter 2.1.7.i.
Since a modification of the motion of charged particles couples to modifications of the local electric and magnetic fields in a plasma, the interaction between a particle and plasma waves is in general nonlinear.
Yet, for some particle species (e.g. particles with a little abundance compared to the main particle species in the SW) the feedback effect to the fields is negligible. These particles can be treated as so called test particles. In a test particle approach only the effects of the fields to the particles are investigated. A brief overview over test particle simulations, which have been commenced as a continuation of the Masters Thesis of Keilbach [2017] is provided in chapter 2.1.7.ii.
This section about wave particle interaction is finished by chapter 2.1.7.iii with a review of quasi-linear theory which provides an approximative mathematical toolbox to describe the modification of particle VDFs in weak turbulence fields using a probabilistic approach.
Apart from the presented approaches, also MHD simulations have been employed to describe wave particle interactions. However, a full description of these and further approaches goes beyond the scope of this work. Also, this chapter focuses on the interaction with cyclotron-waves which are circularly polarized.

2.1.7.i Resonant interactions between gyrating particles and circularly polarized plasma waves The concepts presented in this chapter have been previously described and the reader may reference to e.g. Tsurutani and Lakhina [1997], Lehe et al. [2009].
For any consideration of resonance between wave and particle the doppler shifted wave frequency in the particle's frame of reference is decisive. In the following, only parallel propagating cyclotron waves (e.g. Alfvénic waves) are considered to make this part more instructive. In that regard, the doppler shifted wave frequency ω_d depends on the particle's velocity parallel to the local magnetic field $v_\parallel$ via

$$\omega_d = \omega - k_\parallel v_\parallel \ . \tag{21}$$

For a charged particle (mass m, charge q) in a magnetic field B resonance occurrs between the gyration motion at the frequency

$$\omega_c = \frac{qB}{m} \tag{22}$$

and the doppler shifted wave frequency, if the condition

$$n\omega_c = \omega_d = \omega - k_\parallel v_\parallel \tag{23}$$

is met.
For $n = 0$ (zeroth order resonance), Eq. 23 simplifies to

$$v_\parallel = \frac{\omega}{k_\parallel} \ . \tag{24}$$

Hence, in that special case, resonance is independent of the cyclotron frequency. Rather, the velocity of the particle has to be synchronized with the wave's phase velocity. In reality, first order resonance also applies to particles sufficiently close to the phase velocity, since then the magnetic mirror force accelerates them so, that the particles match the phase velocity. However, at the point of resonance the particles overshoot the resonance point and are then accelerated in the other direction in velocity space, so that the point of zeroth order resonance is an attractor in phase space and the particles behave like a wave rider in location space. This concept is of importance for the test particle simulations presented in chapter 2.1.7.ii.

For the n-th order resonance Eq. 23 is transformed into

$$v_{ph} - v_\parallel = \frac{n\omega_c}{k_\parallel} \ , \text{where} \tag{25}$$

the phase velocity $v_{ph} := \omega/k_\parallel$ has been inserted. The right hand side of Eq. 25 can be interpreted as the n-times multiple of the phase velocity of a wave with the wave's wavevector and the particle's gyration frequency as frequency. For all wave particles the condition

$$const. = \frac{m}{2}\left(\left(v_\parallel - v_{ph}\right)^2 + v_\parallel^2\right) \tag{26}$$

is met, so that the particle's energy in the wave frame is conserved.

2.1.7.ii Test particle simulations of wave particle interactions in an intermittent ion cyclotron wave field As a continuation of the simulation work of Keilbach [2017] test particle simulations have been conducted to investigate the modification of the VDF of O^+ PUIs under the influence of intermittent Alfvénic and ion cyclotron wave fields. The results have been partly presented in Keilbach et al. [2017a,b, 2018, 2019].

2.1.7.ii.a Simulation approach The simulation itself is only briefly described in this work, since the cited works have already presented it in detail and because the simulations are not the main focus of this work. The simulation employs a test particle approach, so that pre-defined analytical functions are employed to model the underlying electric and magnetic fields. The initial approach of Keilbach [2017] was to assume sinusoidal shapes for the x - and y-components of the wave-perturbation of the magnetic field and a constant value for the background magnetic field which points in z-direction and then to integrate the test particles' equations of motion employing Lorentz-force and Electrical-force from the motional electrical

field created by the background plasma which is pertubed by the wave. Intermittency is implemented by the application of a shape function, which models the wave amplitude's evolution over time. The amplitude shape function includes additional frequencies into the fourier spectrum of the otherwise mono frequent wave. Empirically for Keilbach [2017] it has been found, that the effect of additional frequencies is mitigated best if the amplitude is faded in from 0 to its full value within a quarter wave period. Then the wave amplitude is kept constant and if the wave is faded out, this also takes a quarter wave period.

For following works, in particular for Keilbach et al. [2018] and Keilbach et al. [2019] the approach was modified to improve performance: Instead of tracking each particle's position and velocity, for each test particle only the wave phase w.r.t. any wave and the velocity is integrated. The transformation of the particles' equation of motion is simple, since the modification of the particles' wave phase coordinate over time is the doppler shifted wave frequency as experienced by the particles at their velocity. Hence, the integration over the equations of motion is also commenced in a Leapfrog algorithm.

2.1.7.ii.b Nonlinear behavior of particles in the wave field Fig. 9 depicts the simulated pitch angle α distribution of O^+ PUIs sorted by initial doppler shifted wave frequency ω_d under the influence of mono frequent wave fields where each ω_d-slice represents a simulation run with a different wave frequency. The initial distribution of particles for each of these runs is a torus distribution with a pitch angle of 120°. For the simulation, the waves were only faded in and left running for several wave periods. The main findings of Keilbach [2017] were, that the behavior of the pitch angle distribution in such a wave field can be split into three different qualitative types of behavior, which depend on the initial Doppler-shifted wave frequency.
If ω_d is significantly lower than the particles' cyclotron frequency, only a small modification of the pitch angle is seen, which scales with the wave amplitude. The modification has been observed to be constant for different frequencies in that range.
For ω_d signifcantly larger than the particles' cyclotron frequency, the modification of pitch angles decreases with increasing wave frequency and has been observed to vanish towards negligible values.
In the range between those boundary cases, the most interesting findings were observed. A first, second or third order resonance was not found. Instead, the particles accumulated at predominant pitch angles and the pitch angles these particles were observed to accumulate are found at two branches: A branch where the particles accumulate at their initial pitch angle and a branch where the pitch angle of accumulation starts at significantly larger pitch angles and deccreases. For ω_d equal to the cyclotron frequency both branches converge to the same pitch angle.
The accumulations correspond to particles on an oscillatory trajectory. The bottom branch corresponds to the minimum and the top branch to the maximum pitch angle. Since the distribution of Fig. 9 is a time average and oscillating particles spend most times at the extrema of their trajectory, these accumulations appear. So basically, this phenomenon is similar to zeroth order resonance, since the particles oscillate from their initial pitch angles to pitch angles, where the doppler shifted frequency corresponds to their cyclotron oscillation like a wave rider.

Fig. 10 depicts a similar simulation, but this time the wave field is turned on and off randomly. Firstly, at deactivation not all particles remain at the initial pitch angle. At reactivation of the wave field the boundary condition is then a distribution of mixed pitch angles. Hence at deactivation, the pitch angles resulting from wave interactions of the new pitch angles contribute to the simulation. This way, in an intermittent wave field the pitch angle distributions are broadened systematically. This sets limits to the time scale of broadening of the pitch angle

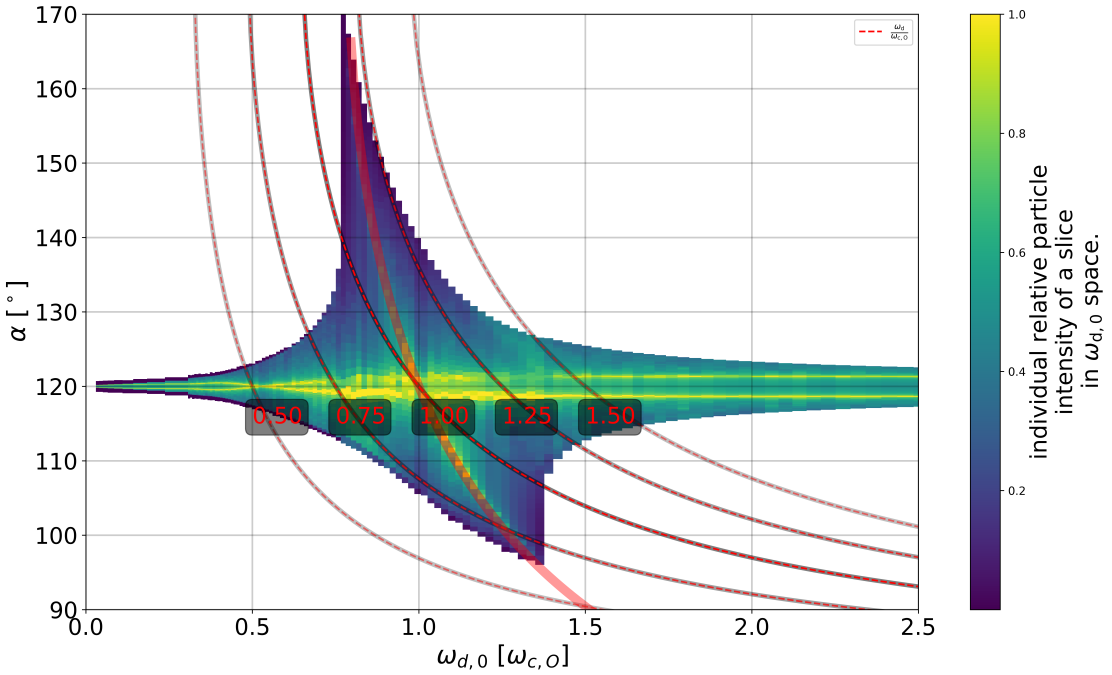

Figure 9: Simulated distribution of pitch angles (α,y-axis) during interaction of a mono frequent wave with a ring beam distribution of O^+ PUIs with an initial pitch angle of 120° accumulated as a time average during interaction. Each x-slice represents a different simulation run wherein for each simulation a different wave frequency is set. The wave frequency is displayed in units of the cyclotron frequency of the O^+ PUIs and the x-axis does no represent the wave frequency in a resting frame, but in the frame of the PUIs at the beginning of the simulation. This is indicated by the symbol $\omega_{d,0}$ which means doppler shifted wave frequency at the initial velocity. During interaction the pitch angle is modified which results in a modification of the doppler shifted wave frequency in a particle's frame. This is indicated by the red dashed lines which indicate the momentary doppler shifted wave frequency ω_d as a function of pitch angle and initial doppler shifted wave frequency. The thick red line indicates the situation of particles which are trapped in the wave field. Each x-slice is normalized to its respective maximum.

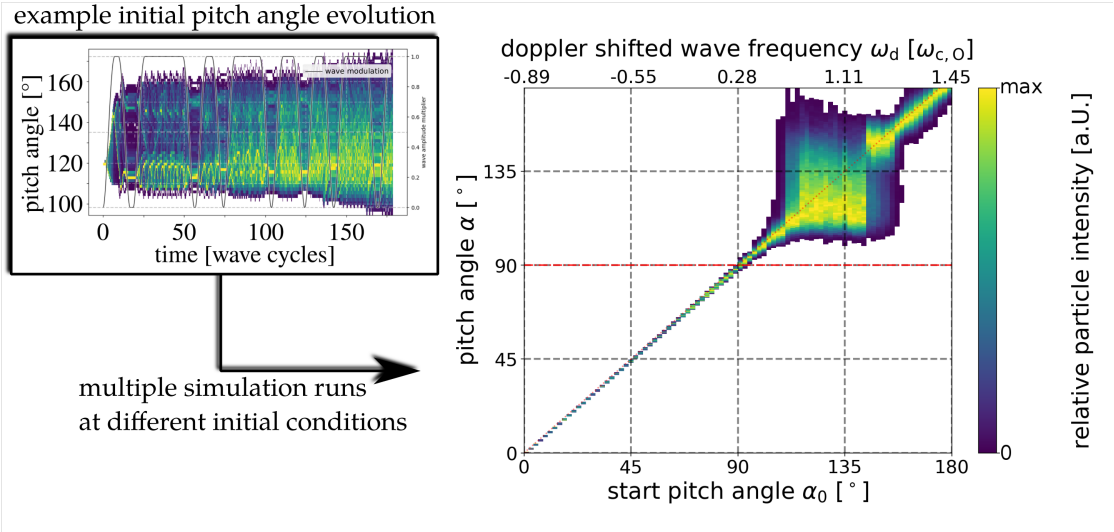

Figure 10: Left plot: Example simulation run for the interaction of O^+ PUIs at similar boundary conditions as in Fig. 9. The relative particle intensity as a function of pitch angle y-axis and time x-axis is color coded and normalized to the maximum of each x-slice. A solid black line depicts the modulation of the intermittent wave field (right x-axis in units of the maximum wave amplitude). Right plot: Through multiple simulation runs at different initial conditions, a plot of pitch angle (bottom y-axis) distribution after interaction with an intermittent wave field as a function of the initial pitch angle x-axis is derived. The top y-axis computes the initial doppler shifted wave frequency from the start pitch angle. For the right plot, the simulation is run for a reasonably long time, so that a time averages steady condition is found for the pitch angle distribution.

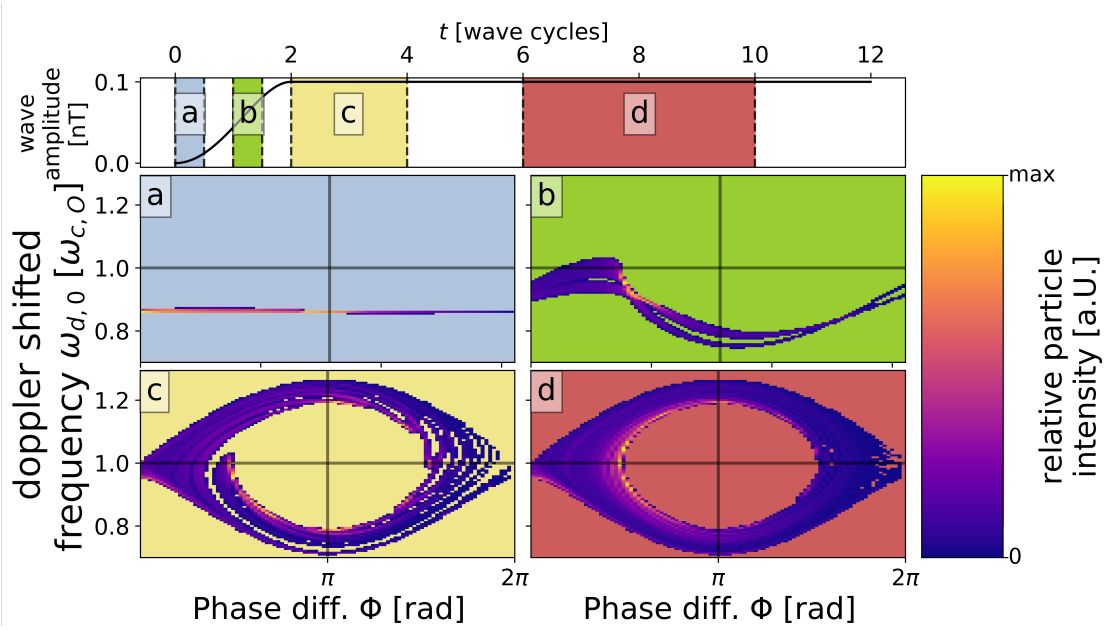

Figure 11: Top plot: Modulated wave amplitude (y-axis) as a function of time (x-axis) in wave cycles. Bottom four plots: Time averaged relative particle intensities as a function of doppler shifted wave frequency (y-axis) and phase difference (x-axis). The plots correspond to different time intervals during the simulation which are indicated by differently shaded areas in the top plot.

distribution of PUIs by mono frequent wave fields which, as is a concern of chapter 2.2.5, since as the chapter reviews a broadening of aniosotropic PUI VDFs towards isotropy under the influence of wave fields has been expected to take place swiftly w.r.t. to the time scales of transport in the SW.

To understand the appearance of the branch structure shown in Fig. 9 and ultimately, in Fig. 10, the particles' parameters of motion were transformed into variables more natural to the interaction of circularly polarized waves with a cyclotron motion. For this, two parameters are defined:

- The phase difference between cyclotron motion and circularly polarized wave oscillation Φ. Since this is directly related to the angle of Lorentz Force it can be derived from the particles' equations of motion, that

$$\dot{v_{\parallel}} = (q/m)\delta B v_{\perp} \sin(\Phi) \tag{27}$$

  applies. The time derivative depends on the difference between momentary doppler shifted wave frequency ω_d and cyclotron frequency ω_c and the following statement applies

$$\dot{\Phi} = \omega_c - \omega_d \tag{28}$$

- The momentary doppler shifted wave frequency ω_d. With the conservation of the energy in the wave frame $\varepsilon := (v_{\parallel} - v_{\phi})^2 + v_{\perp}$, Eq. 27 can be made independent of the perpendicular velocity and it is found, that

$$\dot{\omega_d} = -k\frac{q\delta B}{m} D \sin(\Phi) \quad \text{with } D := \sqrt{\varepsilon - \left(\frac{\omega_{d,0} - \omega}{k} - v_{\varphi}\right)^2} \tag{29}$$

  applies, where $\omega_{d,0}$ is the initial doppler shifted wave frequency.

Eqs. 28 and 29 create a system of differential equations which is analogous to the particles' equation of motion in the paramters location and velocity. Here, the velocity is represented by the doppler shifted wave frequency and the position is represented by the phase difference Φ. The solution of that system of equations of motion is

$$\omega_d = \omega_c \pm \sqrt{\omega_c^2 + \omega_{d,0}^2 - 2\omega_c\omega_{d,0^2} - 2k\frac{q\delta B}{m} D\left(\cos(\Phi) - \cos(\Phi_0)\right)} \tag{30}$$

and Φ_0 is the initial phase difference. Of course, this solution assumes a constant wave amplitude instead of a wave amplitude, which is intermittent and evolves over time. Yet, trajectories derived from this solution can be compared to simulation results. This is shown in Fig. 11, where simulated particle densities in (ω_d,Φ)-space are shown at different stages of the simulation. The particle densities are averaged over the indicated time periods and represent oscillatory as well as circular trajectories. The doppler shifted wave frequency of $\omega_d = \omega_c$ is at the phase differences 0, π and 2π an attractor in the phase space made of ω_d and Φ. Therefore, circular trajectories are found, which evolve around the points. The circular trajectories correspond to particles trapped in the wave field which is a known concept and the reader may refer to the text book of Baumjohann and Treumann [1997].

As a last finding to review, it was found that if a wave is activated in a simulation the range of initial doppler shifted wave frequencies, where a branch structure occurrs, depends on the amplitude of the wave. So the amplitude not only controls the strength of pitch angle modification but

also the range, where the branch structure and therefore strong pitch angle modification exists. This effect originates in the dynamic and nonlinear behavior of the particles in phase space. Initially, the particles are accelerated towards resonance between cyclotron motion and doppler shifted wave frequency. At the same time (while out of resonance) Φ evolves as a function of the difference between the doppler shifted wave frequency and the cyclotron frequency and eventually the sign of $\cos(\Phi)$ changes, if Φ is modified too much. This causes an acceleration in counter resonant direction. Also, since the wave is activated, the accelerating force increases. So if the resonance point is not reached initially during wave acceleration, the particle may not reach or surpass it during interaction with the wave. Then, the particle's trajectory in (ω_d,Φ)-space is small and essentially no branch structure exists. This phenomenological explaination was verified by investigating the dynamic behavior time step by time step, but no analytical expression for the limits of amplitude or frequencies could be derived to this point.

2.1.7.iii Quasi Linear Theory Quasi Linear Theory (QLT) employs a Fourier approach to linearize the electric $\vec{E}$ and magnetic fields $\vec{B}$ employing an approach in the shape of

$$\vec{E} = \delta\vec{E} = \int d^3\vec{k}\vec{E}(\vec{k},t)\exp i\vec{k}\cdot\vec{x} \text{ and} \tag{31}$$

$$\vec{B} = \vec{B}_0 + \delta\vec{B} = \int d^3\vec{k}\vec{B}(\vec{k},t)\exp i\vec{k}\cdot\vec{x} \text{ Schlickeiser [1994] .} \tag{32}$$

However, the limitation to this approach is, that the ratio between wave-inflicted Force and the Lorentz Force from the background magnetic field is low enough, so that their squared ratio is negligible [Schlickeiser [1994]]. For simplification, it is also assumed, that the background magnetic field is oriented in z-direction $\vec{B}_0 = B_0\hat{e}_z$, which effectively makes the problem one-dimensional [Jokipii [1966], Hasselmann and Wibberenz [1970], Schlickeiser [1994]].
Originally, QLT was developed to investigate the propagation of cosmic rays through a diffusion approach. With cosmic rays, the quantity of interest is commonly not directly the particle's pitch angle α, but the pitch angle cosine $\mu := \cos(\alpha)$ [Schlickeiser [1994]]. From either the application of the particles' equation of motion from Lorentz-Force (e.g. Jokipii [1966]) or the application of the Vlasov-Equation (e.g Kennel and Greene [1966], Kennel and Engelmann [1966], Schlickeiser [1994]) a diffusion equation of Fokker-Planck type in μ and z space is found. This is referred to as diffusion approach [Schlickeiser [1994]]. For the scattering of pitch angle cosines and parallel position the diffusion coefficients $D_{\mu\mu}$ and $D_{\parallel}$ are defined.

For negligible variation of particle density in z-direction [Jokipii [1966]] derived expressions for both coefficients in the shape of

$$D_{\parallel} = V^2\int_{-1}^{+1}\mu_1\left(\int^{\mu_1}\frac{(1-\mu^2)}{D_{\mu\mu}}d\mu\right)d\mu_1 \text{ and} D_{\mu\mu} = \frac{<(\Delta\mu)^2>}{\Delta t} . \tag{33}$$

As a typical approach, a functional shape of $D_{\mu\mu} \propto |\mu|^{q-1}(1-\mu^2)$ with $q > 1$ [Beeck and Wibberenz [1986]]. Such a shape of the pitch angle diffusion coefficient is plotted in Fig. 12. The coefficient is zero for values of μ of 0 and ±1 which corresponds to pitch angles of 0°, 90° and 180°. So, at these pitch angles particles are expected to accummulate. Also transport from pitch angles in the range of 0°...90° to the range of 90°...180° may be inhibited in comparison to transport within these ranges (e.g. Isenberg [1997]).

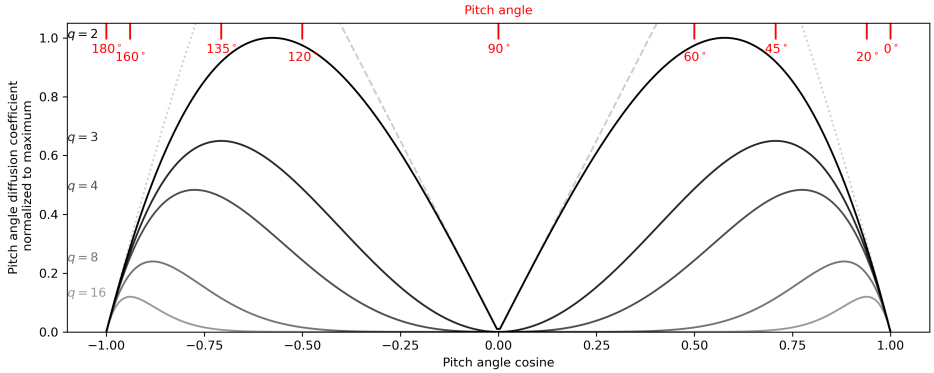

Figure 12: Theoretical pitch angle diffusion coefficients according to the model $D_{\mu\mu} \propto |\mu|^{q-1}(1-\mu^2)$ with $q > 1$ as a function of the pitch angle cosine μ. The purpose of the plot is to visualize the functional shape, not absolute values. Hence, the plot is normalized to the maximum. On the top x-axis pitch angles are provided for the different pitch angle cosines of the bottom x-axis. The differently greyshaded solid curves correspond to different values of q which are provided in the plot. The dashed line plots $|\mu|$ and the dotted line plots $(1-\mu^2)$ for orientation.

2.1.8 Properties of the Solar Wind in velocity space

The categorization of the SW (compare Chapter 2.1.4) often employs statistical measures (e.g. average velocity or temperature) to quantify the characteristics of the SW in velocity space (e.g Bruno and Carbone [2013]). Yet, the VDF of the SW is multimodal, dynamic and its characteristics differ for protons, electrons and heavier ions (e.g. Marsch [2006]). Therefore, this section reviews the properties of the SW in velocity space. Since for this work especially the velocity characteristics of the positively charged part of the SW is of importance, this overview of the SW VDFs omits a description of electrons.

2.1.8.i Protons If the VDF of a thermalized gas is observed, a Maxwellian distribution is expected (e.g. Piel [2017]). A Maxwellian distribution $f_M(\vec{v})$ is a distribution shaped according to

$$f_M(\vec{v}) \propto \exp\left(-\frac{m|\vec{v}|^2}{3k_B T}\right). \tag{34}$$

Here, m is a particle's mass, $\vec{v}$ its velocity, k_B the Boltzmann-constant and T the plasma's temperature. Here, temperature should be understood as a parameter determining the width of the Maxwellian which essentially is a three-dimensional Gauss-type function with a standard deviation $\propto T$ (e.g. Piel [2017]).Hence, it is common practice to determine the temperature of particle populations in the SW from the standard deviation of observed VDFs.
However, the SW is known to exhibit non-Maxwellian (or non-thermal, in that respect) features [Marsch et al. [1982]]. This has also implications for the measurement of the temperature of the SW, since then the temperature as derived from the standard deviation of a velocity distribution may not reflect the temperature in a thermodynamic sense or might need at least additional correction factors depending on the observed velocity distribution.
Also, since the SW is a magnetized and almost fully ionized gas (e.g. Marsch [2006]), the magnetic field should be considered in the observation of the VDF of particles in the SW. A typical approach is expressing the SW VDF by a bi-Maxwellian distribution, which means, that

different temperatures are assumed for the component of the velocity parallel to the magnetic field $v_\parallel$ and perpendicular to it $v_\perp$ (e.g. Marsch [2006]). Let $T_\parallel$ be the parallel temperature and $T_\perp$ the perpendicular temperature. Then the bi-Maxwellian model (e.g. Marsch [2006]) for the VDF can be described as

$$f_{bM}(v_\parallel, v_\perp) \propto \exp\left(-\frac{mv_\parallel^2}{2k_B T_\parallel}\right) \cdot \exp\left(-\frac{mv_\perp^2}{2k_B T_\perp}\right). \tag{35}$$

The proton VDF has first been observed in three dimensional (3d) detail by the Helios spacecraft and are since known to exhibit non-Maxwellian features, which go beyond the extent of different temperatures perpendicular and parallel to the magnetic field [Marsch et al. [1982]]. Obviously, the SW is not fully thermalized, which might arise from the fact, that caused by the sparse density of particles in the solar wind the mean free path for proton-proton collision exceeds 1 AU, when observed at distances from the Sun of 1 AU (e.g. Marsch [2006],Prölss [2013]).
The observations by Helios led to the core-beam model. In this model, the proton VDF is assumed to consist of two main populations: A core distribution, which is represented by a bi-Maxwellian distribution, and a beam distribution, which is called that way, since it is offset w.r.t. the core roughly in direction of the local magnetic field. So far, the core-beam structure was observed under coronal hole SW conditions and typical offset velocities are in the magnitude of the Alfvénic velocity (e.g. Marsch [2006]).

2.1.8.ii Alpha particles and heavier ions The Helios observations were not exclusively limited to protons, but partially also included SW alpha particles [Marsch et al. [2004]], which are known to form Bi-Maxwellian-like structures in velocity space and stream at slightly different velocities than the protons (e.g. Marsch [2006]).
Other than for protons (and partially alphas), the VDF of ions heavier than protons has not been observed in 3d, yet. The Solar Wind Analyser (SWA) suite [Owen et al. [2020]] aboard Solar Orbiter [Müller et al. [2020]] features a Heavy ion Sensor (HIS), which is expected to provide such observations once commisioned. The analysis of the shape of the VDF of protons and alphas very close to the Sun is also enabled by the SWEAP suite [Kasper et al. [2016]] on board of Parker Solar Probe [Fox et al. [2016]].
Alltough the mean proton velocity is a good first estimator of the velocity fo SW heavy ions, their detailed velocity deviates from the proton bulk velocity by velocities in the magnitude of the local Alfvénic speed [Berger et al. [2011], Janitzek et al. [2016]]. This differential streaming w.r.t. the protons is an object of great scientific interest at the moment of writing this work and the exact role, that the magnetic field, which is known to influence the amount and tentatively the direction of the differential streaming [Berger et al. [2011]], is yet to be determined. In addition, there are heavy ions of non-solar origin in the SW. These are considered in Section 2.2.

2.1.8.iii Reference velocities in the solar wind As the foregoing chapter demonstrated, the SW's microphysical and velocity characteristics can not be fully described by the definition of a single solar wind velocity. However, for many purposes the usefulness of a single parameter, which is characteristic for selected aspects of a SW streams, exceeds this loss in information. Such a parameter is especially important for the description of the transport of particles in the SW (e.g. cosmic rays) a reference velocity, in relation to which the mechanic and kinematic properties of the transported particles are represented in their most natural way.
The solar wind velocity is a term often referred to, when the average observed velocity of SW protons is meant. Sometimes this velocity is also called the bulk velocity. However, the proton VDF itself has been observed to be of bimodal nature (compare chapter 2.1.8.i). So sometimes

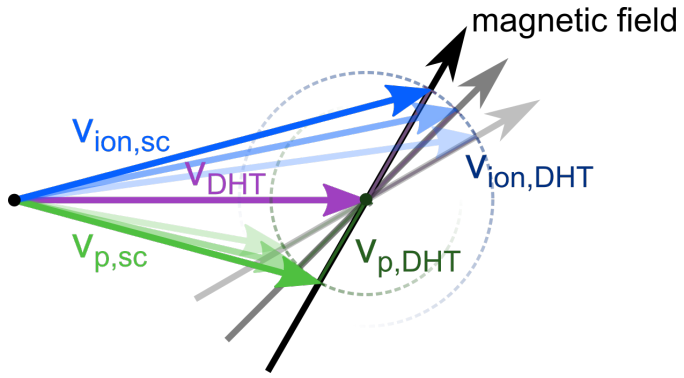

Figure 13: Illustration of the de-Hoffmann-Teller (dHT) frame (green arrow) w.r.t. the proton velocity (red arrow) and the velocity of an example ion heavier than protons, such as e.g. Fe PUIs (purple arrow). This illustration depicts three example configurations of the local magnetic field (black arrow), wherein different shades of the magnetic field's and the velocities' arrows correspond to different configurations. These configurations represent a slow rotation of the magnetic field like during outward propagation of the SW in the model of Parker [1958]. The figure is an adaptation of a figure from Němeček et al. [2020].

also the average velocity of the Maxwellian core is referred to as solar wind velocity. To alleviate ambiguity, in this work, the average proton velocity is referred to as solar wind bulk velocity and represented by the symbol v_{SW}.
While this quantity is practical in the sense of a simple definition, it has been argued, that it is not suited to describe the reference frame for the transport of heavier ions and suprathermal particles [Němeček et al. [2020]]. In the simple model of Parker [1958] the frozen-in magnetic field is carried outward by the SW as it radially expands. In reality the true velocity, with which the interplanetary magnetic field is transported within the SW may differ from the average SW velocity, or the SW velocity referred to by the model of Parker [1958] is differently defined with an expression yet to be found. The differential streaming problem may also be solved, if a more adequate definition of the SW velocity is found.
The reference velocity proposed for this purpose by Němeček et al. [2020] is the dHT velocity [de Hoffmann and Teller [1950]]: The dHT frame is force-free in the sense, that the motional $\vec{v} \times \vec{B}$ electric field vanishes, where $\vec{v}$ represents the velocites of the SW plasmas particles and $\vec{B}$ the local magnetic field. An argument pointed out by Němeček et al. [2020] which supports the dHT frame as a transporting frame is illustrated in Fig. 13. There, the velocity vectors of protons and an example heavy ion species are depicted in an example configuration. The vector of the dHT velocity is located between them. It is expected, that these velocities align along the magnetic field vector. Shaded more transparently are vectors corresponding to a slow gradual rotation of the local magnetic field. In the dHT frame the local magnetic field rotates around the center of the coordinate system. This means, that the guiding center velocities of particles transported in the SW are likely to be rotated together with the magnetic field around the dHT point in velocity space, if that rotation is gradual [de Hoffmann and Teller [1950], Němeček et al. [2020]].

2.1.9 Formation of the Heliosphere

Seen from solar distances of hundreds of AU, the SW is not the only plasma to be found in space (e.g. Spitzer [1942], Crutcher [1982], Lallement and Bertin [1992], Frisch et al. [2011]). For at least the last $\sim$ 4 million years [Innes and Hartquist [1984]], the Sun has been travelling through a thin cavity in the milky way galaxy of a diameter of at least 300 light years called the Local Bubble [Bochkarev [1987], Frisch et al. [2011]]. This cavity, which is embedded into the local interstellar cloud, has supposedly been formed by multiple supernovae [Innes and Hartquist [1984], Clayton et al. [1986], Cox and Reynolds [1987]]. Hence, it is irregularly shaped.
Within this cavity, several smaller bubbles of Local Interstellar Medium (LISM) have been observed in further proximity to the Sun (at the scale of tens of parsecs) and with at least two of which (the Local Interstellar Cloud (LIC) and the G-Cloud) the solar wind collides [Redfield and Linsky [2007], Linsky et al. [2019]].
Since both the SW and the plasma in the neighboring medium are magnetized, they can not be mixed (magnetic field lines can not be crossed) [Axford et al. [1963]]. Therefore, a boundary is formed encapsulating a region governed by the radial expansion of the SW called the heliosphere and the interface region between both is called the heliopause [Hundhausen [1968], Axford [1972]].
Inside the heliosphere, the SW expands and the velocity of the SW is supersonic (e.g. Parker [1958]). Hence, the SW is not continously decelerated as it streams towards the heliospheric boundary. Instead, a shock region is formed: The termination shock [Axford et al. [1963], Holzer [1989]]. The only spacecraft to have yet observed the termination shock in-situ, were the Voyager spacecraft [Stone et al. [2005, 2008]]. Voyager 1 entered the volume called the heliosheath which is the area between the termination shock and the heliopause at a distance of 94 AU from the Sun [Stone et al. [2005]]. Voyager 2 enterd that volume at a distance of 83.7 AU [Stone et al. [2008]]. The $\sim$ 10 AU discrepance between these distances raised the question, whether the heliospheric boundary is irregularly shaped.
This question is still unsolved. Only two spacecraft are known to have crossed the heliopause: Voyager 1 crossed the heliospheric boundary on August 25, 2012 at a distance of $\sim$ 122 AU from the Sun [Stone et al. [2013], Gurnett et al. [2013], Richardson et al. [2019a]] and Voyager 2 crossed the boundary on November 5, 2018 [Richardson et al. [2019b]] whilst travelling in a different direction than Voyager 1 at a solar distance of $\sim$ 119 AU [Richardson et al. [2019a]].

Even though the similarity of both distances may suggest a spherically shaped Heliosphere, the exact shape of the Heliosphere is unknown. The model of Parker [1961] employs a simplified hydrodynamic model of both the LISM plasma and the SW plasma and predicts the heliospheric shape for two boundary cases:

- **comet-tail shaped heliosphere**: If the magnetic field carried by the incident LISM plasma is negligible compared to the SW magnetic field, the heliosphere is shaped like a comet tail. The tail is formed in direction of the velocity of the incident LISM and in opposite direction the nose of that structure is formed.
- **bubble-like heliosphere**: In the opposite case, the heliosphere is shaped like a symmetric bubble.

Of both models, the comet-tail shaped model is broader accepted (e.g. [Baranov and Malama [1993], Schwadron and Bzowski [2018], Opher et al. [2015]]). In addition, a model based on magnetohydrodynamic simulations resulted in another shape of the heliosphere which functions almost like a hybrid of both models. In that model, the tail of the comet-shaped heliosphere is split into two tails so that the heliosphere is more shaped like a croissant. For the LISM

which flows within a plane orthogonal to the axis which connects both tails, the heliosphere is then shaped similarly to the bubble-like model [Opher et al. [2015]]. The observations from the Voyager spacecraft are the only in-situ plasma measurements of the termination shock and the heliopause. Even though energetic neutral atom measurements from the Cassini and Interstellar Boundary Explorer missions provide an alternative to infer properties of heliospheric shape, the strong limitation of observational data makes the determination of the heliospheric shape a challenging field. In addition, energetic neutral atom measurements suggest, that the extent of the heliosphere changes depending on the solar activity cycle [Schwadron and Bzowski [2018], Zirnstein et al. [2017]].

Spectroscopy provides a remote-sensing opportunity to learn more about the Heliospheric boundary: Linsky and Wood [1996] employed spectra of nearby stars obtained with the Hubble Space Telescope and found a discrepancy between the temperature inferred from the He I lines of these stars and the lines of different elements. As a solution to this discrepancy, they suggested the existence of a compressed Hydrogen wall near the Heliopause. As Wood and Linsky [1998] pointed out, the existence of such hydrogen walls provides also a method to detect Astrospheres. Astrospheres are analogous phenomena to the Heliosphere, but evolve around different stars than the Sun. Therefore, apart from demonstrating, that outflowing particles from stars are an ubiquitious phenomenon, Astrospheres provide an outside perspective on Heliosphere-like phenomena (e.g. van Buren and McCray [1988], van Buren et al. [1995]).
The observation of scattered solar light in the He I line spectrum (e.g. Bertaux and Blamont [1971], Thomas and Krassa [1971]) allowed to infer, that the H and He components of the LISM are supersonic [Fahr [1974], Weller and Meier [1974]]. Hence, similarly to the termination shock a corresponding disturbance was expected in the LISM, which is attributed to the Heliosphere as an obstacle for the flow of the LISM: The Bow Shock (e.g. Kallenbach et al. [2000]) which is a magnetohydrodynamic analogon to the bow wave in water forming in front of a ship. Recently, the existence of such a Bow shock has been questioned by McComas et al. [2012], who calculated Alfvénic velocity and the magnetosonic wave velocity in the LISM from observations of the interstellar boundary explorer (IBEX) [McComas et al. [2005]], which observes interstellar neutrals at 1 AU. However, following modelling studies (e.g. Zank et al. [2013], Scherer and Fichtner [2014]) reinstated the expected existence of the Bow shock. Especially, Zank et al. [2013] found, that in their model a LISM flowing at lower velocities than the magnetosonic speed, can not account for Lyα observations like those employed by Linsky and Wood [1996] to predict the existence of a Hydrogen wall.

After traversing the Bow shock which is not identified yet the charged component of the LISM is expected to decelerate and flow around the Heliosphere [Parker [1961], Axford [1972]]. However, the neutral component of the LISM is not affected by electromagnetic forces and its kinematics therefore differ from the kinematics of the charged component (e.g Axford [1972]). The implications of this are the subject of the following chapter.

2.2 Pickup Ions

Unlike charged particles from the LISM, neutral particles may enter the heliosphere (e.g. Axford [1972]). As a neutral particle traverses the heliosphere it is likely to be subjected to certain physical processes, which are

- Modification of the trajectory from gravitational forces (section 2.2.2)
- Modification of the trajectory from radiation pressure (section 2.2.2)

- Ionization processes like photoionization, charge exchange and electron impact ionization (section 2.2.3)

These processes shape the density and velocity profile of interstellar neutrals (ISNs) and create features, which are tracers of characteristics of the LISM (e.g. Vasyliunas and Siscoe [1976]). Therefore, the study of ISNs and furthermore the particles produced from them through ionization provides means of characterizing the LISM.
After ionization, the former ISNs are subjected to the Lorentz-force. Since Lorentz-force points in orthogonal direction to both the local magnetic field lines and a particle's velocity, the trajectory of the newly created ion is governed by circular motion around the local magnetic field vector. The local magnetic field is frozen into the SW; it is transported outward by the SW. So, the guiding center of the former ISNs trajectory will be transported by the SW as well. Hence, the particles were picked up by the SW and are fittingly named PUIs [Möbius et al. [1986], Moebius et al. [1988]].
The study of interstellar PUIs provides insights about ISNs, since the kinetic characteristics of a former ISN at the point of ionization are the boundary conditions of the PUIs motion. However, the mechanism of picking up newly created ions by the SW also applies to ions of non interstellar origin [Geiss et al. [1995a]].

2.2.1 Inner source pickup ions

This section provides a brief introduction into PUIs of non interstellar origin. Since the source of these particles is within the heliosphere, the particles are referred to as inner-source PUIs [Geiss et al. [1995a]].
Originally, Geiss et al. [1995a] found C^+ ions in Ulysses data, which could not be attributed to sources out of the interstellar medium, hence their origin was attributed to sources within the heliosphere. Following studies found correlations between the flux of C^+ and O^+ PUIs of inner source and both the flux of SW O^{6+} and protons, which hints to inner source PUIs being created from neutralized SW [Allegrini et al. [2005], Taut et al. [2015], Berger et al. [2015], Quinn et al. [2018]]. Also, the VDF of inner source PUIs resembles the VDF of the SW [Allegrini et al. [2005]], which also means, that that fraction of inner source PUIs can be expected at significantly lower velocities than the interstellar PUIs, the VDF of which is discussed in the later chapter 2.2.5. In addition to recycled SW material, planets, cometary material and dust grains have been attributed to as probable origins of inner source PUIs (e.g. Vasyliunas and Siscoe [1976], Geiss et al. [1995a], Gloeckler and Geiss [1998], Quinn et al. [2018]).

Since this work is interested in PUIs of interstellar origin, in the following with PUIs those of interstellar origin are meant, unless explicitly stated differently. However, PUIs originating from non interstellar sources might still play a role in the interpretation of this works results and should thusly not be fully neglected.

2.2.2 The trajectory of interstellar neutrals

For ions heavier than protons the radiation pressure influence on an ISN's trajectory is exceeded by the influence of the Sun's gravitational interaction with the particle. Since pickup protons are not the main concern of this work, the effect of radiation pressure on ISNs is neglected in this work. In contrast to protons, for He^+ ions the effect of radiation pressure is negligible to the effect of the Suns gravitation [Shestakova [2015]]. Yet, for completeness, chapter 2.2.2.ii describes this phenomenon in detail.

2.2.2.i Gravitational forces In good approximation it is assumed that the Sun is the only body in the solar system exerting a gravitational pull on the ISNs[4]. And even though the planetary body gravitationally affects the ISNs, these effects are still negligible compared to the ISNs trajectories on the scale of AUs.

The gravitational force $\vec{F}_{\text{grav}}$ exerted by the Sun on an inflowing ISN of mass m_{isn} at a position $\vec{x}$ (where the Sun is the origin of the coordinate system) is given by

$$\vec{F}_{\text{grav}} = -G\frac{M_{\odot}m_{\text{isn}}}{|\vec{x}|^2} \cdot \frac{\vec{x}}{|\vec{x}|} \text{ , where} \tag{36}$$

G is the gravitational constant and $M_{\odot}$ is the Sun's mass [Vasyliunas and Siscoe [1976]]. Since the resulting potential is spherically symmetric and scales with $1/|\vec{x}|$, the situation is analogous to the two-body-problem (e.g. Fließbach [2003]). Therefore an ISNs trajectory may be expressed as ellipses or at entry velocities typical to the ISNs, by hyperbolae.
This has two consequences [Vasyliunas and Siscoe [1976]]:

- The resulting ISN densities in the heliosphere are cylinder-symmetric, wherein the symmetry axis is given by the direction of inflow centered to the Sun.

- Seen from the direction of inflow, the hyperbola trajectories of the ISNs overlap. This creates a region of enhanced density which is roughly conically shaped and is therefore referred to as the focusing cone [Fahr [1968a,b], Lee et al. [2015]]. Since the focusing cone's enhanced densities are carried over into enhanced PUI densities, observations of PUI densities are capable of tracing this region and inferring parameters of the inflow of ISNs from it [Moebius et al. [1995], Gloeckler et al. [2004], Drews et al. [2012], Möbius et al. [2016], Taut et al. [2018]]. While the focusing cone is observed downstream of the ISN flow w.r.t. the Sun, a region of enhanced PUI density, but not increased ISN density is formed upstream w.r.t. the Sun. However, the upstream region of enhanced density is not directly a consequence of gravitational focusing of the trajectory [McComas et al. [2004]]. Hence, it does not directly belong to this point, but is further reviewed in chapter 2.2.4.

2.2.2.ii Radiation pressure The amount of radiation pressure exerted by solar photons on the ISNs is dependent of the cross section for photon absorption and photon reflection and scales linearly with the proton flux in the heliosphere (e.g. Bzowski et al. [2008]).
Radiation pressure plays a significant role in the computation of interstellar hydrogen fluxes and the fluxes of low first ionization potential particles. For these particles the effect of solar radiation pressure compared to solar gravitation is strongest. For some ions radiation pressure even exceeds the gravitational force, so a net repelling force acts on these particles [Shestakova [2015]]. Since absorption is generally wavelength dependent, for a model of acceleration from radiation pressure the wavelength-distribution of the solar radiation and a particles absorption coefficient need to be taken into account (eg. Bzowski et al. [2008], Tarnopolski and Bzowski [2009]). E.g. H absorbs the Lyα line, since it is part of its atomic spectrum [Kramida et al. [2021]]. Since the Doppler effect applies, the wavelength dependent absorption and hence the acceleration is also dependent on a particle's velocity. This has been employed to compute expected radial velocity distributions for incoming interstellar H neutrals by Bzowski et al. [2008], Tarnopolski and Bzowski [2009].

[4]With a mass of $\sim$ 318 earth masses [Williams [2016b]] Jupiter is the heaviest planetary body in the solar system. Yet, this mass is only $\sim$ 0.095% of the Suns mass [Williams [2016a]].

2.2.3 Ionization processes in the heliosphere

An ISN becomes a PUI through ionization in the heliosphere. A list of observed PUIs is provided in Tab. 3. Typically, PUIs are singly charged. This differentiates heavier PUIs (i.e. mass numbers above 4) from SW particles: SW ions are either fully ionized or at very high charge states (compare Chapter 2.1.2). Apart from ionization processes, interstellar PUIs also strongly deviate in their VDF from the VDF of the SW (compare Chapter 2.1.8). Properties of the VDF of PUIs are reviewed in Chapter 2.2.5. This Chapter is concerned with the ionization processes, which create PUIs.

Since the probability of an ISNs ionization is a key component of the appearance of not only

Pickup Ion	First ionization potential in eV	origin	reference
H^+	13.599	interstellar inner source	Gloeckler et al. [1993, 1995] Gloeckler et al. [2000a]
He^+	24.588	interstellar inner source	Möbius et al. [1985] Gloeckler et al. [2000a]
C^+	11.260	inner source	Geiss et al. [1995a], Gloeckler and Geiss [1998]
N^+	14.534	interstellar inner source	Geiss et al. [1994a] Gloeckler and Geiss [1998]
O^+	13.618	interstellar inner source	Geiss et al. [1994a,b] Gloeckler and Geiss [1998]
Ne^+	21.565	interstellar inner source	Geiss et al. [1994a] Gloeckler and Geiss [1998]
Mg^+	7.646	inner source	Gloeckler et al. [2000b]
Si^+	8.152	inner source	Gloeckler et al. [2000b]

Table 3: List of PUIs, their charge state, the first ionization potential of the atom they originated from, whether the PUI is of interstellar origin and the reference for the PUI. The references refer to the PUIs, not the first ionization potentials. The first ionization potentials were extracted from Kramida et al. [2021].

the spatial distribution of ISNs but also of the PUIs [Vasyliunas and Siscoe [1976], Lee et al. [2015], Keilbach et al. [2016]], a familiarization with the different processes ionizing ISNs in the heliosphere is vital to interpret PUI observations.
The probability of a single ionization process herein depends on the species of ISN. An overview of the production rates at 1 AU of a selection of PUIs as to be found in Cummings et al. [2002] is compiled in table 4. An overview of the presented ionization effects can also be found in e.g. Rucinski and Fahr [1989], Bzowski et al. [2008]. Photoionization from solar UVs dominates the PUI production rates for He- and Ne-PUIs at 1 AU, whereas for different elements the charge-exchange with the SW also plays an important role: For protons the charge-exchange ionization rate at 1 AU exceeds the photoionization rate by a factor of almost 4 and for O-PUIs charge exchange ionization and photoionization are both in the same magnitude and almost equally contribute to a considerably higher PUI production rate at 1 AU compared to He-PUIs. In addition, electron impact ionization is known to contribute to the production of PUIs [Rucinski and Fahr [1989]].

The probability of each process is a function of location in the heliosphere. Here, the probability

Element	Charge-Exchange Ionization Rate in s^{-1}	Photoionization Rate in s^{-1}
H	$(6.44 \pm 0.14) \cdot 10^{-7}$	$(1.67 \pm 0.05) \cdot 10^{-7}$
He	$(3.40 \pm 0.39) \cdot 10^{-10}$	$(1.18 \pm 0.10) \cdot 10^{-7}$
C	$(2.51 \pm 0.08) \cdot 10^{-7}$	$(1.44 \pm 0.07) \cdot 10^{-6}$
N	$(1.25 \pm 0.03) \cdot 10^{-7}$	$(4.77 \pm 0.25) \cdot 10^{-7}$
O	$(3.61 \pm 0.08) \cdot 10^{-7}$	$(4.86 \pm 0.30) \cdot 10^{-7}$
Ne	$(4.67 \pm 0.53) \cdot 10^{-9}$	$(3.60 \pm 0.29) \cdot 10^{-7}$

Table 4: Ionization rates for a selection of ISNs at 1 AU. The data (including uncertainties) compiled in the table has been taken from Cummings et al. [2002].

of photoionization scales in good approximation with the inverse squared distance from the Sun. This is obtained by assuming that the ionization probability is proportional to the flux of solar UVs and that the Sun is an isotropic source of UV radiation. Since the latter assumption implies for a time-independent source (which only holds true for a time-independent model [Fahr [1971]]) that the number of UV photons flowing through any sphere centered around the source remains constant, these photons are distributed on a quadratically increasing area with increasing sphere radius. Hence, the flux of UVs scales with distance from the Sun $r_\odot$ by a $r_\odot^{-2}$ power law. So the probability of photoionization follows, in approximation, the same trend [Vasyliunas and Siscoe [1976]].
It is noteworthy that dependencies of the photoionization rates of structures on the Sun and the solar activity cycle (both cause a variation of the emission of solar UVs) have been observed (e.g. Fahr [1971], Rucinski et al. [2003], Bzowski et al. [2008].

The modelling of the spatial evolution of charge ionization and electron impact ionization rates is more challenging, since the former is a function of the local SW density and VDF and the latter is a function of the local electron density and VDF in the SW. Global models assume both to scale proportional to the SW density and assume according to the radial expansion of the SW from the Sun in unison with the model of Parker [1958] the SW density to scale inversely with the solar distance squared (e.g. Parker [1958], Axford [1972], Vasyliunas and Siscoe [1976]).
Since the available in-situ observations of the SW and particles embedded therein are limited to few observations at different radial distances from the Sun (e.g. STEREO, which orbits the Sun at 1 AU) in the heliosphere, these approximations can not be improved by including additional in-situ observational data, however ionization profiles of e.g. hydrogen particles are deducible from backscattered Lyman-Alpha radiation (e.g. Fahr [1971], Rucinski and Fahr [1989]). More sophisticated estimations of the spatial evolution of ISN ionization rates require e.g. modeled parameters of the SW which then are limited to computational constraints (e.g. Bzowski [2001]). Yet, the global characteristics of modeled ISN density distributions have been observed through PUI observations as the following chapter shows.

2.2.4 Features of the spatial distribution of PUIs

The features of the spatial distribution of PUIs include regions of density enhancements, which can be employed to obtain parameters of the LISM (e.g. Drews et al. [2012]). In order to present these in an instructive way, this section presents a simulation approach analogous to Keilbach et al. [2016]. The results of which are employed to visualize the characteristics of the spatial distributions of PUIs. Originally, the simulation has been set up to model boundary conditions for a full PUI simulation (compare chapter 2.2.6).

Duncan Keilbach- Three dimensional Pickup Ion velocity distribution functions observed at 1 AU with STEREO/PLASTIC: Anisotropic features and density enhancements in pitch angle distributions as tools to investigate transport effects

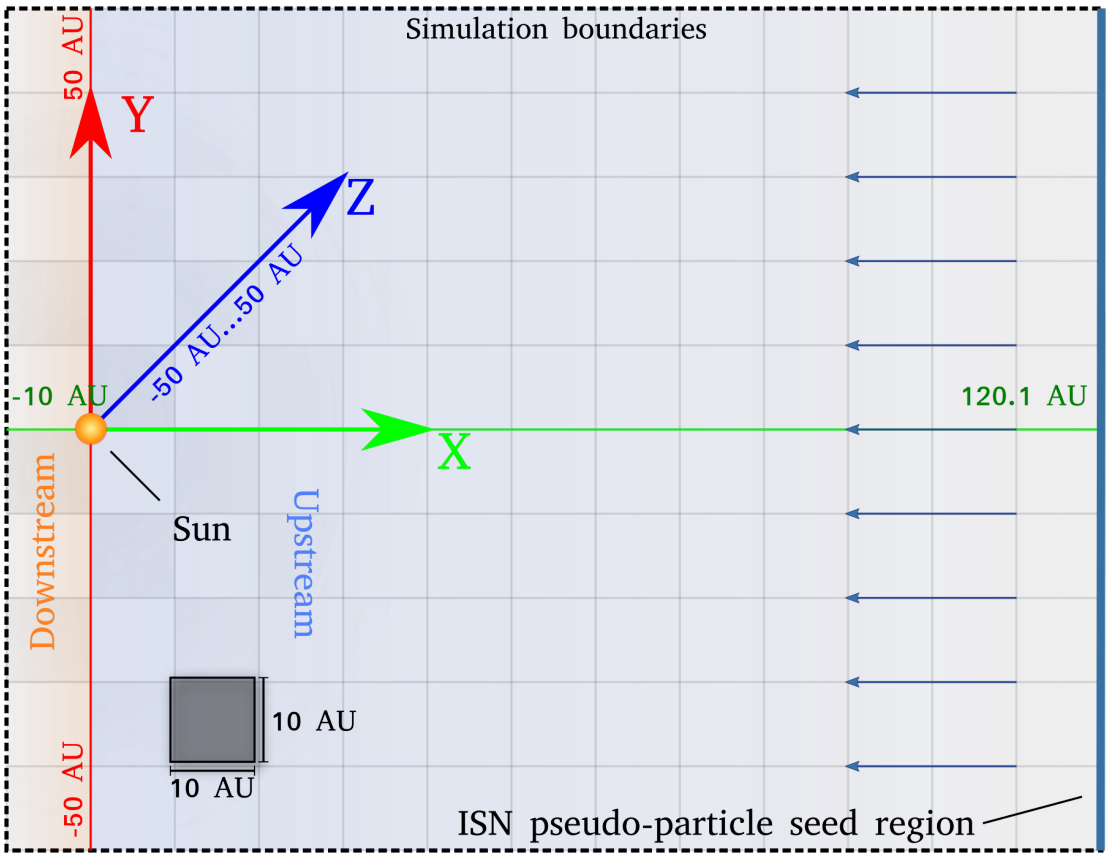

Figure 14: Sketch of the simulated region alongside the region, where ISN pseudo-particles are initialized (pale blue line to the right). The Sun of the model heliosphere is in the coordinate origin. The region an the opposite side of the Sun w.r.t. the interstellar inflow is the Downstream side, the other side is Upstream.

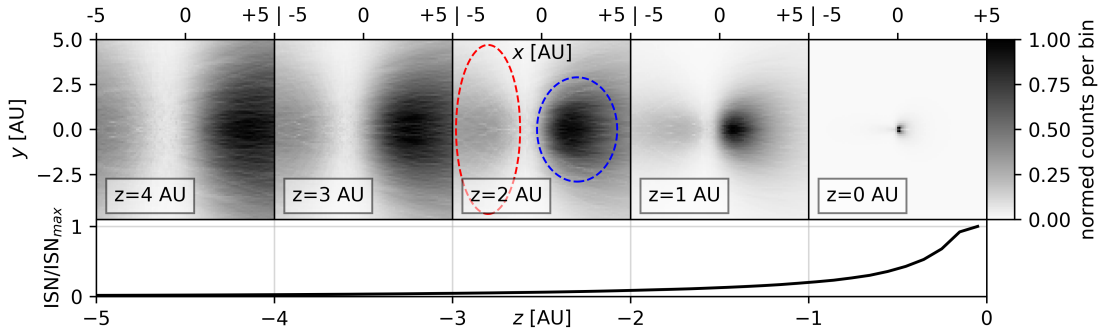

Figure 15: Top: Simulated He ISN densities within a plane parallel to the ecliptic plane, but at a height of the given number z above it. The Sun is located at the coordinate systems origin and the densities are coded in gray scales and normalized to the maximum of each of the panel. Bottom: Simulated He ISN densities as a function of height above the ecliptic plane.

2.2.4.i Simulation approach The goal behind the simulation is to model the inflow of ISN from the LISM to derive ISN densities as well as PUI injection rates. The simulation does not model the motion of PUIs, but of the ISNs they originate from. Therefore, also conclusions about features of the spatial PUI distribution can be drawn.
To simulate the trajectories of traversing interstellar neutrals, the simulation is based on a finite-difference approach (e.g. Press et al. [1989], Birdsall and Langdon [2018]). This means, that the simulation runs in loops, where each iteration represents one finite time step (compare Chapter 2.2.4.i.b). Alongside the simulation of the ISNs kinematics, a Monte-Carlo approach is employed to simulate the ionization of the particles (compare Chapter 2.2.4.i.c). The simulation's coordinate system (sketched in Fig. 14), which is cartesian, is chosen such, that the Sun is in the origin and the (x,y)-layer lies within the ecliptic plane, where $-x$ is the direction of interstellar inflow. The following subparagraphs describe the computational operations of each time step sequentially.

2.2.4.i.a Initialization of particles To keep the program's memory usage within limits defined before the runtime, in the beginning a number of particles to be simulated simultaneously is provided, so that arrays of vectorial particle positions and velocities are initialized before the first time step. Hence, at each time step it is checked, whether any particle is to be re-seeded (e.g. because it is outside the simulation's boundaries or has been ionized) and the required number of particles is overwritten within the array.
The particles' initial positions are uniformly sampled within a box ranging from -50 AU to 50 AU in x and y direction and from 120 AU to 120.001 AU in z direction. Under the assumption, that the LISM is thermalized, the velocities are sampled from a 3d Maxwellian with a temperature of 8500 K. To mimic the relative motion of Sun and LISM, -25.4 km/s are added to the x component of the new particles. Both the temperature and the relative velocity are estimates based on previous PUI studies (e.g. Taut et al. [2018]).

2.2.4.i.b Motional time step If radiation pressure is neglected, the ISNs equations of motion can be directly inferred from the gravitational attraction between an ISN and the Sun (compare e.q 36), so that the equations of motion become

$$\frac{d\vec{v}}{dt} = \frac{\vec{F}_{\text{grav}}}{m_{\text{ISN}}} \text{ and} \tag{37}$$

$$\frac{d\vec{x}}{dt} = \vec{v} \text{ , where} \tag{38}$$

m_{ISN} is the particles mass. With the finite-difference approach, the time derivatives are approximated by $\Delta v/\Delta t$ and $\Delta x/\Delta t$ and the Δv and Δx are obtained by evaluating the equations' right hand sides and multiplying them with Δt. To increase computational efficiency while retaining a given amount of precision, Δt is computed for each particle individually based on the particles' position and velocity. Therefore, each particle is situated at a different time which is unproblematic since the simulation is interested in accumulating densities. On the other hand, this step is necessary since for the precision of the densities a small time step is needed for particles close to the Sun, but at the same time this time precision is unnecessary for particles far away from the Sun and causes those particles to evaluate a large number of time steps before they reach the Sun.
To account for this, the individual time step Δt is computed based on the relative error in absolute gravitational force which, based on gaussian error propagation (e.g. Demtröder [2018]), is

expressed by

$$\varepsilon = \frac{\left|\frac{\partial|\vec{F_{\text{grav}}}|}{\partial t}\right|}{|\vec{F_{\text{grav}}}|}\Delta t \ . \tag{39}$$

To obtain an expression which can be computed per simulation step, the time derivative is substituted by a location derivative. With the definition of the gravitational potential (e.g. Fließbach [2003]), the force derivative then reads

$$\frac{\partial|\vec{F_{\text{grav}}}|}{\partial t} = \frac{\partial|\vec{F_{\text{grav}}}|}{\partial \vec{x}} \cdot \frac{\partial \vec{x}}{\partial t} = \left(\vec{\nabla}|\vec{F}|\right) \cdot \vec{v} = 2GM_{\odot}m_{\text{ISN}}\frac{\vec{x}\cdot\vec{v}}{|\vec{x}|} \ . \tag{40}$$

And the length of the time step is computed by

$$\Delta t = \varepsilon \cdot \frac{|\vec{F_{\text{grav}}}|}{\left|\frac{\partial|\vec{F_{\text{grav}}}|}{\partial t}\right|} \ . \tag{41}$$

2.2.4.i.c Ionization time step Each particle is assigned a statistical weight, as if it would represent an ensemble of particles. Therefore instead of randomly deleting the particles to model their ionization, the ionization probability of the particles is deducted from their densities. With this approach, the simulated entities (which combine the qualities of single particles and a particle ensemble) are called pseudo-particles. A pseudo-particle's ionization probability is derived from the distance to the Sun with an inverse-squared power law, which scales values observed at 1 AU (compare tab. 4). Per pseudo-particle, the ionization probability is scaled to the length of a pseudo-particle's individual motional time step under the assumption that the process follows a geometrical distribution similar to an approach explained in e.g. Piel [2017]. This means, that if $p_{ion,1s}$ is the ionization probability of a single particle of the pseudo-particles ensemble during one second, then $1 - p_{ion,1s}$ is the probability that during that second, that particle is not ionized. So $(1-p_{ion,1s})^2$ is the probability, that a single particle of the ensemble is not ionized within two seconds and $1-(1-p_{ion,1s})^2$ the probability, that this particle is ionized at least once during the two seconds. In approximation, the simulation applies that principle to estimate a probabilistic ionization rate for the pseudo-particle during the length of the motional time step Δt via $(1-(1-p_{ion,1s})^{\Delta t/(1\text{ s})})$. To apply the ionization time step, the result is multiplied with the pseudo-particle's associated density which returns the density deduction due to ionization for this pseudo-particle during the ionization time step. Equally, this returns the pseudo-particle's contribution to the PUI production rate during that time step.

2.2.4.i.d Cleanup and logging For each pseudo-particle the simulation evaluates, whether the pseudo-particle has run out of the simulation's spatial boundaries. Also the current pseudo particles' positions, velocities and densities are employed to accumulate contributions to spatial grids in which the particle density, average PUI production rate, and average vectorial ISN velocity are stored.

2.2.4.i.e Features of the ISN spatial distribution Here, the spatial distribution of ISNs is presented as a result of the simulation. It is noteworthy, however that the conclusions drawn from the simulation results are not new. In fact, the interested reader may refer to Axford [1972], Vasyliunas and Siscoe [1976], Kallenbach et al. [2000], Gloeckler et al. [2004] or Lee et al. [2015].
The spatial distribution of ISN densities (compare fig. 15 for an example simulation result) may be described as a superposition of three aspects.

(1) The PUI production rate has the tendency to increase with decreasing distance to the Sun. This is the consequence of the ionization probability to scale with solar distance (e.g. Vasyliunas and Siscoe [1976]). Where the PUI production rate is increased, density is depleted from the ISN distribution which also affects the downstream (i.e. opposite direction, from the ISN inflows as seen from the Sun, compare Fig. 14) densities (e.g. Lee et al. [2015]).

(2) In upstream direction a region of increased PUI production rates is formed (blue ellipse in Fig. 16), where the distance from the Sun depends on the particle species and the region is roughly crescent shaped [Drews et al. [2012]]. This region is especially pronounced for particles with lower first ionization potentials or a generally high probability of photoionization and is generally formed by the increase of ionization probability with decreasing distance to the Sun. For a variety of ion species (e.g. O^+,Ne^+), the crescent can be observed with a strong density signature at earth's orbit while e.g. He^+ with a higher first ionization potential shows no significant signature of a crescent [Drews et al. [2012], Sokół et al. [2016]].

(3) Downstream (seen from the Sun) another region forms, which is dominated by a gravitational focusing of the ISNs trajectories [Axford [1972], Vasyliunas and Siscoe [1976]] and the subsequent local increase in densities (red ellipse Fig. 16). This focusing area is a region of increased PUI production rates, because the ISN densities are increased there.

Fig. 16 sketches the crescent region (2) and the focusing cone region (3) in the case of a low ionization probability (Tab A) and in the case of a high ionization probability (Tab B). A pronounced focusing cone is to be expected from particles with low ionization probabilities (refer to Tab. 4), since for the ISNs to form a pronounced focusing cones, the particles must not have been ionized to that point. Hence e.g. the He^+ PUIs form a stronger focusing cone (in relation to e.g. the average of densities at 1 AU) than O^+ PUIs. On the other hand, in observations of O^+ PUI the crescent is stronger pronounced than in He^+ PUI densities.

2.2.5 The velocity distribution function of PUIs

The VDF of PUIs is challenging to observe in full detail, since instrumental limitations limit its observation to one-dimensional projections in most studies [Berger [2018], Keilbach et al. [2021]]. Another limitation on the observation of the PUI VDF is the positioning of spacecraft capable of observing them. Before the launch of Parker Solar Probe in 2018 [Fox et al. [2016], Bernasconi et al. [2018]] and Solar Orbiter in 2020 [Müller et al. [2020]], the available observations were limited to distances from the Sun of $\sim 1AU$ or larger distances as observed with the Ulysses [Wenzel et al. [1989], Gloeckler et al. [1992]] and New Horizons [McComas et al. [2008]] spacecraft. Because of the instrumental challenges first studies which observe 3d VDFs of PUIs [Berger [2018], Fischer [2019], Keilbach et al. [2021], Fischer et al. [2021]] are very recent and report proof-of-concept type results. Hence, it is timely to extend the observational knowledge of PUI VDFs by observing three dimensional He^+ PUIs which is the goal of this work.

2.2.5.i PUI injection and the initial PUI VDF The theoretical description of the PUI VDF is best started at the point of injection into the SW. The main mechanical difference between an ISN and a PUI is, that the PUI is subjected to electromagnetic forces, especially the Lorentz force from the interplanetary magnetic field (e.g. Axford [1972]). Since the interplanetary magnetic field is carried by the SW (the limit case of a frozen-in magnetic field applies, compare chapter 2.1.3), a PUI not only gyrates around the local magnetic field, but the guiding center

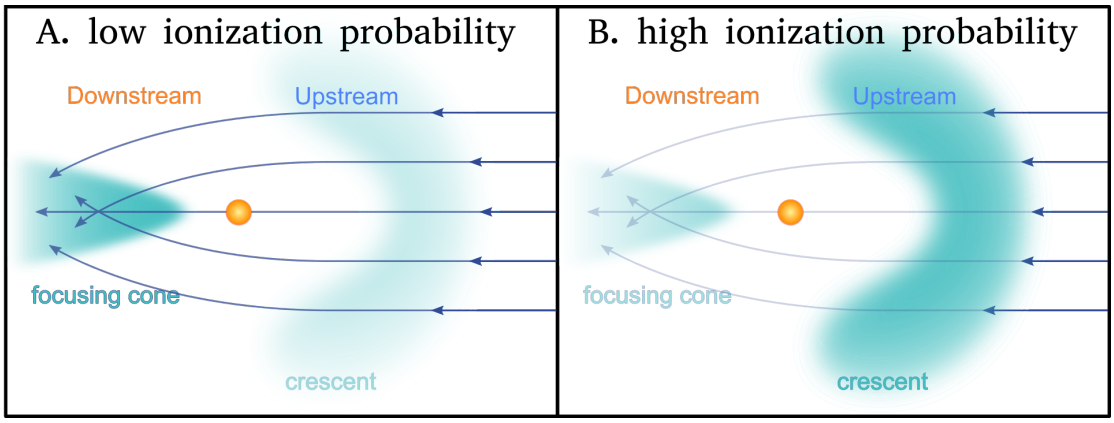

Figure 16: Top down view of the heliosphere showing an area with a diameter of $\sim$ 20 AU centered around the Sun (yellow dot). The blue arrows are example trajectories of the ISNs inflowing into the heliosphere. In the upstream region (direction, from where the ISNs inflow seen from the Sun) a distinct spatial structure of ISN ionization enhancement is formed (turquoise shaded), which is called the crescent [Drews et al. [2012]]. In downstream direction (direction, to where the ISN inflow points seen from the Sun), another region of enhanced ISN ionization is seen (also turquoise shaded), which is the focusing cone [Axford [1972], Vasyliunas and Siscoe [1976]]. Both panels show the same region, but compare ISNs of low ionization probability (A) with those of high ionization probability (B). In the first case, a lesser pronounced crescent is expected than in the latter case. Conversely, in case B a less pronounced focusing cone is expected than in case A.

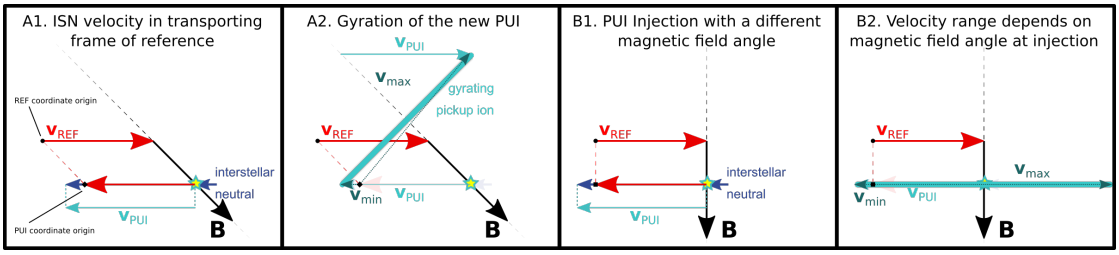

Figure 17: Sketch of the injection process of an interstellar PUI for two magnetic field configurations: Configuration A models a magnetic field in a 45° angle to the reference velocity v_{REF} in the SW. Configuration B models a magnetic field perpendicular to the reference velocity. The constructions depicted in A1 and B1 construct the PUIs initial velocity, which is the velocity of the former ISN in the transporting reference frame. The gyration of the PUI creates the spectrum of minimal and maximal velocities to be found in the initial VDF of a PUI as shown in A2 and B2. The range of velocities is thereby dependent on the angle between local magnetic field and transporting velocity. In all panels, the coordinate system, in which the transporting frame and the magnetic field are shown is offset w.r.t. the coordinate system of the ISNs and the PUIs. This offset has been done purely for visualization purposes, so that the main features of the PUI injection process are better visualized. The origins of both coordinate systems have been depicted by a black circle (transporting frame) and a black square (PUIs).

of the gyration is governed by the motion of the magnetic field lines the SW carries outward. The consequence of this is sketched in fig. 17. Seen from a coordinate system moving with the velocity of the transport of the magnetic field $\vec{v}_{\mathrm{REF}}$, the velocity of an ISN with a velocity of $\vec{v}_{\mathrm{ISN}}$ in a Sun-centered coordinate system is given by the difference of $\vec{v}_{\mathrm{ISN}}$ and $\vec{v}_{\mathrm{REF}}$. So a PUI is injected into the SW with a velocity of $\vec{v}_{\mathrm{PUI}} = \vec{v}_{\mathrm{ISN}} - \vec{v}_{\mathrm{REF}}$. Since the PUI is forced to gyrate around the local magnetic field by Lorentz-force, the velocities the PUI will exhibit initially, rotations of $\vec{v}_{\mathrm{PUI}}$ around the local magnetic field. If PUIs are accumulated at different times, their gyration phases differ from each other yielding a torus-shaped velocity distribution (e.g. Axford [1972]). The range of absolute velocities a PUI is initially expected to be observed in is at a maximum if the local magnetic field is perpendicularly oriented to $\vec{v}_{\mathrm{REF}}$. This means, that the minimum absolute velocity a PUI is initially expected at in the transporting reference frame, is $-|\vec{v}_{\mathrm{ISN}}|$ and the maximum velocity is $|\vec{v}_{\mathrm{ISN}} - \vec{v}_{\mathrm{REF}}|$. Observed in a frame of reference centered at the Sun this translates into a minimum expected velocity of $|\vec{v}_{\mathrm{REF}} - \vec{v}_{\mathrm{ISN}}|$ and a maximum expected velocity of $|2\vec{v}_{\mathrm{REF}} - \vec{v}_{\mathrm{ISN}}|$. Since $\vec{v}_{\mathrm{ISN}}$ is smaller than the SW by a factor of ten or more, a general rule of thumb is that PUI velocities range from $|\vec{v}_{\mathrm{REF}}|$ to $2|\vec{v}_{\mathrm{REF}}|$ (e.g. Axford [1972], Möbius et al. [1985], Gloeckler and Geiss [1998]).
Since the initial kinematic properties of PUIs are determined by the velocity of the transporting frame, it is useful to normalize the PUI velocity to the velocity of the transporting frame. Thus, the quantity

$$w_{\mathrm{REF}} = \frac{|\vec{v}_{\mathrm{PUI}}|}{|\vec{v}_{\mathrm{REF}}|} \tag{42}$$

is motivated. From fig. 17 it is evident that the initial PUI distribution (apart from a velocity component, which is parallel to the magnetic field) is centered around the velocity of the transporting frame. So a more meaningful quantity is obtained by transformation of the PUI velocity into the reference frame before normalization. Hence, the transformed version of w_{REF} is introduced, namely

$$\varpi_{\mathrm{REF}} := \frac{|\vec{v}_{\mathrm{PUI}} - \vec{v}_{\mathrm{REF}}|}{|\vec{v}_{\mathrm{REF}}|} \ . \tag{43}$$

This definition of ϖ_{REF} neglects the direction of velocity. Also, it does not distinguish between particles slower than the reference frame and faster the reference frame (as seen in the reference frames direction). However, since interstellar PUIs are expected to be systematically faster than their reference frame, it is helpful to distinguish between faster and slower particles for a separation of PUIs from other particles in the SW. For better separation between SW and PUIs it is practical to alleviate that employing the direction of relative PUI velocity w.r.t. the radial direction with the definition of a signed version (compare Gloeckler and Geiss [1998]). This signed version $\varpi^{\pm}_{\mathrm{REF}}$ is defined by

$$\varpi^{\pm}_{\mathrm{REF}} := \varpi_{\mathrm{REF}} \cdot \mathrm{sign}\left(\vec{v}_{\mathrm{PUI}} - \vec{v}_{\mathrm{REF}}, \hat{e_r}\right). \tag{44}$$

Here, $\hat{e_r}$ is a unit vector pointing in radial direction and can be seen as a proxy for the direction of SW flow. If the direction of the reference velocity is precisely measured, the radial unit vector can also be replaced by the direction of the reference velocity. If observed in the correct frame (a frame moving at the velocity of the particle transport), the rule of thumb for the PUI velocities translates to $0 \lessapprox \varpi_{\mathrm{REF}} \lessapprox 1$, although the ISN velocity shifts the initial velocity slightly (e.g Lee et al. [2015], Möbius et al. [2015]):
At the down-stream side (w.r.t. the interstellar inflow) of a Sun-centered coordinate system, the ISN velocities are approximatively parallel to the radial outflow of the radial outflow of the SW. In up-stream direction it is the opposite. So the expected maximum of PUI velocities is

a function of location in the heliosphere w.r.t. the direction of interstellar inflow at the downstream side a local maximum is expected. This effect has been employed by Möbius et al. [2015, 2016], Taut et al. [2018] to determine the direction of interstellar inflow. Before the direction of interstellar inflow has been determined by finding the location of distinct features within the longitudinal PUI density distribution (e.g. Moebius et al. [1995], Drews et al. [2012]).
In addition, it is useful to relate the particles' velocity to the local magnetic field $\vec{B}$, since the Lorentz force governs the particles' motion. Within the transporting reference frame, the particle velocity may be described via a component perpendicular $v_\perp$ and parallel $v_\parallel$ to the local magnetic field (e.g. Piel [2017]). Together with the reference-frame transformed absolute velocity $|\vec{v}_{\mathrm{PUI}} - \vec{v}_{\mathrm{REF}}|$ a rectangular triangle is formed and the inclination angle of which w.r.t. the magnetic field is the pitch angle α with

$$\alpha = \arctan\left(\frac{v_\perp}{v_\parallel}\right) \ . \tag{45}$$

Since it is unknown which frame is the physically correct choice for a transporting frame, in the following the pitch angle is indexed with the reference frame the velocities of concern are obtained from. Typically, (e.g. in Gloeckler and Geiss [1998] or Drews et al. [2015]) the velocity is related to the SW proton bulk velocity. In the context of this work, the proton bulk velocity is obtained from different methods corresponding to the following indices:

SWm The proton bulk velocity is determined by an onboard algorithm of STEREO based on PLASTIC data (compare chapter 3.1.5.i).

SWp The proton bulk velocity is determined by a fit of a Maxwellian model function to STEREO/PLASTIC proton observations (compare chapter 4.2.3)

SW This index is employed if general statements about the PUI velocity (regardless of the method of the SW reference velocity determination) are made or when a work is referred to, which employed a general term for that velocity.

Recently, the dHT frame velocity (compare chapter 2.1.8.iii) has been computed from spacecraft observations [Němeček et al. [2020]]. Since this frame is per definition force free [de Hoffmann and Teller [1950]], it may be more meaningful to relate the PUI velocity to this velocity than to the SW proton bulk velocity. In preparation of a study which investigates the feasibility of the dHT velocity as a reference frame to relate the PUI velocity to, the technique of Němeček et al. [2020] has been adapted to STEREO/PLASTIC observations. This is outlined in Section 4.2.6.
The different definitions of relative particle velocities make significantly different quantities for observation. In this work, particle data from a time-of-flight mass-spectrometer is employed. Such an instrument measures the particle velocity in terms of its total energy in the frame of the spacecraft. Fig. 18 provides a sketch of the velocity of an example PUI w.r.t. the aperture of an instrument and depicts, how the different definitions of relative particle velocity are computed from it. Centered at the spacecraft velocity, surfaces of constant w_{REF} are concentric shells, where with increasing radius w_{REF} increases. This directly scales with the absolute velocity which the instrument measures. Surfaces of constant ϖ_{REF} are concentric shells which are centered at $\vec{v}_{\mathrm{REF}}$. Hence, geometrical differences must be carefully considered, when the data is analyzed: The instrument assigns digital bins to the particle energies, which introduces a statistical uncertainty to w_{REF}. Since the shells of constant w_{REF} and ϖ_{REF} originate from different locations, the resulting uncertainty of ϖ_{REF} depends nonlinearly on the uncertainty in w_{REF}. This is further investigated in Chapter 5. So the sketch in Fig. 18 emphasizes the observational differences between both relative velocities. From Fig. 18, it is also clear, that

interpretations of distributions of w_{REF} are likely to include a systematic error, since a rotation of the reference velocity without a modification of the PUI velocity already modifies w_{REF}, while ϖ_{REF} is unchanged (also compare Gloeckler and Geiss [1998], Drews et al. [2012], Taut et al. [2018]).

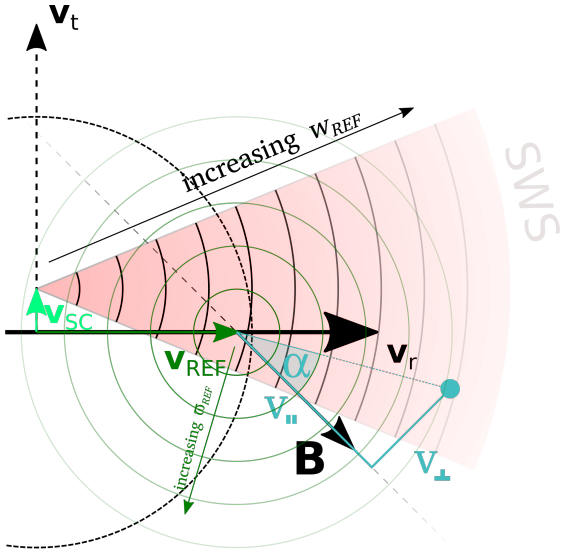

Figure 18: Illustration of the different definitions of PUI relative velocity w.r.t. the reference frame velocity $\vec{v}_{\mathrm{REF}}$. For the depicted reference frame, it is assumed, that it represents the velocity by which the PUIs are transported in the SW. Then, since the PUIs (represented by a single turquoise dot) gyrate around the local magnetic field, it is convenient to split the PUI velocity in the reference frame into a component parallel and perpendicular to the local magnetic field $\vec{B}$. From these quantities also the pitch angle α can be computed. For simplicity, the vector of the reference velocity points in this example in radial direction (which is the figure's x-axis). The figure's y-axis is tangential direction. For observation with a time-of-flight mass spectrometer (compare Chapter 3.1), additionally the spacecraft's velocity ($\vec{v}_{\mathrm{SC}}$) needs to be respected. Shaded in red, the aperture of the Solar Wind Sector of the Plasma and Suprathermal Ion Composition instrument onboard of the Solar Terrestrial Relations Observatory (compare Chapter 3.2.1) is depicted. The concentric circles which are centered at the origin of the aperture indicate, that the instrument measures primarily absolute velocity in the spacecraft frame from which shells of equal w_{REF} are found. For the computation of ϖ_{REF}, equal shells of which are indicated by concentric circles centered at the reference velocity, coordinate transformations are required.

2.2.5.ii Phase space transport The initial PUI VDF is modified by a variety of transport processes during the transport of PUIs from their point of creation to the spacecraft observing it.

2.2.5.ii.a Pitch angle scattering Since after ionization the former ISN is subject to electromagnetic forces in the SW, it is also exposed to the turbulent nature of the SW. The interaction with waves in the SW is believed to modify the PUI VDF strongly and is commonly approximated through stochastical processes like diffusion in velocity space (e.g. Jokipii [1966], Fisk et al. [1997], Saul et al. [2007]).

Duncan Keilbach- Three dimensional Pickup Ion velocity distribution functions observed at 1 AU with STEREO/PLASTIC: Anisotropic features and density enhancements in pitch angle distributions as tools to investigate transport effects

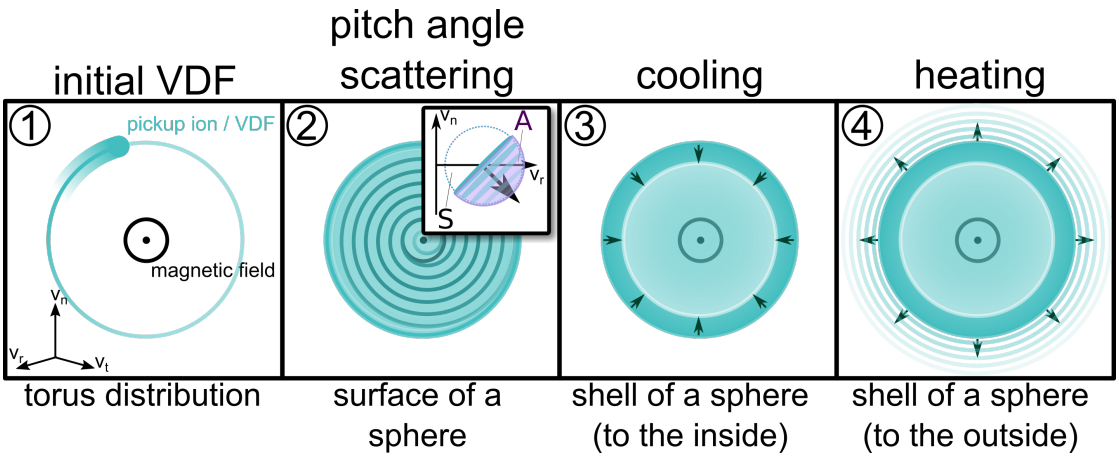

Figure 19: Sketch of the PUI VDF (turquoise shaded) subjected to different transport effects in order of the sequence of the four panels. The magnetic field (black arrow) points out of the drawing layer. In panel (1) also a sketch of the coordinate system is shown, where the radial $\vec{v}_r$, tangential $\vec{v}_t$ and normal velocity $\vec{v}_n$ create a orthonormal coordinate system. Panel 1 depicts an initial torus distribution. Panel 2 depicts the effect of pitch angle scattering on fast time scales: a VDF, where the density is distributed on the surface of a sphere. An insert into Panel (2) depicts the hemispherical model of fast pitch angle scattering, where the VDF is differently scattered on the sunward (S) and antisunward (A) hemisphere. In Panel (3) it is shown, that cooling narrows the radius of the sphere, onto which the PUIs are distributed. So, then velocity shells with velocities slower than the transporting velocities are also populated and the VDF becomes a thicker shell. In Panel (4) it is shown, that the width of the VDF is significantly increased, if heating processes are applied to it. The heating processes create suprathermal tails.

Initially, it was assumed that the interaction between PUIs and turbulent features of the SW modified the PUIs pitch angle swiftly compared to the expansion of the SW leaving no traces of the initially anisotropic distribution (sketched in fig. 19(1)) to observe [Vasyliunas and Siscoe [1976]].
However, anisotropic features in the PUI VDF have been observed [Moebius et al. [1995], Gloeckler and Geiss [1998]]. Oka et al. [2002] even observed a distinct torus VDF for He PUIs and estimated that during about one fifth of the time period of observation a torus-like distribution was visible. Finally, Drews et al. [2015] employed STEREO/PLASTIC observations to obtain two-dimensional VDF projections and observed density maxima hinting towards an anisotropic distribution. These density maxima were roughly correlated to a direction perpendicular to the local magnetic field.

Therefore, the wave-particle interaction driven process modifying the PUI VDF which is often referred to as pitch angle scattering (compare fig. 19(2), is less efficient than originally suggested [Moebius et al. [1995], Gloeckler and Geiss [1998]]. To obtain a transport model matching the observations of that time better, Isenberg [1997] divided the velocity space into two hemispheres: An anti-sunward hemisphere (with pitch angles $< 90°$) and a sunward hemisphere (with pitch angles $> 90°$) and suggested, that while the diffusion within either of the hemisphere is swift, but inhibited between both. One motivation for this assumption is the diffusion model by Jokipii [1966], which predicts a local minimum of the pitch angle diffusion rate of particles undergoing wave-particle interactions at a pitch angle of 90°. Originally pitch angle scattering was believed

to scatter a torus-like distribution onto the surface of a sphere in velocity space. The model of Isenberg [1997] describes the VDF similarly as sphere shells, but with different fluxes on either hemisphere (compare fig. 19(2)). Since PUIs are injected into the anti-sunward hemisphere, this model expects most PUIs in the antisunward hemisphere, which accounts for anisotropic distributions, but not completely for traces of torus like VDFs observed by Oka et al. [2002] or Drews et al. [2012].
The interesting question in the field of PUI VDF is therefore, whether a typical torus distribution like it is expected for freshly created PUIs prevails (or at least in traces) through transport in the SW and is even observable at 1 AU. The observation of (partial) shell like distribution might also be an effect of observation in a reduced number of dimensions.

2.2.5.ii.b Cooling processes PUI transport on short time scales is dominated by pitch angle scattering, but on more global time scales different processes are relevant in the description of PUI transport. A commonly referred to process is called adiabatic cooling [Moebius et al. [1988], Chen et al. [2013]] : This model assumes, that

- the PUIs can be described in analogy to an ideal gas
- and that the average velocity of a PUI distribution w.r.t. the transport frame can be related to the thermal velocity of the distribution.

The second assumption implicitly requires Maxwellian qualities for the PUI VDF, otherwise the existence of a thermal velocity, at least in the sense of kinetic gas theory (e.g. Fließbach [2003]) is questionable. An argument to justify these assumptions is the swift pitch angle scattering, i.e. a small mean free path for scattering compared to the SW expansion. The swift scattering leads to an isotropic VDF [Moebius et al. [1988]]. However, with typical SW densities of several particles per cm^3 (e.g. Marsch [2006]) and PUIs only making up a small fraction of that density, the mean free path for particle collision is significantly larger, which leaves the caveat to the argument, that the ensemble of PUIs is unable to self-thermalize (e.g. Baumjohann and Treumann [2012]).
In the model of adiabatic cooling the radial expansion of the SW wherein the PUIs are embedded is considered. Since the expansion means an increase in volume with constant number of particles, the density decreases. Under the assumption of an adiabatic process, it is a consequence of the ideal gas equation that the temperature (ergo the thermal velocity) of the PUI ensemble decreases with a power law [Moebius et al. [1988], Chen et al. [2013]]. This results in a gradual slowing of the PUI VDF from a ϖ_{SW} of 1 (at the injection of the PUIs) to shells of smaller ϖ_{SW}. This process is visualized in Fig. 19(3). Under the assumption that this process dominates the PUI VDF over other effects, the ϖ_{SW} can then be seen as an indicator of the particles origin: Particles with slower values of ϖ_{SW} have undergone more cooling and thus have been ionized further inside the heliosphere [Moebius et al. [1988], Chen et al. [2013]].

2.2.5.ii.c Acceleration processes Neglecting inner source PUIs and assuming a constant solar wind velocity and quiet conditions in the SW, it would be a consequence of adiabatic cooling that the lower velocity shells of a PUI VDF represent populations of PUIs which have been injected earlier than PUIs on shells of higher velocity. This would be an interesting way to probe the history of a PUI distribution w.r.t. its radial evolution during transport in the SW. However, the existence of different acceleration processes in the SW skews that idea (compare fig. 19(4)).
Recently, suprathermal tails have been observed in the He^+ PUI VDF and linked to compression regions in the SW [Moebius et al. [2019], Bower et al. [2019], Yang et al. [2020]], which hints to acceleration of PUIs in proximity to these regions. Analogously, the interaction of PUIs with coronal mass ejection is expected to also accelerate PUI VDFs.

2.2.6 Theoretical PUI velocity distributions at 1 AU derived from test particle simulations

As a conclusion for the introduction into interstellar PUIs, this chapter presents a PUI sandbox simulation software, which employs a test particle approach to simulate the propagation of PUIs from their injection to 1 AU. The simulation has been designed with focus on the influence of the velocity of the transporting frame to PUI VDFs on the one hand and on the other hand on the ability to select and isolate physical processes and theoretically observe their effect to the VDFs. The focus of the simulations is to determine, whether selected concepts, which are further explained in this section, create apparent traces of acceleration and deceleration processes.

2.2.6.i Simulation design Compared to proton densities, interstellar PUIs do not make up a large fraction of the total density of particles in the SW. So, a test particle approach is justified. In a test particle approach, the forces of electric and magnetic field to the particles are evaluated, however, the fields, that the particles create themselves are not evaluated (e.g. Birdsall and Langdon [2018]). While this is an approximation, it grants the advantages of better control of the field conditions during the simulation and less computational load. Also, for the simulation of the evolution of the VDFs, the evaluation of (partly phenomenological) model functions is employed instead of a computation of the particles equations of motion. This course of action has mainly been selected, because the simulation is concerned with the radial evolution of the VDFs under the influence of selected effects to provide expectations for PUI observations and has not the scope to fully simulate every physical aspect of PUI VDFs. Therefore the simulation is heavily dependent on the models, which are fed into the simulation.

After a successful run, the simulation returns theoretical PUI VDFs as a function of radial distance from the Sun. Thereby, it is assumed, that the observed VDF follows the SW in radial direction. So, as an input parameter the position as longitudinal and latitudinal angle in a J2000 heliocentric coordinate system is required. Also, the particles are treated as a representation of a particle ensemble, which means, that in addition to a velocity attribute (3-vector), also each particle is associated with a density attribute. The density attribute attributes a statistical weight to each particle.
The simulation is evaluated by stepping from a minimum solar distance towards a maximum solar distance. On the way, new PUIs are sampled from an injection model and based on pre-defined model the modification of the already existing particles from one distance step to the next is computed. Then, the combination of the modified and newly sampled particles is employed as input for the next step. A schematic representation of a simulations timestep is also provided via a flowchart in Fig. 20.

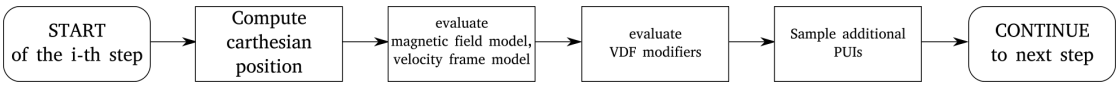

Figure 20: Overview flow chart of a computational time step of the PUI sandbox simulation. The position of the distribution of particles, the radial evolution of which the simulation models, is intrinsically defined by the quantities radial distance to the Sun, longitude and latitude. So, in the first step these are converted into a cartesian coordinate system. Then, models for the local magnetic field and local transporting frame velocity (chapter 2.2.6.ii.b) are evaluated. Afterwards, models of VDF modification are evaluated (chapter 2.2.6.ii.c). As a last part of the step, additional PUIs are sampled based on input injection models (chapter 2.2.6.ii.a).

2.2.6.ii Description of employed models In the first step of the simulation, the procedure deviates from Fig. 20 such, that the VDF modifiers are not evaluated, since firstly PUIs need to be sampled. To sample PUIs in the context of the simulation, a model is required, which returns the local PUI production rate. Under the assumption of PUI injection at randomized gyration phases and based on principles presented in chapter 2.2.5, a torus distribution with an even distribution of gyration phases is selected as a model for the VDF to sample particles from.

2.2.6.ii.a PUI injection models For the torus VDF both a velocity frame, a local magnetic field vector and the velocities of the former ISNs, which seed the PUIs are required as well as the local PUI production rate. For both the ISN velocities and the PUI production rate the results of the ISN simulation presented in chapter 2.2.4.i are employed, whereas for the ISN velocities only a local average of the velocities is available. Future implementations of the ISN may feature the computation of a local ISN VDF. However, the storing of VDFs as a function of position within a three-dimensional grid requires a large amount of memory compared to saving averages as a function of location. Yet, the probability of a systematic error to the initial PUI velocities arising from the averaging process can not be ruled out, especially if local ISN VDFs are skewed or multimodal. Since simulated ISN velocities are in the magnitude of about a tenth of the SW velocity (compare e.g. Keilbach et al. [2016]), the relative error in sampled velocities is not expected to influence the significance of the simulation too much, especially since the simulation itself is a sandbox approach. Yet, it needs to be kept in mind, that due to the nonlinear nature of some processes, which modify the VDFs, the actual error may reproduce stronger than initially expected.
This model, which employs simulated ISN densities and per location an averaged ISN velocity, per location in the model heliosphere a torus with a single pitch angle is yielded. For reference, this basic model is called *torus_ vdf*. In addition, a modification is implemented, which does not take into account the simulated ISN velocities for reference. This model is referred to with *torus_ vdf_ noISNvelocities*.
In addition, two versions have been implemented, which create a broader pitch angle distribution:

- *torus_ vdf_ 1eV* This is a so called hot-model of the ISN VDF, which samples ISN velocities with a Maxwellian, which has the averaged velocity from the ISN simulation as a center and an estimation of the ISN temperature outside the heliosphere as a standard deviation, before sampling torus distribution from the Maxwellian distributed velocities.
- *torus_ vdf_ wave* This model assumes, that a wave is overlayed with the local magnetic field during PUI injection and samples PUIs on torus distributions corresponding to rotated versions of the local magnetic field.

Both may also be combined with the addition of *_ noISNvelocities*.

2.2.6.ii.b Magnetic field and velocity frame model As a model for the local magnetic field an implementation of the Fisk-Parker IMF model has been created (compare chapter 2.1.3.ii). Most interesting for the simulation are the models for the velocity frame. Hereby, with a velocity frame, the velocity is meant, with which the PUIs are actually transported. This is directly connected with the question, with which velocity the frozen-in magnetic field is carried by the SW (compare chapter 2.1.8.iii). Assuming a different frame during observation than the actual transporting frame may have a significant influence on observed quantities like pitch angle and distributions of relative velocities. Therefore, assuming a transporting frame for observation, which is not the actual transporting frame, may also result in apparent acceleration and deceleration effects [Keilbach et al. [2020]].
As model frames, three different variants were implemented.

- *constant_ solar_ wind_ frame* (also *SW*) This is a model for the proton bulk frame, which models a vector pointing constantly in radial direction with a fixed absolute value.
- *dHT_ frame* This is a model for the dHT frame (compare chapter 2.1.8.iii), for which it is assumed, that the dHT frame is shifted w.r.t. the local solar wind velocity (modeled here with the constant radial velocity) in approximation with the Alfvénic velocity in direction of the local magnetic field. For this implementation, the Alfvénic velocity is assumed constant.
- *dHT_ frame_ vA* This model refines the *dHT_ frame* model's approximation by taking into account, that the Alfvénic velocity scales with radial distance from the Sun. The model *dHT_ frame* is not really a good approximation of the dHT frame. However, it is yet suited to observe theoretically, how a VDF behaves, if the frame is shifted w.r.t. the local SW velocity and this is the scope of the sandbox simulation.

It needs to be noted, that both *dHT_ frame* and *dHT_ frame_ vA* interestingly produce the same PUI velocities at injection as *constant_ solar_ wind_ frame*, since both the frames' velocities differ from the velocity of *constant_ solar_ wind_ frame* by a vector which is parallel to the magnetic field. This can directly be seen by a computation of a velocity of the initial PUI VDF after injection into one of the shifted frames. W.r.t. the velocity of *constant_ solar_ wind_ frame* $\vec{v}_{swf}$ the shifted frames can be expressed by $\vec{v}_{sf} := \vec{v}_{swf} - v_A\hat{e}_\parallel$, where v_A is the Alfvénic velocity and $\hat{e}_\parallel$ is a unit vector parallel to the local magnetic field. Let $\vec{v}_{isn}$ be the ISNs velocity at ionization. Then the initial velocity of the PUI in the shifted frame is $\vec{v}_I = \vec{v}_{isn} - \vec{v}_{sf} = \vec{v}_{isn} - \vec{v}_{swf} + v_A\hat{e}_\parallel$. To obtain a torus distribution from this initial velocity, the initial velocity is split into a parallel part $v_\parallel := \vec{v}_I \cdot \hat{e}_\parallel$ and a perpendicular part $v_\perp := \vec{v}_I \cdot \hat{e}_\perp$. Here, $\hat{e}_\perp$ is a unit vector perpendicular to the magnetic field. The exact direction of that vector determines the position of the velocity on the torus (e.g. define $\hat{e}_{\perp,1}$ and $\hat{e}_{\perp,2}$ with $\hat{e}_{\perp,1} \perp \hat{e}_{\perp,2}$, so that $\hat{e}_\perp = \cos(\varphi)\hat{e}_{\perp,1} + \sin(\varphi)\hat{e}_{\perp,2}$ with $\varphi \in [0, 2\pi]$ as a phase on the circle). The parallel and perpendicular velocities compute to

$$v_\parallel = (-\vec{v}_{swf} + v_A\hat{e}_\parallel)\cdot\hat{e}_\parallel = -v_{\vec{swf}}\cdot\hat{e}_\parallel + v_A\underbrace{|\hat{e}_\parallel|^2}_{1} \tag{46}$$

$$v_\perp = (-\vec{v}_{swf} + v_A\hat{e}_\parallel)\cdot\hat{e}_\perp = -\vec{v}_{swf}\cdot\hat{e}_\perp + v_a\underbrace{\hat{e}_\parallel\cdot\hat{e}_\perp}_{0} = -\vec{v}_{swf}\cdot\hat{e}_\perp \ . \tag{47}$$

The velocity of the PUI is then

$$\vec{v}_{PUI} := v_\parallel\hat{e}_\parallel + v_\perp\hat{e}_\perp + \vec{v}_{sw} \ , \text{ which} \tag{48}$$

computes to

$$\vec{v}_{PUI} := (-\vec{v}_{swf}\cdot\hat{e}_\parallel)\hat{e}_\parallel\underline{+v_A\hat{e}_\parallel} - (\vec{v}_{swf}\cdot\hat{e}_\perp)\hat{e}_\perp + \vec{v}_{swf}\underline{-v_A\hat{e}_\parallel} = (-v_{\vec{swf}}\cdot\hat{e}_\parallel)\hat{e}_\parallel - (\vec{v}_{swf}\cdot\hat{e}_\perp)\hat{e}_\perp + \vec{v}_{swf} \ . \tag{49}$$

Since the field-parallel velocity shifts of the frame cancel out, this velocity is the same as the velocity, if injection would take place into the *constant_ solar_ wind_ frame*.

As a consequence, it can not be distinguished from velocity, whether the PUIs have been injected into the *constant_ solar_ wind_ frame* or a frame shifted by a field-parallel velocity to that frame. Therefore, in the following the simulation only computes distributions in the *constant_ solar_ wind_ frame*. Yet, it needs to be noted, that for real data it is not guaranteed, that the dHT frame is shifted w.r.t. the SW frame by exactly a field-parallel vector. So, more sophisticated models may be justified for a future study. Also, as a second consequence, since a

velocity distribution without additional information can not indicate, whether the actual frame of transport is shifted by a field-parallel vector w.r.t. the referenced frame of transport, and since $v_\perp$ is the same for injection in both frames, but not $v_\parallel$, the pitch angle distribution is not the same for both frames. So, in the special case of a field-parallel shifted velocity frame this example computation illustrates, that apparent modifications of the pitch angle distributions may arise from incorrectly chosen reference frames for computation of pitch angle distributions from observational data.

2.2.6.ii.c Models for the modification of PUI VDFs On the technical side, the modification models put into the simulation are functions, which accept arrays of velocities and densities as well as radial distance at the current step and at the next step and also the transporting frame velocities and magnetic field vectors at both and return modified densities and velocities for the next radial step.
On the physical side, the models implemented so far are mostly based on phenomenological considerations. To simplify the discussion of the simulation's results, in the following the models are given names. Each simulation run can feature a single model, a combination of these or none.
The modification model *radial_ expansion* scales the density with distance, since during radial expansion the density of expanding particles becomes thinner (scaling with a r^{-2} power law) (e.g. Parker [1958]).
The following two models take slow gradual changes into account. Under the assumption, that a slow rotation of the magnetic field vector (e.g. from the radial evolution of the Parker spiral) causes the VDF rotate with the frame, the modification model *rotate_ with_ frame* rotates the VDF accordingly each step. The modification model *translate_ with_ frame* is implemented such, that the VDF is translated with the radial evolution of the transporting frame velocity, wherein translation is not meant in location space, but in velocity space.
These models are basic in nature, but through the simulations sandbox approach and the implementations modular nature the simulation is ready to be expanded to new models for future studies.

The simulation's scope is defined from a twofold question: In which way do modifications of the PUI VDF during transport from the PUIs injection to 1 AU modify the VDF to the point of observation and how interpretations of the VDF change, if a wrong transporting frame is assumed by an observer. The second part of the question can also be formulated as whether observed accelerations or decelerations are actually apparent, because during analysis the transporting frame was not chosen correctly.

Although these questions are the concern of a future study for which this simulation is designed, preliminary results are presented here, since these are instructive to visualize problems and caveats which concern the presented theory of PUI transport. For this synopsis four simulations were run which were set up in an incremental fashion. The first simulation of which resulting PUI VDFs are shown in Fig. 21 does not employ a modification model for the VDF. Rather, the first simulation is a basic setup on which the remaining simulation setups base. In this first simulation, simulated ISN ionization rates (compare Chapter 2.2.4.i) are employed to model the densities of newly created PUI densities per simulation step. To keep the example more instructive and reduce the number of variables, no ISN velocity model is put into the simulation. As a magnetic field, a Fisk-Parker-type magnetic field is employed and as an initial VDF for newly created PUIs a torus distribution is assumed. For the following simulations of which resulting PUI VDFs are shown in Fig. 22, modification models for the VDF are introduced incrementally. At first the model *rotate_ with_ frame* is employed, then in addition to that model also the model *translate_ with_ frame* is employed. Finally, in addition to these models

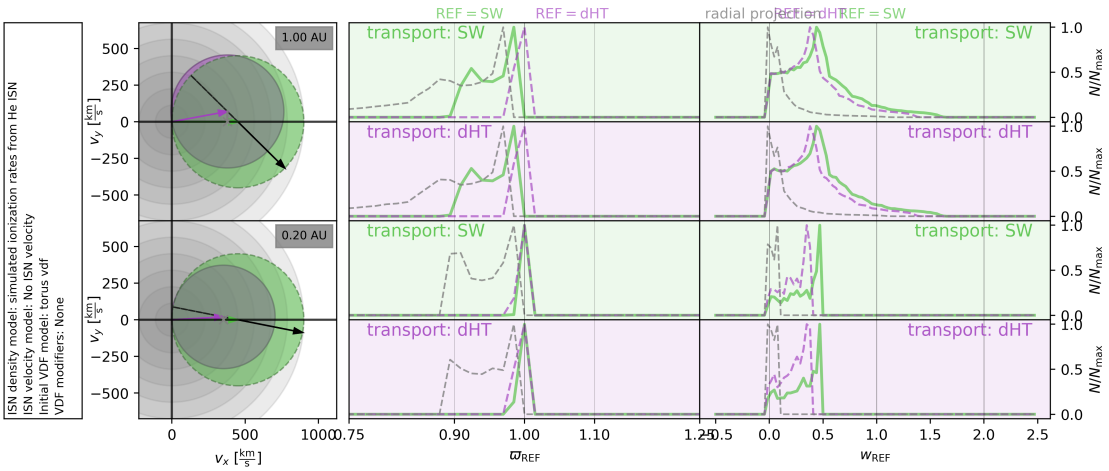

Figure 21: Simulated PUI VDFs with a basic initial setup which is briefly indicated in the left box. The left left column of plots is a sketch of the SW frame velocity (green arrow), the dHT frame velocity (purple arrow) and the magnetic field (black arrow) as a projection to the (v_x,v_y)-plane. In addition circles are drawn around the SW and dHT frame velocities which have these velocities as a radius and therefore represent an absolute velocity equal to the frame velocity within as observed within that frame. The spacecraft observes in a frame close to the coordinate origin. Hence, shells of equal velocity as observed from the origin are drawn in gray shades. The two rows of the left plots are for two different distances from the Sun. The four rows of right plots are made such, that two of each accord to one of these distances. The difference between a pair of rows which belong to the same distance is that for the green shaded plots for the simulation the SW frame is employed by the simulation as the transporting frame and for the purple shaded plots the dHT frame is employed as the transporting frame. The two columns of plots display histograms of different definitions of relative PUI velocity. The left of these show the relative PUI velocity with the reference velocity subtracted from it before normalization (compare eq. 43) and the right show the relative PUI velocity normalized to the reference velocity (compare eq. 42). The employed reference velocity is different for the different plotted histograms. The green ones assume the SW frame as a reference frame and the purple ones the dHT frame as a reference frame. The dashed gray lines depict a radial projection of the velocity which is then normalized. For these always the simulations' transporting frame is employed. Each histogram is normalized to it's individual maximum.

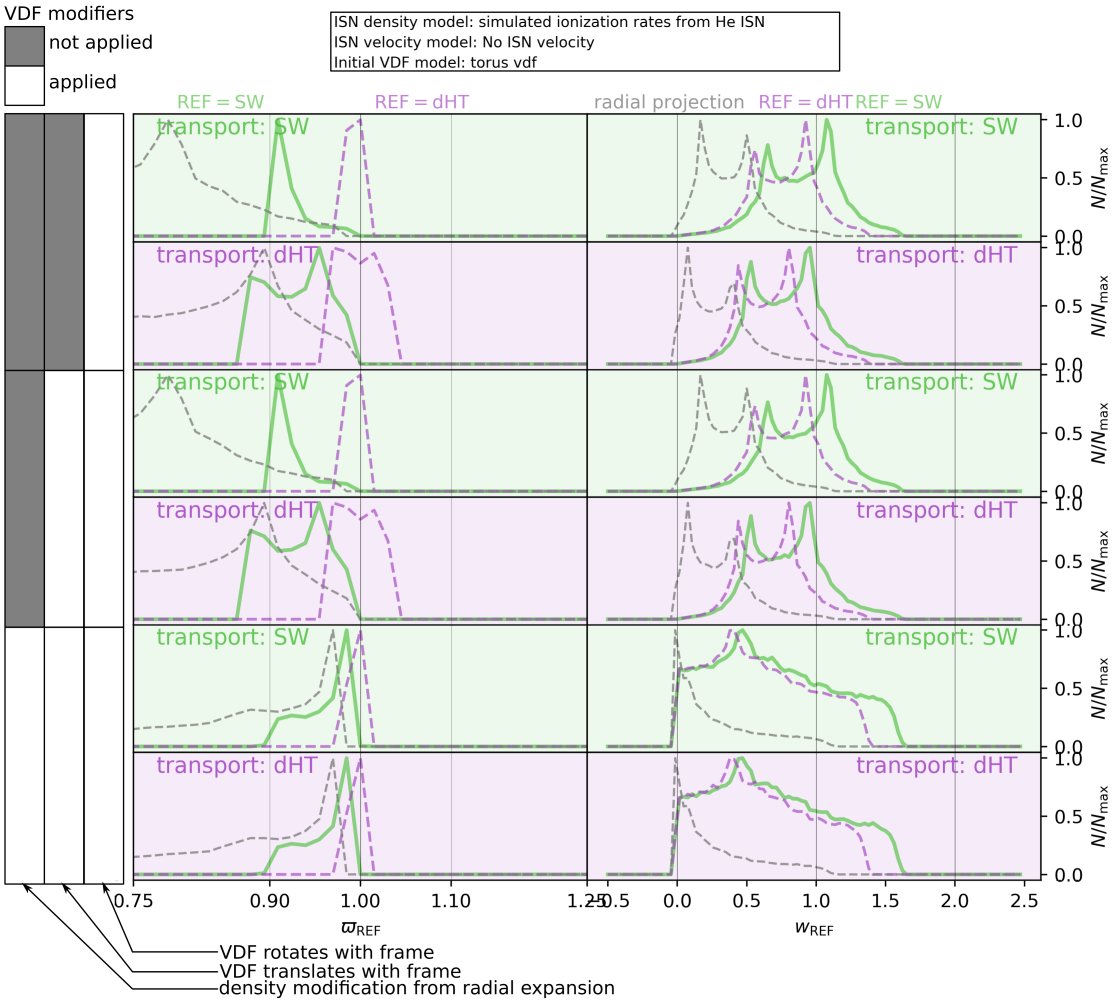

Figure 22: Histograms of simulated PUI VDFs analogous to Fig. 21. In contrast to Fig. 21, all histograms are for a distance from the Sun of 1 AU and feature modification models for the PUI VDF. A matrix on the right of the plots shows for which plots which modification model is employed.

Duncan Keilbach- Three dimensional Pickup Ion velocity distribution functions observed at 1 AU with STEREO/PLASTIC: Anisotropic features and density enhancements in pitch angle distributions as tools to investigate transport effects

at each step of the simulation the previous VDF is rarefied in density according to an adiabatic expansion which results from the expansion of the SW.

Fig. 21 depicts histograms of the PUI relative velocity according to Eq. 42 and according to Eq. 43 while different reference frames are employed to compute these relative velocities. In addition, for the simulation on different runs either the SW frame or the dHT frame was employed as a transporting frame, so that the plots display a mixture of assumed refence frame and simulated transporting frame. Also, in Fig. 21 the histograms are shown for two different distances from the Sun. The simulation starts at 0.2 AU and the histograms show the ϖ_{REF} and w_{REF} (for the discussion of the simulation REF is either SW and dHT) distributions at the first step of the simulation.
Since the construction of the model dHT frame is, that the frames velocity is shifted by the Alfvénic velocity v_a in parallel direction to the local magnetic field, it is expected, in Fig. 21 where no VDF modifiers are applied the VDFs at 1 AU (two upper panels of Fig. 21) are initially the same with both the SW frame as the simulated frame of transport as for the dHT frame, since at the initial time step the same VDFs are initialized (two lower panels of Fig. 21). That under the same conditions in both frames the PUIs are picked up at the same relative velocities is shown in Chapter 2.2.6.ii.b. Therefore, no differences between the VDFs are expected as a function of the transporting frame in Fig. 21 and at 0.2 AU (two lower panels of Fig. 21) the histograms of ϖ_{REF} are delta peaks at 1.0. However, for w_{REF}, a varying pattern between 0 and 0.5 is observed. This already points out, that the construction of w_{REF} makes the interpretation of the VDF challenging. Even though the PUIs are just initialized, without knowledge of the initial pitch angle, one could lead to the conclusion, that deceleration processes have modified the VDF.
At 1.0 AU an interesting result is found: For both frames of transport, ϖ_{dHT} is a delta peak at 1 AU while ϖ_{SW} is a bimodal distribution with a similar peak at ϖ_{SW} slightly lower than 1. The values of ϖ_{SW} are systematically lower than for ϖ_{dHT}. That ϖ_{dHT} and ϖ_{SW} are the same with the SW frame and the dHT frame as simulated frames of transport, is unexpected when it is considered, that ϖ_{dHT} and ϖ_{SW} differ from each other. Future tests of the simulation need to be made in order to verify these results. What can be observed with certainty already is that w_{dHT} and w_{SW} again look systematically different. Here, not only in both non-delta-peak-like distributions are found, but also distributions with a tail from $w_{\mathrm{REF}} = 0.5$ to 2.

Even though the simulation code still requires testing, here a first look at the effect of VDF modification models is provided. Fig. 22 depicts histograms of ϖ_{REF} and w_{REF} analogously to Fig. 21, but only at 1 AU, since the initial PUI VDFs are the same for each depicted simulation run. Here, the resulting distributions are depicted as a function of the applied VDF modifiers. The two top panels plot the resulting distributions with only the modifier *rotate_ with_ frame* applied. Differences between the frames of transport are mainly found in the shapes of ϖ_{REF}. For transport in the SW frame, the distributions of ϖ_{SW} resemble more a delta peak than for transport in the dHT frame. The two middle panels show a simulation where in addition to *rotate_ with_ frame* the modifier *translate_ with_ frame* is applied. Interestingly, the results are the same as with only *rotate_ with_ frame* applied. For this it can be accounted, that the main factor to the shape of the VDF is the Lorentz-Force. The Lorentz-Force is perpendicular to the field and therefore does not modify field-parallel components of velocity. In the bottom two panels additionally model *radial_ expansion* is applied. Interestingly, the distributions of ϖ_{REF} are similar to Fig. 21 at 1 AU. However, there are differences in w_{REF} between the bottom panels of Fig. 22 and Fig. 21.

These initial simulation results show that, even though the initial pui VDF is the same with both investigated frames of transport, transport effects are sensitive to different frames of transport and the choice of a velocity frame for data analysis is relevant for the interpretation of PUI VDFs. Hence, the simulation will provide a necessary tool for future studies to find observational constraints to which frame actually transports the PUIs.
Also, additional models are planned for implementation. E.g. a SW velocity and magnetic field direction which changes gradually over distance from the Sun. Also, the introduction of adiabatic focusing or magnetic bottles (e.g. Piel [2017]) as models for the modification of the VDF are expected to provide interesting results.

3 Instrumentation

In this chapter the instruments which acquired the data, which this work analyzes are reviewed. The review is split into three parts:

- A general introduction into time of flight mass spectrometers (Chapter 3.1) with focus on measurement principles common for this class of instrument alongside a discussion of the challenges of obtaining their data, which arise from their accommodations onboard of a spacecraft.
- A review specific to the time of flight mass spectrometer PLAsma and SupraThermal Ion Composition (PLASTIC) onboard the Soler TErrestrial RElations Observatory (STEREO) spacecraft (Chapter 3.2). In this chapter, also the STEREO spacecraft is reviewed.
- A review of the Magnetometer (MAG) onboard the STEREO spacecraft (Chapter 3.3).

3.1 Time-of-flight mass spectrometers

Time-of-flight mass spectrometers have been present on many spacecraft during the course of the last decades and are still a relevant and versatile class of space-borne instruments to detect positive ions in the energy range of typical solar wind particles (several keV/e) up into the suprathermal range of energies (tens of keV/e) (e.g. Galvin et al. [2008]). A non exhaustive list of examples for time of flight mass spectrometers is provided in Tab. 5.
This section is deemed to describe the general common working principle of time-of-flight mass spectrometers such as these listed in Tab. 5. The following description heavily focuses on the deliberations and descriptions of these instruments given in their respective papers. The general description is followed by a specific section about the PLASTIC instrument, as this work focuses on that instrument's data.

In general, the detection principle (compare Fig. 23 for a schematic overview of the principle) is based on the observation of three quantities: An ion's total energy E_{ion} (purple part of Fig. 23), its energy per charge $\varepsilon_{\mathrm{ion}}$ (yellow part of Fig. 23) and its total velocity v_{ion} (pink part of Fig. 23). Before measurement of either of these quantities, an entrance/aperture system guides and filters particles via electrostatic deflection (green part of Fig. 23). There is a variation in whether time of flight mass spectrometers are totally, partially or not equipped with the capability to measure total energy through direct measurement. E.g. PLASTIC is only equipped with solid state detectors in parts of the instrument. Hence, only two data products are observed in these cases: energy per charge and total velocity. Events in an instrument described by two of these

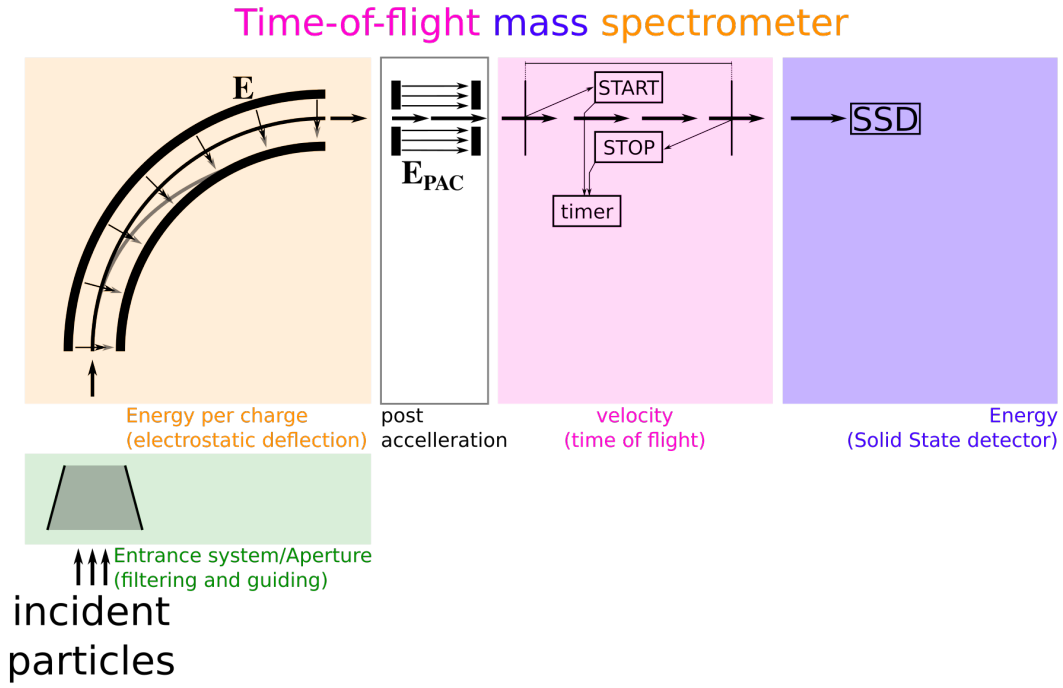

Figure 23: Illustration of the basic elements of a time of flight mass spectrometer. All structures depicted are examples and sketches. The particles first enter an entrance system (green shaded area), which employs electrostatic deflection to guide particles (compare Chapter 3.1.6). Afterwards, the particles enter an energy per charge analyzer (orange shaded area, compare Chapter 3.1.1). Then, post acceleration is applied to the particles, before they enter time of flight measurement system (pink shaded area, compare Chapter 3.1.2). As a last stage of detection, the particles meet an energy analysis system (purple shaded area, compare Chapter 3.1.3).

Launch year	Mission	Abbreviation	Instrument	Abbreviation	Reference(s)
1990	Ulysses	-	Solar Wind Ion Composition Spectrometer	SWICS	Wenzel et al. [1989], Gloeckler et al. [1992]
1995	SOlar and Heliospheric Observatory	SOHO	Charge Time Of Flight	CTOF	Hovestadt et al. [1995]
1997	Advanced Composition Explorer	ACE	Solar Wind Ion Composition Spectrometer	SWICS	Stone et al. [1998], Gloeckler et al. [1998]
2006	Solar TErrestrial RElations Observatory	STEREO	PLAsma and SupraThermal Ion Composition	PLASTIC	Kaiser et al. [2008], Galvin et al. [2008]
2020	Solar Orbiter	-	Heavy Ion Sensor	HIS	Müller et al. [2020], Owen et al. [2020]

Table 5: A non exhaustive list of time of flight mass spectrometers onboard spacecraft.

data products will be referred to as double coincidences (DCs), as opposed to triple coincidences (TCs) with all three quantities. For conciciveness, the following overview does not explicitly state references, since the basic principles of time of flight mass spectrometers are well described in all the references to the instruments listed in Tab. 5.

3.1.1 Energy per charge separation

As a first stage (after the entrance system), particles enter an electrostatic analyser (ESA), where they are filtered by their energy per charge. In the listed instruments (in the following listed instruments refers to those of Tab. 5) this step is achieved by electrostatic deflection through a transversal electric field (w.r.t. the particle's trajectory). This part of a detector is built analogous to a parallel plate condensator, but employs sections of circles as plate geometry. This curvature results in an electric field which for correct energies per charges results in the deflecting force being always transversal to the particle velocity and hence signifies a centripetal force of a circular motion. Since particles of energies per charges which do not meet this criterium will not pass this part of the detector, the energy per charge is filtered (compare Fig. 23).
To resolve a variety of different energies per charge, the instrument sweeps through a range of different voltages thereby allowing different energies per charge to pass into the instrument. Since SW particles enter the instrument with a velocity of hundreds of kilometers per hour and the cross section of an ESA on an instrument is not larger than several 10...20 cm, voltages in the magnitude of kV are required to generate electric fields, which deflect the particles sufficiently. At the same time the plates of the detector need to be as close together as possible to ensure a good resolution in energy per charge state and ideally the field generating voltages should be changed swiftly (time scales of nanoseconds) to obtain a good time resolution of the observation as a whole. This makes the planning of an ESA a delicate procedure and even though the

Duncan Keilbach- Three dimensional Pickup Ion velocity distribution functions observed at 1 AU with STEREO/PLASTIC: Anisotropic features and density enhancements in pitch angle distributions as tools to investigate transport effects

instrument operates in the vacuum of space, voltage breakdowns within the condensator have to be carefully avoided. Also the swift change of high voltages is a challenge onboard a spacecraft, since the instrument may only consume power in the magnitude of milliwatts.
The energy-per-charge resolution of the instrument not only depends on the discrete values of the stepped voltages, but is also a function of the ratio between inner radius and plate distance for the ESA which effectively is a dome capacitor. This is evident from fig. 24, where a sketch of an example ESA is shown and three trajectories traversing it. The trajectory with the smallest radius possible is traversing the dome just above the inner boundary. So the minimum radius of a particle's trajectory is well approximated by the inner radius of the instruments ESA which is defined by r_0. The geometrically possible trajectory of maximum radius is depicted as a violet line. This trajectory enters the instrument just below the outer boundary, almost hits the inner boundary mid-flight and leaves the ESA again just missing the outer boundary. However, this trajectory is physically unsound, since the electric force at many points of the trajectory is not pointing to the center of that circular trajectory. So a particle entering the instrument in that way would not run a circular trajectory and would hit the boundaries of the ESA. The trajectory with the largest radius under the condition, that the electric force is always perpendicular to the trajectory is in good approximation one with a radius of $r_0 + \Delta r$, where Δr is the distance between the boundaries. To relate the radius to particle energy the well known relation

$$F_z = \frac{m_{ion} v^2}{r} = \frac{2E}{r} \tag{50}$$

for the centripetal force F_z, is employed, where m_{ion} is the particle mass, v its velocity, r the radius of the circular trajectory and E the particle's kinetic energy. Approximating the electric force within the dome capacitor by a parallel-plate capacitor (for the instruments of interest $d << r_0$ applies), the electric force F_{el} exerted on the particle, which has a charge of q_{ion} and is at a voltage of U given by

$$F_{el} = q_{ion} \frac{U}{\Delta r} \ . \tag{51}$$

Since the electric force holds the particle on a circular trajectory, $F_{el} = F_z$ applies and with the shorthand definition of $æ_{ion} := E_{ion}/q_{ion}$ the energy per charge is a function of radius and and thickness defined by

$$æ_{ion} = \frac{U}{2} \frac{r}{\Delta r} \ . \tag{52}$$

With the above deliberations, the minimum and maximum energy per charge, which would pass the analyzer at a voltage setting of U are found and are written as

$$æ_{ion,min} = \frac{U}{2} \frac{r_0}{\Delta r} \text{ and } æ_{ion,max} = \frac{U}{2} \left(\frac{r_0}{\Delta r} + 1 \right) \ . \tag{53}$$

The average of both is

$$\bar{æ}_{ion} = \frac{U}{2} \left(\frac{r_0}{\Delta r} + \frac{1}{2} \right) \text{ and} \tag{54}$$

the average differs from the minimum and maximum value by

$$\Delta æ_{ion} = \frac{U}{4} \ . \tag{55}$$

This implies a fractional error of

$$\frac{\Delta æ_{ion}}{\bar{æ}_{ion}} = \frac{1}{2\frac{r_0}{\Delta r} + 1} \text{ for} \tag{56}$$

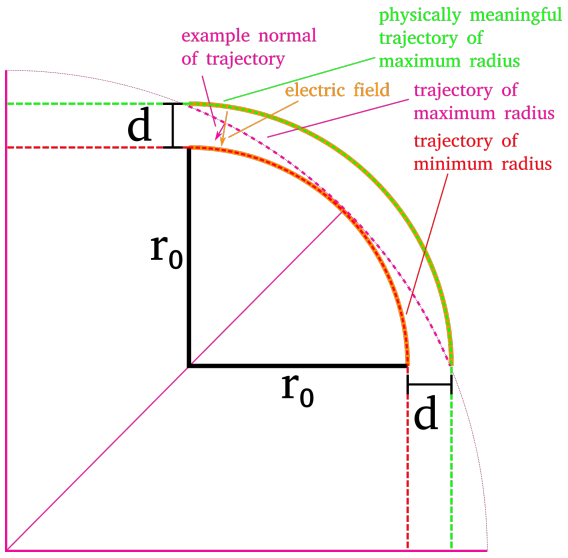

Figure 24: Sketch of a dome shaped electrostatic analyzer. The analyzer consists of two half spheres. The inner has a radius of r_0. The outer has a radius of $r_0 + d$. Depicted are three trajectories: minimum radius, maximum radius and a trajectory of maximum radius which respects the condition, that the electric field needs to be perpendicular to the trajectory. The radii of the trajectories are required for a derivation of instrumental uncertainty.

the energy per charge measured by the instrument. Employing CAD drawings of PLASTIC, for PLASTIC a relative error of 2.9% is found. An alternative approach to constructing an analyser for mass per charge employs Lorentz force. Yet, the required magnetic field is more difficult to contain than the previously mentioned electric field. Therefore, it is more challenging to ensure, that an instrument based on the Lorentz force does not disturb different instruments accomodated on the spacecraft.

3.1.2 Time of flight measurement

One of the simplest ways to measure linear velocity is a two point observation: Once an object has passed the first point, a timer starts which is stopped when the object reaches the second point. With the known distance between both points, the velocity is then directly determined from the time.
This principle is also employed by time-of-flight mass spectrometers. So after an electrostatic analyser a time-of-flight chamber follows. When an ion enters the chamber, it traverses through a thin carbon foil and releases a shower of electrons. When the particles traverse the foil, they are likely stripped of all electrons. Hence, the following measurements do no depend on the particles' initial charge. Also, within the foil a significant amount of energy is lost, which depends nonlinearly not only on the particles' energy, but also on the particle species. Since a full description of that is beyond the scope of this work, the interested reader is referred to Gonin [1995] on the topic of effects to particles which traverse the foil. In this work, the energy loss is accounted for implicitly by calibration parameters. This is further explained in Chapter 4.1.
A specially shaped electric field guides the electrons into a detection mechanism (commonly a micro channel plate) and a timer is started. At a fixed distance behind the first (start triggering) carbon foil a second carbon foil or in some instruments a micro channel plate or a solid state

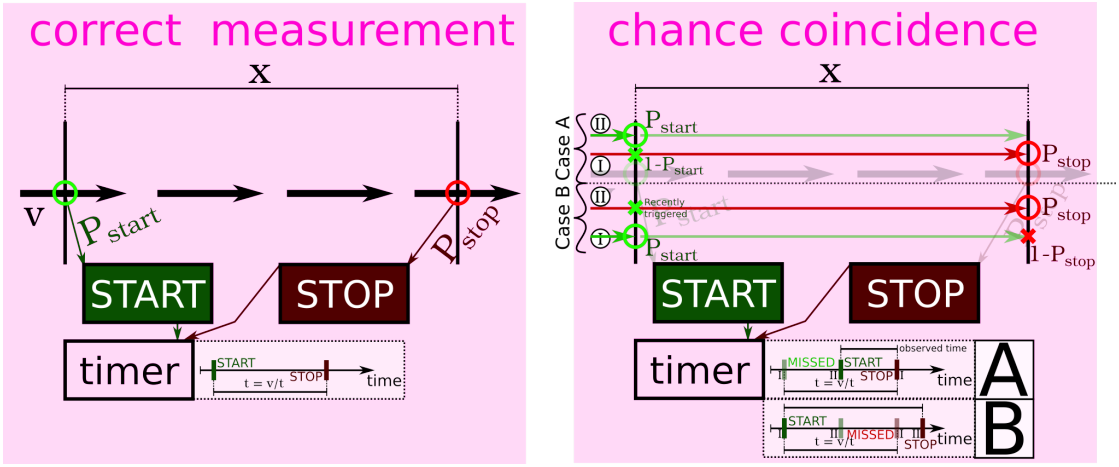

Figure 25: Illustration of the process resulting in a chance coincidence time of flight measurement. The left panel depicts a correct time of flight measurement: A particle enters the chamber with the velocity v and triggers with a probability of P_{start} a start signal for a timer. When leaving the chamber, a stop signal is triggered with the probability of P_{stop}. The onboard timer has observed a time, which (besides time needed for start and stop electrons to reach the trigger and time needed for the trigger logic) is given by the particle traversing the chambers length x with its velocity. However, the measurement in the right panel does not reflect the particles velocity as it traverses the chamber. Here, a first particle (I) does not trigger a start signal as it enters the chamber (with a probability of $1 - P_{\text{start}}$). However, a second particle (II) triggers the start signal, before particle (I) triggers a stop signal. The time observed by the timer in this case is randomly distributed.

detector are found. Analogous to the first foil, a stop signal is triggered in the instrument and the time difference between both is the measured time of flight $\tau_{\text{ion}} = d_{\text{TOF}}/v_{\text{ion},1}$, where d_{TOF} is the length of the time of flight chamber.
To increase the efficiency of the time of flight chamber (which is the likelihood of releasing electrons, when an ion passes the chamber), a constant voltage drop U_{PAC} is put in front of the chamber accelerating the ion. We call the velocity before post-acceleration $v_{\text{ion},0}$ and the velocity after post-acceleration $v_{\text{ion},1}$. The gained energy in the electric field is proportional to the ion's charge. Hence, the observations following the post-acceleration are indirectly entangled with the ion's charge.

3.1.2.i Chance coincidences Chance coincidences are an inconvenient side effect of the time of flight measurement principle. Fig. 25 compares a correct detection (left panel) of a particle alongside two cases, where a chance coincidence is created (right panel). For a correct measurement a particle triggers a stop signal after a start signal is triggered by the same particle and before another particle triggers a start or stop signal.
The two sketched cases of a chance coincidence are labelled with A and B in Fig. 25. In case A of a chance coincidence a particle enters the chamber, but does not trigger a start signal. Then, a second incidenting particle can trigger a start signal before the first particle triggers a stop signal. This results in a shorter measured time of flight, than the first particle's actual time of flight. However, the energy and energy-per-charge signals, the time of flight measurement is combined with, are valid. Also, the second particle is disregarded by the instrument, since it's

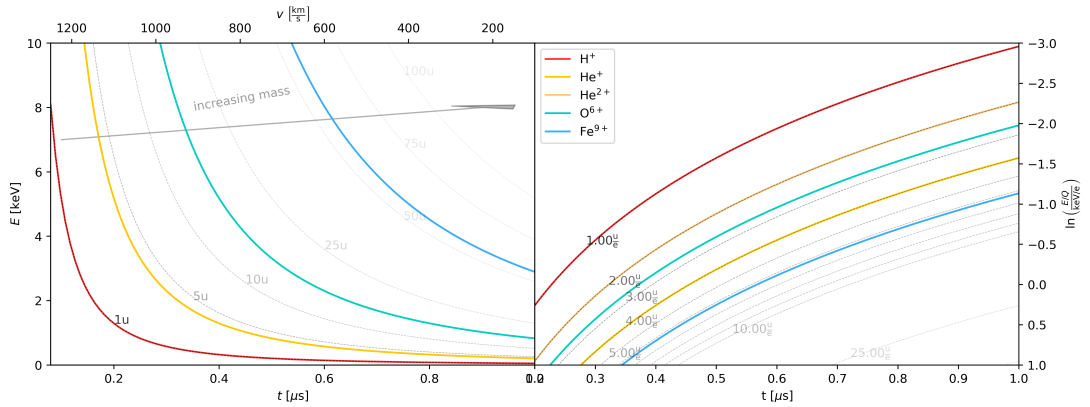

Figure 26: Modelled traces of different ions in a time of flight mass spectrometer. Left: time of flight (x-axis) vs. total energy (y-axis). Additionally, the particle velocity is given at the top x-axis for reference. Right: time of flight (x-axis) vs. energy per charge (y-axis). For both models, pulse height defects, post acceleration and energy loss in the foil were not included. These effects influence the ions' traces significantly and this plot serves merely for visualization. As length of the time of flight chamber the value of PLASTIC's chamber in the SWS section is employed. In addition to the colored solid lines which represent different ions, dashed lines are plotted in gray shades which plot the trace of selected ion masses (left) or energies per charge (right) as a guide. In the left figure the direction of increasing mass is indicated by a grey arrow.

start signal is attributed to the first particle.
In case B a first particle triggers a start pulse, but misses to trigger a stop signal. The start (and stop) detection mechanism is affected by a so-called dead-time t_d, which means, that it is unable to detect incidenting particles for a certain time period, after it has detected an incidenting particle. This means, that particles are now likely to enter the time of flight chamber without detection. Yet, the onboard electronics still waits for a stop signal. So, when a second particle triggers a stop signal, the measured time of flight is longer than the first particle's actual time of flight.

In both cases, chance coincidences create a time of flight signal which does not represent the actual velocity of the involved particles, but is combined with a valid energy and energy-per-charge signal. As a result, particles which are measured by chance coincidences might be misidentified as different ions.
Chance coincidence signals are especially common for protons, since protons make up the largest fraction of particle flux in the SW and therefore in the instrument as well. This is a complication for the signal of singly charged heavy ions. The contribution of protons to the signal of He^+ ions is discussed based on STEREO/PLASTIC observations in chapter 4.

In this section, the probability of chance coincidences and the distribution of resulting time of flight measurements are derived. Fig. 25 illustrates the involved quantities. In both cases which lead to chance coincidences, the probabilities that a particle triggers a signal for either the start or the stop of the measurement are essential quantities. Let therefore P_{start} and P_{stop} be the probabilities that a start signal or respectively, a stop signal is triggered. From these, a probability distribution for the times of flight of a chance coincidence can be derived for both

Duncan Keilbach- Three dimensional Pickup Ion velocity distribution functions observed at 1 AU with STEREO/PLASTIC: Anisotropic features and density enhancements in pitch angle distributions as tools to investigate transport effects

cases. In Appendix A this is done for case A.

3.1.3 Total Energy

The last part of the ions trajectory through the instrument is the residual energy measurement (if present in the instrument, compare introduction of Chapter 3.1) which is achieved by a solid state detector which is intended to stop the particle.
Within a solid state detector, the energy of particles stopped in the detector is directly converted into an electric signal. Particles, which were not completely stopped in the detector, leave a fraction of that energy in the detector and have to be considered, if the data products produced by the detector are analyzed.

3.1.4 Combining the measurements (Particle identification)

The combination of all three measurements allows for particle identification. A particle is identified, if its mass, m_{ion}, and charge,q_{ion}, are known. So, the energy per charge $æ_{\mathrm{ion}} := E_{\mathrm{ion}}/q_{\mathrm{ion}}$ measured in the instrument's first section is a suitable starting point. With $E_{\mathrm{ion},0} = m_{\mathrm{ion}} v_{\mathrm{ion},0}^2/2$ we find

$$æ_{\mathrm{ion}} = \frac{E_{\mathrm{ion},0}}{q_{\mathrm{ion}}} = \frac{m_{\mathrm{ion}}}{q_{\mathrm{ion}}} \cdot \frac{v_{\mathrm{ion},0}^2}{2} \text{ , which} \tag{57}$$

is proportional to the ion's mass per charge and the squared initial ion velocity. To compute the initial ion velocity from time of flight, the persistence of energy is acknowledged with

$$E_{\mathrm{ion},1} = E_{\mathrm{ion},0} + E_{\mathrm{PAC}} \tag{58}$$

where $E_{\mathrm{ion},1}$ is the ions energy after post-acceleration and $E_{\mathrm{PAC}} = q_{\mathrm{ion}} U_{\mathrm{PAC}}$ is the energy gained from post-acceleration. Here, the energy loss in the carbon foil is neglected to visualize the main principle. Memorizing, where it was neglected during computation, it can be reintroduced during later steps.
Solving Eq. 58 for $v_{\mathrm{ion},0}$ results in

$$v_{\mathrm{ion},0} = \sqrt{v_{\mathrm{ion},1}^2 - 2\frac{q_{\mathrm{ion}}}{m_{\mathrm{ion}}} U_{\mathrm{PAC}}} \, . \tag{59}$$

Inserting this into eq. 57 we find

$$æ_{ion} = \frac{m_{\mathrm{ion}}}{q_{\mathrm{ion}}} \cdot \frac{v_{\mathrm{ion},1}^2}{2} - U_{\mathrm{PAC}} \tag{60}$$

and with $v_{\mathrm{ion},1} = d/\tau_{\mathrm{ion}}$ we obtain

$$æ_{ion} = \frac{m_{\mathrm{ion}}}{q_{\mathrm{ion}}} \cdot \frac{d^2}{2\tau_{\mathrm{ion}}^2} - U_{\mathrm{PAC}} \, . \tag{61}$$

So, the trend of mass per charge as a function of time of flight is a squared hyperbole constantly shifted in mass per charge space by post acceleration and scaled mass per charge or differently phrased: In plots depicting energy per charge versus time of flight, lines of constant mass per charge are squared hyperbola. This is visualized in fig. 26.
A similar result is found if the residual energy is related to time of flight, which obtains

$$E_{\mathrm{ion},1} = \frac{m_{\mathrm{ion}}}{2} \frac{d^2}{\tau_{\mathrm{ion}}^2} \, . \tag{62}$$

So if residual energy is plotted versus time of flight, lines of constant mass are squared hyperbola. Fig. 26 visualizes this. It is noteworthy that if the residual energy is obtained from solid state detector observations, the pulse height defect has to be accounted for. Interestingly, eq. 62 is not directly dependent on the post-acceleration voltage. This is the case because both the time of flight and the total energy in this equation are measured after applying the post-acceleration. So the functional trend is unchanged, but the range of observed energies will change as well as the range of observed times of flight. The former has the advantage, that the particles' energies have increased, while the pulse height defect remains constant (e.g. Galvin et al. [2008]).

For particle identification typically the particle events are histogrammed into energy vs time-of-flight and into time-of-flight vs. energy-per-charge. Fig. 26 shows the expected positions of the most abundant ions in such plots for an example model detector.

3.1.5 Onboard moments, matrix rates and Pulse Height Analysis (PHA) data

One of the major challenges in space exploration is data retrieval. In a laboratory experiment probes in a plasma are typically connected with a data acquisition unit with a cable. Evidently, this method of connection is not suitable for space exploration. Instead communication with spacecraft is established via electromagnetic waves (commonly in the radio wave spectrum). On the earth side of communications, the retrieval and sending of information from and to spacecraft is achieved by high gain antennas/dishes. Noteworthy here is the Deep Space Network (DSN) which is a facility of various complexes of ground-based space antenna spread over the globe.
Compared to a data cable in a laboratory environment with data transfer rates in the range of hundreds of MBit/s or even GBit/s, radio wave based space communication is limited to hundreds of kBit/s which is a considerable limitation. Even though the solar wind is a rather dilute medium, such data rates do not allow all events which incident into an instrument to be transmitted. Moreover, with protons making up the largest fraction of the ions in the SW by a big margin (compare chapter 2.1.2), the method of just transmitting ion events as they are detected without any pre-selection on board would most probably result in an insufficiently resolved spectrum of heavier ions.

3.1.5.i Onboard moments As evident from Fig. 34 in Chapter 4.1, protons are fairly well separated from all other ions in energy per charge space (compared to the heavier ion species). Therefore, based on ground calibration the instrument's Data Processing Unit (DPU) can be programmed to roughly distinguish protons by simple methods which do not require too much computational capability.
Under the assumption that all separated events are protons, the DPU can then compute proton densities, averaged proton velocities and (from the second moment of the acquired VDF) a proton temperature, which can then be transmitted to earth. So if one is only interested in proton moments, this variant of data would be telemetry-saving. Such moments are available e.g. from the STEREO/PLASTIC instrument.
However, since instruments are only allotted a small amount of power on a spacecraft, the computational capabilities of the DPU are limited. Hence the separation and computational schemes for these onboard moments are crude and difficult to check for consistency with the computational capabilities onboard. If the initial calibration of the DPU is affected by errors or if the VDFs which arrive the instrument deviate from the expected VDF, from which the computation algorithm of the moments is derived, the onboard moments are affected by a systematic

Duncan Keilbach- Three dimensional Pickup Ion velocity distribution functions observed at 1 AU with STEREO/PLASTIC: Anisotropic features and density enhancements in pitch angle distributions as tools to investigate transport effects

error. This error firstly will not be detectable from the moment data alone and secondly will most probably not be fixable, since the underlying distribution remains unseen for a later data analysis, if additional data is not sent in addition to the moments. Therefore, onboard moments alone should not be considered as a meaningful data product. However, together with further information about the underlying events in the instrument, they may provide a guideline for data analysis.

3.1.5.ii Matrix rates If a large number of events is to be acquired per time interval, the transmission of a histogram of them is often less data rate consuming than the transmission of every single event. This is the main idea behind a matrix rate. Based on ground calibration, the instrument's DPU is programmed to recognize certain ions or at least roughly divide the events into bins and accumulate events during a given period of time. Then, the accumulated events are transmitted.

3.1.5.iii Pulse Height Analysis (PHA) data Another more direct approach w.r.t. the incidenting particles is to pre-select incoming particle events based on a priority scheme before transmission. This way an instrument can be programmed to strongly favour heavy ions w.r.t. protons and therefore increase a heavy ion's chance to be transmitted. Since this systematically affects the observed particle distributions, additional information must be transmitted.

3.1.5.iii.a Basics of priority weighting Following such approaches, the DPU of the instruments listed in Tab. 5 (except CTOF) is programmed to divide observed particles into several boxes, whereas the boxes' boundaries have been determined based on expected positions of ions in energy, energy per charge and time of flight space. Theses boxes are employed to prioritize less common ions like the heavier ions in the SW over more common ones like protons (compare chapter 2.1.2 for the elemental composition of the SW).
E.g. one of the prioritization boxes of PLASTIC is set in such a way, that it contains protons and Helium ions, one for ions with medium masses like Oxygen ions and another prioritization box for ions in the mass range of Iron ions. Based on the expected abundance of ions in those boxes as well as the observational goals of the instrument, the DPU will favour ions out of certain boxes more than others.
This is achieved by keeping track of how many events from each of these boxes have been written on a limited buffer (here, the buffer is what will be transmitted to Earth) of the DPU during a measurement cycle and the programmer has instructed the DPU to acquire a certain number of events per prioritization box.
The number of total events per priority range (transmitted or not) is also transmitted to Earth to attempt to correct the observational bias created by the observational prioritization scheme: The total number of events during an observational interval and within a prioritization box $R_{\mathrm{prio},i}$ (called priority rate) and the observed number of events during an observational interval within a certain prioritization box $R_{\mathrm{base},i}$ (called base rate) are known, where i is the number of the prioritization box. So, each particle is assigned a weight W with

$$W := \frac{R_{\mathrm{prio},i}}{R_{\mathrm{base},i}} \text{ , which} \tag{63}$$

based on the statistical law of large numbers balances the observational bias out, at least for long-term observations.
Generally, Pulse Height Analysis (PHA) data is the best resolved data, but the number of events per measurement cycle it is based on is strongly limited by telemetry. So special caution is

necessary if PHA data is analyzed on short time scales. Compared to matrix rates, PHA data is also more versatile since the calibration of the data may also be performed while the mission runs and does not need to be transmitted to the instrument. This is especially useful, if the actual ion positions in instrumental space deviate from their positions expected from ground calibration when the DPU was programmed.

3.1.5.iii.b Statistical problems with priority weighting However, even with carefully chosen priority schemes for the DPU, the concurrency of differently abundant ion species in a single priority box may skew the portion of data sent to Earth.
An example for this is the priority box number 1 of the solar wind sector of STEREO/PLASTIC (which is introduced in section 3.2. In Fig. 27 energy vs. time of flight histograms of PHAs from this portion of the instrument are shown. For the histogram, only data from energy per charge step number 44 is selected. In the top axis a histogram of data from all of PLASTICs four prioritization boxes is shown. At the time of flight channel of ~ 200 and an energy channel of ~ 55 a broad peak is visible, which tentatively belongs to O^{6+}. For this peak, alongside ions heavier than O^{6+} (e.g. the charge states of Fe) the instruments prioritization number 2 is intended. The peak of He^{2+} is found at an energy channel of ~ 25 and a time of flight channel of ~ 170 and in the plotted energy per charge step is found in both the prioritizations number 0 and 1. The bottom axis of Fig. 27 shows three histograms, wherein each of the histograms corresponds to a different prioritization and each histogram is normalized to its respective maximum. This way of plotting the data makes it more clearly visible, that the peak is found in both prioritizations. Tentatively, prioritization number 0 is intended especially for protons. However, at the selected energy per charge step, protons are not found and the majority of prioritization 0 is made up of a portion of the peak of He^{2+}. Yet, most parts and the actual maximum of the distribution of He^{2+} is found in prioritization 1. For the situation of the He^{2+} peak, it is conceivable that with a correctly chosen weighting factor applied to one of the prioritizations' data, a continuous transition of the peak from one prioritization into another can be achieved. Yet, for prioritization box number 1 different ions also need to be taken into account as both the peaks of O^{6+} and another ion leak from prioritization 2 into prioritization 1. So whether the application of a weighting factor to the data of prioritization 0 results in a correct shape of the He^{2+} at the boundary between prioritizations 0 and 1 also depends on the weighting factor of prioritization 1.
More problematic for the data of the ions, which leak from prioritization 2 into prioritization 1 is, that they are considerably less abundant than He^{2+}. The probability of the leaking ions to be selected for transmission in prioritization number 1 is therefore much lower than the probability of He^{2+}. Hence, only a small fraction of their data is selected in prioritization 1. The effect of this is visible in the histogram of prioritization 1 in Fig. 27: The fraction of the O^{6+}, that is visible in prioritization 1 is much noisier and statistically less significant than the fraction of the O^{6+} peak in prioritization 2 and the peaks shape in prioritization number 1 is represented by a little amount of events. Hence, a full reconstruction of the shape of the peak of O^{6+} is hardly possible. Scaling the part of this peak which is in prioritization 1 with a weight factor will therefore not be feasible to fully reconstruct the peaks shape and the distribution of O^{6+} (and also of the other leaking ion) is skewed.
This also means that data products deduced from the observation of ions of ESA steps wherein their peak is close to the boundary of a prioritization need to be treated with extra caution since they result from an artificially skewed distribution.

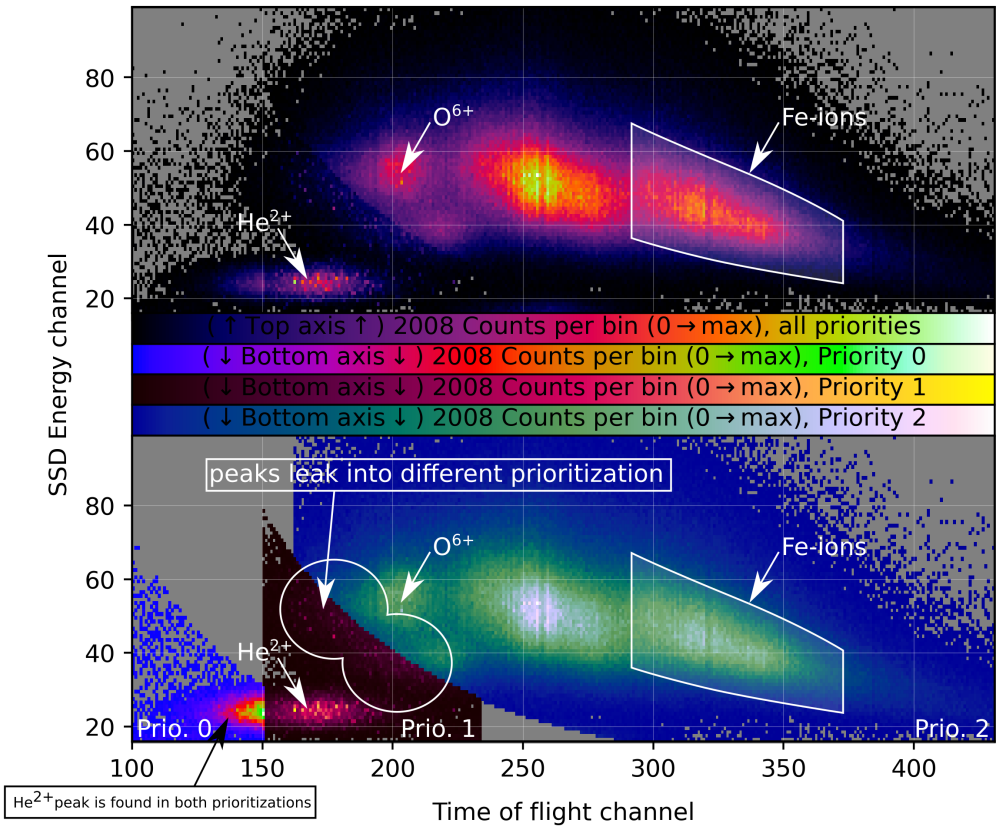

Figure 27: STEREO/PLASTIC PHA data of the Solar Wind Sector accumulated over the year 2008 histogrammed in time of flight channel vs. SSD energy channel. The data is limited to the instrumental energy per charge step 44. Top axis: The data from all of the 4 of the instruments prioritizations in a single histogram. The top colorbar corresponds to the histograms color key. Bottom axis: Three histograms plotted into the same axis, wherein the histograms correspond to three different prioritizations. The histograms differ from each other in their energy and time of flight ranges since these ranges correspond to the prioritizations. Also different color keys have been employed to represent the counts in each of the histograms. The second top colorbar represents the leftmost histogram's color key and corresponds to the instrument's Priority 0. The third top colorbar represents the histogram of data from Priority 1 and the bottom colorbar corresponds to the histogram of data from Priority 2, which is the leftmost of the histograms. On both axes, the histograms are normalized to their respective maximum and the colorbars represent values from 0 to maximum from left to right.

3.1.6 The instrumental entrance system and acceptance angles

For the instruments listed in Tab. 5 there are spatial limitations to the phase space volume, that can be observed at a time. The angle, from which incoming particles can be observed w.r.t. e.g. the central axis of the instrument depends on how the entrance system is built. The entrance system of an instrument has the purpose to screen particles and to guide and collimate the particles onto a trajectory, which fits to the intended trajectories through the energy per charge analysis system.
Since entrance systems work through electrostatic deflection, the amount, by which they influence a particle's trajectory is a function of energy per charge. So, the entrance system's deflection needs to be synchronized and/or adjusted to the expected energy per charge. In the SWICS instruments a two channel deflection system is realized, which guides protons into a different channel for the following steps of analysis than ions heavier than protons. In PLASTIC, two channels are realized, which have different acceptance angles. However, in PLASTIC these channels are not built to work simultaneously. Rather, the instrument works with the Main Channel, until fluxes are too high and then switches into the smaller Channel (compare Chapter 3.2).

The entrance systems of both SWICS have limited acceptance angles in both azimuth and elevation. However, the instruments are spun with the spacecraft, so that after one rotational period full coverage is achieved in azimuth. PLASTIC's entrance system is dome-shaped, so that a full azimuthal field of view is theoretically possible. However, spacecraft accommodations and packaging issues of structural and electronics elements introduce limitations to the azimuthal field of view (compare Chapter 3.2).

3.2 STEREO/PLASTIC

One of the Solar TERestrial Observatory (STEREO) mission's [Kaiser et al. [2008]] main goals at its conception was to add a new dimension to the remote observation of structures and events on the Sun employing a stereoscopic view (e.g. Aschwanden et al. [2008]). Hence, the STEREO mission consists of two (almost) identically built spacecraft. Both orbit the Sun approximately at the same distance as the Earth, but the spacecraft STEREO ahead (A) orbits the Sun slightly faster than Earth ($\sim$ 347 days) while the other, STEREO behind (B) orbits slightly slowlier ($\sim$ 388 days) [NASA [2021]], so that both spacecraft separate by $\sim 45°$ in ecliptic longitude from each other per year [Kaiser et al. [2008]].

After launch at 26 Oct. 2006, the spacecraft entered ecliptical orbits around the Earth for about three months to undergo the commissioning phase of the mission [Kaiser et al. [2008], Thompson et al. [2009]]. Employing swingby maneuvers at 12 Dec. 2006 (both spacecraft) and at 21 Jan. 2007 (STEREO B), the spacecraft entered their orbits around the Sun designated for their scientific operation [Thompson et al. [2009]].

In their heliocentric orbits, both spacecraft are three-axis stabilized, so that the front side of the spacecraft points in sunward direction [NASA [2021], Kaiser et al. [2008], Galvin et al. [2008]]. At the point of writing this work, the STEREO mission is ongoing. However, contact with STEREO B was lost on 1 Oct. 2014. After a brief period of limited contact from 21 Aug. 2016 to 23 Sept. 2016, attempts to recover the spacecraft ended on 17 Oct. 2018 [Kucera [2018a]]. During the short period of contact in 2016, only a small amount of data was received,

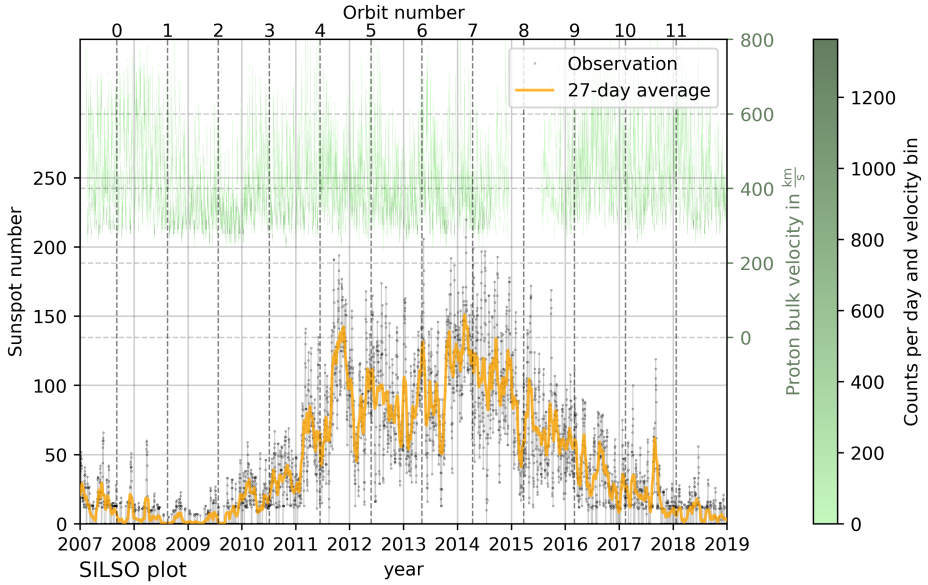

Figure 28: Timeseries of daily Sunspot number observations (left axis, in black) over the years (x-axis) of STEREO A data availability. A 27-day average of the Sunspot number is superimposed in orange and shaded in green a two-dimensional histogram of solar wind proton bulk velocity over time is plotted alongside (right axis). The Sunspot number data for this plot has been taken from SILSO World Data Center [2007-2019].

including telemetry, which indicated a low charge within the onboard battery and that the solar panels did not point in sunward direction anymore [Kucera [2018a]].

This work focuses on data from STEREO A's instruments. Not only, since STEREO B was lost and a longer period of data from STEREO A is available, but also since for reasons not completely clear, the data from STEREO B's PLASTIC instrument indicates major malfunctions of the instrument. During the still ongoing mission period more than ten orbits around the Sun have been completed. Since the data from the mission's first phase are affected by calibration operations, the earliest data considered in this work is from 2008. Therefore, the numbering of orbits this work employs starts at 0 with the first orbit in 2008. An overview of the orbits of STEREO A alongside with information of the Sunspot number indicating the solar activity cycle as well as the measured solar wind proton bulk velocity is shown in Fig. 28. Judging from the number of years and the Sunspot number almost one solar cycle is covered in the period of 2008 to 2019 with the mission starting within a solar minimum. However, data from 2015 on needs to be treated differently, since the STEREO A was rotated by 180° around the radial axis in 2015. At the same time, the spacecraft was behind the Sun (seen from Earth), so that communications with the instrument were blocked by the Sun. The communication loss with STEREO B initially occurred, when STEREO B was in the same situation. Fortunately, contact with STEREO A could be reestablished as planned in contrast to STEREO B [Kucera [2018a]] and STEREO A is to the point of writing still operational [Kucera [2018b]].

SWS (Main ch.)	SWS (Small ch.)	WAP
2°	0.4°	6°

Table 6: Out-of-ecliptic angular acceptance of PLASTICs different sections. The SWS angular acceptances are stated as per deflection voltage step. In total SWS achieves a ±20° FOV.

3.2.1 PLAsma and SupraThermal Ion Composition (PLASTIC)

The PLAsma and SupraThermal Ion Composition (PLASTIC) instrument is a time of flight mass spectrometer built to detect protons, alphas and heavier positively charged ions in the SW at energies per charge ranging from ∼ 0.3 keV/e to ∼ 80 keV/e [Galvin et al. [2008]]. In addition, it aims to provide a 360° view of the incoming direction of the particles in azimuth and is partially equipped to resolve the incoming ions in out-ouf-ecliptical direction. Fig. 31 provides computer-rendered cross sections of the instrument. PLASTIC is built cylindrically symmetric (apart from electronics and special sections in the SW direction) and the instrument is divided into two sections: The solar wind sector (SWS, marked red in Fig. 31) which has an azimuthal width of 45° and points in SW direction and the wide angle partition (WAP). In Fig. 31 only parts of WAP are marked. Essentially, WAP is the whole part of the instrument which is not SWS. In the SWS the focus lies in the measurement of the bulk SW with high resolution in both energy and direction. Also, since in this section high proton fluxes are expected, efforts have to be made to reduce fluxes within the SWS at energy-per-charge settings which favor SW protons. The aim behind these efforts is to measure protons and the less abundant ion species in the SW at the same time.

3.2.1.i Entrance system SWS and WAP mainly differ from each other by their entrance system. This can also be seen in Fig. 31. In the SWS, the entrance system is split into two apertures of ∼ 45° width in azimuth. One of these is smaller than the other in elevation. By setting deflection voltages at these apertures, both can be opened or closed for particles. The larger aperture of both is called the Main Channel and is initially open. It is closed, when the flux of incoming particles triggers a threshold. Then, the Small Channel (the smaller one) opens. This operation is in the literature referred to as small channel switch [Galvin et al. [2008]]. As Chapter 3.2.1.iii explains, the instrument ramps between different energies per charges in alternating direction (low energies per charge to high energies per charge and back). If during a cycle of detection a Small Channel switch occurs, it will occur, when the energy per charge is ramped in direction of lower energies per charge. In the following reversion of energy per charge, the switch is reversed, when the energy per charge is reached, at which the Small Channel switch occurred [Galvin et al. [2008]].

The deflection voltages set at the apertures of the SWS also serve as vertical steering of the incoming ions, so that different deflection settings allow for different out-of-ecliptic incoming angles. Per energy-per-charge step the deflection voltage is stepped through 32 individual voltages to achieve linearly spaced bins within a ±20° out-of-ecliptic field of view.

Within the wide angle partition, no electrostatic deflection system is available, so that the wide angle partition has a constant FOV centered to the ecliptic plane. The angular acceptance angles of both systems are comprised in table 6.

3.2.1.ii Electrostatic analyzer and timing The instrument's ESA resolves particles by their energy per charge with a dome-shaped electrostatic analyzer. Within the dome, voltages

Duncan Keilbach- Three dimensional Pickup Ion velocity distribution functions observed at 1 AU with STEREO/PLASTIC: Anisotropic features and density enhancements in pitch angle distributions as tools to investigate transport effects

from $\pm 10V$ to $\pm 6000V$ are logarithmically stepped with 128 individual settings. From ground calibration, the nominal energy per charge response, in terms of physical energy per charge $æ_{ion}$ energy per charge channel $æ_{ch}$ of the instrument is

$$æ_{ion} = 0.2 \cdot 1.04895^{127-æ_{ch}} \frac{\text{keV}}{e} \ . \tag{64}$$

Apart from filtering incoming particles by their energy per charge, the electrostatic analyzer determines the timing of the instrument's scientific operation. Per measurement cycle the energy per charge is swept through each of its settings. Hereby, the instrument is stepped upwards in one cycle and downwards in the next one, so that large changes in the electrostatic analyzers voltage are avoided. The timing of the stepping of the analyzer is sketched as a time line in Fig. 29. The top part of Fig. 29 shows the timing of one cycle of measurement. Nominally, such a measurement cycle takes 60 s while for one energy per charge step a time of 435.6 ms is allocated. This way 4.243 s remain of the minute. This time is allotted for the data processing unit (DPU) to do housekeeping. Per ESA step all settings of the aperture's electrostatic deflection are set sequentially. This is shown in the bottom time line of Fig. 29, which depicts the timing during one ESA step. At the beginning of an ESA step, 26 ms are allotted for voltage accommodation. Afterwards, the 32 deflection steps are swept at constant energy per charge analyzation voltage with one step taking 12.8 ms.
This way, theoretically the instrument has a cadence of one minute. However, for reasons of the DPUs limitations, the priority rates are kept and sent with 5 minute resolution. So a full, statistically meaningful sample is achieved after 5 cycles. However, knowing the start time of a measurement cycle the exact time of each PHA event entering the instrument can be determined with a precision of tens of milliseconds.

3.2.1.iii Time of flight and azimuthal angle measurement After traversing the electrostatic analyzer, particles undergo a post acceleration through an electrostatic potential of ~ -25 kV. The post acceleration prepares the particles for traversing a thin carbon foil. The passing through the foil almost always strips the particles of their electrons, so that in the following parts of the instrument the particles' behavior can be assumed independent of their initial charge. In the foil, the particle also loses a non negligible amount of energy which, amongst other quantities, depends on its atomic mass number [Gonin [1995]].

As it leaves the foil, the particle triggers a shower of electrons which is guided by electron optic elements within the instrument into a target micro channel plate (MCP). The resulting electron shower is steered onto an anode which signals the time of flight measurement to start. The time measurement is resolved into 1024 individual bins with a nominal time resolution of < 0.2 ns within a detection range of ~ 4 ns to ~ 250 ns.
With different azimuthal angle of incident the particle passes the instrument at a different part. For reference, a top down sketch of PLASTIC's azimuthal angle detection capabilities is provided with Fig. 30. Apart from the SWS/WAP segmentation, the instrument is further segmented into four quadrants: SWS fully resides in one quadrant, which in the following is named Q0. The numbering of the other quadrants Q1, Q2 and Q3 proceeds clockwise.

3.2.1.iii.a Stop detection and position measurement in the first quadrant In contrast to the other quadrants, Q0 is equipped with solid state detectors (compare Figs. 30 and 31) at the end of the time of flight path which in Q0 is 5.8 cm long. The impact into the solid state detector releases secondary electrons which are also accelerated into an MCP, after which the resulting electron shower hits a resistive anode. This electron shower then triggers a stop

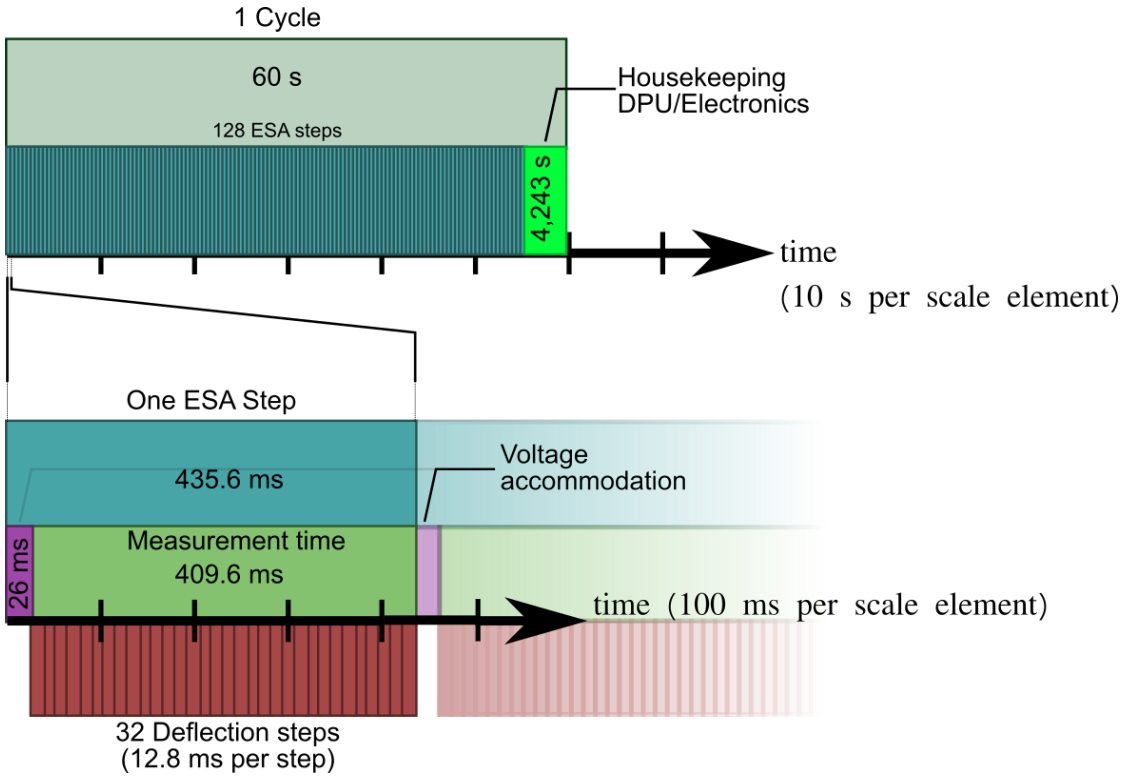

Figure 29: Overview over the timing of a measurement cycle of PLASTIC. Top plot: Time line of one cycle, which take 60 s ramps through 128 ESA steps, which take 4.243 s less than a minute. In these seconds, housekeeping operations are performed. Bottom plot: Time line of one ESA step. The ESA step takes 435.6 ms and begins with 26 ms allotted for voltage accommodation. Afterwards 32 sequential deflection steps are perfomed, which take 12.8 ms each.

Duncan Keilbach- Three dimensional Pickup Ion velocity distribution functions observed at 1 AU with STEREO/PLASTIC: Anisotropic features and density enhancements in pitch angle distributions as tools to investigate transport effects

signal.
In the resistive anode, which spans the whole Q0, the deposited charge from the electron shower triggers a signal which depends on the impact position. A digital-analogue converter resolves the signal in 64 individual digital bins, so that (assuming linear voltage response with azimuthal angle of the incident particle) a digital angular resolution of $45°/64 \approx 0.7°$ is achieved. However, the instrumental response, measured with test beams before flight, is nonlinear. At a beam azimuth of $\sim \pm 3°$ (with 0° being the center of the SWS aperture), particles hit a support beam of the carbon foil and the instrumental response becomes ambiguous. Hence, digital bin numbers between ~ 22 and ~ 37 might either result from particles arriving from the nominal azimuthal angle or from the center. The small portion of the resistive anode which corresponds to the aperture of WAP, has a poor instrumental response, i.e. azimuthal angles between $-45°$ and $-35°$ and between 35° and 45° trigger almost the same signal for both ranges, respectively. Hence, the statistical error of the positional measurement is expected to span several digital bins. This is discussed in more detail in Sections 4.3.1.i and 5.4.

3.2.1.iii.b Stop detection and position measurement in the other quadrants In the quadrants Q2 and Q3 no solid state detector is fitted (compare Figs. 30 and 31). In these quadrants, a particle directly hits a micro channel plate at the end of the time of flight track which in these quadrants is 8.0 cm long. The resulting electron shower hits one of the instrument's discrete anodes which cover an angular width of 22.5° each. The incident angle is reported by the number of the discrete anode, so that a nominal angular resolution of 22.5° in azimuth is achieved here. It is noteworthy, that in Q0 the MCPs are smaller than in the other quadrants. In Q1, Q2 and Q3, they span a whole quadrant, so that the positional bins share MCPs [Wimmer-Schweingruber [2022]].

3.2.1.iv Energy measurement Fig. 31 shows top down views of renditions of PLASTIC based on CAD drawings. In that figure, the positioning of the solid state detectors is visible. As already mentioned, only Q0 and Q1 are equipped with solid state detectors (also compare Fig. 30). Hence, in the other quadrants no total energy measurement is available. So, in Q2 and Q3 double coincidences are measured. Since Q2 and Q3 reside in WAP, this part of the instrument is called WAPNOSSD.
The parts of Q0 and Q1, which are also covered by WAP are called WAPSSD and triple coincidence is achieved for particles above a threshold energy. The segmentation of the instrument into SWS, WAPSSD and WAPNOSSD is commonly employed in literature regarding the instrument. In SWS and WAPSSD a total of 16 individual solid state detector pixels is fitted, the signal of which is converted by a analogue-digital converter with 1024 bins resulting in an almost linear response of the instrument.
A caveat to the solid state detectors is that on top of them a dead layer is found through which particles must first pass to deposit a readable signal. This results in an additional energy loss in the detector and in a threshold energy for detection. Additional nonlinearities within the detector cause further energy loss, which is referred to as pulse height defect.

The number of a triggered SSD pixel may be employed as a second information of a particle's azimuthal position in addition to the resistive/discrete anode system. Unfortunately, the exact geometry of these pixels has not been documented within Galvin et al. [2008]. However, employing a Computer Aided Design (CAD) model of the instrument, the azimuthal positioning and geometry of the pixels has been reconstructed (compare Fig. 31). Only taking into account geometrical deliberations, each pixel has an azimuthal FOV of 5.5°, except for pixels coinciding with the edge of apertures (or the completely blocked pixel). There, the aperture geometrically

obstructs 0.5° of a pixels FOV.

3.2.1.v Ground calibration data for the resistive anode Galvin et al. [2008] provides data from an experimental test of the azimuthal direction resolution which was performed with the flight spare model. In the experiment, a maxwellian beam of ionized particles is directed into the instrument from a pre-defined direction and the instrument is rotated. At the same time, the particles detected by the instrument are tracked. Fig. 32 plots the average response of the position measurement in the resistive anode as a function of the azimuthal angle of the calibration beam w.r.t. an axis which points from the instrument's center outward through the center of SWS. The data of the figure is from Galvin et al. [2008]. Even though the instrumental response to different azimuthal angles is reportedly nonlinear as outlined, in this work the azimuthal response is approximated with a linear approach, because the data of Galvin et al. [2008] employs a maxwellian beam of non-SW particles and the data for Fig. 32 depicts average measured directions from that beam. Whether the initially symmetric distribution is skewed by measurement is unknown. A more meaningful set of data would be a two dimensional histogram of instrumental response as a function of beam direction, so that the actual distribution of instrumental responses to the beam can be analyzed. Especially for the central part, where the instrument seems to create an ambiguous response, would have to be observed closer to derive a more meaningful approach to invert the instrumental directional response. Hence, the linear approach can be seen as an approach of minimum knowledge, where the errors of different and seemingly more sophisticated models can not be definitely deterimined. The idea behind this is not to introduce additional errors into the analysis by a too complicated model for which not enough knowledge about the instrument has been obtained.

3.2.1.vi Priority Ranges For reasons of limited data transmission rate from the instrument to earth, not all particle events which are measured by the instrument are transferred. Instead, the instrument selects 12 events every 2 energy per charge steps for transmission [Kistler and Ellis [2007]]. So that heavier ions are likely included into this limited set of events alongside the statistically dominant species of protons, the instrument assigns priorities to the events before a decision is made which events are sent. The priorities are based on the ion's positions in energy per charge, time of flight and total energy space and are based on where a certain ion species is expected. This also includes, that the ranges of time-of-flight and energy at which a priority is assigned, change as a function of the energy per charge step. Fig. 33 visualizes the priority ranges of the SWS. In contrast to WAP which has 2 priorities, SWS has 4 priorities. The four priorities are intended to suit different particle species. Nominally, priority 0 is for protons, priority 1 is for singly and doubly charged He and the priorities 2 and 3 are for heavier ions [Kistler and Ellis [2007]]. As outlined with an analysis of STEREO A/PLASTIC SWS data in Chapter 4, there are events which also contribute to priorities different from their nominal one. This is especially problematic, if a part of the distribution of protons (priority 0) is found in the other priorities. Chapter 4 also discusses the purpose of Priority 3, which is the second priority of heavier ions. It seems, that Priority 3 is not only intended to contain heavier ions but mostly events which can be considered as faulty. This is also suggested by the more irregular shape of the data in the priority as seen in Fig. 33, which in SSD Energy and time of flight space overlaps with Priority 2.
The purpose of priorities, to increase the number of actually transmitted PHA events of ions with mass numbers larger than 2 compared to protons and He is emphasized by the nominal minimum number of transmitted events per priorities. Of the 12 events which are transmitted every 2 energy per charge steps, the data processing unit selects one out of priority 0, one out

of priority 1, 4 out of priority 2 and 4 out of priority 3 for SWS. In addition one event for each of the two priorities of WAP are selected. If space remains in the data buffer, additional events are selected for transmission as they enter the instrument. Thus, the number of actually transmitted deviates from the nominal minimum numbers. As discussed in Chapter 3.1.5.iii.a, the PHA events need to be weighted, so that in approximation the statistical distribution of analyzed events matches the distribution of actual events.

3.3 STEREO/MAG

This study not only requires in-situ particle but also in-situ magnetic field observations. These are provided by the magnetometer (MAG) [Acuña et al. [2008], Luhmann et al. [2008]] which is part of the In-situ Measurements of Particles And CME Transients (IMPACT) aboard both STEREO spacecraft.
To reduce the spacecraft's effects on the local magnetic field within the observations, the instruments are mounted on a ~ 3 m boom. The instrument is a triaxial magnetometer and is designed to measure magnetic fields of a magnitude of up to ~ 512 nT. However, for higher resolution the detector can also be operated at a range of ± 65.536 nT. For each axis, these field ranges are processed via 16-bit analog to digital converters, so that for each axis a digital resolution of 0.015 nT or 2.0 nT is achieved depending on the range of operation. For normal science operations the nominal absolute accuracy is ± 0.1 nT. Concerning time resolution, the instrument allows for three operational modes: A high-resolution burst mode allowing for one value per 1/32 s, the normal mode with one value per 1/8 s and a beacon mode with one value per 10 s. The highest continuous mode available is the normal mode, hence this study employs the 8 Hz data.

Each axis of the instrument is a fluxgate magnetometer (e.g. Acuna [1974, 2002]). Fluxgate magnetometers employ a ring core, which is driven periodically into and out of saturation at a pre-defined frequency. For MAG the frequency is 50 kHz. Around the ring core, a second coil is wound to measure the induced signal. The periodic drive into saturation modulates the ambient magnetic flux by twice the driving frequency and induces a signal within the coils which is then measured. The signal depends on magnitude, direction and phase of the local magnetic field w.r.t. the instrument. This way, with three orthogonal sensors of this type, the local magnetic field is observed as a vector.

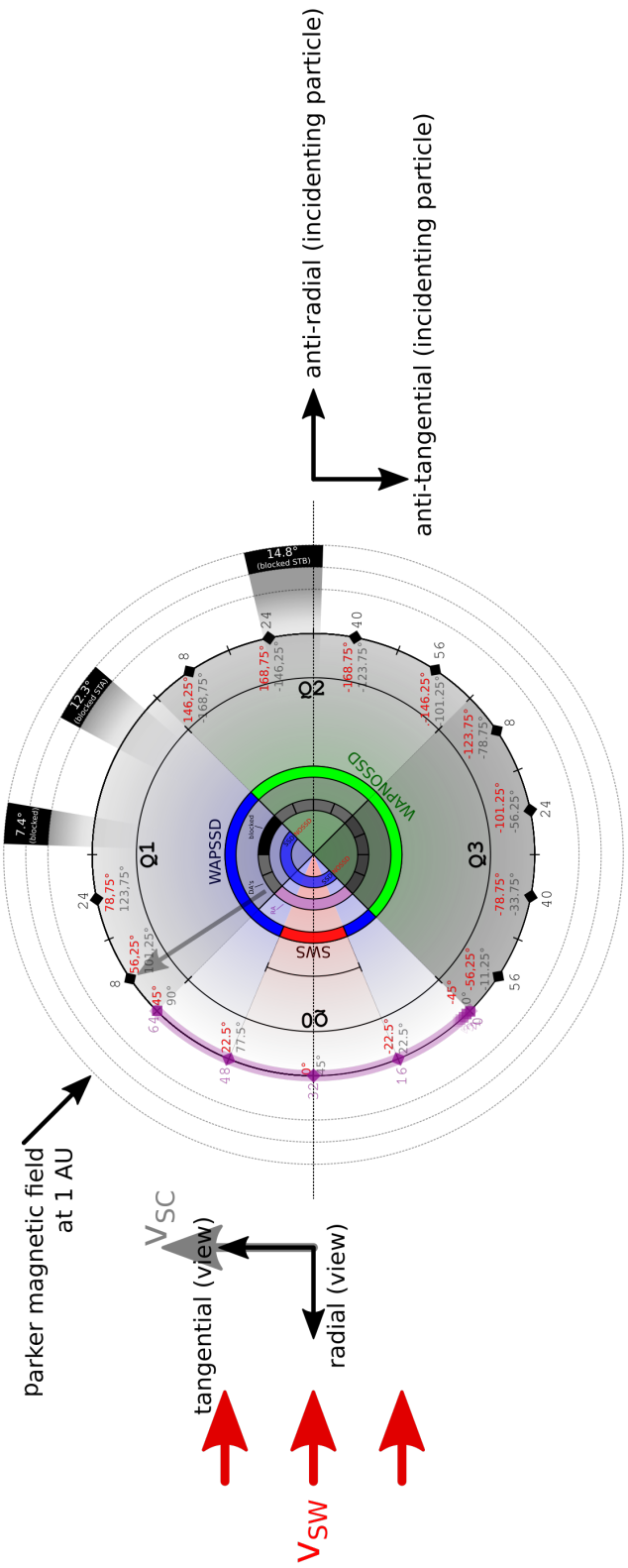

Figure 30: Top-down sketch of the segmentation of PLASTIC and its longitudinal position detection capabilities. Hereby, the instruments FOV is sketched as concentric circles. Parts of the instrument are blocked. These blockages are shown in the outermost circles which are dashed. Two of these blockages only apply to either of STEREO A (STA) and STEREO B (STB). The longitudinal incident angle resolution based on the instrument's position detection anodes is drawn on the outmost of the solid stroked circle. The instrument is divided up into for quadrants: Q0, Q1, Q2 and Q3. In Q0 the azimuthal incident angle is measured with a resistive anode (purple colored), which divides the 45° covered by Q0 into 64 bins. In the other quadrants four discrete (black and gray) anodes per quadrant measure position. The numbers in scripted font indicate the instrumental number assigned to a longitudinal bin. The number in serifless font indicate the corresponding angle in degrees. The central rings of the figure indicate from the outer rings to the inner rings to which section of the instrument a direction corresponds, whether that direction corresponds to a resistive or a discrete anode and whether an energy measurement with a solid state detector (SSD) is in that direction. Outside the sketch of the instrument black arrows provide an orientation of radial, tangential, anti-radial and anti-tangential direction as well as the magnetic field according to the model of Parker [1958] at 1 AU. A gray arrow points into the direction of the spacecraft's velocity. Red arrows indicate the direction of inflowing SW.

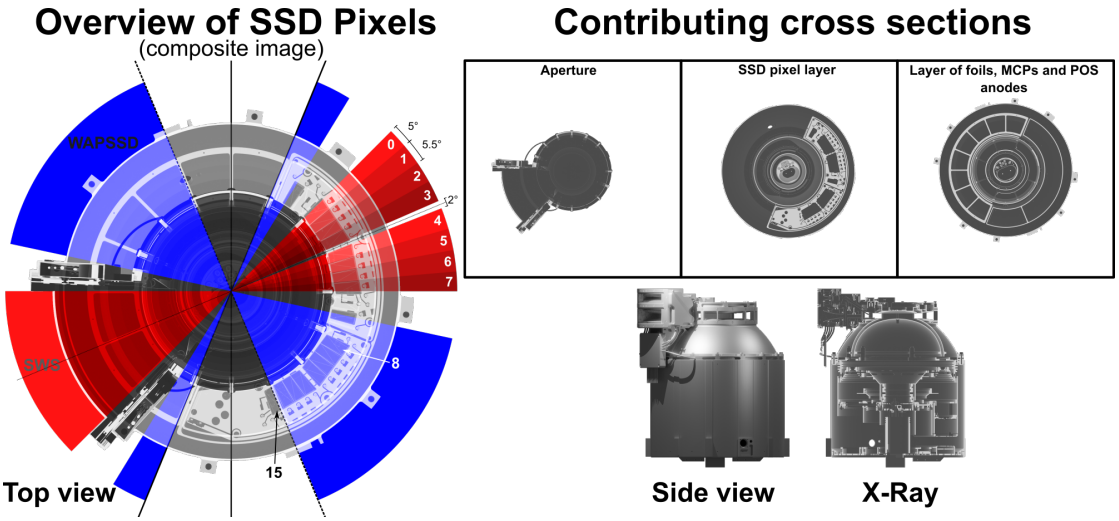

Figure 31: SSD Pixel geometry and FOVs as viewed and geometrically reconstructed from renders of a CAD model of PLASTIC. The renders were produced using the open source software blender. In the left figure, a wireframe representation was superimposed over the SSD pixels to emphasize their geometry. Tentative numbers were labeled to the pixels.

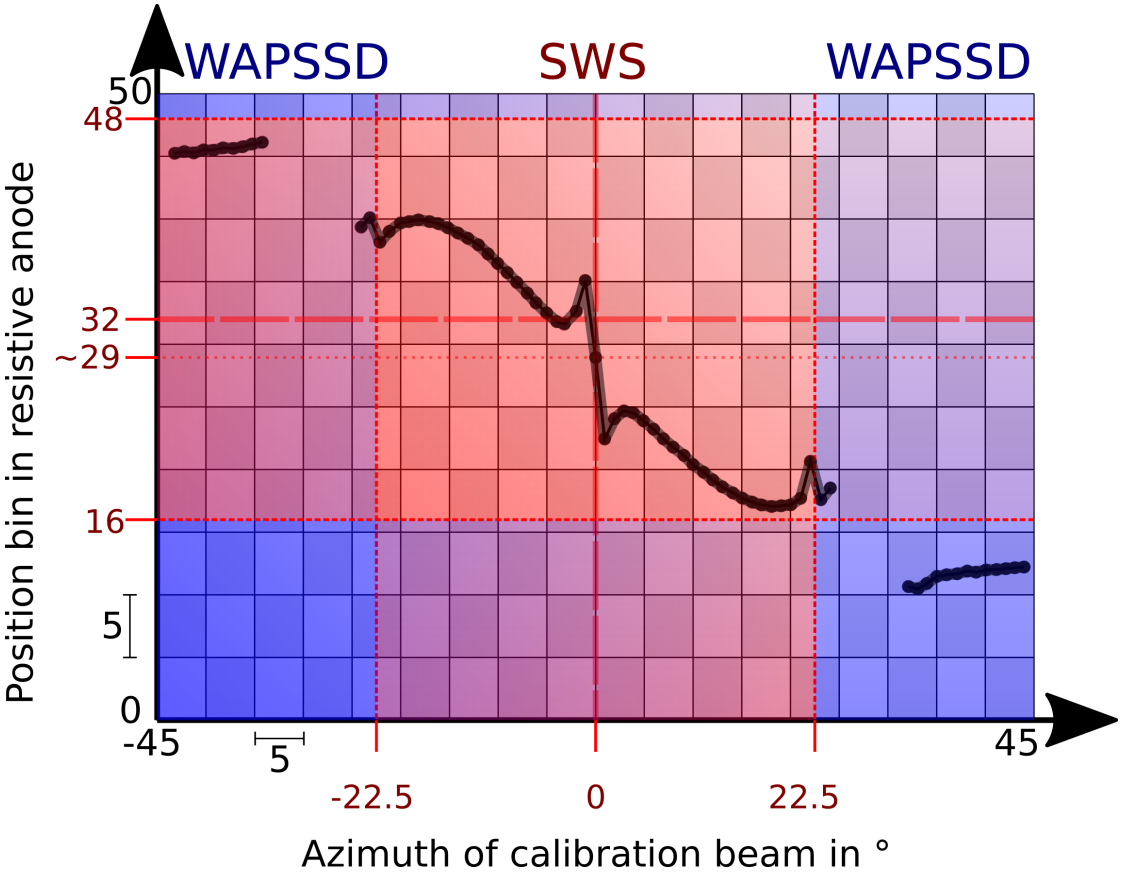

Figure 32: Ground calibration data for STEREO PLASTIC from Galvin et al. [2008]: The average position bin (y-axis) with which the resistive anode responds to a calibration beam of an azimuthal angle which is provided by the x-axis plotted in black. In addition, the nominal zones in both azimuthal angle and position bin of SWS are shaded in red and of WAPSSD in blue. At points where these overlap, the colors are mixed.

Duncan Keilbach- Three dimensional Pickup Ion velocity distribution functions observed at 1 AU with STEREO/PLASTIC: Anisotropic features and density enhancements in pitch angle distributions as tools to investigate transport effects

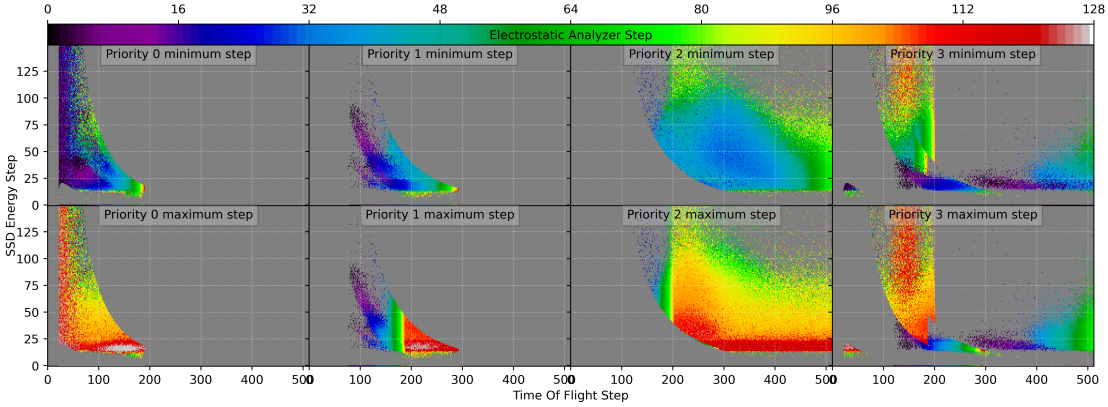

Figure 33: Maps of instrumental energy per charge steps in the plane of measured total energy vs. time of flight from STEREO A/PLASTIC SWS PHA data from 2008 to 2015. Each column refers to a different of the four instrumental priorities. The top row depicts the minimum energy per charge step per pixel and the bottom row the maximum energy per charge step pixel. These are color coded, where each plot utilizes the same key which is visualized by the colorbar on the top.

4 Preparation of STEREO / PLASTIC and STEREO / MAG data

In order to employ data from STEREO/PLASTIC and STEREO/MAG to derive He^+ PUI VDFs, calibration and preparation steps are necessary. Firstly, a calibration of the PHA data of STEREO/PLASTIC is necessary. The matrix rates were not employed, since they were not suitable for this work's purpose. The main problem with the matrix rates is, that they were derived onboard. As this chapter and the following result chapters outline, the instrument is affected by grave instrumental errors. Evidently, these have not been corrected onboard. In this chapter a method is shown with which He^+ ions are identified which is robust in spite of these errors. Secondly, auxillary data products which base on STEREO/PLASTIC and STEREO/MAG observations need to be merged with the data set of extracted He^+. The main problem for this is to synchronize the time indices of these products correctly. Finally, basic observations are outlined to verify the data analysis methods and the results of the calibration. In the final part of this chapter the resulting calibration is also critically discussed and a first look at instrumental errors is provided.

4.1 Separation of He^+ pickup ions from STEREO / PLASTIC PHA events

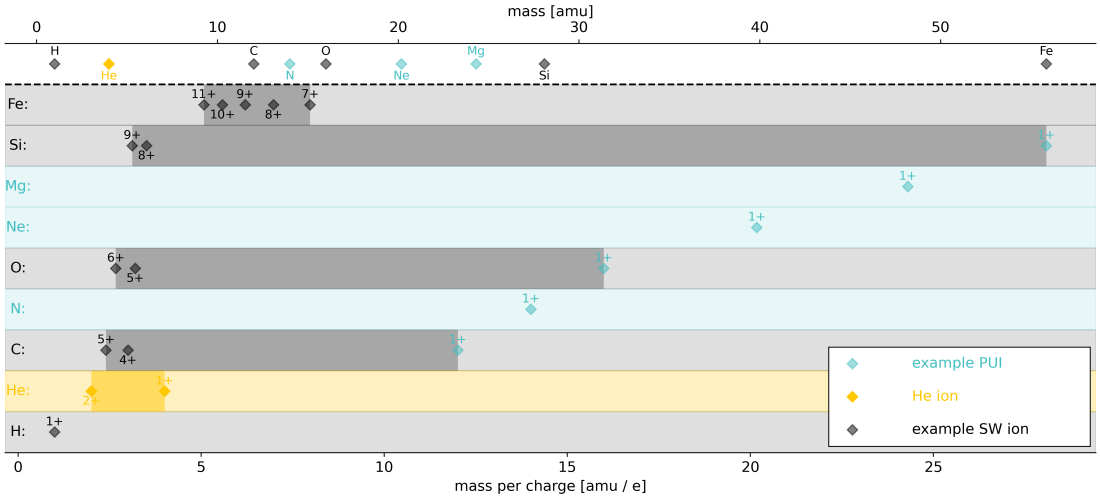

Figure 34: A selection of the ions present in the solar wind sorted by their mass (top axis) and their mass per charge (bottom axis). The top and bottom axes are separated by a dashed line. Example SW ions are plotted in grayscale. Example PUIs are plotted in turquoise and He ions are plotted in yellow. Some ions (e.g. H^+) are found as PUIs as well as as SW ions. In that case, in the figure only one of both of the ions' functions is plotted. He^+ is more clearly separated in mass space than in mass per charge state.

In order to obtain three dimensional VDFs of He^+ PUIs, these particles must be identified from the PHA event data.

Duncan Keilbach- Three dimensional Pickup Ion velocity distribution functions observed at 1 AU with STEREO/PLASTIC: Anisotropic features and density enhancements in pitch angle distributions as tools to investigate transport effects

In general, identifying particles via histograms of energy per charge vs time of flight is best suitable for identifying the particles of PHA events, since these contain information about the particles' mass per charge (compare chapter 3.1). In contrast to histograms of total energy vs time of flight, which contain information about the particles' mass, any identification derived from them is independent of the measurement of total energy. This means, that such a selection scheme works for triple coincidences as well as double coincidences.
Yet, as seen in fig. 34 because of their relatively low mass compared to other ions the He ions are better separated from the other elements in mass space than in mass per charge space. Hence, as a first step a separation scheme based on mass is derived, which yields a subset of the PHA events with a tentative mass of 4 amu. Then, the ions of this subset are investigated with regard to their position in energy per charge vs time of flight histograms. This yields an indication of where the He events of double coincidences are expected. With the application of filters based on estimated particle velocity compared to the momentary solar wind velocity measured by on board moments, the data is then filtered for pickup ion events. Also based on the expected functional dependence between energy per charge and time of flight a separation scheme for He^+ is derived with regard to their mass per charge.

4.1.1 Derivation of a mass separation scheme

For a separation in mass space, the position of PHA events in energy and time of flight space is an appropriate object of investigation (compare chapter 3.1). For visualization, Fig. 35 provides energy vs time of flight histograms of PHA observations during 2009 and visualizes estimated positions of H^+, He^+ and ${He_2}^+$ ions in those.
The relation between energy $E_{\mathrm{ion},1}$ and time of flight τ_{ion} (eq. 62) has been derived in chapter 3.1. Neglecting the pulse height defect it is described by a squared hyperbola function. Since by standard they are converted into physical quantities [Galvin et al., 2008], the following model function for the instrumental energy channel E_{ch} and the instrumental time of flight channel τ_{ch} is motivated by this:

$$E_{\mathrm{ch}} = \left(\frac{A}{\tau_{\mathrm{ch}}}\right)^2 . \tag{65}$$

Empirically a rough boundary for the form parameter A has been found, which makes up a search space for A. I.e. the model function is in rough proximity to the trace of He in E_{ch} vs τ_{ch} space for values within $]0, 1250]$. Optimal values for A are found employing the following algorithm:

- Accumulate a histogram of all PHA events $H_{mod}(E_{\mathrm{ch}}, \tau_{\mathrm{ch}})$. Each event accumulated in the histogram is weighted with a weight w, which is chosen such, that events in lower energy per charge steps are prioritised, since generally more He events are found in higher energy per charge steps. Since for this step the whole track of He events is of interest, the weights are deemed to counteract this effect. Let $N_{æ}(æ_{\mathrm{ch}})$ be the number of events per instrumental energy per charge step $æ_{\mathrm{ch}}$. Then the weight of any event at that energy per charge step is given by

  $$w = \frac{(128 - æ_{\mathrm{ch}})^2}{N_{æ}(æ_{\mathrm{ch}})} . \tag{66}$$

  The resulting histogram is normalized to the respective maximum of each energy channel slice.

- Do the following for each integer number A_{search} in the search interval of A: Find all points of H_{mod}, which are touched by the curve given by the model function for $E_{\mathrm{ch}}(\tau_{\mathrm{ch}})$ as defined

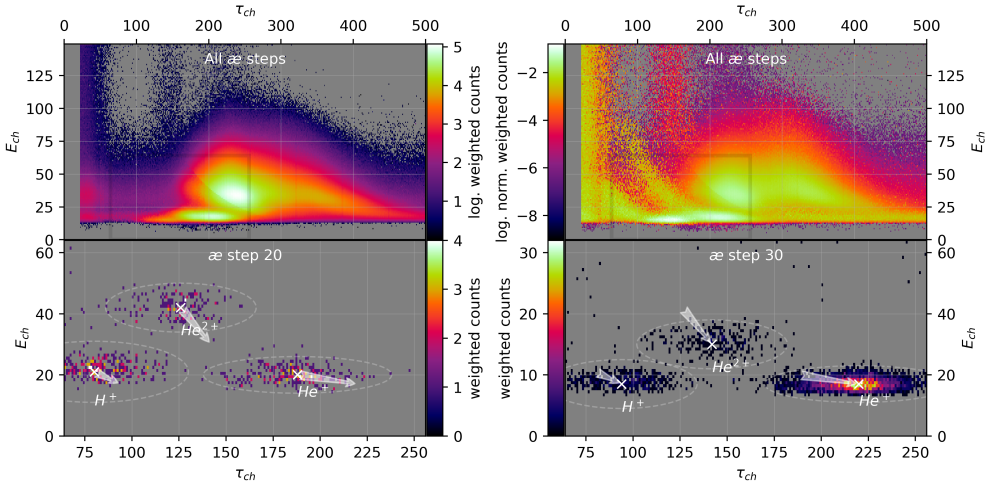

Figure 35: Two dimensional histograms of Energy channel (E_{ch}) and time of flight channel (τ_{ch}) of STEREO/PLASTIC SWS PHA events accumulated in 2009. Top left: The sum over all energy per charge steps is histogrammed. The histograms decadic logarithm is plotted. Top right: Analogous plot to the top left one, but first all counts were histogrammed per energy per charge step and then all energy-per-charge-wise histograms were normalized to their respective maximum. Plotted is the sum of these, normalized to the maximum of each E_{ch}-slice and then modified by a decadic logarithm. Bottom left and right: Analogous to top left, but for energy per charge steps 20 and 30 only and not plotted on a logarithmic scale. In both the peaks of H^+, He^+ and He^{2+} are visible. At these low energy per charge steps heavier ions do not appear, even though they are clearly visible in the top plots, which sum over all energy per charge steps. Based on visual reference the estimated position of the peaks is plotted and their movement when the energy per charge step changes is indicated by arrows.

by eq. 65 with the parameter A_{search} inserted as A and compute the sum $H_{mod,\sigma}$ of their respective histogram values.

- The 1250 sums computed by the following step are plotted as a function of the form parameter A. Apply the noise reduction algorithm described in appendix B.1 with the parameters $level = 31$ and $f = 0.1$ to obtain $H_{mod,\sigma,s}$. Since the track of He is the most prominent in the search area of A, the absolute maximum estimates the form parameter of the model function, which represents the center of that track.

- The function $H_{mod,\sigma,s}$ is expected to be multimodal, since the tracks of other ions (H^+ towards smaller values of A and O^{6+} and heavier ions towards larger values of A) are also present in the histogram. So the local minima of $H_{mod,\sigma,s}$ are an estimation for the point, where the contribution of two neighboring ions is the same or differently put: A crossover point in A between different ions.

- With a one-dimensional smoke ring algorithm the local minima closest to the absolute maximum are found. All in all the parameters A_{min} (the lower boundary for the He peak), A_{max} (the upper boundary) and A_{peak} (the maximum of the peak) have been obtained.

Now, a subset of particles with a tentative mass of 4 amu is obtained by filtering for all particles, which fit into a region defined by area between the model function of eq. 65 with the parameters $A_{min} = 557$ and $A_{max} = 1034$, the parameter of maximum integrated normalized counts has been determined at $A_{peak} = 799$.
A caveat of this method is, that now the resulting subset of particles is affected by spill of the neighboring ions. This is visible, when histogramming the particles from the subset in energy per charge vs time of flight space. Since He is expected to exhibit two charge states in the SW (compare fig. 34), two distinct traces are expected there. When different traces are visible as well, these are either from instrumental effects like pile-ups or chance-coincidences or from other ions. Since the filter applied at this stage is not deemed as a final selection of the particles, but rather determine the position of the peaks, A_{min} and A_{max} are modified by moving them closer A_{peak}. The parameters $f_{min}, f_{max} \in [0, 1]$ are defined, which determine, how close a parameter is moved towards the peak. Then modified boundaries are determined by

$$A_{k,mod} = f_{min|max} \cdot (A_{min|max} - A_{peak}) + A_{peak}. \tag{67}$$

In general, the peaks of ions are asymmetric (especially w.r.t. time of flight), so that the contribution of different ions to the peak is also asymmetric. Values for f_{min} and f_{max} are found empirically by iteratively modifying them and inspecting the energy per charge vs time of flight histograms of the resulting subsets. Hereby, the values $f_{min} = 0.4$ and $f_{max} = 1.0$ have been found as a good fit. The result is also visualized in Fig. 36.

4.1.2 Derivation of a mass per charge separation scheme

Analogous to the mass separation scheme of the foregoing chapter in this chapter a mass per charge separation scheme is derived based on the expected position in energy per charge space as a function of time of flight. But in contrast to the foregoing chapter the model function employed for this can not be described by a simple power law function, since the behavior of the ions throughout the instruments energy per charge analysation steps is dominated by the transition between two limiting cases: In one case the particles velocity during the time of flight is dominated by the particles energy per charge, when it enters the instrument. The post acceleration is negligible compared to the initial energy per charge. As the energy per charge

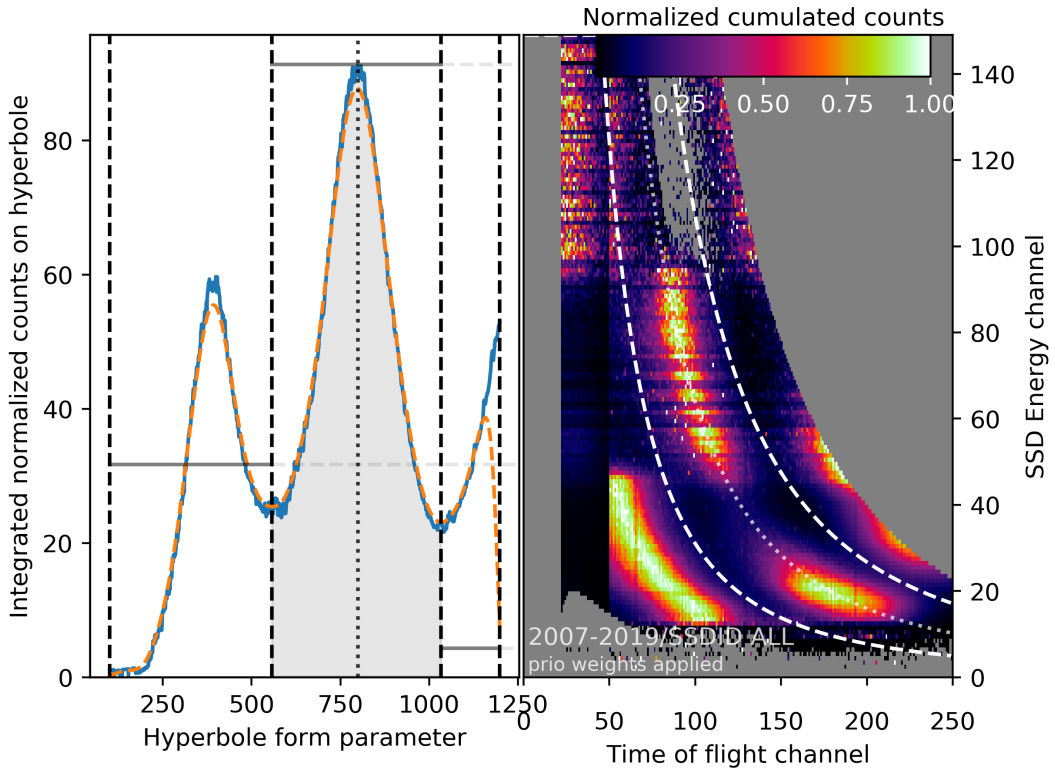

Figure 36: Left plot: Integrated normalized counts along the model function (y-axis) as a function of the functions model parameter (x-axis). Where the model functions matches the combined track in energy vs. time of flight space of He^+ and He^{2+} events best, the integrated counts reach an absolute maximum within the search space of the hyperbola parameter. Left and right of the maximum local maxima are found, whereas the left is associated with H^+ events and the right is associated with heavier ions (most probably $O_6{}^+$ leaking into the priority ranges. The necessary local minima in-between are interpreted as points of equal probability to obtain He events or different ions within the peak. Hence, this is a sensible boundary for events with a tentative mass of 4 amu. Right plot: A time of flight channel vs energy channel histogram modified according to the descriptions of this chapter. The blue line displays the derived parameters per bin and the orange dotted line a moving average of them. Three distinct ion tracks are visible from left to right: H, He (singly and doubly charged) and heavier ions at the edge of the selected priority ranges. As dashed white lines the model function is plotted using the derived hyperbola parameters for the boundary of He selection. A dotted white line represents the model function with the parameter at the left plots maximum.

decreases with the instrument stepping through increasing energy per charge channels, the post acceleration becomes dominant over the particles initial energy per charge. To second case is found, where the particles initial energy is negligible to the post acceleration voltage and therefore the time of flight will remain constant for the following energy per charge steps.

4.1.2.i Derivation of the model function In standard calibration [Galvin et al., 2008] the instrumental channels are converted into physical units through linear functions. Therefore the following will derive a model function for the physical parameters and absorb such a linear calibration into fit parameters.
Also the foil loss of a particle entering the time of flight chamber is neglected in the derivation. In that case, eq. 61 describes the relation between energy per charge and time of flight. To account for the instrument stepping logarithmically through energy per charge space, a natural logarithm is applied to both sides of the equation obtaining

$$\ln\left(æ_{ion}\right) = \ln\left(\frac{m_{\text{ion}}}{q_{\text{ion}}} \cdot \frac{d^2}{2\tau_{\text{ion}}^2} - U_{\text{PAC}}\right) \ . \tag{68}$$

This motivates a fit function of the form of

$$\ln\left(æ_{ion}\right) = \ln\left(a \cdot \left(\frac{1}{\tau_{ion}^2} - \frac{1}{\tau_{0,ion}^2}\right)\right) \ , \text{ where} \tag{69}$$

for $\tau_{ion} \to \tau_{0,ion}$ the function diverges, so that the behavior, that at the point where the post acceleration dominates over the initial energy per charge, the time of flight is constant with decreasing energy per charge, is modelled correctly. In order to isolate τ_{ion}^{-2} in eq. 69, the factor $(m_{ion}/q_{ion}) \cdot d^2/2$ must be extracted from the difference in the logarithm at the right right side of eq. 68 obtaining

$$\ln\left(æ_{ion}\right) = \ln\left(\frac{m_{\text{ion}}}{q_{\text{ion}}} \cdot \frac{d^2}{2} \cdot \left(\tau_{\text{ion}}^2 - \frac{2q_{ion}U_{\text{PAC}}}{m_{ion}d^2}\right)\right) \ , \text{ which} \tag{70}$$

means comparing with the variables of eq. 69, that a is defined by

$$a = \frac{m_{\text{ion}}}{q_{\text{ion}}} \cdot \frac{d^2}{2} \ \text{ and} \tag{71}$$

for $\tau_{0,ion}$ the following is stated

$$\frac{1}{\tau_{0,ion}^2} = \frac{2q_{ion}U_{\text{PAC}}}{m_{ion}d^2} \ \text{or} \ \tau_{0,ion} = \sqrt{\frac{m_{ion}}{q_{ion}}} \cdot \frac{d}{\sqrt{2U_{\text{PAC}}}} \ . \tag{72}$$

Employing calculus rules of the logarithm the product of a and the differences of the inverse squared times of flight in eq. 69 is converted into the sum of two logarithms and $\bar{A} := \ln a$ is defined. To transition from physical quantities to the instrumental channels an extra scaling factor c is defined obtaining

$$\ln(æ_{ch}) = c \cdot \left(\bar{A} + \ln\left(\frac{1}{\tau_{ch}^2} - \frac{1}{\tau_{0,ch}^2}\right)\right) \ . \tag{73}$$

To make the function more suitable to fitting, it is practical to find another expression for A, which allows for explicitly stating a point, the function lies on. Let $(\tau_{x,ch}, æ_{x,ch})$ be this point. Then the requirement

$$\ln(æ_{x,ch}) = \ln(æ_{ch})|_{\tau_{ch}=\tau_{x,ch}} \tag{74}$$

yields

$$\bar{A} = \frac{\ln\left(æ_{x,ch}\right)}{c} - \ln\left(\frac{1}{\tau_{x,ch}^2} - \frac{1}{\tau_{0,ch}^2}\right) \ . \tag{75}$$

By insertion into eq. 73 the model function in its final form is obtained, namely

$$\ln(æ_{ch}) = \ln(æ_{x,ch}) + c \cdot \ln\left(\frac{\tau_{ch}^{-2} - \tau_{0,ch}^{-2}}{\tau_{x,ch}^{-2} - \tau_{0,ch}^{-2}}\right) \ . \tag{76}$$

In order to correctly represent the energy per charge stepping, where smaller instrumental channels mean higher physical energies per charge, c must be negative.

4.1.2.ii Analysis of the parameters of the model function In order to interpret the results of the fit it is useful to discuss some of the fit functions parameters and their relation to physical quantities in detail.

4.1.2.ii.a The functions divergence, mass per charge and post acceleration Eq. 72 states two relations, which are of interest for this study's analysis: The maximum time of flight achieved by an ion scales with the square root of its mass per charge as well as with the reciprocal of the square root of the post acceleration voltage. So, if the post acceleration voltage is changed during the mission, this will directly translate into a shift of an ions track, which is unsurprising. Still, it is an indicator to watch out for during data analysis and can be viewed as a second method of identifying a change in post acceleration voltage next to the voltage value transmitted via housekeeping data.
The dependency of mass per charge is more interesting, since it may help estimating positions of ions, the tracks of which do not allow to observe the point of divergence directly. With the definition of a according to eq. 71 and the relation of A and $\tau_{x,ch}$ and $\tau_{0,ch}$ in eq. 75, the distance between $\tau_{x,ch}$ and $\tau_{0,ch}$ can be directly related to mass per charge. Since 71 is defined through physical quantities and 75 through instrumental quantities, a linear scaling function sc is introduced, which reflects the calibration of the instrument. This leads to the equation of

$$\frac{\ln\left(æ_{x,ch}\right)}{c} - \ln\left(\frac{1}{\tau_{x,ch}^2} - \frac{1}{\tau_{0,ch}^2}\right) = \ln\left(\mathrm{sc}\left(\frac{m_{\mathrm{ion}}}{q_{\mathrm{ion}}} \cdot \frac{d^2}{2}\right)\right) \ , \text{ which} \tag{77}$$

transforms into

$$\frac{1}{\tau_{x,ch}^2} - \frac{1}{\tau_{0,ch}^2} = \frac{æ_{x,ch}/c}{\mathrm{sc}\left(\frac{m_{\mathrm{ion}}}{q_{\mathrm{ion}}} \cdot \frac{d^2}{2}\right)} \ . \tag{78}$$

So the distance between $\tau_{0,ch}$ and $\tau_{x,ch}$ (albeit their squared reciprocals) is controlled by the particles mass per charge. Moreover, it is also controlled by the length of the time of flight chamber d, which means that the calibration for parts of the instrument, where SSDs are fitted, differs from those without them. Moreover the ratio of mass per charge of He^+ and He^{2+} is $(m_{He^{2+}}/q_{He^{2+}})/(m_{He^+}/q_{He^+}) = 0.5$ and the length of the time of flight chamber is in the section with SSDs is $d_{ssd} = 8.0$ cm and in the section without SSDs is $d_{nossd} = 5.8$ cm, which results in $d_{nossd}^2/d_{ssd}^2 = 0.525625$. Hence, in combination with eq. 71 it is concluded that the position of the track of He^{2+} in a section fitted with SSDs is an approximation for the track of He^+ in a section without SSDs. So, it can also be employed as a first guess when parameterizing the He^+ track in a section without SSDs.

4.1.2.ii.b Transformation of the parameter space to an arbitrary second point For some ions the value of $\tau_{0,ch}$ is challenging to determine, since they too seldomly record events at energies per charges small enough. He^+ pickup ions, which are generally considered suprathermal, are a fitting example for that. One roughly expects those at total energies corresponding to velocities of at least the SW mean velocity to twice the SW mean velocity. So it is necessary to not define the parameters of the model function from where it diverges but from a second point $(\tau_{y,ch}, æ_{y,ch})$. Requiring

$$\ln(æ_{y,ch}) = \ln(æ_{ch})|_{\tau_{ch}=\tau_{y,ch}} \tag{79}$$

one obtains

$$\tau_{0,ch} = \sqrt{\frac{\frac{æ_y - æ_x}{c} - 1}{\frac{æ_y - æ_x}{c} \cdot \tau_{x,ch}^{-2} - \tau_{y,ch}^{-2}}} \,. \tag{80}$$

This equation is another way to define the location of the model function of eq. 76: With this equation of $\tau_{0,ch}$ a second point $(\tau_{y,ch}, æ_{y,ch})$ is required to construct the function. Opposedly, if 78 to define $\tau_{0,ch}$, the point of divergence is required.

4.1.2.iii Optimization of the model function for events in the solar wind sector With the triple coincidences already filtered for the mass of He events according to chapter 4.1.1 a histogram depicting energy-per-charge against time of flight is less crowded than with unfiltered data or with double coincidences . In fact, if the filtering process of chapter 4.1.1 performs well, the histogram features only two tracks, which represent the two charge states of the He events. The following describes the steps leading to parameters of the model function from eq. 76 optimized to the He tracks and how these are employed to separate both charge states from each other. These steps are only performed for data from the solar wind sector of the instrument, since the length of the time-of-flight chambers is different in parts of the instrument, where SSDs are present, than in parts of the instrument without an SSD.

4.1.2.iii.a Preparation of the PHA events Two dimensional histograms of instrumental energy per charge channel and time of flight channel are accumulated from data out of the years 2008 to 2019. So these histograms represent a long-term average of the events incidenting the instrument. An initial means of distinguishing is provided from topological arguments: Since the tracks of He^+ and He^{2+} events in the histogram are well separated (at least for energy per charge channels above a channel number of 10), a map is created depicting all areas of the histogram, which exceed the average value of all histogram pixels. Then connected areas inside this map are searched. The two largest of which roughly represent the two charge states. For this analysis all energy per charge channels above a channel number of 10 are employed.
Since the mass per charge of He^{2+} is smaller than the mass per charge of He^+ (compare fig. 34), the track of He^{2+} is expected to roam further left in the histogram than the track of He^+ as a consequence of eq. 72. Thus the resulting areas are attributed to their respective ion.

4.1.2.iii.b Determination of optimal parameters modelling the track of He^{2+} events Both the observed He^{2+} and He^+ events are embedded into the SW, where He^{2+} is expected to be to the most part of solar origin and He^+ to consist of a considerable amount of PUIs. Therefore assuming, that both species have the same energy with their energies corresponding to the SW bulk velocity, the mass per charge of He^+ exceeds the mass per charge of He^{2+}. Considering, that the pickup component of He^+ is expected at velocities of up to two times the SW bulk velocity, He^+ is expected to roam at lower energy per charge steps than He^{2+} (the instrumental energy per charge step is reversed w.r.t. increasing energies per charge). Therefore

the parameter $\tau_{0,ch}$ can not be obtained from He^{+}, since such low energies of this species have not been observed. Also He^{2+} is more abundant. Hence an optimization of the model function from the track of the latter ion is more robust.
The following steps are performed only on the part of the histogram belonging to the provisional area of He^{2+}, which has been described in the foregoing section. First, the parameter $\tau_{0,ch}$ is determined from the He^{2+}. For this, the time of flight channel of the maximum of each energy per charge slice is obtained. The maximum of which is then the parameter $\tau_{0,ch}$. Since the histogram contains data accumulated over a considerable amount of time, the signal to noise ratio of the histogram is sufficiently low to employ this method.
Now the parameters $\tau_{x,ch}, æ_{x,ch}$ and c remain to be determined. Since the time of flight channels of maximal counts have already been determined for each energy per charge step, these are employed as a sample of probable values of $\tau_{x,ch}$ and $æ_{x,ch}$. For each of them a parameter c exists, which maximises the histogram curves accumulated along the model function. The optimization process for c is described by algorithm 1. The minimum and maximum of the search space has been determined empirically by adapting the model function by eye. For the final result a precision of 10^{-10} has been employed. For the analysis only values of $\tau_{x,ch}$ and $æ_{x,ch}$ have been employed, which originate from histogram slices, which are not empty. Also only values of $æ_{x,ch} < 80$ were respected, since the rest is too close to the divergence value $\tau_{0,ch}$ and therefore tends to be numerically unstable. From the obtained combinations of $\tau_{x,ch}$, $æ_{x,ch}$ and c, the combination with the largest sum of counts along the model function is chosen as the optimal parameter combination.

Algorithm 1 Optimization algorithm for the parameter c

Input:$\tau_{0,ch}$, $\tau_{x,ch}$ and $æ_{x,ch}$, precision Δc
If this is the first iteration, set $s_{min} \to 0$ and $s_{max} \to 100$.
Initialize the search space S, as a set of 10 equidistant values between s_{min} and s_{max}.
Initialize a 10 value array for the counts n.
for c_i in S **do**
    Accumulate all counts along the model curve with the parameters $\tau_{0,ch}$, $\tau_{x,ch}$, $æ_{x,ch}$ and c_i as c.
    Store those in the i-th value of n.
Determine the index j of the maximum value within the array n.
if $j = 0$ **then**
    $s_{min} \to c_{j-1}$
else if $j = 9$ **then**
    $s_{max} \to c_{j+1}$
else
    $s_{min} \to c_{j-1}$
    $s_{max} \to c_{j+1}$
if $s_{max} - s_{min} > \Delta c$ **then**
    The search space has been refined. Evaluate this algorithm recursively. Store the result in c.
else
    $c \to c_j$
Output:c

4.1.2.iii.c Transition to He^{+} events As described in section 4.1.2.i, the scale parameter c is a conversion factor from instrumental channels to physical units. It also intrinsically

contains the energy loss of the particles in the foil as they enter the instruments time of flight chamber. Since the foil loss is predominantly sensitive to particle mass over charge states Gonin [1995], it is assumed constant for both He charge states in good approximation.
Since therefore the primary shape of the model function is retained from He^{2+} to He^{+}, it is legitimate to shift the function in τ_{ch}-space until the counts accumulated along the model function are maximal, where this time the accumulated counts are taken from the provisional He^{+} area of chapter 4.1.2.iii.a only. In addition to this procedure, the consequence of eq. 77, namely that the difference of $\tau_{x,ch}$ or $\tau_{y,ch}$, respectively and $\tau_{0,ch}$ is increased for He^{+} compared to He^{2+}, has to be acknowledged. Hence, the aforementioned shift in τ_{ch}-space is only applied to $\tau_{x,ch}$, while for each value of $\tau_{x,ch}$ evaluated during this procedure, a respective value of $\tau_{0,ch}$ is searched, which maximizes the counts along the resulting model function. Here, the counts originate from a histogram, which is a modified version of the histogram of He^{+} of chapter 4.1.2.iii.a. The modification is, that the histogram is normalized to the maximum of each slice in $æ_{ch}$.

Finally, the boundaries of He^{+} in energy per charge vs. time of flight space are estimated by a width parameter of the accumulated counts as a function of time of flight shift. The introduction of a scale parameter is necessary, since the peaks of the ions are asymmetric. Hence, e.g. the approach of the width at half maximum as a boundary is not expected to yield a meaningful value. By observation of the resulting boundaries (compare e.g. Fig. 36) an empirical criterion for the scale parameter is found. This is described in the following chapter.

4.1.2.iv Identification of He^{+} events in different sections The ion tracks in WAPSSD in $æ_{ch}$ vs. τ_{ch} are expected to reside within the same parameters as for SWS, since the basic detection principles and TOF chamber lengths are the same, but in WAPNOSSD, a different TOF flight path is expected, so that a different approach must be employed.
It has already been established, that the ion tracks of He^{+} in WAPNOSSD reside between the ion tracks of He^{+} and $He_2{}^{+}$ in SWS, which is a consequence of eq. 78 in combination with $(m_{He^{2+}}/q_{He^{2+}})/(m_{He^{+}}/q_{He^{+}}) = 0.5$ and $d^2_{nossd}/d^2_{ssd} = 0.525625$. So to find the optimal model parameters fo He^{+} in WAPNOSSD, only pixels within the $æ_{ch}$ vs. τ_{ch} histogram are respected, which are located between the two model functions obtained in SWS. Secondly, c is assumed a constant scaling factor. So in the next step $\tau_{0,ch}$ and $\tau_{x,ch}$ are optimized to fit the condition, that the highest number of summed histogram counts lies on the model curve. After the maximum is found, the function is shifted left and right in τ_{ch} space in order to determine the approximate width of the ion track, which is later employed as a cutoff criterion to extract the He^{+} events from the PHAs. As a criterion for the resulting shift on both sides, it is determined, that the total counts, which are integrated over the shifted model curve are lower than a given fraction of those integrated over the optimized model curve.
Since the time of flight signal tends to scatter more in positive direction, here a lower value (one fifth) is employed than on the negative direction (one fourth). The calibration results for all sections of the instrument are displayed in Fig. 37.

4.2 Auxilliary data products

In addition to the He^{+} PHAs, other data products were employed for this work. Here, a brief overview of these and, if necessary, references to their authors are provided.

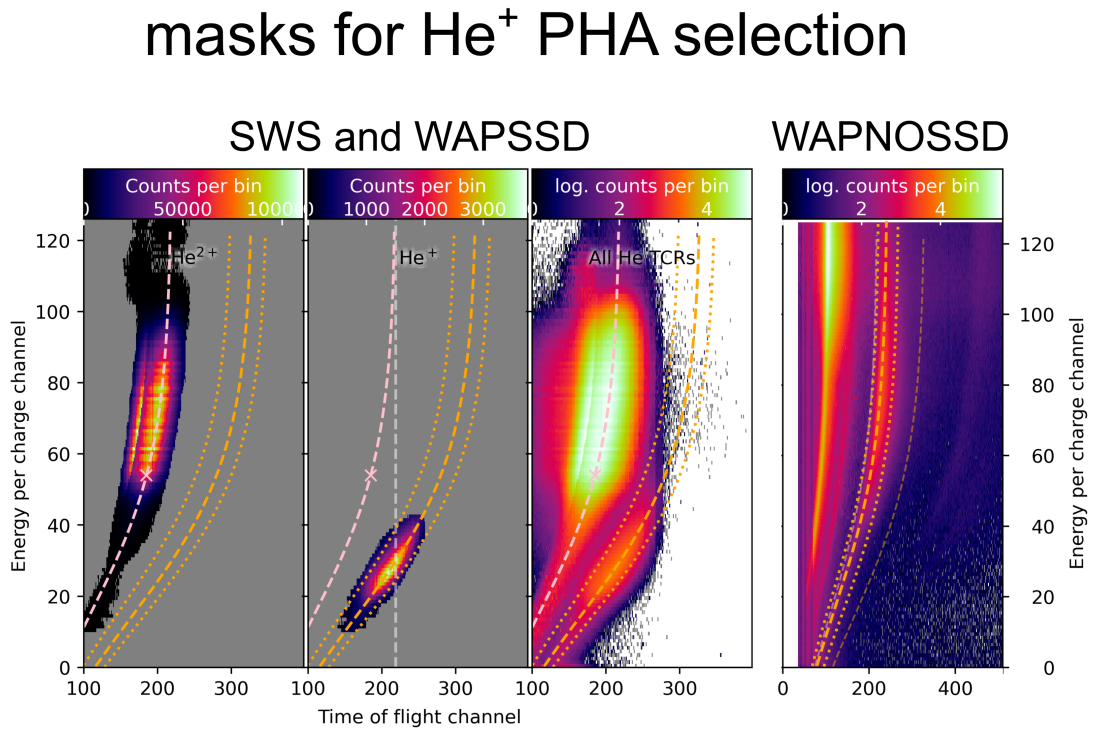

Figure 37: Display of the final masks employed for the extraction of He^+ PHAs. All plots are histograms of energy per charge versus time of flight in instrumental channels. The three left plots correspond to the calibration of SWS and WAPSSD and the right plot to WAPNOSSD. The first left plot depicts a coarse selection of He^{2+} PHAs which was selected by thresholding the histogram in the third left plot and finding connected areas. To that coarse selection a curve for the maximum of He^{2+} was fitted (pink). In the second left plot, an analogously found selection of He^+ PHAs is displayed. The orange dashed left line displays the calibration curve for He^+. The orange dotted lines left and right from it the boundaries, so that all PHAs in between the orange dotted lines are considered He^+ PHAs. The third left plot displays all He TCRs and the calibration curves. For WAPNOSSD, the right plot displays a histogram of all events. The less opaque orange dotted curve is the calibration line for He^+ in SWS and WAPSSSD. For WAPNOSSD, the parameters of the curve were modified to fit to the different length of WAPNOSSD's time-of-flight chamber. The orange dotted line is the result for the fit to the maxima and the area in between the orange dotted lines is the mask for He^+ in WAPNOSSD.

Duncan Keilbach- Three dimensional Pickup Ion velocity distribution functions observed at 1 AU with STEREO/PLASTIC: Anisotropic features and density enhancements in pitch angle distributions as tools to investigate transport effects

4.2.1 The heliospheric position of STEREO

To put the analyzed data into context information about STEREOs position is required. For this purpose, Ephemeris data in form of so called SPICE-Kernels [Semenov [2021]] have been employed. Using the software *ET SPICE* [von Forstner [2021]], the information contained within them has been converted into time series of J2000 coordinates.

In the J2000 standard (e.g. Murray [1989], Seidelmann [2006]), the spacecraft's position is expressed in a spherical coordinate system w.r.t. the Sun's position as a coordinate origin. So in addition to the distance from the Sun two additional coordinates are obtained. As a reference plane the in-ecliptic plane is chosen, so that the azimuthal angular coordinate is the in-ecliptic longitude φ_{ecl} and the elevation angular coordinate is the out-of-ecliptic latitude ϑ_{ecl}. The point of $\varphi_{\mathrm{ecl}} = 0$ refers to the first point of aries and φ_{ecl} is defined such, that it ranges from 0 to 2π. For ϑ_{ecl} the definition is, that it ranges from $-\pi$ to π with $\vartheta_{\mathrm{ecl}} = 0$ being the ecliptic plane.

4.2.2 Treatment of the magnetic field data

The STEREO MAG magnetic field is obtained in RTN (radial, tangential, normal w.r.t. the spacecraft-Sun axis) coordinates from UCLA [2022] with a data rate of 8 Hz. To merge with PLASTIC observations, the magnetic field observations are averaged to a nominal resolution of 5 min. For this, for each measurement cycle of PLASTIC, the corresponding 8 Hz magnetic field vector components are averaged. The resulting data product is referred to as $B_{\mathrm{R,5m}}$,$B_{\mathrm{T,5m}}$ and $B_{\mathrm{N,5m}}$ for the averaged vectorial components.

4.2.3 Combination with Maxwellian fits of Solar Wind Velocity Distribution Functions

As a level 2 data product, one-dimensional Maxwellian fits to proton VDFs measured with PLASTIC are provided by Galvin et al. [2017] with 1 min time resolution. Analogously to the magnetic field data, this data product is averaged to the full 5 min cycles and are in the RTN coordinate system as well. The data products will be referred to as $v_{p,R}$, $v_{p,T}$ and $v_{p,N}$. Any product derived within the frame of the SW velocity as indicated by these Maxwellian fits are tagged with the label SWp indicating the SW proton bulk frame.

4.2.4 Observations of ICMEs, SIRs and interplanetary shocks

Available as level 3 data of STEREO/IMPACT observations are lists of times, when acceleration regions, such as ICMEs, SIRs and interplanetary shocks passed the instrument [Jian et al. [2013, 2018, 2019], Kucera [2022]]. The PHA data observed during any event of these lists has been tagged accordingly, so that it can be classified and sorted during later analysis.

4.2.5 Pre-filtered Fe PHA events

For some of the observations it is convenient to compare with Fe PHAs. However, a separation of the various Fe charge states in the SW is beyond the scope of this work and would need a different approach than the one employed for this work to separate He^{+} PHAs. Becker [2020] has developed a separation algorithm to identify the charge states Fe^{7+}, Fe^{8+}, Fe^{9+}, Fe^{10+} and Fe^{11+} and provided separated PHAs for the year 2008. For an example time period, the absolute velocities of these ions are plotted as a time series in Fig. 38. Hence, this study will employ their data, if Fe observations are required.

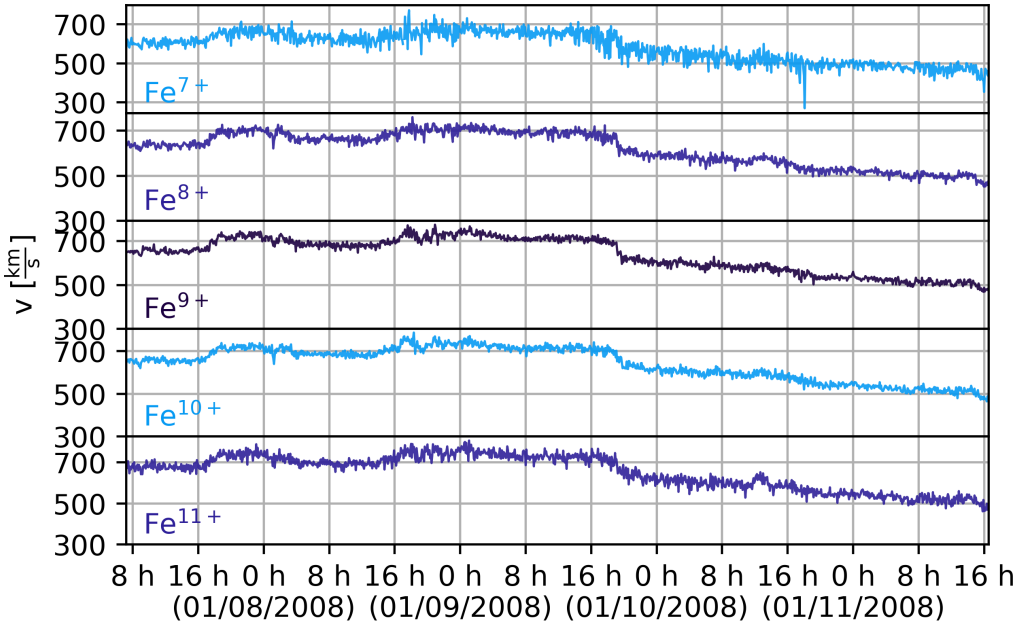

Figure 38: Time series of $\sim$ 5 days of STEREO A/PLASTIC Fe^{7+},Fe^{8+},Fe^{9+},Fe^{10+} and Fe^{11+} observations. The x-axis corresponds to the date and time of day and the y-axis to the ions' absolute velocities.

4.2.6 Derivation of the de-Hoffmann-Teller frame from STEREO / PLASTIC and STEREO / MAG observations

Parts of the work and results this chapter presents have been presented by Keilbach et al. [2020]. Němeček et al. [2020] proposed a method to compute the dHT frame from ACE and Wind observations. Since the dHT frame (compare chapter 2.1.8.iii) might play an important role in the transport of PUIs (compare chapter 2.2.6), an adaptation of their method to STEREO/PLASTIC data is expected a fruitful course of action.
The dHT frame is defined by the condition, that if observed in that frame, the motional electric field (the $\vec{v} \times \vec{B}$-field) of the plasma vanishes [de Hoffmann and Teller [1950], Němeček et al. [2020]]. From spacecraft observation for an ion i a time series of velocities $\vec{v}_i(t_j)$, where t_j is the j-th time of the time series, and a time series of magnetic field vectors $\vec{B}(t_j)$ are available, which are affected by statistical errors. So, Němeček et al. [2020] computed the dHT velocity $\vec{v}_{HT}(t)$ at the time t by minimizing the time averaged squared motional electric field, which is proportional to

$$m := \sum_{t_j \in [t-dt, t+dt]} \left| \left((\vec{v}_i(t_j) - \vec{v}_{HT}(t)) \times \vec{B}(t_j) \right) \right|^2 . \tag{81}$$

Hereby, dt determines the time interval, over which the averaging runs. The choice of dt is vital for the results. A lower dt makes the result more reactive to changes within the SW conditions on shorter time scales, but on the other hand increases the influence of statistical errors. The reverse is the case for higher values of dt. Němeček et al. [2020] chose a time interval of 60 minutes length. In the following ways are discussed to benchmark the precision of the minimization.

Based on momentary knowledge of differential streaming (e.g. Berger et al. [2011], Janitzek et al. [2016]), data from heavier ions is best suited to compute the dHT frame from, since their average velocity differs most from the proton bulk frame. So, in this work data of the Fe charge states as derived by Becker [2020] from STEREO/PLASTIC observations (compare chapter 4.2.5) is employed as ion data for the minimization of eq. 81. For the computational implementation of the minimization scipy's minimize function and the L-BFGS-B algorithm are used [Liu and Nocedal [1989], Virtanen et al. [2020]]. The availability of different Fe charge states also has the advantage, that since they roughly reside at the same location in velocity space, more statistical significance is gained by including all ions at once in the minimization of the expression in eq. 81.

In the following, computed dHT velocities are presented for five selected days of SW data. A time series of relevant SW quantities is provided in fig. 39. The time period is sufficiently long to observe the effect, that differently chosen dt have on the computed dHT velocity. Fig. 40 depicts the computed dHT velocity for $dt = 30$ min, Fig. 41 for $dt = 250$ min and Fig. 42 for $dt = 2500$ min. While for the first settings the residuals between the Fe charge states velocities and the dHT velocities are apparently very similar, for the larges time interval, the residuals are significantly larger. Also, the dHT velocity is shaped more like a running average of the proton and Fe velocity. Small scaled changes are not represented within the computed dHT velocity for this setting. The effect, that for larger values of dt the dHT velocity becomes smoother can also be seen for the settings of $dt = 30$ min and $dt = 250$ min. Here, the dHT frame velocity follows the average Fe velocity reasonably well, although of course closer for $dt = 30$ min. However, this does not necessarily mean, that a smaller setting of dt is the most reasonable choice, since the dHT frame velocity may also follow the noise in the data as discussed earlier.
Another method of determining the optimal dt must be found. A tracer for this might be the residual motional electric field in the computed dHT frame, since per definition in the dHT frame this quantity vanishes. So the magnitude of the residual field is a tracer for the goodness of the minimization and of the chosen dt. Also, for the minimization an averaged squared motional field is employed. In the test, the absolute of the instantaneous field can be computed, namely

$$\left|\vec{E}_{res}\right| := \left|(\vec{v}_i(t_j) - \vec{v}_{HT}(t)) \times \vec{B}(t_j)\right| \ . \tag{82}$$

With this quantity at hand, a condition needs to be derived as to which statistical measure of the residual field is best suited to represent an indicator for the goodness of the optimization. So, Fig. 43 provides an overview of values of the most obvious statistical measures for the resulting array of electric field magnitudes as a function of dt. The data utilizes the five days of data as before. Right away the minimum can be dismissed as a reasonable measure. The average field seems to be the most stable quantity. However, in this case it monotonically increases with increasing dt and without a clearly pinpointable local minimum, although areas of increased and decreased increase can be found. The maximum is the only quantity, that is attributed with a reasonably visibly local minimum (which is close to $dt = 250$ min, incidentally). Yet, the maximum does not seem to be a stable option as an indicator for the goodness of the minimization. The median has also been shortly considered as a measure for the goodness of minimization, but lead to similarly inconclusive results.
Further studies need to be commenced to determine a condition for an optimal value of dt. Lastly, dt might also not be a fixed quantity, but be different for each SW stream or between solar minimum and maximum. Maybe, in future studies, which determine the dHT velocity, the velocity has to be computed for different values of dt. The right choice of dt may even depend on the studied particles, e.g. depending on inertial length or plasma frequency, since each ion species is expected to react to accelerations on different time scales. Therefore, no definitive

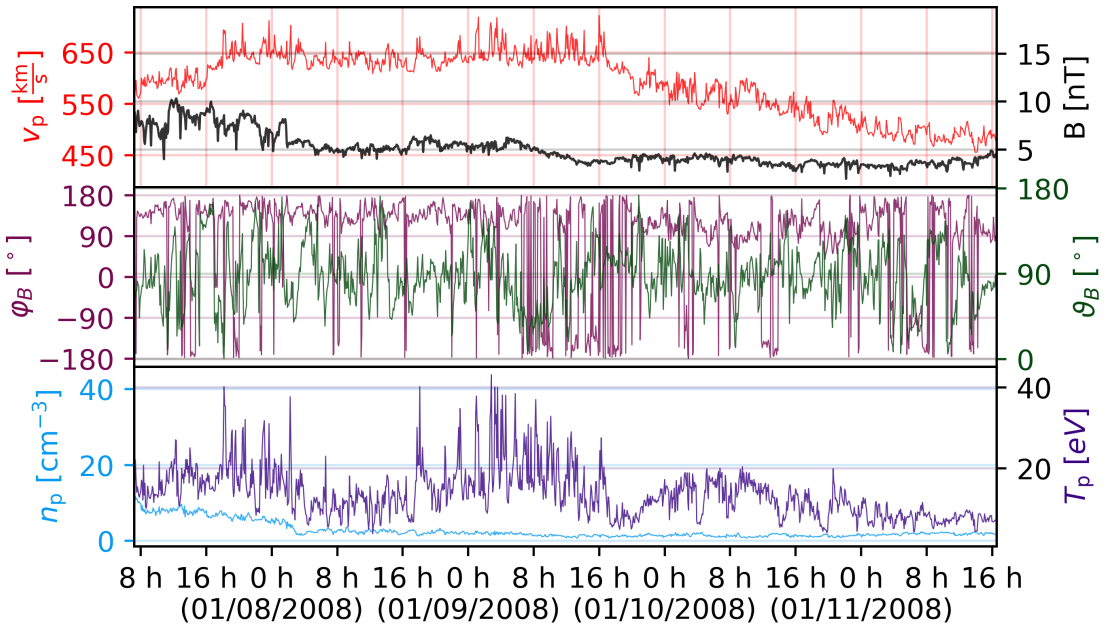

Figure 39: Time series of STEREO/PLASTIC proton and STEREO/MAG magnetic field observations. The x-axis corresponds to time and depicts date and time of day. All panels share the same x-axis. Top panel: Average proton velocity (red, left y-axis) and absolute magnetic field (black, right y-axis). Center panel: Azimuthal angle of the magnetic field (dark violet, left y-axis) and elevation angle of the magnetic field (green, right y-axis). Bottom panel: Proton density (light blue, left y-axis) and proton temperature (purple, right y-axis).

indicator for the goodness of the computed dHT velocity is found, yet. However, the tools have been implemented to enable the computation of the dHT velocity from STEREO/PLASTIC data and may enable more insights into differential streaming of heavy ions in the SW as well as into the transport of PUIs.

4.3 Verification of data analysis methods and results of the instruments calibration

Special attention has been exercised on the validity of the newly calibrated STEREO/PLASTIC data of this work. Hence, this chapter focuses on the verification of the obtained data.

4.3.1 Mapping of the instruments azimuthal position and quadrant bins

To determine the azimuthal position of a PHA event, the spacecraft provides three different data products: The position bin (integer numbers between 0 and 63, inclusively), the quadrant flag (0,1,2 or 3) and the section flag (0,1,2 or 3). Unfortunately, the mapping of these has not been documented well, so that it is necessary to deduce the mapping of the bins from instrumental

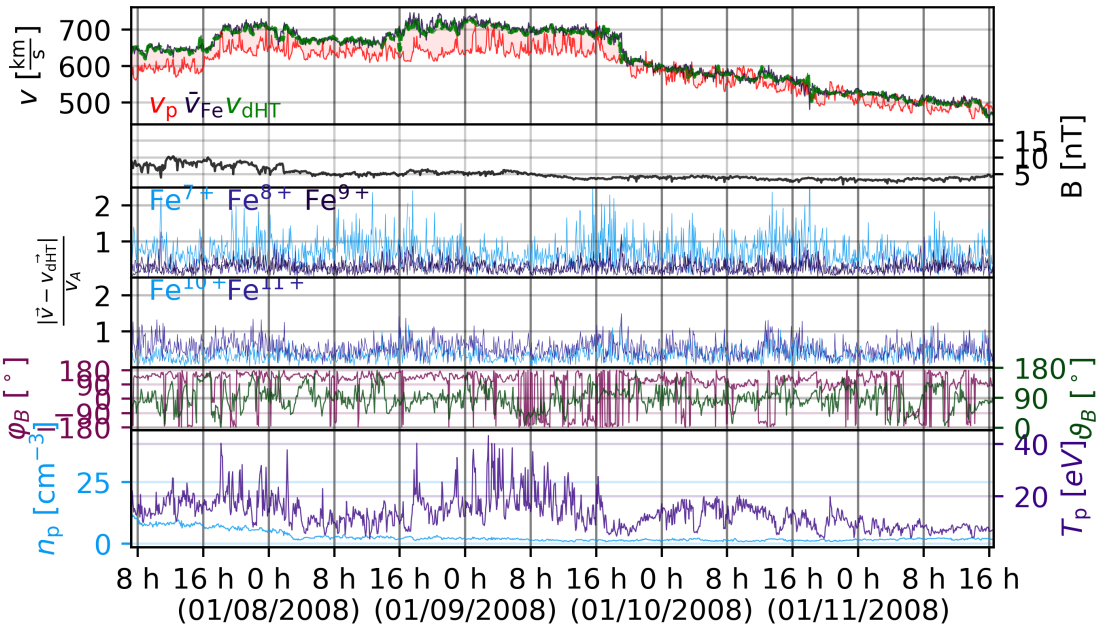

Figure 40: Time series of STEREO/PLASTIC proton and STEREO/MAG magnetic field observations. The x-axis corresponds to time and depicts date and time of day. Also, the same time interval is shown as in Fig. 39. Top panel: Proton velocity (red), Fe velocity averaged over the depicted charge states (very dark blue) and computed dHT velocity (green). The parameter dt was set to 30 min for computation. Second top panel: Absolute magnetic field. Third and fourth top panel: Absolute of the difference vector between the velocity of an Fe charge state and the dHT velocity divided by the Alfvénic velocity for the charge states Fe^{7+}, Fe^{8+}, Fe^{9+}, Fe^{10+} and Fe^{11+}. Fifth top panel: Azimuthal angle of the magnetic field (dark violet, left y-axis) and elevation angle of the magnetic field (green, right y-axis). Bottom panel: Proton density (light blue, left y-axis) and proton temperature (purple, right y-axis).

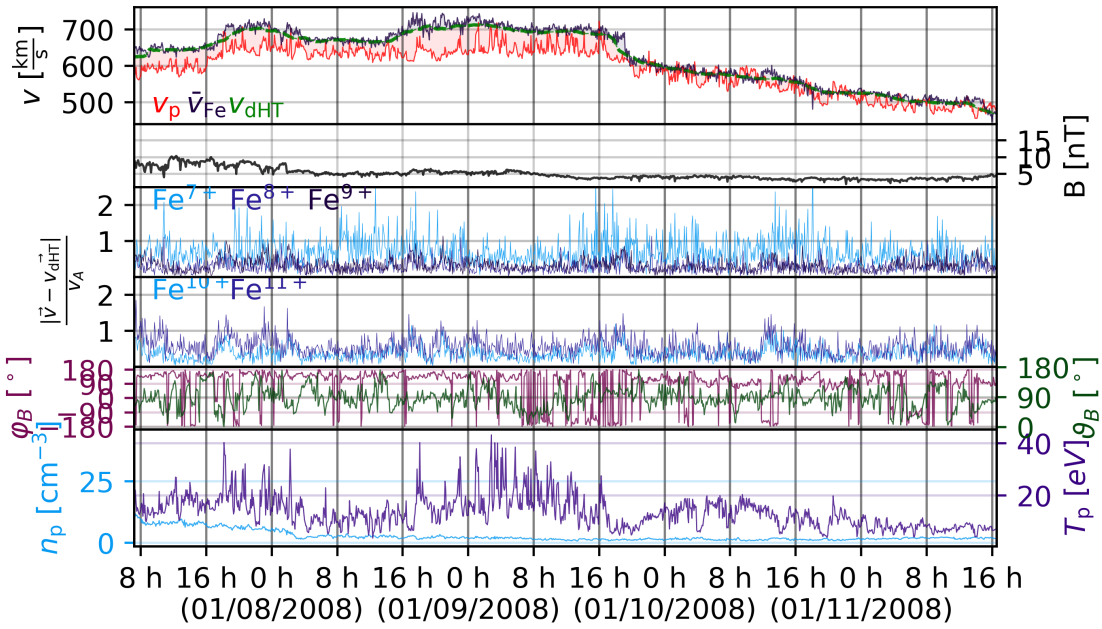

Figure 41: analogous to Fig. 40, but for $dt = 250$ min.

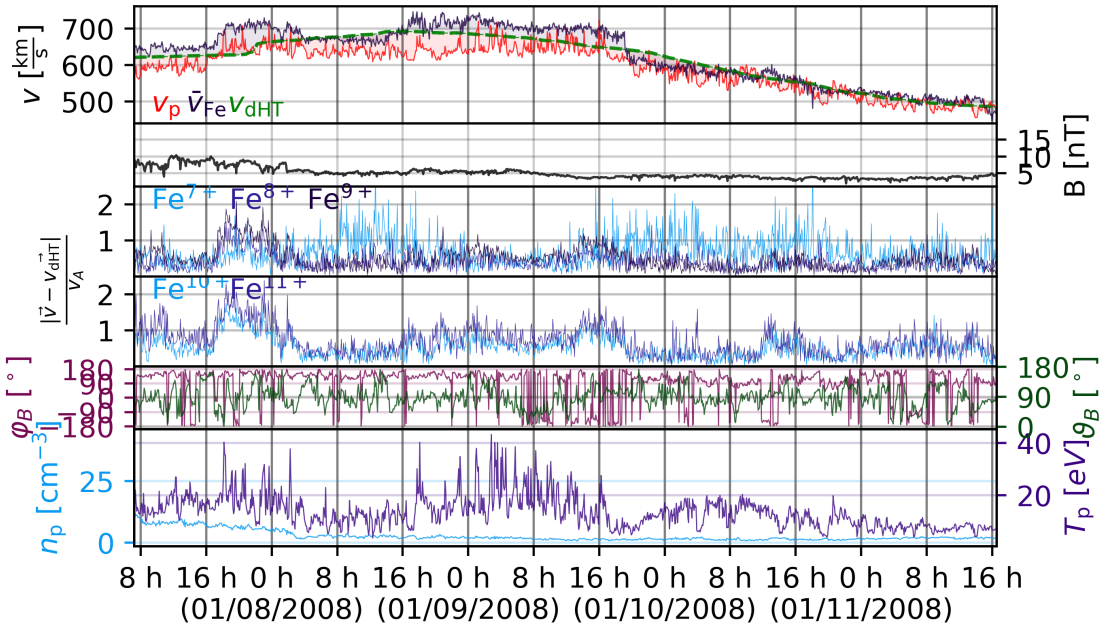

Figure 42: analogous to Fig. 40, but for $dt = 2500$ min.

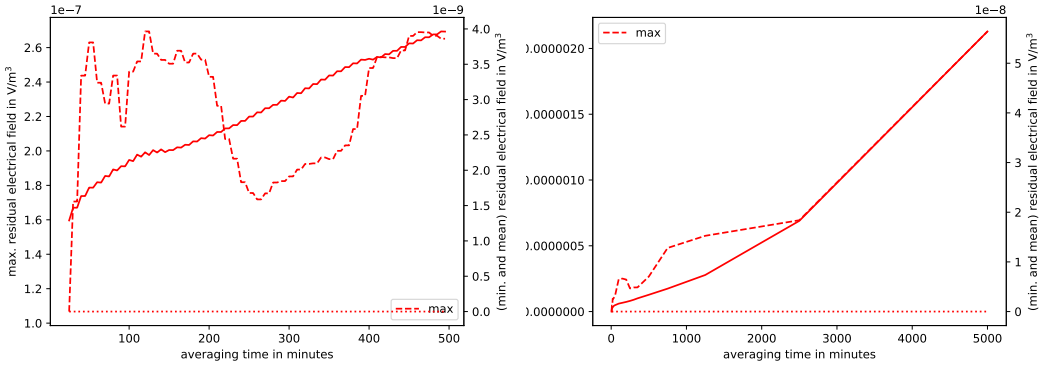

Figure 43: Maximum residual electric field (left y-axis, dashed), average residual electric field (right y-axis, solid line) and minimum residual electric field (right y-axis, dotted) as a function of the averaging time dt in minutes. The residual electric field is the $\vec{v}\times\vec{B}$ field which remains if the Fe-ions' velocities are transformed into the dHT velocity computed with the indicated averaging time. The right plot shows all averaging times which were considered and the left plot is a zoom into the interval of $dt \in [0, 500]$ min to show the trend of the residual electric field in more detail for these lower values of dt.

constraints.
Fig. 44 (left) shows histograms of the instrumental position bins, whereas in each of the 16 plots the data has been filtered for a certain section (S) and quadrant (Q) combination. Quadrant 0 is the only, in which the counts are continuously distributed amongst the position bins. Hence, this Quadrant contains the resistive anode. Therefore, it is likely the Quadrant in which SWS resides. However, SWS only makes up 45° of the 90° of a quadrant. The other part of the quadrant is likely WAPSSD. The reason for that conclusion is shown in Fig. 44 (right), where instead of position bins, the data is histogrammed for SSD energy channels. Quadrants 0 and 1 are the only, where data with data in SSD energies above 0 is found. Given, that the positional bins in Section 0 and Section 1 only span from 16 to 48 (with the exception of Position bin 0 in Section 0, which is likely reserved for errors) and lie therefore centrally within Quadrant 0, Sections 0 and 1 correspond to SWS (with one of which referencing the Main Channel and one the Small Channel). Section 2 spans over two quadrants and, in combination with having SSD energy information, is WAPSSD. The two empty position bins in Section 2 Quadrant 1 correspond to a blockage in the instrument.
The only remaining Section of the instrument is WAPNOSSD, which is linked to Section 3, since no SSD energy information is availabile in Section 3 and only discrete position bins (8 in total) are available.

To make an assessment of which of Section 0 or 1 is the Main Channel, in Fig. 45 histograms of instrumental energy per charge are shown, filtered for the Section flag. Whenever a threshold flux is reached as the instrument steps upwards in the energy per charge channels, the instrument switches from Main to Small Channel. Therefore it is expected to predominantly find events with high energy per charge channel numbers in the Small Channel and oppositely in the Main Channel. The first is the case for Section 1, which therefore is the Small Channel. The small number of counts in Section 0, which are found at high energy channels, are likely caused by times, when the Small channel did not switch.

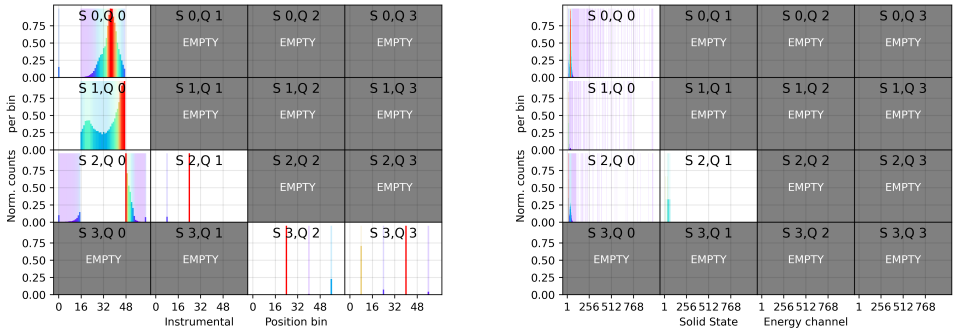

Figure 44: Matrices of histograms of instrumental position bin (left) and solid state energy channel (right). Both the left and right matrices of histograms are sorted in the same way: For each row, data is filtered for different sections of the instrument and for each column filtered by quadrant. This way, each histogram displays a different combination of section and quadrant.

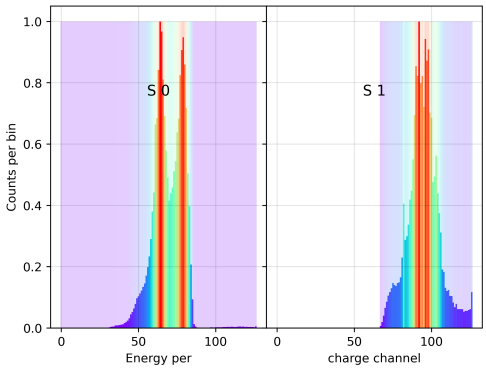

Figure 45: Histograms of energy per charge normalized to a histogram's respective maximum. The left histogram only considers data from the instrumental section labeled 0 and the right histogram only section 1 data.

4.3.1.i Comparison between triggered solid state detector pixel and instrumental position bin Since the solid state detector is the first step in the position detection of particles in SWS (release of secondary electrons upon impact, compare chapter 3.2), it is an interesting tracer of instrumental effects influencing the position detection of the resistive anode to investigate the position as determined by the resistive anode as a function of the solid state pixel the particle triggered. Of course, this analysis is only feasible for particles, which have actually triggered a signal in a solid state detector, so the instrumental response to doubles may vary.
Fig. 44 suggests, that the instrumental onboard algorithms assign Section and Quadrant information based on the triggered discrete or resistive anode. Since in quadrant 0 the resistive anode overlaps between WAPSSD and SWS, a potentially erroneous assignment arises from this. So, as a first assessment an analogous series of histograms is created, but with ssd pixel numbers

replacing the instrumental position bins (compare Fig. 46 (left)). From the SSD ID histograms of Section 2 Quadrant 0 it becomes apparent, that events from SSD pixels, which do not belong there, accumulate count rates. Apart from being caused by events from the solar wind sector detected by the resistive anode at a position belonging to WAPSSD and then being misassigned, this may also be a sign of the instrumental trigger logic not working correctly.
To remedy that assumption, a new sector flag is introduced, which is based on the SSD Pixel (where applicable) by an algorithm outlined by a flow diagram in Fig. 47 and the SSD IDs are histogrammed per Section based on the Pixel IDs in Fig. 46 (right). Apparently, the SSD Pixels are not misassigned within this Scheme. However, as seen in Fig. 48, the instrumental position bins do not exactly correlate anymore with their expected Section, if the Section is assigned based on the SSD Pixel ID, which has to be kept in mind. The right part of Fig. 48 suggests, that most misassigned events occur close to the boundary between SWS and WAPSSD. Especially, most misassigned events occur on the WAPSSD side of that boundary, which can be attributed to particles from the SWS (the part of the instrument, where most counts are expected), scattering or triggering a signal in the resistive anode, which is skewed by statistical error and therefore being assigned by the instrument to WAPSSD.

In order to obtain a measure of uncertainty of the position detection within the resistive anode, the instrumental position bins triggered by events occurring in individual SSD pixels within the solar wind sector are histogrammed individually. The result, which is shown in Fig. 49 has to be interpreted with care, since for the SSD pixels at the edge of the aperture of SWS the profile of counts per position bins may be skewed by scattering at the aperture. This is seen especially well within the curve of Pixel 7, which shows an excursion at position bin 48, which actually accumulates more counts, than at the nominal position of that SSD pixel. A similar, but less pronounced excursion occurs at pixel 6.
Also, each SSD pixel has a width of 5.5° in azimuthal space, which means, that it is expected, that the profile has at least that width. Each SSD pixel's histogram is shifted, so that their respective maxima line up, an average profile is created, for which the SSD pixels 1, 7 and 8 are disregarded. This profile has a width of 7 positional bins as observed by the full width at half maximum. Since a single SSD Pixel nominally observes 1.40625° of azimuth (disregarding scattering), in total a width of 9.84375° or $\sim 10°$ is found. The obtained curve can be seen as a superposition of individual scattering processes, for which the expectation value is shifted within a range of 5.5°. However, unfolding these while the underlying distribution is unknown, in order to obtain a more exact error estimation is not needed for this work, since known systematic errors exceed this error, and may not be possible without more knowledge about the resistive anode. Yet, this assertion shows, that the distributions significantly exceeds the SSD pixels width of 5.5° and hints towards a statistical error of at least $\sim 5°$ for the position determination within the resistive anode.

4.3.2 One dimensional transformed w spectra in the context of azimuthal position

Employing the He^+ data extracted from STEREO A/PLASTIC PHAs as described in the foregoing chapter, these findings have been qualitatively reproduced. In Fig. 50 two dimensional histograms of ϖ_{SWp} (which is the transformed w w.r.t. the 1d maxwellian proton fits from the STEREO science center) and ecliptic longitude φ_{ecl} are shown. Both panels contain data from the years 2008 to 2020. All PHA events have been scaled in their intensity employing priority rate weighting and the data is limited to WAP and SWS. In the left plot, the color scale is normalized to the maximum of the whole histogram, so that the count rates between each bin can

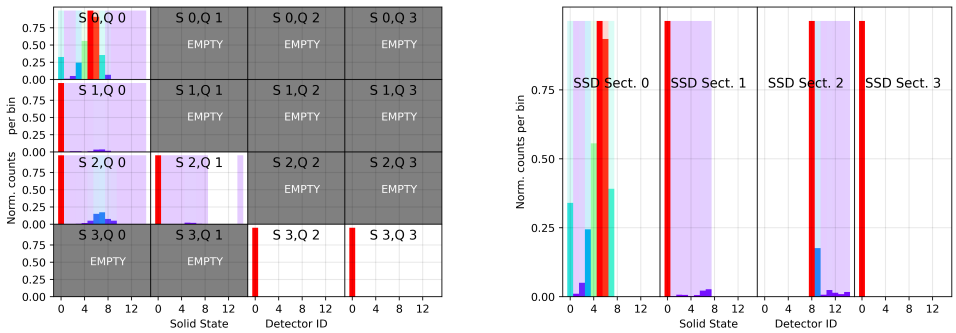

Figure 46: Left plot: Analogous matrix of histograms to Fig. 44. Here, the ID of a solid state detector is histogrammed. Right plot: Four histograms of solid state detector ID, where each histogram only considers data from a different of the four SSD sections where SSD section is a data product derived from instrumental quantities with an algorithm outlined in Fig. 47.

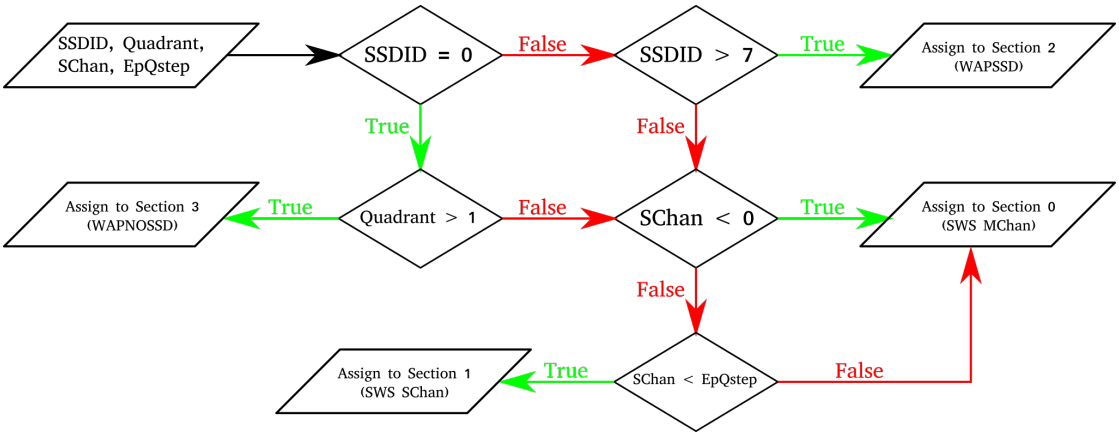

Figure 47: Flow chart which displays the algorithm to derive the data product SSD Section from SSD ID, quadrant, small channel occurrence and energy per charge step information.

be compared. Expected focusing cone and crescent directions are plotted through white dashed lines. In the expected direction of the focusing cone, a distinct density maximum is visible, which can be attributed to the focusing cone. To the ϖ_{SWp} spectra it is stated, that the velocity ranges within the expectation, that PUIs should roughly reside within $\varpi_{SW} \in [0, 1]$. However, not necessarily all data depicted within the histogram are PUIs. The He^+ filter does not filter for PUIs or no PUIs. Rather, it filters for mass per charge. Therefore the density increase at lower ϖ_{SW} values can also be attributed to differentially streaming SW He^+ or different SW particles leaking into the filtered range. The closer the particle velocity is to the indicator of the SW velocity, the more likely the particle may not be a PUI. Also, since the VDF of inner source PUIs is expected to significantly deviate from the VDF of interstellar PUIs, i.e. to reside at significantly lower velocities. So also inner sources PUIs may partly be a cause of that density increase. At higher ϖ_{SWp} values (around ~ 1) a point is reached, where the counts per bin

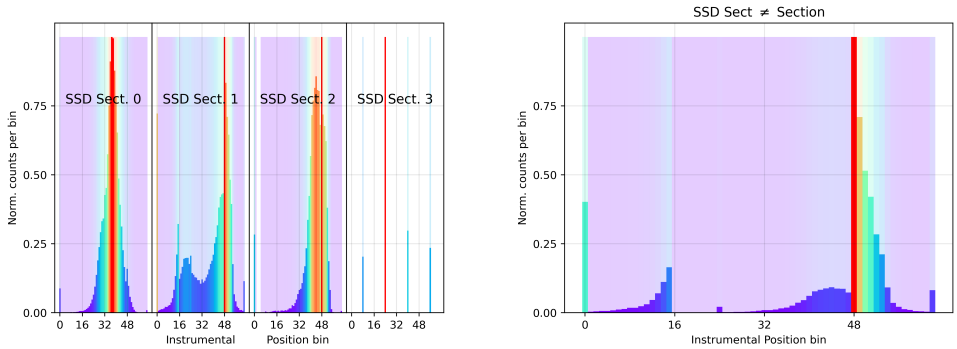

Figure 48: Left: Four histograms of instrumental position bin where each histogram only considers data from a different of the four SSD sections, where SSD section is a data product derived from instrumental quantities with an algorithm outlined in Fig. 47. Right: Histogram of instrumental position bin, where only events are considered for which the SSD section data product is not equal to the instrumental section provided by the original data.

rapidly decline with increasing ϖ_{SWp}, which is typical for interstellar PUIs. This point of rapid decrease is called the PUI velocity cutoff.
To visually investigate the He^+ PUI cutoff, in the right panel each pixel of the histogram is normalized to the vertical maximum. Also, the data has been limited to $\varpi_{SWp} > 0.5$ in the right panel to decrease the probability of SW particles overlaying with the PUI data. The longitudinal trend of the PUI cutoff in Fig. 50 qualitatively matches the expectations of Möbius et al. [2015], Lee et al. [2015], Keilbach et al. [2016], Taut et al. [2018].

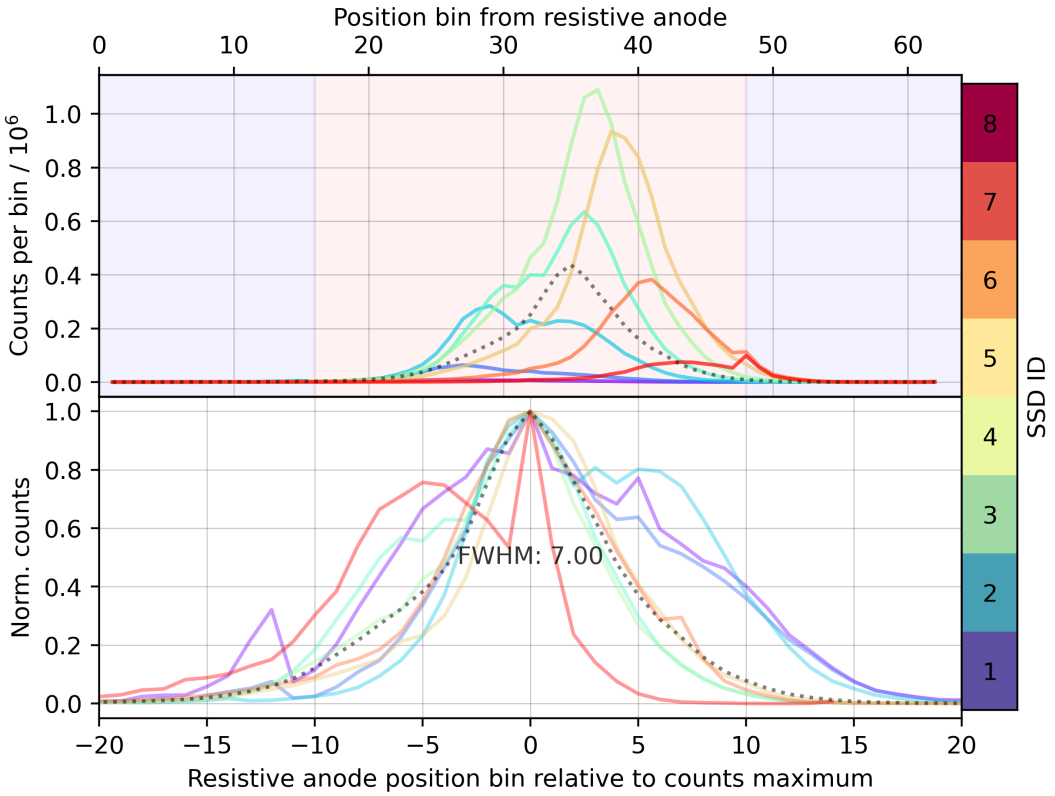

Figure 49: Histograms of resistive anode position, where each differently colored histogram corresponds to data filtered for a respective SSD ID which is indicated by the color key provided in the right bar. In the top plot, the histograms are not normalized and not aligned to each other in terms of their maximum. So, the actual distribution of positions measured by the resistive anode is visible with the x-axis indicating the instrumental bins of position on the top. In the bottom plot, each histogram is normalized to its respective maximum and the coordinate system on the corresponding x-axis on the bottom is distance in instrumental position bins from the histograms' respective maxima. A dotted line indicates the average histogram (with the exception of SSD ID 8) for which a full width at half maximum of 7 bins is found.

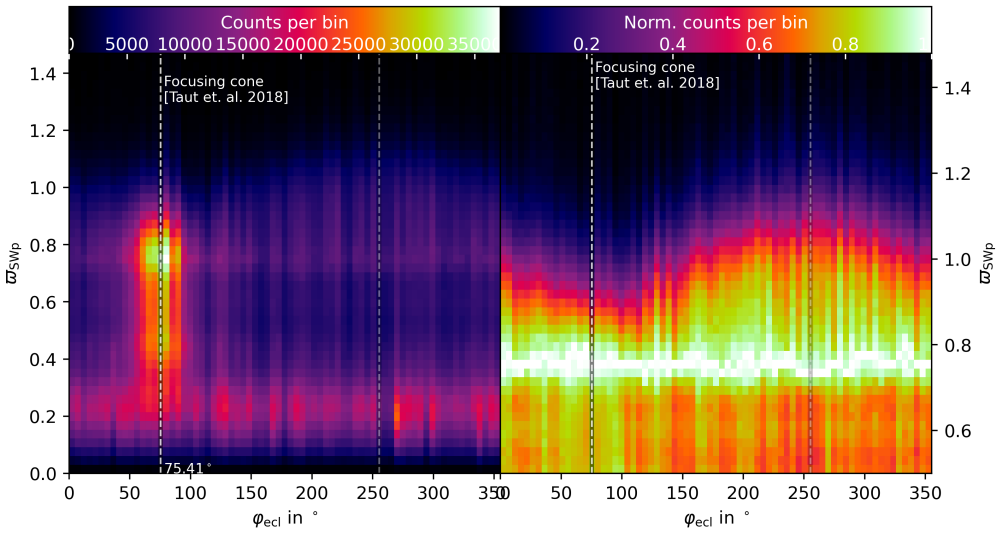

Figure 50: Two dimensional plots of ϖ_{SWp} as a function of the ecliptic longitude for He^+ PHAs. In the left histogram priority weighted counts per bin are shown and in the right plot the histograms are normalized to each φ_{ecl}-slice. The location of the focusing cone according to Taut et al. [2018] is indicated by a strongly visible white dashed line. The according location of the crescent is indicated by a less opaque white dashed line.

5 Signatures of the He^+ pickup ion torus in three dimensional velocity distribution functions observed with STEREO / PLASTIC

The He^+-filtered PHA events of STEREO/PLASTIC allow for the observation of three dimensional PUI velocity distribution functions, which are presented in this section. The presentation of the observations starts with an overview over the whole instrumental FOV. However, since the data from WAP hints towards major problems within the instrument and since Solar Wind Sector (SWS) is the only section equipped with an azimuthal filtering system, afterwards the observation is limited to SWS. Then three dimensional He^+ VDFs are presented followed by a discussion which stresses a probable instrumental effect which probably influences the observed distributions which is not yet fully understood. Hence, strategies to mitigate this effect are presented.
Since the spacecraft was rolled during 2015 [Kucera [2015]], in the following, only data from 2008 to the end of 2014 is considered.

5.1 Two dimensional projections of the He^+ pickup ion velocity distribution function

To obtain an overview of the He^+ ion incidents from different directions into the instrument, two dimensional projections of the He^+ PUIs are accumulated over the instrument's complete azimuthal FOV.
As an overview, Fig. 51 shows a histogram of He^+ PHAs as they incident into PLASTIC's aperture. The azimuthal bins were chosen such that the instrumental position bins are matched. Analogously, the instrumental energy per charge steps are matched by the velocity binning. Alongside that plot, Fig. 51 depicts an overview of the solar wind conditions and magnetic field angle configurations during the selected time period. In SWS, only data was included for which the instrumental deflection accepted ions within $\pm 3°$ within the ecliptic plane for a comparison of SWS and WAP, so that the nominal elevation angle acceptance of WAP is matched. Also small channel data was disregarded.
While the events within SWS appear to be smoothly shaped, the data within WAP is observed with a jumpy and irregular behavior. Some of the discontinuities within the WAP are explainable by blockages in the instrument and on the spacecraft. However, the theoretically unblocked bins also show an unexpected discountinuous behavior.
In Figs. 52 and 53 the magnetic field has been limited to $\pm 10°$ out of the ecliptic plane and to azimuthal angles of $\pm 10°$ around $90°$ and $-90°$, respectively. In combination with Fig. 51 one deduces from these that mainly two pixels within the WAP section exhibit statistically meaningful signals. The other not blocked pixels within WAP only acquire very low count rates and are strongly affected by noise. This unexpected behavior is not dependent on the magnetic field orientation (in addition to the shown configurations this has been checked with a variety of magnetic field configurations).
Another interesting point is the range of the observed velocity as a function of the maximum proton bulk velocity. Here, the upper limit of the proton bulk velocity is the upper boundary of

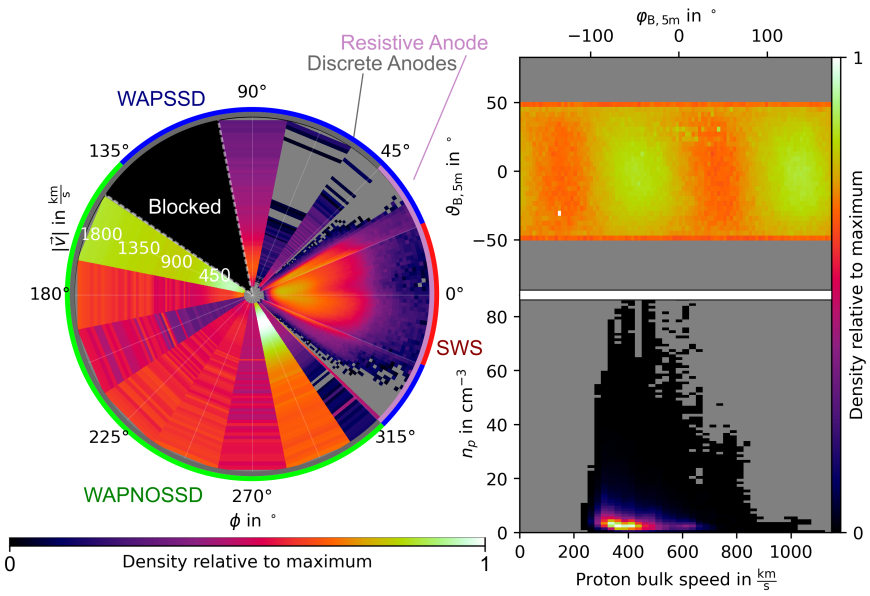

Figure 51: Left: Azimuthal angular distribution of He^+ PHAs as a function of absolute velocities in the instrument frame accumulated from 2008 to 2015. Colored circles around the plot indicate, to which parts of the instrument the angular bins belong: Red for SWS, green for WAPNOSSD and blue for WAPSSD as well as gray for bins from discrete anodes and purple for the resistive anode. The right plots which display the occurrences of magnetic field azimuthal vs. elevation angles (top) and proton bulk speed vs. proton density (bottom) not only indicate the different conditions in the SW during that time, but are also deemed to indicate the selection of data: The respective coordinate limits of the axes display, to which angles, densities and bulk speeds the data was limited before accumulation. In comparison to Figs. 52 and 53 here, all data is selected. However, in the other two analogous figures the data is limited to different sets of parameters.

the x-axis of Fig. 51 which is the maximum observed velocity by PLASTIC during the period this work analyzes. Within the aperture of SWS the events with relative densities exceeding ~ 0.5 are contained within a factor of ~ 2 of the upper limit of the proton bulk velocity. In the pixels of WAP, which show a significantly high number of counts a relative density of ~ 0.5 is the number of background counts, however densities above ~ 0.75 are in these pixels also only observed within the boundary of about twice the maximum proton bulk velocity. In the other WAP pixels such a clear trend with the proton bulk velocity is not observed against expectation.

5.2 Probable causes for the unexpected behavior of the WAP pixels

If WAP data is omitted, only 45° of the instruments azimuthal FOV remain for observation. Hence, before the data from that part of the instrument is dismissed, probable causes for the unexpected behavior of the pixels are discussed. Especially the question arises whether unknown deficiencies hinder all but two pixels from observing count rates as high as the other pixels or

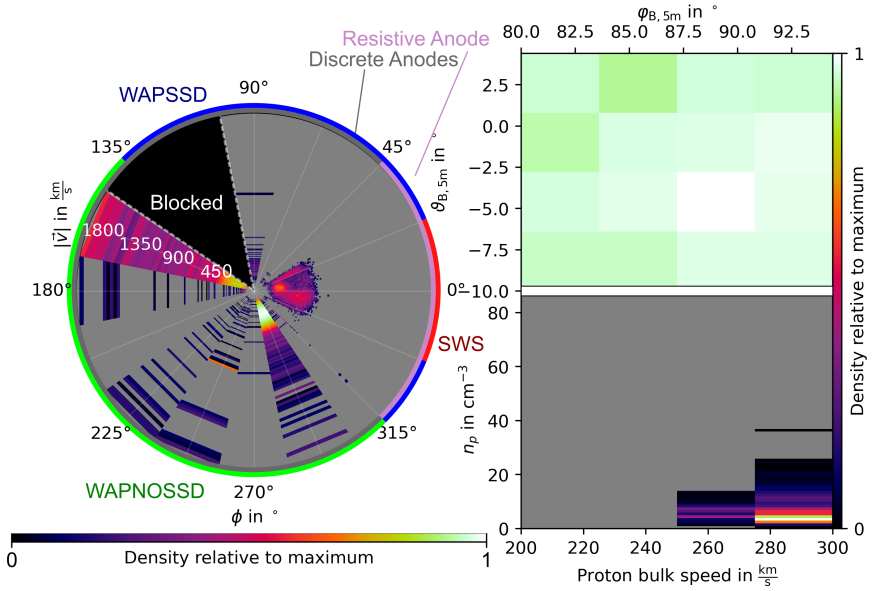

Figure 52: Analogous figure to Fig. 51 with a different set of limiting parameters. The limits in ϕ_B, ϑ_B, n_p and proton bulk speed are represented by the right plots' axis limits. In addition, the azimuthal angles of particle incidence are limited to $\pm 10°$ around the ecliptic plane.

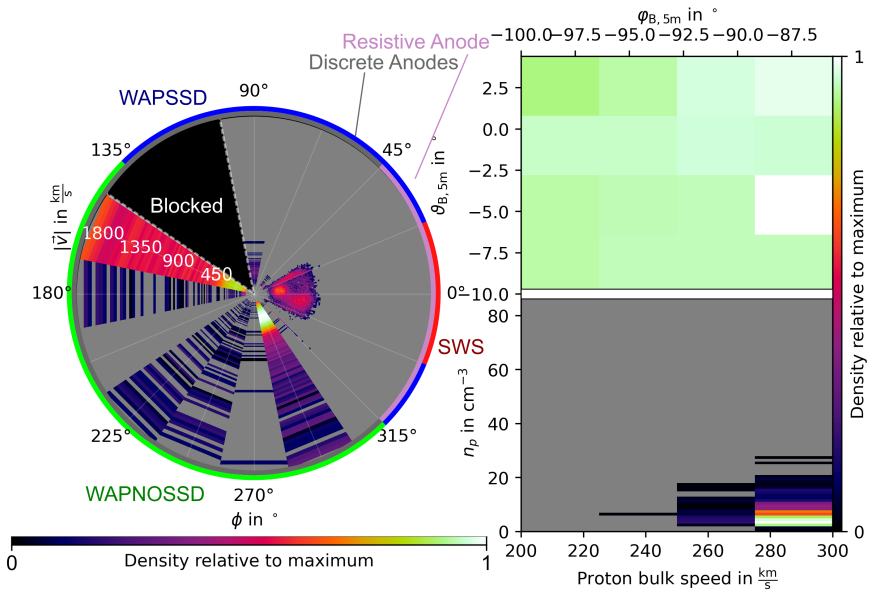

Figure 53: Analogous figure to Fig. 52 with a different set of limiting parameters.

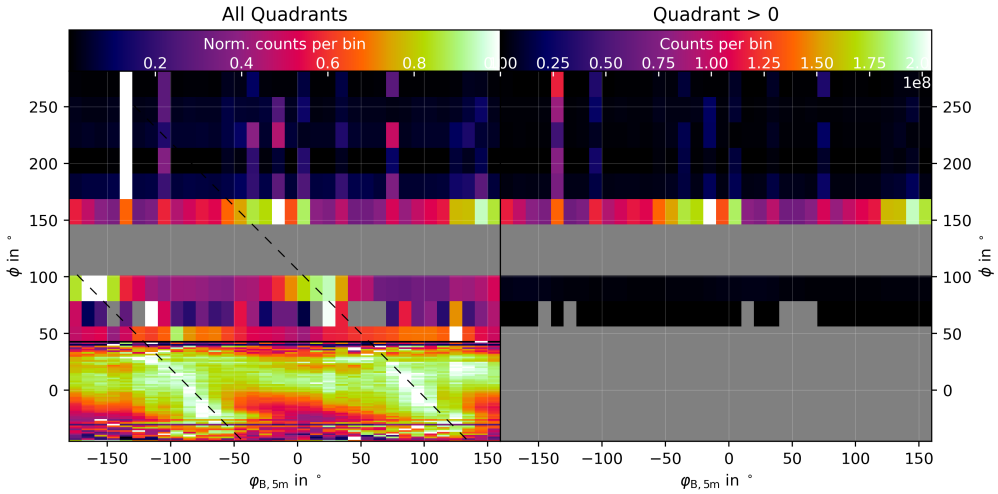

Figure 54: Histograms of He^+ PHAs as a function of magnetic field azimuthal angle and azimuthal angle of a particles velocity. The ϕ bins have been chosen such, that each bin corresponds to one instrumental position bin. In the left plot, all Quadrants of the instrument are shown and the histogram is normalized to the maximum of each ϕ-slice. In the right plot, Quadrant 0 is omitted to make the relations between the instrumental position bins more visible. For both histograms, each contributing event has been weighted according to appendix B.2.1. For the histograms, data between 2008 and 2015 has been accumulated.

vice versa. The first case would mean that only two pixels exhibit meaningful data. The latter case implies that all but two pixels exhibit meaningful data, but unfortunately lack statistical significance. Of course it is also a possibility that both groups of pixels may not work as intended. The pixel within WAPSSD, for which the count rates are maximal, lies within Quadrant 1 and is situated next to a blockage of the instrument caused by a solar panel on the spacecraft. Hence it is conceivable, that the particles incidenting into that pixel are actually SW deflected from the solar panel. Upon impact on the solar panel the particles are expected to be stripped of charge. The depicted data is already filtered for He^+ PHAs. So parts of the He^+ events within that data set may originate from deflected He^{2+}, if deflection of the SW on the solar panels occurs.

To investigate this hypothesis, the He^+ PHA counts as a function of magnetic field orientation are investigated. Since parts of the VDF of particles in the SW are expected to change as a function of the magnetic field orientation (compare Chapter 2.1), in normally working pixels a functional dependence of densities and velocities of the orientation of the magnetic field orientation is expected. In Fig. 54 the count rates within each instrumental position bin are histogrammed w.r.t. the magnetic field azimuthal angle. The elevation angle of the magnetic field is limited to $\pm 10°$ of the ecliptic plane. In the lower part of the plot quadrant 0 is situated with the resistive anode, which divides the quadrant into finer bins than the other quadrants. Again, independent of the magnetic field orientation, the pixels within WAP vary significantly in count rates. However, a magnetic field dependency is visible in the behavior of the count rates in the pixels with high statistics. In SWS, the He^+ PHAs exhibit two distinct enhancements in count rates which reach $\phi \sim 0°$ at $\varphi_{B,5m} \sim \pm 90°$. These distinct enhancements follow the magnetic field (the enhancements are indicated by the black dashed lines, which have been

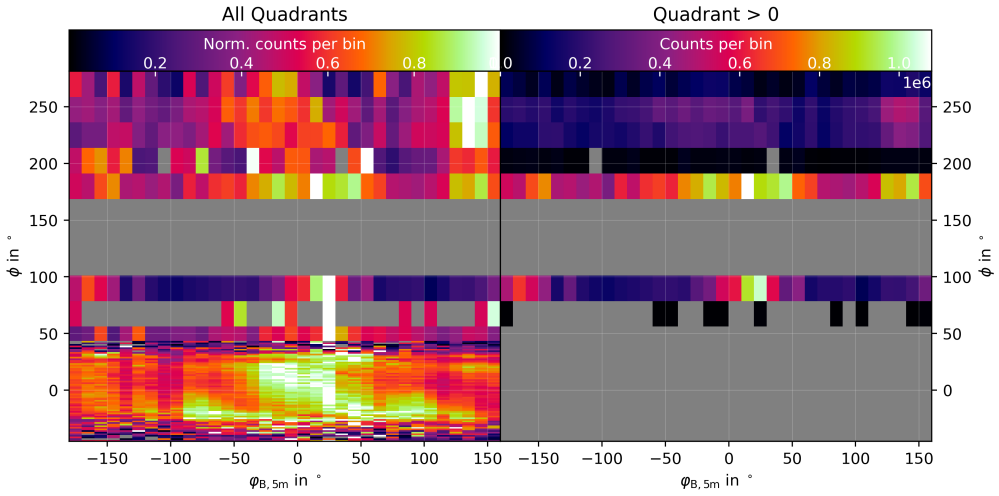

Figure 55: analogous plot to Fig. 54, but for 2008 only.

drawn by eye and only serve to guide the eye). Within the pixels with better statistics (at $\phi \sim 90°$ and $\phi \sim 150°$ especially), count enhancements are visible which follow the trend of the enhancements within SWS. In Quadrant 3 the PHA counts seem to be independent of the magnetic field orientation or are observed with too few counts to obtain a statistically meaningful sample. Interestingly, as indicated by Fig. 55, more counts are found within the pixels of Quadrant 3 in 2008 and two of the pixels even roughly extend the density enhancements, which follow the magnetic field orientation, but not very clearly. The very small count rates in these pixels as seen from comparison with Fig. 54 start earliest in 2009 and then continue at low levels.

If the enhanced count rates within some of WAPs pixels were reflected SW originating from the Maxwellian Core of the SW VDF, then it were expected that they would not follow the magnetic field direction. However, if originating from the Beam distribution, a functionality of the magnetic field orientation were expected. Then, beam particles might still contribute to density enhancements, since it is conceivable that the magnetic field is at times oriented such, that Beam particles incident into the pixel's aperture without modification of their trajectories. Yet, these should not occur significantly, since He^{2+} makes up the major fraction over He^+ in the SW. However, also at directions, where deflections of He^{2+} SW particles incident into the aperture, He^+ enhancements were expected since at the deflection at the solar panels, He^{2+} loses charge and becomes He^+. Fig. 54 does not support deflection or direct incident of He^{2+}. Rather, the He^+ events in the two WAP pixels with most statistics follow the magnetic field direction dependent density enhancements which are also visible within SWS. Yet, it is noteworthy that due to a large number of background counts it can not be discounted, that at least some particles also incident the aperture after deflection. However it can be discounted, that the distinctly higher count rates within some of WAPs pixel originate from deflection at the solar panels. Rather, the data point towards the hypothesis that the pixels with lower count rates are affected by an unknown defect which renders the pixels almost inoperative.

This hypothesis is also supported by Fig. 56 where the He^+ PHAs are histogrammed in energy per charge vs. azimuthal magnetic field orientation, again with an elevation angle of the

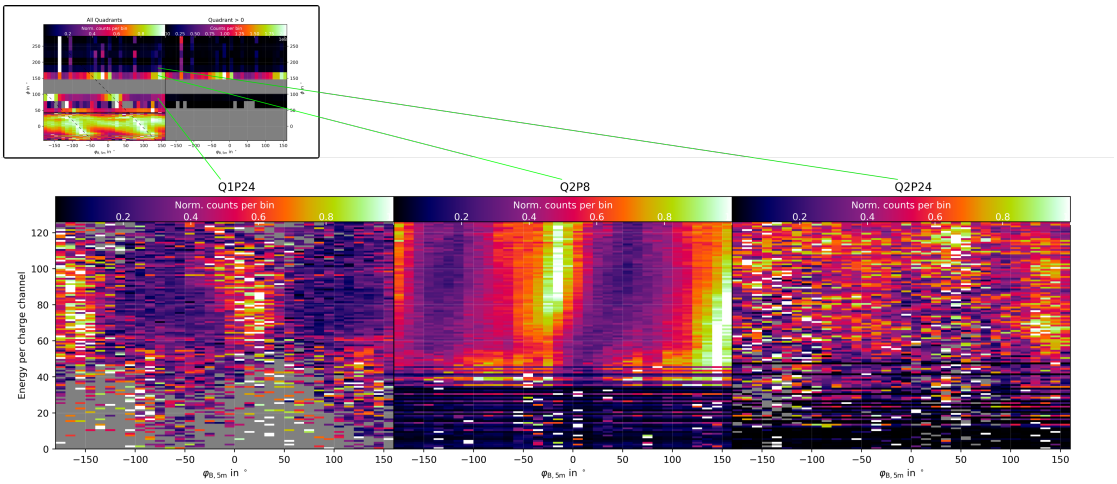

Figure 56: Histograms of He^+ PHAs as a function of magnetic field azimuthal angle and instrumental energy per charge channel. The three plots correspond to three instrumental position bins. For both histograms, each contributing event has been weighted according to appendix B.2.1. For the histograms, data between 2008 and 2015 has been accumulated.

magnetic field limited to ±10° of the ecliptic plane. While the left and and the middle panel show the events of a pixel within WAP which exhibits relatively high statistics, the right panel shows events of a pixel with low count rates. While distinct patterns are followed by the events within the first two, the right plot is dominated by noise.

It is not known what is the reason why some of the pixels of WAP show more meaningful patterns. However, for future studies it would be worthwhile to investigate these pixels further, since these few pixels may still contribute to the total FOV of PUI studies. However, it is unlikely, that meaningful data is found from the other pixels of WAP. Whether this is due to a blockage within the instrument or efficiency problems within the instrument detection, is unknown. Also the priority rate scheme and the resulting selection of events which the DPU sends may be faulty. In SWS, the scheme is different from WAP [Galvin et al. [2008]]. So it is conceivable that it works within SWS while it is faulty in WAP. Finally, some pixels of WAP share a two-pixel wide aperture, while others have their own aperture. Maybe, scattering at the aperture causes some pixels to be less exposed than others. However, no clear correlation between the aperture width and the count statistics of the pixels in WAP has been found.
For the moment, the most meaningful way of proceeding is to limit the observations of this study to SWS.

5.3 Three dimensional He^+ pickup ion velocity distribution functions observed within the Solar Wind Sector

The determination of directionally resolved ϖ_{REF}-spectra in any frame of reference is a non-trivial undertaking, since the instrument resolves incoming ions by their energy per charge which scales with their total velocity. The direction is resolved in angular bins. So all measured events cover a section of a ring (two dimensions) or a volume best described as a square section of a hollow sphere with a wall-thickness of non-zero (whereas, the square is seen in angular space). The origin of the observed velocities lies within the frame of the spacecraft's motion, which implies a computationally expensive transformation of the instrumental bins in order to derive ϖ histograms. In addition, a bin in both w and ϖ space is not constant in v space (and therefore also not in the instrumental energy per charge space) since the reference velocity (e.g. the SW velocity) varies over time. The following describes the methods employed by this work to obtain these w and ϖ histograms, discusses simplifications for special cases and their limits. Special emphasis is provided on the instrumental resolution and its implications on the analysis methods.

5.3.1 Theoretical considerations for histograms of w and φ in the special case of a radial reference velocity

The problem behind the transformation of an instrumental energy and direction bin into ϖ-space is sketched in fig. 57A. For each bin in ϖ-space all instrumental bins falling into that bin must be investigated for their contribution to the bin which is proportional to the fraction of velocity space volume that both bins intersect with the area of the instrumental bin. Computing these areas is computationally expensive.

In the special case that the reference velocity $\vec{v}_{\mathrm{REF}}$ is radial and that the spacecraft's velocity is neglected, the incoming angles (azimuthal and ecliptical) of a particle's velocity are the same in v space as well as in w_{REF}-space. This means that an angular bin in v-space is directly translated into the same angular volume in w_{REF}-space. With these assumptions the problem of Fig. 57A becomes effectively one-dimensional as sketched in the B-panels of Fig. 57, if the following simplification is applied: Instead of binning the events in (ϖ_r,ϖ_t)-space, the events are binned in (φ, w)-space. Afterwards the bins are transformed into (w_r, w_t)-space and then moved by -1 in w_r direction to effectively obtain an instrumental grid in (ϖ_r, ϖ_t)-space. Especially the simple shift by -1 only yields a meaningful result, if the reference velocity always points in radial direction. Otherwise, such a shift has to compensate for each event for the direction of the reference frame velocity.
For computation from the instrumental bins, in the outlined simplified case, a absolute velocity and a direction information is required. As bins in φ the instrumental position bins are employed. As for the bins in w-space, obtaining a guideline for the binning from the instrumental bins is more difficult, since w not only scales with the particle but also with the reference velocity. The consequence is depicted in fig. 57B2. If the reference velocity is sufficiently fast, an instrumental velocity bin might fall completely into just one bin, but for slower reference velocities, an instrumental velocity bin usually spans over several bins or only one bin. To keep a constant binning while accounting for the instrumental resolution, algorithm 2 is employed to histograms in w-space. There is one caveat to the method, which is that the method does not account for the uncertainty in reference velocity.
In the algorithm, the relation of the area in which the instrumental bin intersects with the input bin to the total area of the instrumental bin is computed. Defining w_0^* and w_1^* as the extents of the instrumental bins, Δw as the desired bin width and w_0 as the lower edge of the first bin, the total area of an instrumental bin residing within the directional angles φ_0 and φ_1 is a section of

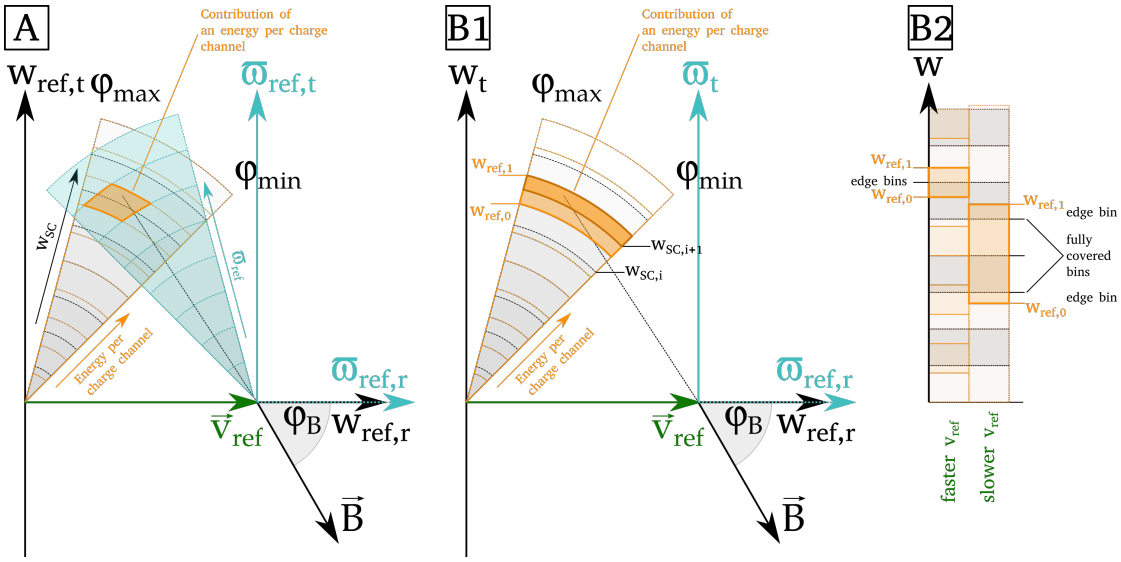

Figure 57: Panel A: The instrument measures particle velocity in terms of their energy per charge which corresponds to total velocity in the spacecraft frame. In a coordinate system with the spacecraft velocity as origin, contours of constant energy per charge are concentric circles. So a bin of energy per charge is in velocity space represented by the area between a circle and the next. Also, the instrument resolves particles by incoming direction. In a two-dimensional simplification, this can be represented by a minimum and a maximum azimuthal acceptance angle ϖ_{min} and ϖ_{max}. Here, the isocontours of constant energy per charge are dotted in orange and limited by these acceptance angles. Since contours of constant velocity are similarly shaped, w_{SC} (dotted in black) is readily available. However, the contribution of an energy per charge bin to a bin in ϖ_{REF} is less trivial: An analogous velocity space element to the element of a w_{SC}-bin is also the section of a ring, but with the central point of the circles which constitute the ring shifted by the velocity of the reference frame. This creates an irregularly shaped area in velocity space for the contribution of an energy per charge bin to a bin in ϖ_{REF} (marked in solid orange). Also, multiple energy per charge bins can contribute to a bin in ϖ_{REF}. Panel B1: Analogous to Panel A, but without an overview of velocity space elements of ϖ_{REF}. Instead, in solid orange a bin of w_{REF} is shown. For a bin in w_{REF}, a single or multiple energy per charge channels can contribute. However, other than for ϖ_{REF}, the velocity space volumes of contribution are always concentric regular rings. Panel B2: Reduction of the transition from energy per charge or, analogously w_{SC} bins to w_{REF} bins for two example values of v_{REF}.

a ring and therefore given by

$$A_{instrbin} = \frac{w_1^{*2} - w_0^{*2}}{2}(\varphi_1 - \varphi_0) \ . \tag{83}$$

Here, φ_0 and φ_1 are in radians. For the i-th bin of the histogram which is to be obtained the lower edge of the area of intersection between the instrumental bin and the histogram bin is derived from $\max(\{w_0^*, w_0 + i \cdot \Delta w\})$ and the upper edge from $\min(\{w_1^*, w_0 + (i+1) \cdot \Delta w\})$. So the histogram weights to the contribution of each particle to the i-th bin is

$$\frac{A_{intersection}}{A_{instrbin}} = \frac{(\min(\{w_1^*, w_0 + (i+1) \cdot \Delta w\}))^2 - (\max(\{w_0^*, w_0 + i \cdot \Delta w\}))^2}{w_1^{*2} - w_0^{*2}} \ , \text{ if} \tag{84}$$

the instrumental bin lies (at least partially) within the i-th bin. If not, the numerator is negative. If the instrumental bin resides completely within the i-th bin, the denominator simplifies to $w_1^{*2} - w_0^{*2}$ and the total weight is 1. If the i-th bin is completely within the instrumental bin, the denominator simplifies to the difference of the squared bin edges. There is a lower boundary

Algorithm 2 Histogram routine respecting instrumental uncertainty in w space.

1: **Input:**particle velocities v, uncertainty of particle velocities Δv, reference frame velocities v_a
2: It is assumed, that v, Δv and v_a are arrays
3: **Input:**lower edge of first bin in w space w_0, width of bins Δw
4: For each element of the arrays: $w_0^* \leftarrow \frac{v}{v_a}$
5: For each element of the arrays: $w_1^* \leftarrow \frac{v+\Delta v}{v_a}$
6: Determine the bins, where each w_0^* and each w_1^* reside, name these i_0 and i_1.
7: Histogram all values of w_0^* with the given binning. Compute histogram weights according to eq. 84. Store the result into h.
8: analogously histogram all values of w_1^* and add the result to h.
9: Compute the number of bins between i_0 and i_1, namely Δi.
10: **for** i in $[1, \max(\Delta i) - 1[\cap \mathbb{Z}$ **do**
11: Find a subset of the values of Δi, where $\Delta i < i$ applies. Employ the following action only for values of i_0 corresponding to that subset.
12: Histogram $w_0 + (i_0 + i) * \Delta w$ with the weights corresponding to the area of the $(i_0 + i)$-th bin divided by the total area defined by instrumental bin boundaries.
Output:h

for Δv which is based on the measurement principle of the instrument. Since particle velocity is determined from either the energy-per-charge steps or time-of-flight steps of the instrument, the minimum meaningful value for Δv (and Δw, consecutively) is fixed by the distance between instrumental steps.

5.3.2 Generalization of the histogram method for generalized reference velocity directions

This work is interested in accumulating histograms in (ϖ_x,ϖ_y)-space. To achieve this while acknowledging the probabilistic width of an event, the volume each particle covers in (v,φ)-space is rasterized. Afterwards each point on that grid is transformed into the reference frame and histogrammed. In detail, to obtain the (ϖ_x,ϖ_y)-coordinates i-th raster point in a raster of N^2 points of a PHA event coming from the direction φ with the absolute velocity v, first w_a is

derived and based on the instrumental velocity acceptance Δv the acceptance in w_a, which is Δw_a. This, together with the angular acceptance $\Delta\varphi$ leads to the computation of the location of the i-th raster point in (w_a,φ)-space, namely

$$\varphi_i = \left(\varphi - \frac{\Delta\varphi}{2}\right) + \Delta\varphi \cdot \frac{i \mathrm{mod} N}{N} \tag{85}$$

$$w_{a,i} = \left(w_a - \frac{\Delta w_a}{2}\right) + \Delta w_a \cdot \frac{\left\lfloor \frac{i}{N} \right\rfloor}{N} \ . \tag{86}$$

The resulting coordinates in (ϖ_x,ϖ_y)-space are

$$\varpi_{x,i} = w_{a,i}\cos(\varphi_i) - \frac{v_{a,x}}{v_a} \tag{87}$$

$$\varpi_{y,i} = w_{a,i}\sin(\varphi_i) - \frac{v_{a,y}}{v_a} \ . \tag{88}$$

$$\tag{89}$$

This method is computationally more demanding, as for each event the number of grid points is histogrammed, yet it is flexible enough to fit to any given geometry.

There is still a caveat to this method which is that this method orthogonally projects all events into the plane, regardless of their value in φ_z direction. This makes the interpretation of the resulting histograms challenging.
Detrimental to the signal to noise ratio, but concerning the three-dimensionality of the problem probably more suited is the generalization of the approach to three dimensions. For this, the instrumental height angle ϑ and the instrumental acceptance in height angle $\Delta\vartheta$ are employed and the two dimensional grid in (w_a,φ)-space is replaced by a three dimensional grid in (w_a,φ,ϑ)-space via

$$\varphi_i = \left(\varphi - \frac{\Delta\varphi}{2}\right) + \Delta\varphi \cdot \frac{i \mathrm{mod} N}{N} \tag{90}$$

$$\vartheta_i = \left(\vartheta - \frac{\Delta\vartheta}{2}\right) + \Delta\vartheta \cdot \frac{\left\lfloor \frac{i \mathrm{mod}(N^2)}{N} \right\rfloor}{N} \tag{91}$$

$$w_{a,i} = \left(w_a - \frac{\Delta w_a}{2}\right) + \Delta w_a \cdot \frac{\left\lfloor \frac{i}{N^2} \right\rfloor}{N} \ . \tag{92}$$

Then, the grid points are transformed into cartesian coordinates employing

$$\varpi_{x,i} = w_{a,i}\cos(\varphi_i)\cos(\vartheta_i) - \frac{v_{a,x}}{v_a} \tag{93}$$

$$\varpi_{y,i} = w_{a,i}\sin(\varphi_i)\cos(\vartheta_i) - \frac{v_{a,y}}{v_a} \tag{94}$$

$$\varpi_{z,i} = w_{a,i}\sin(\vartheta_i) - \frac{v_{a,z}}{v_a} \ . \tag{95}$$

$$\tag{96}$$

For this work, the generalized approach is employed.

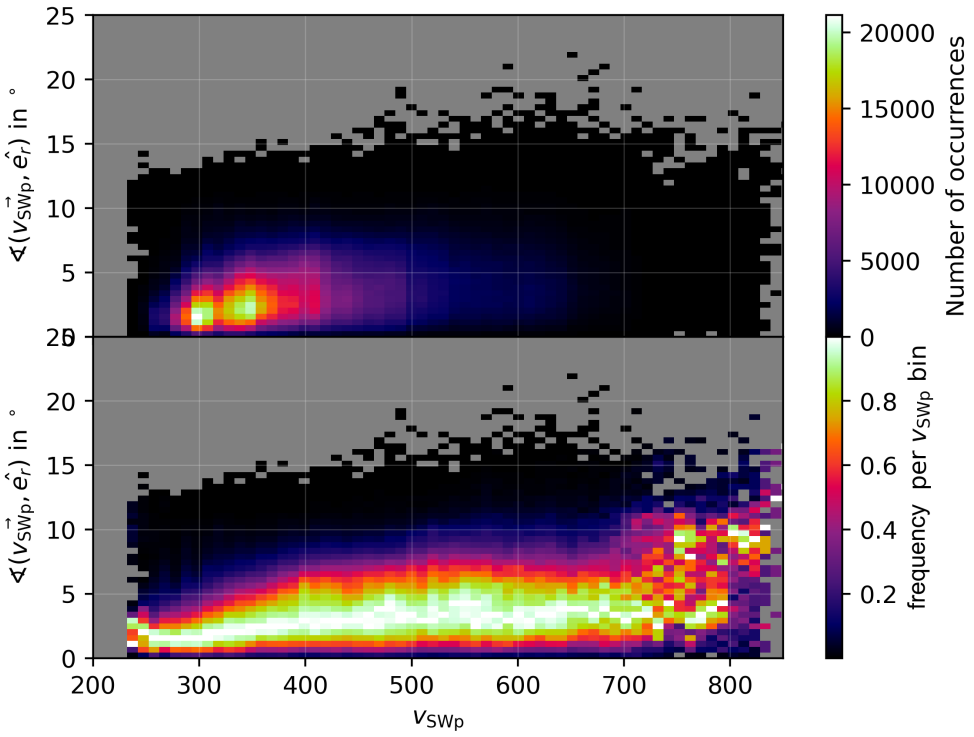

Figure 58: Proton bulk velocity (x-axis) and unsigned angle between Proton bulk velocity and the radial direction (y-axis) derived from one-dimensional Maxwellian fits with PLASTIC data inclusively between 2008 and 2014.

5.3.3 Observed velocity distribution functions

To relate the observations to relevant SW quantities, instead of absolute velocities, the transformation and histogram method outlined in section 5.3.2 is employed in order to obtain three dimensional φ_{SWp} distributions as observed within the SWS aperture of PLASTIC.
The computationally more demanding approach which allows for deviations of the direction of the SW velocity from the radial direction (in comparison to the procedure of section 5.3.1) is necessary. This is evident from Fig. 58 where the angle between proton bulk velocity and radial direction is plotted. The majority of data is found at angles between 2° to 4°. However, Fig. 58 is not to be interpreted, that on average the SW incidents from a preferential non-radial direction, since this angle is unsigned and always measured within a plane defined by the velocity and the radial direction. Yet, it shows that for the proton bulk velocity discrepancies from the radial direction by small angles are common. Hence, the method deduced in section 5.3.1 is prone to an error within that magnitude.

It is necessary to refine the filter imposed on the PHAs in order to reduce the contribution of different ions than He^+ PUIs. Especially, the signed transformed velocity in the SW frame is employed to create a filter condition which separates most misassigned SW ions from the He^+

PUIs through the requirement $\varpi^{\pm}_{SWp} > 0.4$.
Also, to mitigate the effect that acceleration regions like ICMEs and CIRs may have on the PUI VDFs, only times are considered when none of these events occurred (according to the event lists outlined in chapter 4.2.4). In addition, the data has been filtered for the observed solar wind type according to the scheme of Xu and Borovsky [2015] (compare Chapter 2.1.4.iii). Since three-dimensional VDFs can not be directly plotted onto two dimensional media, in the following 2D-slices out of them are shown. Fig. 59 is deemed as a visual guideline for these two dimensional cuts through the He^+ PUI VDF. The cuts are represented by stacked planes which intersect with the aperture. It is visible that depending on vertical distance to the central plane the minimum observable velocity varies. Every slice is parallel to the instrumental radial-tangential plane. As a consequence of the instrument's geometry, the range of observable velocities varies with vertical distance from the radial-tangential-plane. The more distance from the plane, the larger is the minimum observable velocity. Since in the following the velocity is shown in ϖ_{SWp} space, it is noteworthy that the minimum observable ϖ_{SWp} is also a function of the SW bulk proton velocity. Therefore, whenever possible (or necessary), two values for the minimum and maximum value of that lower boundary are given. Also, unlike the visualization of Fig. 59, the 2D-slices are of finite width, caused by low statistics. Empirically, a division of the $\varpi_{SWp,z}$ interval from -1 to 1 into 12 bins has been selected as a reasonable choice. This was experimentally found out by the creation of plots with different resolutions with the aim to find a compromise between the display of significant details and a good signal-to-noise ratio. The selected binning means, that each $\varpi_{SWp,z}$-slice has a width of ~ 0.17. In addition, the shape of the VDF has been investigated as a function of the azimuthal magnetic field direction, while only times are selected, when the elevation angle of the local magnetic field is within $\pm 10°$ of the in-ecliptic plane. To ensure inter-comparability of the histograms, a normalization to the statistical probability of magnetic field directions has been performed, which is described in appendix B.2.1. In short, the normalization works as follows: A histogram of the magnetic field directions measured in 5 minute intervals is created and divided by the sum of all bins. For each PHA event, a normalization weight is found by finding the bin of the histogram which corresponds to the magnetic field direction which is observed while the PHA event occurred. The reciprocal of the bin's value is the normalization weight. The normalization has the caveat that the units of the plots are not counts any more, but arbitrary units. However, since larger instrumental issues, which have already partly been observed with the WAP section and are further discussed in chapter 5.4 cause systematical errors, the absolute counts of each bin lack meaning for themselves and can be seen as a first guideline result. Therefore omitting physical units and moving to arbitrary units is not a substantial problem. On the other hand, the normalization mitigates one of the systematic errors, which affect the results. To streamline the readability of the results, all VDFs normalized in that way are called in the following Magnetic field Direction Normalized velocity distribution functions (MDNVDFs).
In the following, example slices of the observed 3d MDNVDFs are presented and discussed. A complete overview of all slices and each magnetic field direction belonging to the shown plots are provided in appendix D.

5.3.4 Absolute velocity distribution functions

Fig. 60 depicts four slices through the observed 3d He^+ PUI MDNVDFs. For each slice the same $\varphi_{SWp,5m,n}$ coordinate was chosen, but different magnetic field azimuthal angles were selected for each panel of the figure. It is common to all panels of Fig. 60, that the instrument exhibits enhanced count rates at one side ($\varphi_{SWp,5m,t} < 0$) in comparison to the other side ($\varphi_{SWp,5m,t} > 0$). For conciciveness in the following discussion, the side of $\varphi_{SWp,5m,t} < 0$ is called the negative side

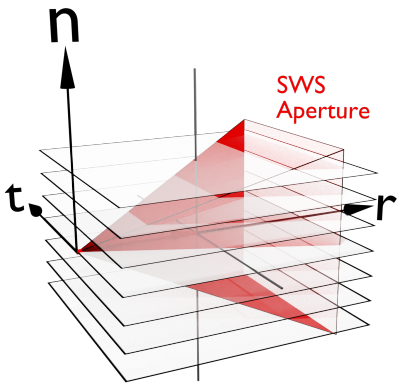

Figure 59: Artistic rendition of the radial (r), tangential (t) and normal (n) coordinate system (black arrows) and the aperture PLASTICs solar wind sector (red marked pyramidoid). Inside the aperture the SW bulk velocity is sketched as a red arrow.

in the following and accordingly the other the positive side. The count rate asymmetries seem at a first glance independent of the magnetic field orientation. In Fig. 61 an analogous plot is shown, but there each panel selects different SW types instead of different magnetic field orientation. Here, at a first glance, the asymmetries in the count rates are persistent throughout different SW conditions. This asymmetry is likely caused by asymmetries within the instrumental particle detection efficiency and not due to underlying physics in the SW. Chapter 5.4 discusses these further. Also, the resistive anode which measures azimuthal incoming direction, has a nonlinear response (compare chapter 3.2). Although from ground calibration this response is expected to be symmetric, asymmetries in the resistive anode's response can not be discounted and are the subject of chapter 5.4 as well. Also, the resistive anode's response spikes at the center of the aperture of SWS. This behavior of the center is actually due to particles being scattered at a support structure within the instrument. Due to that scattering smaller count rates are expected at the center of the instrument than further away from the center, even though a non-bimodal distribution enters the instrument. In both figures, this behavior is visible as two islands of high counts form at the positive and negative side, where the center of the instrument shows relative consistent smaller counts in all plots.
Two features which are consistent with expectations are that at absolute values of $\vec{\varpi}_{SWp,5m}$ lower than 0.4 a circular area is carved out, which originates from the filter of $|\vec{\varpi}_{SWp,5m}| > 0.4$. Also, the overall shape of the areas with more than 0 counts resemble a conic shape which is an imprint of the apertures boundaries.

5.3.5 Differential velocity distribution functions

Since the absolute MDNVDFs are strongly affected by instrumental effects, it is not possible to make meaningful direct observations about the MDNVDFs from those absolute plots alone. A comparison of each pixel of the derived MDNVDFs compared to the pixels average for all

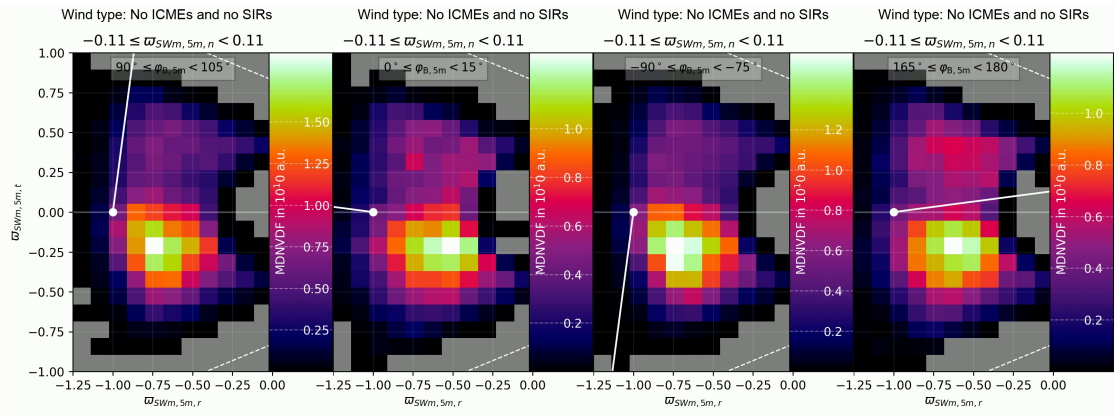

Figure 60: Two dimensional slices within the ($\varpi_{\mathrm{SWp,5m,r}}$,$\varpi_{\mathrm{SWp,5m,t}}$)-plane of the He^+ VDF observed from 2008 to 2015. For the VDFs only measurement times are considered, where no ICMEs or SIRs were observed. The normal coordinate range of the slice is indicated on top of the plot. The orientation of the magnetic field vector is plotted by a white line originating from a white dot which represents the coordinate origin in the ($\varpi_{\mathrm{SWp,5m,r}}$,$\varpi_{\mathrm{SWp,5m,t}}$)-plane. Discrepancies between the direction of the white line and the indicated magnetic field direction arise from the aspect ratio of the plot. In white dashed lines the ±22.5° boundary of PLASTICs SWS aperture is plotted.

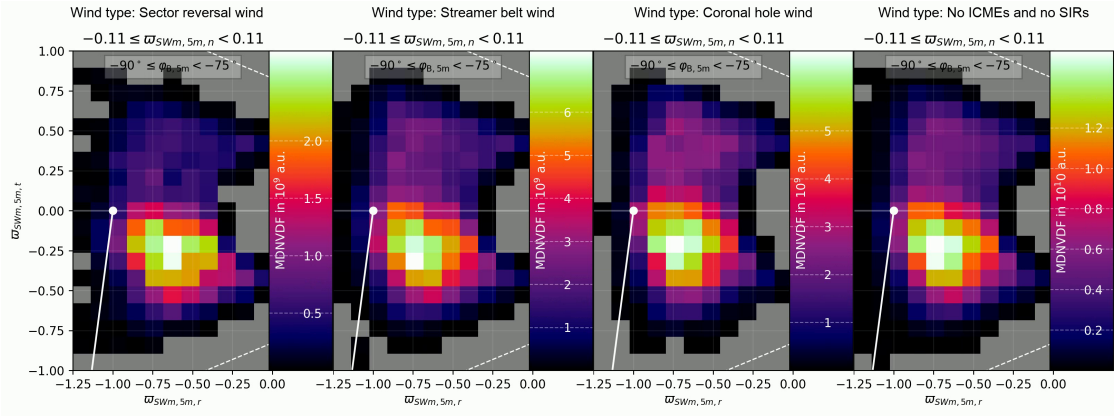

Figure 61: Same as in Fig. 60, but here only measurement times are considered in which no ICMEs or SIRs were observed.

observed magnetic field directions (similar to the approach of Drews et al. [2015]) could lead to a more fruitful observation.
In the following, differences between between the pixels' values and the respective average value of the pixels throughout slices in the ($\varpi_{\mathrm{SWp,5m,r}}$,$\varpi_{\mathrm{SWp,5m,t}}$)-plane are presented.

For comparability, as a first view, in Fig. 62 the analogous configuration to Fig. 60 is shown where for each pixel the average over this pixel is subtracted. In the following these differences are defined as differential MDNVDF. The $\sim 84°$ configuration still exhibits slightly enhanced differences in the negative half, which is expected, since the value of the difference still depends on the base value. Yet, the differential MDNVDFs are from a first glance better suited to depict features of the observed MDNVDF. Unfortunately, low count statistics introduce noise into the data and the differences increase the visibility of noise. Yet, a distinct increase in differential counts is observed at magnetic field azimuthal directions of $\sim \pm 84°$, which is perpendicular to the magnetic field and at $|\vec{\varpi}_{SWp,5m}|$ values in the area of ~ 0.6 to ~ 1.0, which might indicate traces of a PUI ring beam distribution. Such an observation would fit to the findings of Drews et al. [2015]. However, without an investigation of further configurations such an observation would be premature. At azimuthal directions of $\sim 0°$ and $\sim \pm 180°$ no distinct features are found.

The possibly systematic behavior of the PUI VDFs as a function of the local magnetic field direction is further investigated with Fig. 63. Now the magnetic field azimuthal direction is stepped finer around an angle of $\sim -90°$. In the differential VDFs at the four selected angular configurations a region of enhanced counts emerges at the negative side from values of $\varpi_{\mathrm{SWp,5m,r}} > 1$ towards and wanders at the negative edge of the aperture towards lower $\varpi_{\mathrm{SWp,5m,r}}$ during rotation of the magnetic field towards anti-radial direction. Again, the density enhancement is observed roughly at $\sim 90°$ of the local magnetic field and seems to rotate with it. However, in the rightmost panel of 63 the distinct signature begins to shift towards edge bins of the SWS aperture. Also at different magnetic field angles this trend is continued. At different layers above the $\varpi_{\mathrm{SWp,5m,r}}$,$\varpi_{\mathrm{SWp,5m,t}}$)-plane similar trends are also found. To illustrate, a full overview over the MDNVDF for the same SW conditions as in 63 is provided by Fig. 64. Throughout the different layers of the MDNVDF a pattern is found, where density enhancements appear most prominent at magnetic field azimuthal angles around $\sim -135°$ and $\sim 60°$ (a distance within the bin width of $15°$ of $\sim 180°$) and most prominent density depressions around azimuthal magnetic field angles around $\sim -45°$ and $\sim 135°$ (again within the bin width margin of $15°$, these angles are $\sim 180°$ apart from each other). Interestingly, the enhancements and depressions appear roughly about $90°$ apart. These observations, which are consistent throughout the different layers (with the exceptions of layers close to $|\varpi_{\mathrm{SWp,5m,n}}| = 1$) point towards rotating signatures within the He^+ PUI MDNVDF, thus indicating the existence of anisotropic features. Anisotropic features of pitch angles of $90°$ are also found in an investigation of pitch angle distributions in Chapter 6.2.3.

The absolute values of $\vec{\varpi}_{\mathrm{SWp,5m}}$, at which most of the enhanced count rates occur, is interesting. Drews et al. [2015] observed most anisotropic features at values of $|\vec{\varpi}_{\mathrm{SWp,5m}}|$ close to 1. Yet, Figs. 63 and 64 suggest that the most prominent signatures of anisotropic PUI MDNVDFs are located at $|\vec{\varpi}_{\mathrm{SWp,5m}}| \sim 0.8$. Under the assumption that adiabatic cooling dominates the PUI transport, this would mean that the observed anisotropic features originate from PUIs, which are not freshly injected into the SW. However, the values of $|\vec{\varpi}_{\mathrm{SWp,5m}}|$, where the strongest difference is observed, are also influenced by the underlying absolute distributions which provided the original values for the difference. Examples of these are Figs. 60 and 61, where it is seen that most of the MDNVDFs density is found at these values. Unfortunately, very small densities of the MDNVDFs are found close to $|\vec{\varpi}_{\mathrm{SWp,5m}}| \sim 1$. Otherwise a normalization of the differences,

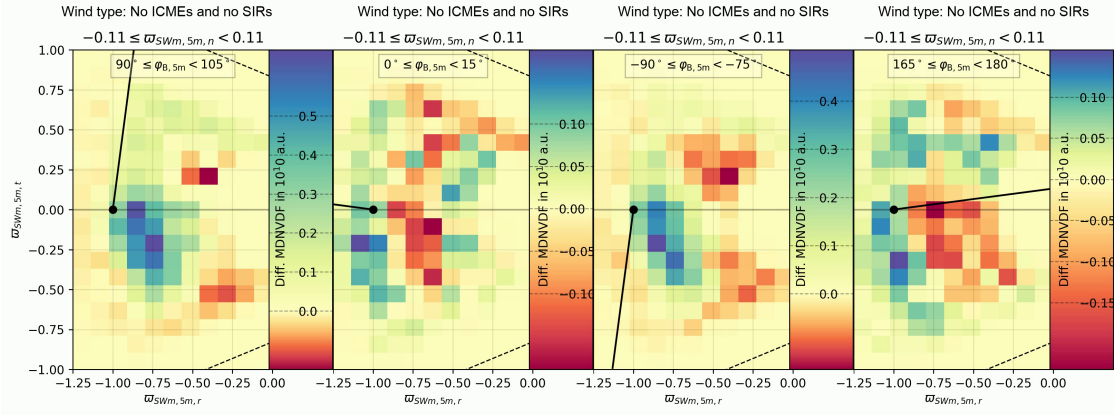

Figure 62: Analogous set of plots to Fig. 60, but with differential MDNVDFs on display instead of MDNVDFs.

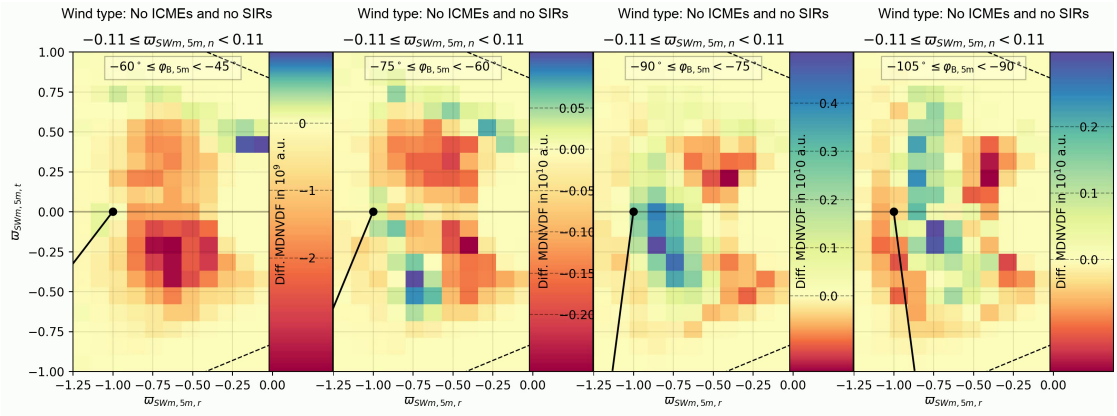

Figure 63: Analogous set of plots to Fig. 62. However, in this figure the magnetic field azimuthal angle steps through windows of a width of 15° in sequential order from −45° to −90°.

which takes this into account or a division of the MDNVDFs by average MDNVDFs as a different way of expressing a differential-like MDNVDF would be more suited to expose anisotropic features. since within the area of roughly $0.5 < |\vec{\varpi}_{\mathrm{SWp,5m}}| < 0.8$, observed MDNVDFs densities do not seem to decrease systematically depending on where in $|\vec{\varpi}_{\mathrm{SWp,5m}}|$ they peak, in these areas the differences are more reliable for inter-comparison. However, closer to the edges of the distribution, edge-effects make it challenging to make concluding remarks about the actual range of $|\vec{\varpi}_{\mathrm{SWp,5m}}|$, for which anisotropic features exist.

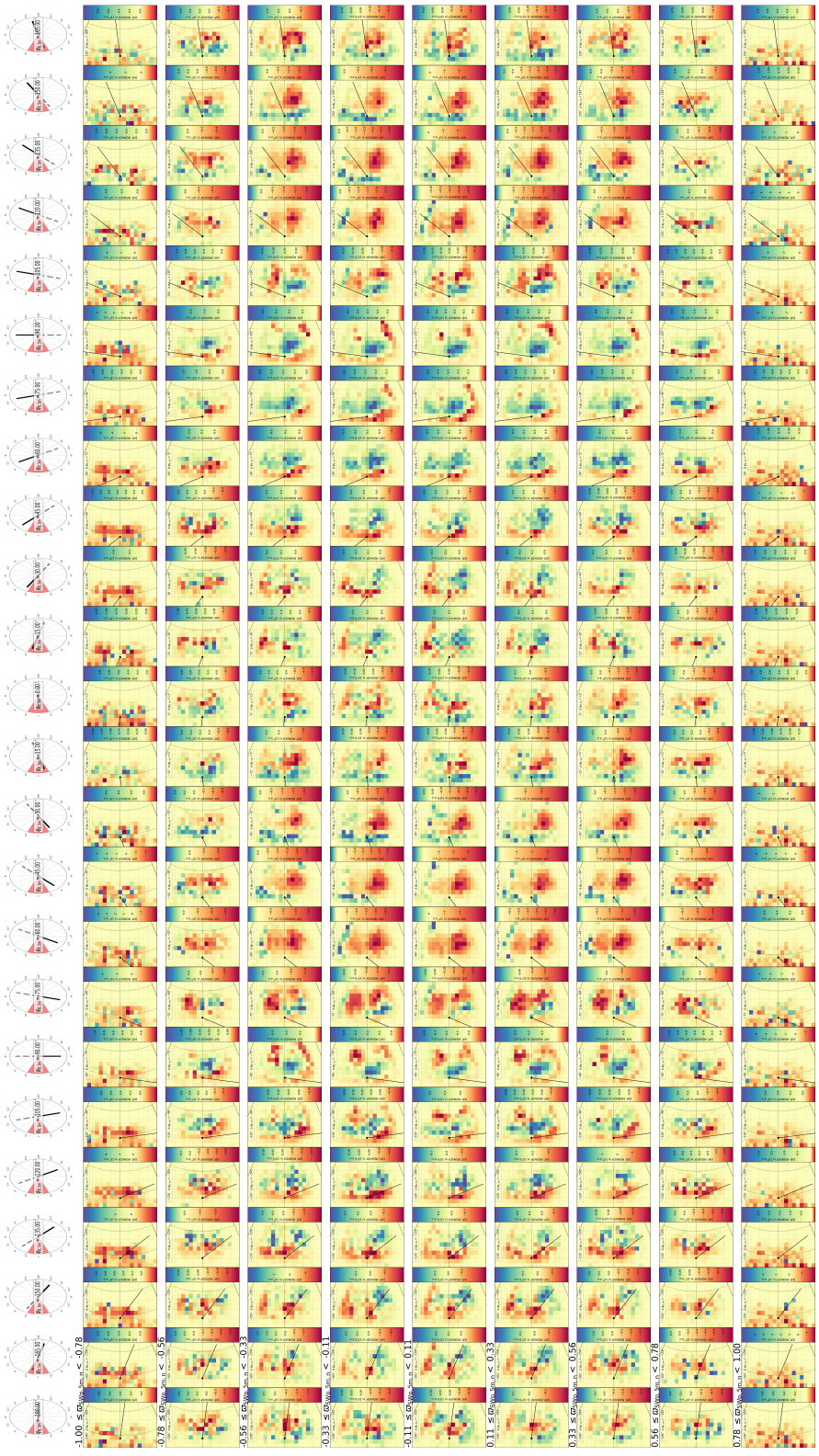

Figure 64: Collection of all MDNVDFs for all configurations of magnetic field azimuthal directions in the current setups displayed as 2d-slices through three dimensional velocity space. The plots are sorted in rows corresponding to a certain slice and columns corresponding to a certain magnetic field angle. This figure aims to provide an overview. Therefore, for reasons of space x and y axis labels are omitted. If labeled, the axes are analogously labeled to the plots of Fig. 63. All plots correspond to a selection of SW conditions analogous to Fig. 63 (all wind, but without ICMEs or SIRs).

5.3.6 Differential velocity distribution functions in the context of different solar wind regimes

The results of chapter 5.3.5 point towards anisotropic features within the He^+ PUI MDNVDF. However, these observations were integrated over a broad selection of time periods which, apart from the limitation, that no ICMEs and no SIRs are included, are not specifically sorted for conditions in the SW.
The driving question for this section is to what extent the SW species in which the PUIs are observed, influences the abundance and magnitude of anisotropic features. Therefore, in the following different MDNVDFs are presented, where each is observed during time periods when one of the SW types according to chapter 2.1.4 is observed at STEREO A.

5.3.6.i Comparison between coronal hole wind, streamer belt wind and sector reversal wind The comparison between the different SW types starts with analysis of the azimuthal magnetic field angle, where based on the results of chapter 5.3.5 most signatures are expected: at angles close to 90°. Fig. 65 compares differential MDNVDFs obtained during coronal hole, streamer belt and sector reversal wind periods (one row of plots per wind type) with each other by depicting these for different azimuthal angular configurations of the local magnetic field (each column of plots represents a different angular configuration). At the depicted configurations the differential MDNVDF's behavior is qualitatively very similar for all three wind types. However, in sector reversal wind which is attributed to conditions similar or close to SIRs or CIRs (interaction of different SW streams) preferredly the left half of the aperture is filled with more events than on average. In the other wind types counts in one half are more similar to the other half (but not equal). However, since yet unsolved directional efficiency problems dominate the instrument's particle detection capability, no quantitative analyses should be performed, yet. Still, qualitatively in the streamer belt wind and coronal hole wind broader pitch angle distributions are expected than in the sector reversal wind. And this comparison can be made even without knowing the exact directional efficiencies since all plots are expected to be similarly affected by such a systematic error.

A second observation is provided by flipping the magnetic field angle around the radial direction to observe now at angles close to −90°. The analogous situation to before is depicted in Fig. 66, but with the magnetic field direction on the opposite side. Compared to Fig. 65 stronger differences between the solar wind types emerge. At this configuration, for coronal hole wind there is a small number of pixels which show density enhancements, usually a pixel in the center at $\varpi_{\mathrm{SWp,5m,r}} = 1$. The enhancement remains at this location for all four depicted magnetic field directions. However, in the rightmost panel the observed features may also be due to noisy data. Compared to the opposite magnetic field direction, the coronal hole wind data is now dominated by areas of density decrease rather than enhancements. This trend is less prominent to not existent for the differential MDNVDF in the streamer belt wind. There, a similar trend as in Fig. 65 can be be seen. The same can also be noted for the differential MDNVDFs in the sector reversal wind. Hence at this configuration the qualitative behavior of the differential MDNVDF in the coronal hole wind deviates strongly from the other SW types. There are some probable explanations for this behavior. For one, there might be an accidental selection effect in the coordinates where the PHAs are observed. E.g. if by chance more coronal hole wind is found close to focusing cone regions than other types of SW. However, this is unlikely and a time series of SW types (e.g. the fourth panel of Fig. 87 in Chapter 6) shows, that this selection effect can be discounted. A different behavior in the coronal hole wind can also be an indicator for different transport processes than in other SW types (e.g. more wave-particle interaction).

As Fig. 67 depicts, the density decreases of the differential MDNVDF within coronal hole wind, at velocity space coordinates where the differential MDNVDFs in the other wind types increase, seem to be compensated by density increases at a different angle, where now the differential MDNVDFs of other wind types (represented here be the streamer belt wind) decrease. This is the case for $165° \leq \varphi_{B,5m} < 180°$. In the opposite direction (around $\sim 0°$) such a trend can not be found. This may be due to the data being noisier at that configuration or an actual physical process. If any, here the situation that differential MDNVDF decreases while the other increases, is reversed.

To conclude the comparison of differential MDNVDFs within different SW regimes, Fig. 68 digests the main information of the deliberations about density in- and decreases of the differential MDNVDFs into a reduced form. As already discussed, the depicted differential MDNVDFs have been observed as a function of SW regime and azimuthal magnetic field direction. This leaves a three-dimensional data product per configuration. For Fig. 68 the dimensionality was reduced by averaging for each configuration separately over the layers of $\varpi_{SWp,5m,n}$. From these averaged differential MDNVDFs then a maximum and a minimum value are obtained and divided by each other (with a negative sign to account for the negative minimum). The result is a quantity which is a measure for the tendency of direction into which a differential MDNVDF deviates from its average (compare how the differential MDNVDFs are obtained) at a pre-defined configuration of magnetic field angle and SW regime. A value of 1 suggest, that minimum and maximum are the same in the corresponding differential MDNVDF, whereas a value larger than 1 suggests, that at least one positive bin within the differential MDNVDF is further away from zero than any negative bin. Without further information the obtained quantity is neither a reliable measure for how much a differential MDNVDF deviates from its average nor for the tendency of a distribution to go in one or the other direction. However, from plots like Fig. 64 it can be deduced that in most cases a larger absolute maximum value of the differential MDNVDF in comparison to the absolute minimum value of the same differential MDNVDF is connected to the tendency of the differential MDNVDF to deviate in positive direction and vice-versa for a negative direction. Hence, Fig. 68 provides an overview over the systematic behavior of density enhancements and depressions within the differential MDNVDFs as a function of magnetic field direction and SW configuration.
Firstly, as already seen, the strongest indication of anisotropic features is found in the sector reversal wind. Here, for $\varphi_{B,5m} \sim \pm 90°$ peaks in the comparison between maximum and minimum are found. In proximity to 0° and 180° minima are found, which are below 1. Even though the maxima in the streamer belt wind are less pronounced, a similar behavior as a function of the magnetic field angle is found, but with the exception that in addition to the maxima $\varphi_{B,5m} \sim \pm 90°$ another maximum at $\varphi_{B,5m} \sim 30°$ is found. Finally, the weakest trend is found in the coronal hole wind. As observed earlier, the points where most anisotropic features are found, is shifted in comparison to the sector reversal wind and also the maximum at $-90°$ does not significantly differ in density from the surrounding bins. Clearly, the observations remarked earlier in this section concerning three-dimensional differential MDNVDFs integrated during coronal hole wind conditions are more reliable. Still, earlier the observation was made that the MDNVDFs during coronal hole wind conditions have the tendency to feature anisotropic signatures at different angles and in a less pronounced way, but not as little as indicated by Fig. 68. Fewer anisotropic features within PUI VDFs during coronal hole wind conditions are expected, since this wind type is expected to feature the most waves and turbulences (with the exception of SIRs and ejecta) [Xu and Borovsky [2015]], because it is commonly expected, that the interaction with turbulent fields leads to an isotropization of VDFs (compare Chapters 2.1.6 and 2.2.5).

Yet, slightly unexpected is that most anisotropic features are found during sector reversal plasma periods, since sector reversal plasma categorizes plasma close to SIRs and different structures within the magnetic field, where the direction of the magnetic field changes comparatively swift. In situations attributed to these regions stronger accelerations and scattering of the PUI VDFs are expected to take place (e.g. Yu et al. [2018]). Leaving out ICMEs, the fastest on average is then coronal hole wind and at velocities in between the streamer belt plasma is found. Of course, these observations strictly speaking only apply to estimated velocity ranges (e.g. percentiles) from long-term observations (again e.g. Fig. 4 in chapter 2.1.4), since the velocity ranges of these SW types overlap. Still, the observation, that fewer anisotropic features occur in the fastest SW type and the clearest anisotropic signatures are found in the slowest SW type leads to the approach to observe differential MDNVDFs as a function of proton bulk velocity. Also, to make further assessments about acceleration and scattering processes, the computation of pitch angle distributions corresponding to the PHA data contributing to the observed differential MDNVDFs may help. These are the subject of chapter 6.

5.3.6.ii Solar Wind sorted by velocity The initial analysis of differential MDNVDFs indicated the possibility that the observed magnitude of anisotropic, magnetic field dependent signatures observed in differential MDNVDFs is a function of the velocity carrying the SW. To investigate this hypothesis, in the following, differential MDNVDFs are computed from PLASTIC data filtered analogous to before, but at this time instead of observing differential MDNVDFs as a function of the SW archetype, different differential MDNVDFs are obtained with the SW velocity as a filter. To partly mitigate the effect that disturbances in the SW are expected to exert on PUI VDFs, periods of ICMEs and SIRs are still excluded. Again, the magnetic field is limited to elevation angles of $\pm 10°$ within the ecliptic plane and the SW velocity is divided up into five intervals: $[200, 300]$ km/s, $[300, 400]$ km/s, $[400, 500]$ km/s, $[500, 600]$ km/s and , $[600, 800]$ km/s. The last group spans over twice the velocity range of other groups, since compared to the other group only a short amount of time periods is available with velocities in that range.

In Fig. 69 again the differential MDNVDFs are compared at magnetic field configurations close to 90° azimuthal angle. Similar to the findings at positive azimuthal angle within the comparison of differential MDNVDFs for different SW types, anisotropic features appear within all velocity groups at the positive configuration, which is depicted in the top row of plots in Fig. 69. The bottom row of plots in Fig. 69 is more interesting in that respect, since it is filtered to the configuration of a negative magnetic field azimuthal angle close to $-90°$ and within it an anisotropic signature is found at small velocities, which for the first three ranges remains about similarly visible, but decreases in prominence as the velocity increases to the fastest two intervals of SW velocity.

In analogous fashion to the comparison of Fig. 68 within different SW types, minimum and maximum values of the differential MDNVDFs are compared in Fig. 70. Again, this kind of overview comparison tends to omit details of the differential MDNVDFs, but allows for a more global comparison. The linear scaled version of the plot depicts the appearance of anisotropic features close to $\pm 90°$ clearly. Interestingly, the fraction of minimum versus maximum is at 90° of similar value for both the fastest and the slowest of the selected velocity intervals. For the intermediate intervals, comparatively lower and less distinct values of the fraction of minimum versus maximum are observed. Yet, the three intermediate velocity intervals (300 km/s to 600 km/s in this discussion), all depict a more or less distinct double peaked structure of the maximum at positive angles, which has also been observed in the streamer belt type wind earlier. There are no distinct aberrations between the curve representing the fastest interval of SW in

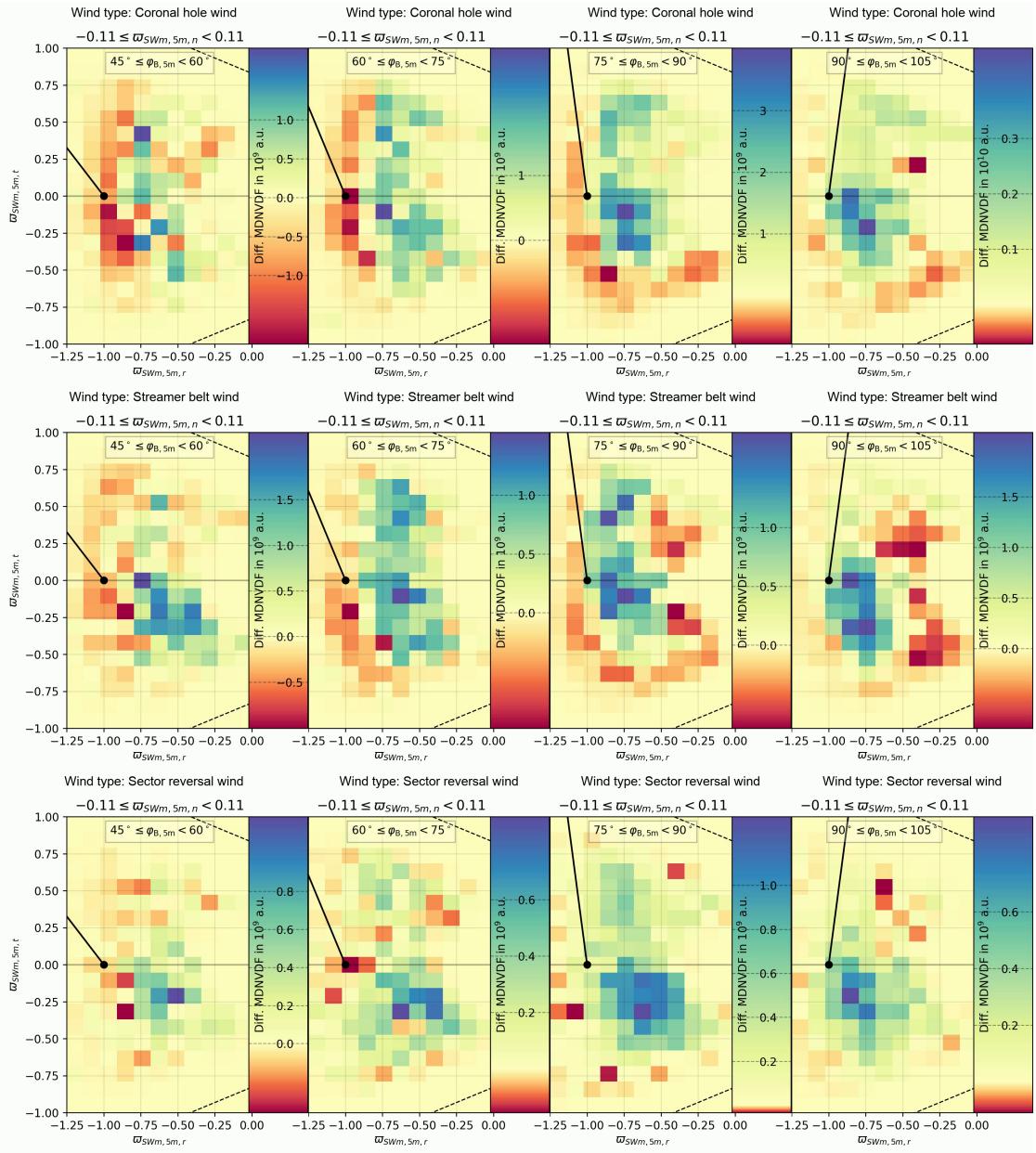

Figure 65: Differential MDNVDFs observed for four different magnetic field azimuthal angles. Each column of plots hereby represents one angular configuration. Each row represents one different type of SW. The plots compare MDNVDFs observed in three different SW types: coronal hole wind, streamer belt wind and sector reversal wind. It is important to point out that the MDNVDFs the shown differential MDNVDFs originate from are not normalized to the number of events that contribute in total to a MDNVDF. Hence, only the plots within each row are comparable with each other in terms of numbers. However, the signs of the pixels are comparable, since the tendency to show a density enhancement or a decline are invariant of the aforementioned normalization.

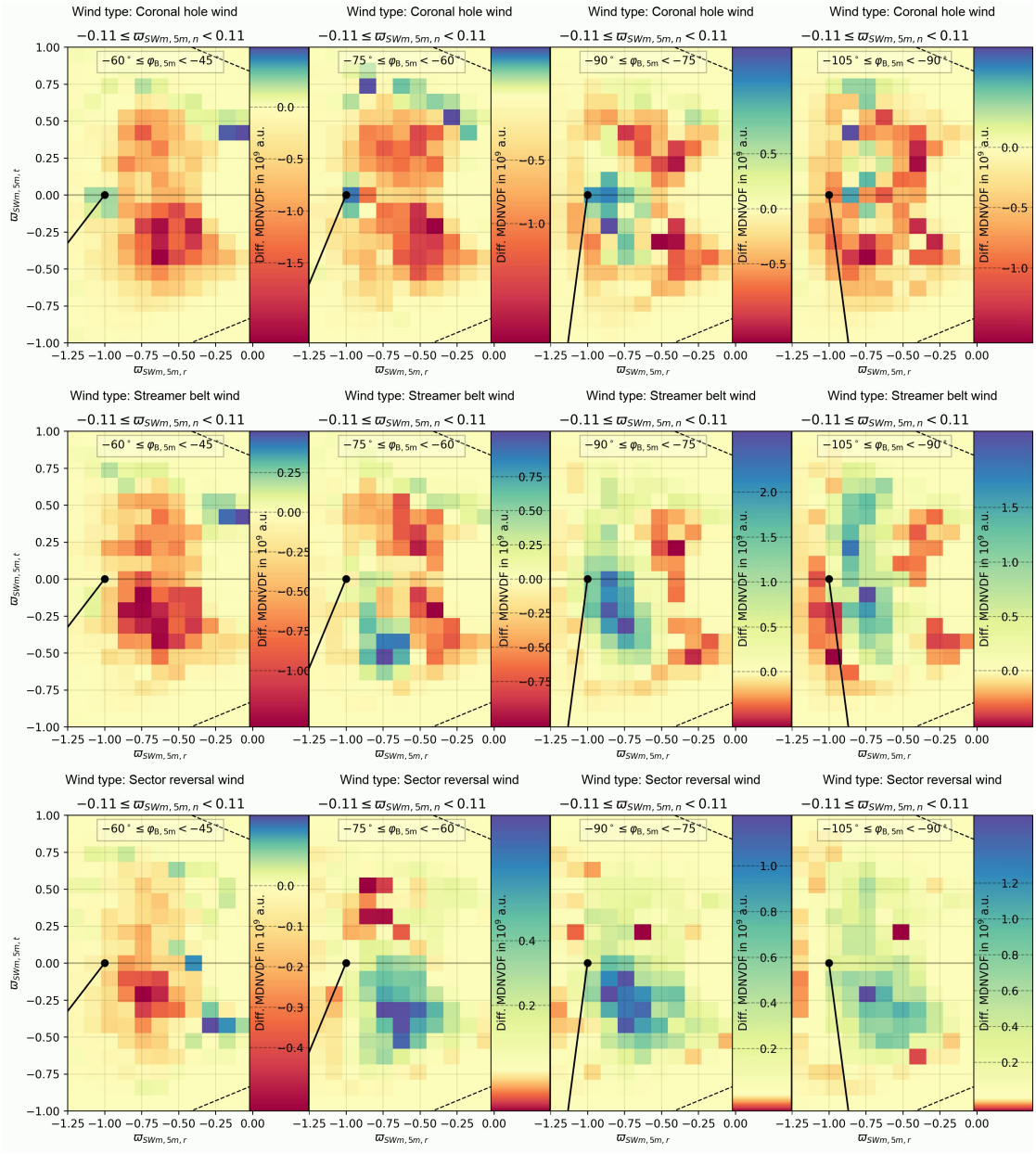

Figure 66: Analogous plot to Fig. 65, but with angles at the other side of the radial direction.

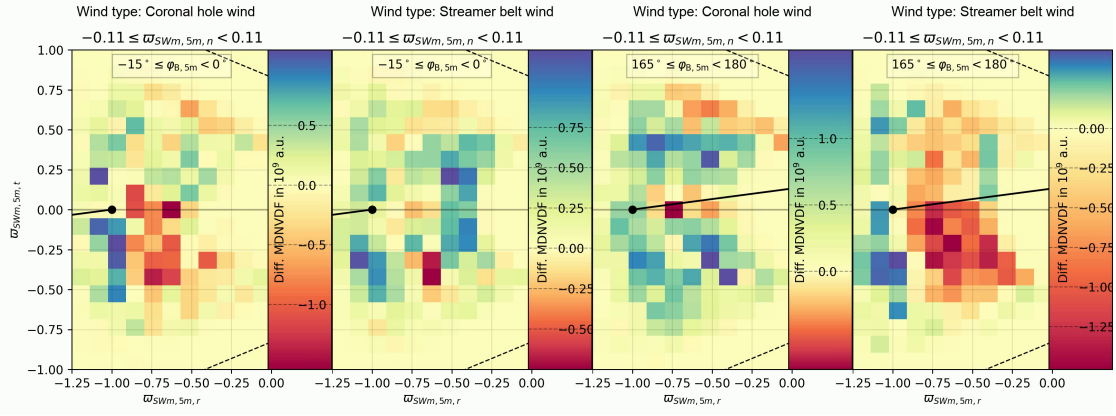

Figure 67: Analogous plot to a row of 65. Here, the different panels compare differential MDNVDFs during Coronal hole wind conditions (first and third panel from left) to differential MDNVDFs during Streamer belt wind conditions (second and fourth panel from left) for two settings of the magnetic field azimuthal angle: $-15° \leq \varphi_{\mathrm{B,5m}} < 0°$ (first and second panel) and $165° \leq \varphi_{\mathrm{B,5m}} < 180°$ (third and fourth panel).

Fig. 70 and the coronal hole wind as in Fig. 68.
The findings hint towards the SW velocity being a controlling parameter for the amount of isotropization of PUI VDFs. This is expected, since in faster wind streams a stronger abundance of turbulence is expected (compare Chapter 2.1.4). However, the question remains whether the underlying physics of acceleration processes of which probable traces have been observed in this chapter, is generally controlled by the velocity of the SW or the archetype of the SW stream. This question can not be answered by the comparisons made in this chapter, since if the controlling parameter were the SW velocity, then characteristics of acceleration processes in the different SW archetypes were directly influenced by these archetypes having their distinct, but partly overlapping, velocity selections. On the other hand a direct influence of the archetype of SW (for which it must additionally be stated, that since the classification of SW is a field of increasedly ongoing research, the employed classification is by no means a complete distinction between SW streams and their properties) would in the same way influence the acceleration processes during different SW velocities, since the overlapping velocity ranges of the SW archetypes then cause a mix of different velocities, where the selection of SW archetypes per velocity group directly depends on velocity.
Still, the comparison of data grouped by different velocity intervals provides the means of dividing the SW conditions into more groups than with the different archetypes and since a trend of the significance of anisotropic features with the velocity has been observed, the question arises, whether or to which SW velocity dependent systematic errors influence this chapter's observations. As a first idea the limited acceptance of the SWS aperture might introduce such an error since in absolute velocity space a point of reference which is further away from the coordinate origin introduces more space for different velocities to be observed. Yet, the MDNVDFs are observed in $\vec{\varphi}_{\mathrm{SWp,5m}}$ space, which is normalized by the SW bulk velocity. Therefore concerning the extent of the shown coordinate systems in absolute velocity space, the mathematical theorem of intersecting lines can be referenced and since the acceptance angle of the SWS aperture remains the same through every energy per charge step, the observable range of $\vec{\varphi}_{\mathrm{SWp,5m}}$ remains uninfluenced (neglecting of course the effects caused by a limited number of energy per charge

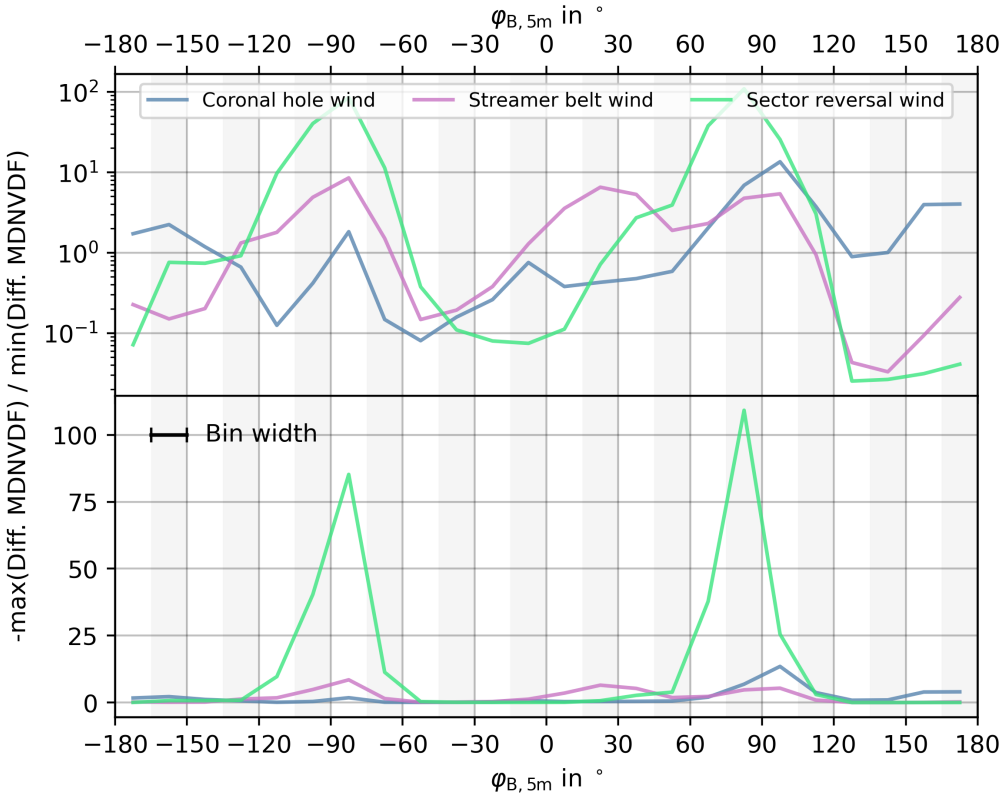

Figure 68: For this plot, for each $\varphi_{B,5m}$-bin an average over all $\varpi_{\mathrm{SWp,5m,n}}$-layers has been computed, so that 2d-averaged-differential-MDNVDFs are obtained per $\varphi_{B,5m}$-bin. From these the maximum and minimum value (again per $\varphi_{B,5m}$-bin) have been determined and divided by each other. This is the data product, which the y-axis represents. The x-axis represents the azimuthal magnetic field direction. Both panels depict the same data, but the top panel has the y-axis logarithmically scaled, while the bottom panel is linearly scaled. The differential MDNVDFs for this plot were observed during three conditions in the SW (each curve represents a different one).

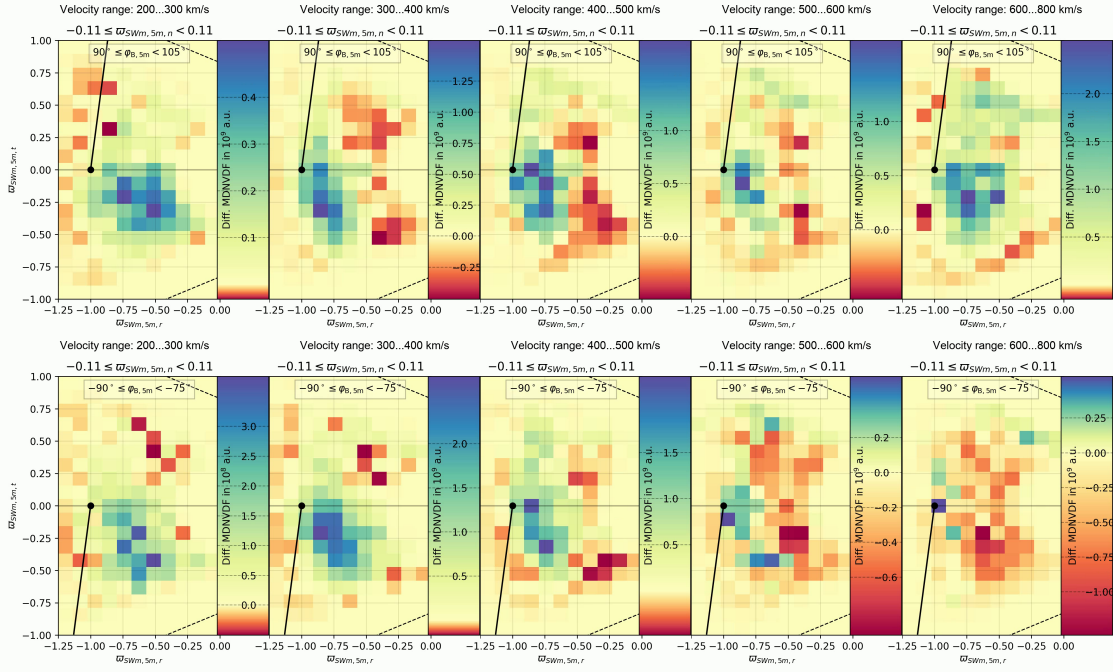

Figure 69: Analogous plot to two rows of Fig. 65. Here, the differential MDNVDFs are displayed for different SW proton bulk velocities instead of different SW types. The top panels show differential MDNVDFs for $90° \leq \varphi_{\mathrm{B,5m}} < 105°$ and the bottom panels for $-90° \leq \varphi_{\mathrm{B,5m}} < -75°$.

bins, which is for the observed velocity ranges not important).
A second idea is the fact that increasing SW velocities mean, that at a constant range of $|\vec{\varphi}_{\mathrm{SWp,5m}}|$ values are attributed with increasing absolute velocities. One of the main challenges during selection of He^+ PHAs in calibration of STEREO/PLASTIC (see Chapter 4.1) was that in particular SW protons have increasingly similar positions in total energy and time of flight at higher energies. This means, that some of the particles which are shown here as He^+ PUIs can actually be missassigned SW protons. The likeliness for this increases with energy.
It has to be stated, that in this analysis (apart from ICMEs and SIRs and the ejecta class) only the SW classification according to Xu and Borovsky [2015] was employed to distinguish between states of SW. While this is superior to a classification by SW average velocity alone (compare Chapter 2.1.4), the intention behind the scheme is to employ in-situ quantities to classify the SW by origin. Since from the Sun to the spacecraft the SW has travelled a large distance, there is a caveat to the precision of the classification by origin. Also, a classification by kinetic processes within the SW instead of the origin may be more suited for an investigation of SW transport. Maybe, in future studies PUI VDFs can even be employed to find a new classification for the SW, which classifies the SW by its particle transport properties.

5.3.6.iii ICMEs and SIRs There are two classes of SW within the classification scheme employed in this work which have been explicitly excluded from observation of MDNVDFs so far. The reason is that these types, the ICMEs and SIRs, stand out since they are considered major structures and disturbances in the SW, which have been observed to accelerate particles (e.g. Yu et al. [2018]). Since these events are in general highly variable (e.g. Jian et al. [2006,

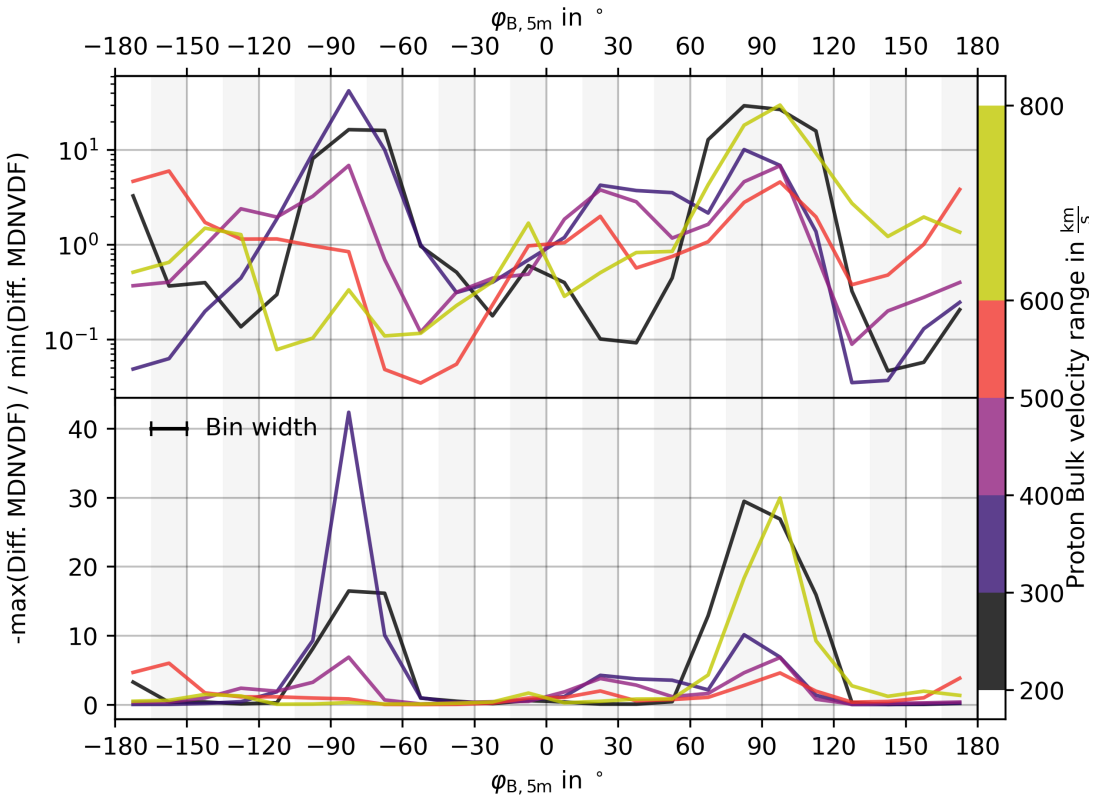

Figure 70: Analogous plot to Fig. 68. The different lines correspond to different SW proton bulk velocity ranges as indicated by the colorbar on the right of the plot.

2019]), this part will only present results, but not discuss them further, since the observation of PUIs during ICME and/or SIR conditions is a topic for a work of its own and the observations of PUIs during these conditions is not the main focus of this work. The interested reader may also refer to Bower et al. [2019] and Moebius et al. [2019]. The following observations are added for the sake of completeness and also mix a broad range of different time periods. If count statistics allows, a follow-up study which observes PUI VDFs in the case of SIRs separates conditions before and after a stream interface or shock, respectively and compares these might reveal new insights towards the acceleration of charged particles in these SW structures. For a meaningful study of PUI VDFs in or close to ICMEs, the VDFs would need to be observed on a per-event bases or at least (if a classification is possible) as a function of different ICME classes. Judging from this works' observations of PUI VDFs with STEREO/PLASTIC which integrate over seven years of data and still observe noisy results due to a small number of events it is doubtful, that data from STEREO/PLASTIC is feasible for such studies. Maybe newer or future instruments (e.g. the Heavy Ion Sensor aboard Solar Orbiter [Owen et al. [2020], Müller et al. [2020]]) provide sufficient data for such purposes.

Here long-term integrations, for which the current data is feasible have been commenced for SIR and ICME conditions separately and examples of the resulting differential MDNVDFs are found in Fig 71. Interestingly for both conditions the resulting distributions feature very distinct anisotropic features, which are similar to observed features during sector reversal wind conditions but even more distinct. For the histograms in Fig. 71 the magnetic field azimuthal angles have been selected such that for each quadrant the strongest signature (in positive or negative direction) of the angular bins is shown. Thus, the shown plots are not always 90° apart and the shown angles partly vary for the different classes. Maybe, preferential acceleration effects globally dominate the PUI distributions in these conditions. However, with the current data no meaningful conclusion can be made.

Similar to the observations of different SW categories, an overview plot of the development of maximum and minimum average differential MDNVDF has been compiled for Fig. 72, in which the results for all wind conditions, which do not include ICMEs and SIRs are also included for comparison. What is interesting, is that one of the local maxima during SIR conditions exceeds every plot within Fig. 68 by almost a factor of ten. Also the maxima of SIRs are shifted by $\sim 20°...40°$ indicating a different pitch angle distribution. Even though for the above mentioned reasons only an incomplete analysis of these conditions can be provided, the observations of pitch angle distributions in chapter 6 also feature an analysis of ICME and SIR conditions.

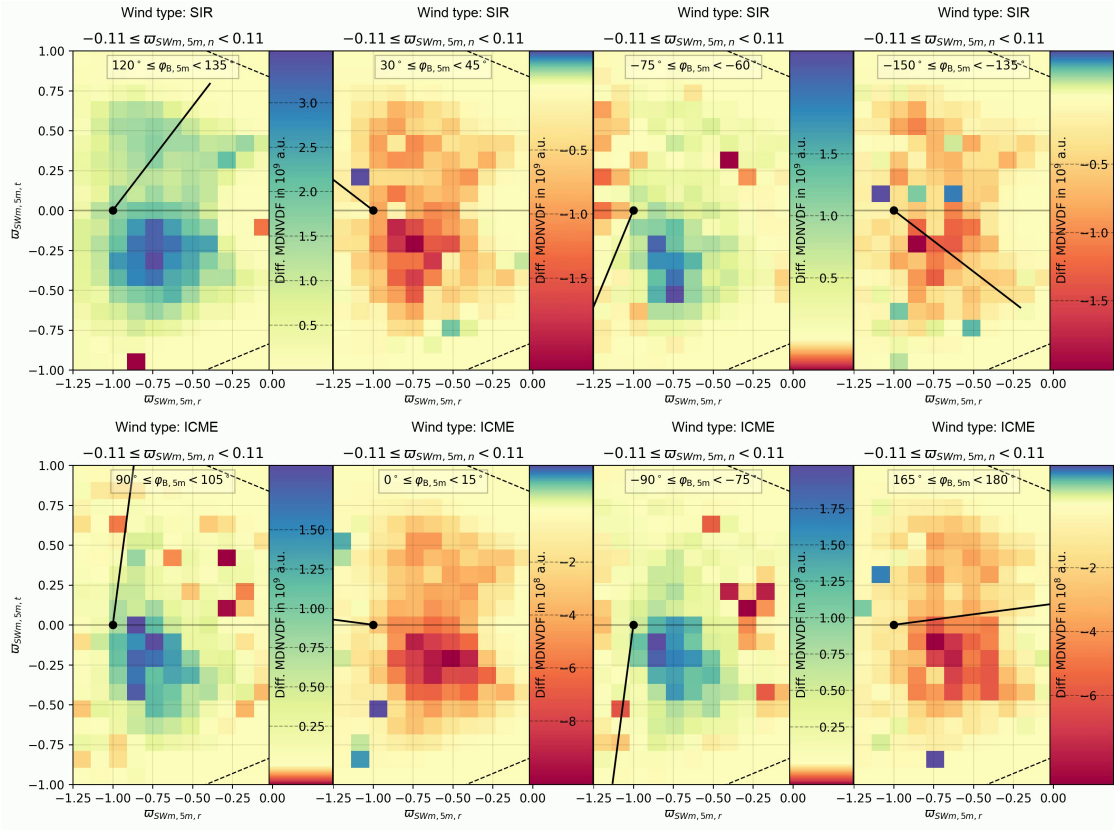

Figure 71: Analogous plot to two rows of Fig. 65. Here, the top row shows differential MDNVDFs during SIR conditions and the bottom row during ICME conditions.

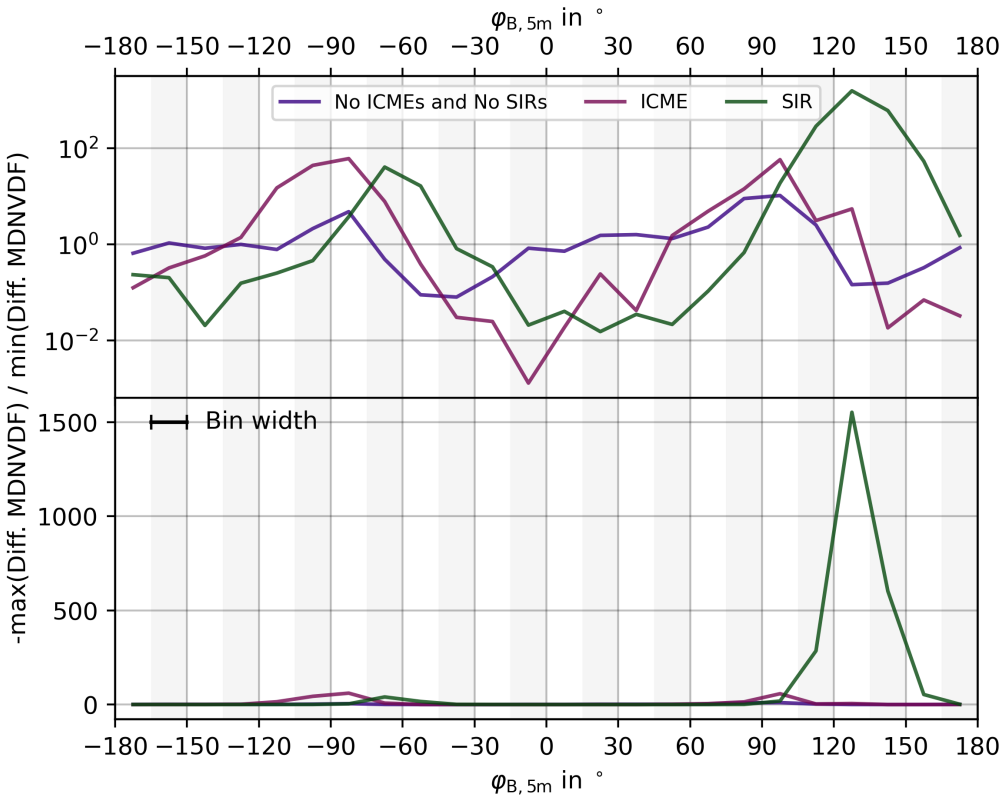

Figure 72: Analogous plot to Fig. 68, but with a comparison of differential MDNVDFs during ICME and SIR conditions to those during all SW conditions, except ICMEs and SIRs.

5.4 Azimuthal differences in the particle detection efficiency

The results of Chapter 5.3 may be affected by the instrument detecting particles with different efficiencies depending on the direction of a particles velocity. This section focusses on probable causes for such an effect and on methods to quantify detection efficiency differences.
The term of detection efficiency means in the context of this chapter, which fraction of incident particles actually contribute to counts derived from PHAs, not the fraction to which the instrument itself detects the particles. This distinction is important, since not all detected events may contribute to PHA derived particle counts, because the data processing unit down-selects detected events for transmission. Therefore, this definition of the term of detection efficiency is more meaningful in the context of this work.

5.4.1 Comparison of the solar wind sector's aperture halves over time

The spacecraft has been rotated by 180° around the radial axis during a period when it was situated behind the Sun seen from Earth [Kucera [2015]]. During that period (end of March to mid-July, 2015) no data and telemetry was submitted, so that for the most part of 2015 no data is available. More interesting for this study is that the spacecraft was flipped during conjunction. This provides an opportunity to investigate the detection efficiency as a function of incoming azimuthal direction. Therefore, in Fig. 73 moving averages of 7 day counts in the main channel of SWS are plotted over time. Hereby, the counts were accumulated over all instrumental azimuth bins from 16 to 32 (left) and from 32 to 48 (right). For Fig. 73, the events were separated into double and triple coincidences. The advantage of that is that effects which only apply to the counts in the SSDs can be visualized this way: For a double coincidence in SWS, a particle must go through the same parts of the instrument (energy-per-charge analyzer and time-of-flight chamber) as a for the beginning of a triple coincidence. For a triple coincidence, in addition a signal in the SSD must be triggered (compare Chapter 3.2.1.iv). A comparison between both can reveal effects which only apply to SSDs (e.g. aging effects).
In addition, the comparison between the left and right halves of the instrument before and after the rotation can yield information about instrumental asymmetries. If there are different detection efficiencies within both halves and these remain constant, it is expected that the ratio of counts within both halves reverses during the spacecraft's flip.
In Fig. 73, for both doubles and triples the left half of the instrument observes higher count rates than the right half before the solar conjunction period of data outtage. This may hint towards an asymmetric detection efficiency. Interestingly, before solar conjunction, the ratio between left and right triples remains fairly constant while the ratio between left and right doubles is more variable: At the beginning of 2008 the ratio is almost 1. Then the double counts in both halves deviate more from each other with a maximum deviation reached mid-2009. Then, the double count rates in both halves become more similar to each other and from 2012 to the solar conjunction data outtage, the ratio between left and right varies slightly with values close to, but larger than 1. Since there is a SSD dependent threshold-energy for a signal to be triggered (e.g. Galvin et al. [2008]), the restriction to double coincidences implicitly selects particles of lower energies compared to triple incidences. So, a direct comparison between doubles and triples is also affected by such selection effects. This is especially problematic for an assessment of the instrumental asymmetries, if there are lower energy populations, which incident into the instrument from a preferred direction. This caveat leads to a matter of concern to the comparison of the counts in the aperture's halves with regard to instrumental qualities: Depending on SW type and magnetic field direction, it is conceivable that parts of the VDF of incidenting particles are asymmetric (compare Chapters 2.1.8 and 2.1.8.iii). These natural asymmetries can at the moment not be directly disentangled from instrumental asymmetries. However, from 2008 on to $\sim$ 2014 the sunspotnumber increased (compare Fig. 28). So, the trend of the double asymmetries observed between 2009 and the solar conjunction period can be an effect of the solar activity cycle, since a different mix of SW condition is expected during solar maximum than in the minimum. The initial increase in asymmetry in the double counts may be due to aging of the instrument. Since the triple count rate comparison is constant, that aging effect has no or minimal effect to triples. A valid stop signal for the time-of-flight measurement is in both cases triggered by electrons which are released out of the SSD on impact of a particle [Galvin et al. [2008]]. For lower energy particles the number of released secondary electrons is lower than for higher energy particles (e.g. Galvin et al. [2008]). So, the likelihood to trigger a valid signal can be smaller for doubles than for triples. For detection, the secondary electrons are guided into a micro-channel-plate to enhance the signal. Afterwards, the particles hit a resistive anode to

trigger the signal. If either the micro-channel-plate or the resistive anode age and therefore lose parts of their detection capability, the weaker signals are more likely to be affected at earlier stages of aging than the stronger signals. Also, it is possible, that parts of the resistive anode or cells of the micro-channel-plate age at a different rate than the other parts. So, aging of these parts can lead to an increase asymmetry, which is visible for doubles but not for triples. However, for this the aging must be limited such, that it only affects double efficiencies and this seems unlikely. For triples, there is an initial asymmetry. So, there is still an effect which is not trivial to be disentangled from the actual asymmetries in the SW VDF during observation.

The trend after the solar conjunction is in its morphology similar for triples and doubles. For conciciveness, the labels for left and right were also flipped after the spacecraft was flipped. Initially the former right half observes drastically more counts than the former left half. Yet, the ratio of new left versus new right quickly decreases and reverses in 2017 for doubles. For triples, it reverses before 2017 as it decreases interestingly quicklier for triples. Apart from a superposition of actual asymmetries in the SW VDF, this reversion in count rates could be explained, if there were an initial aging effect which depends on the number of actually observed counts. Then, in the period before solar conjunction the right half of the instrument might age less because of an initial asymmetry. This is somewhat contradicted by the almost constant left-to-right ratios in the triples, but would explain, why the ratios change so quickly after conjunction.
All in all, the initial comparison between the left and right halves of SWS shows, that it is likely, that there is an asymmetry in the instrumental detection efficiency. However, the curves in Fig. 73 are a superposition of actual asymmetries in the observed particle distributions and instrumental effects. Also, the expectation, that a direct comparison between the ratios before and after the instrument is flipped, is too optimistic. A direct comparison over such large time periods averages over varying SW conditions during different stages of the solar cycle. More fruitful might be a comparison over smaller time scales.

5.4.2 Azimuthally varying detection efficiencies as derived from SECCHI calibration rolls

For calibration of the spacecraft's magnetometer within the SECCHI suite, regularly the spacecraft is rolled by 360° around the radial axis. Each roll maneuver has a duration of 3 hours and about four rolls are commenced per year. An overview of dates of rolls is provided by Tab. 7. Under the assumption, that the conditions in the SW remain similar during the time of interest, it is expected, that the instrument observes a directional distribution mid-roll, which resembles the flipped directional distribution before and after roll. As a visible reference for this, the supplementary figure to Tab. 7 can be considered. Even though a comparison of these is only capable of obtaining the product of the efficiencies of the compared bins, it is possible to obtain, if the instrument observes particles with different probability depending on direction. Therefore such an analysis may lead to means of mitigating instrumental effects in the observed multidimensional VDFs.

For each roll the He^+ events have been histogrammed w.r.t. the azimuthal position in terms of the instrumental bins and time. The analysis is only performed for the main channel of the solar wind sector and per histogram bin the events of two instrumental position bins are accumulated to increase the signal to noise ratio. The time bins have been chosen such that the event accumulation begins 6 h before a roll and ends 6 h after a roll. In terms of temporal resolution, low counting statistics only allowed for 12 bins during the 3 h rotational period (15 mins per bin). Employing the same time resolution for the whole observed time, this results in a total of 60

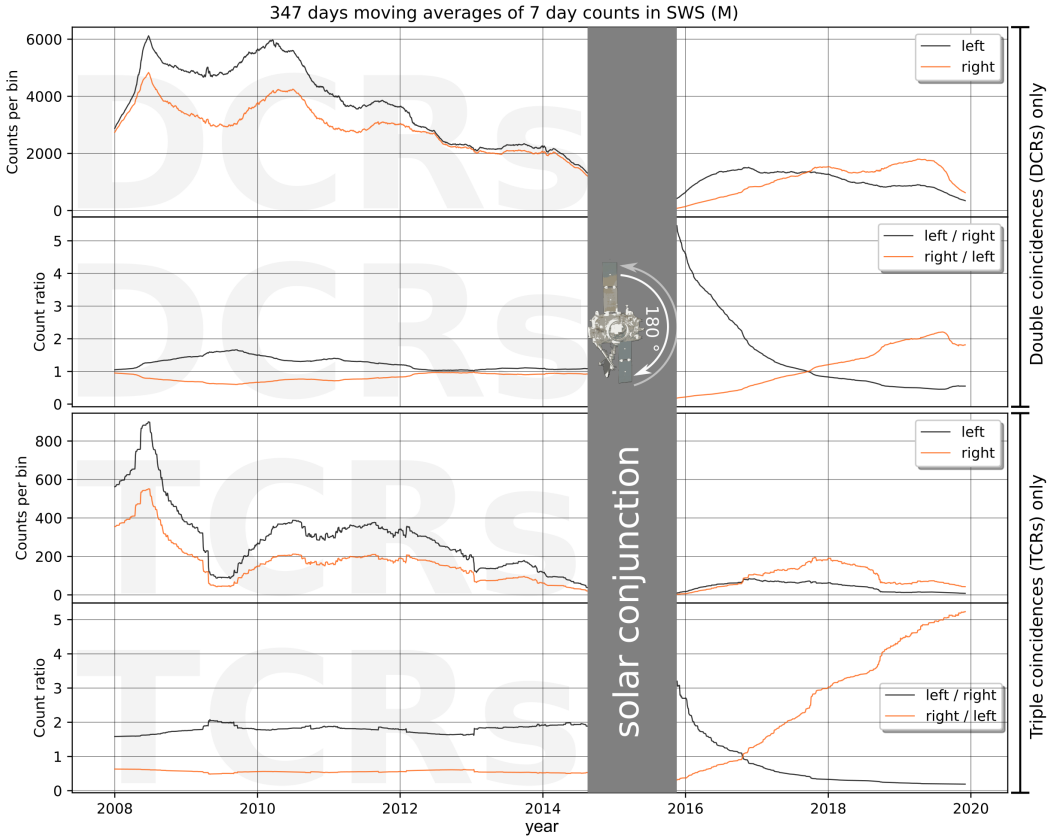

Figure 73: First and third plot from top to bottom: Time series of counts per day for the left half of SWS (black) and the right half of the instrument (orange) averaged with a sliding average over 347 days. The first plot restricts the counts to double coincidences and the third to triple coincidences. Second and Fourth plot from top to bottom: Ratio between left and right half of the instrument (black) and it's reciprocal (orange). The second plot restricts counts to double coincidences and the fourth to triple coincidences. During a period of solar conjunction between Earth and the spacecraft, there was a data outtage. This period is shaded in gray. For completeness, a finer positional binning is provided for TCR counts in Fig. 97 in Appendix C.

time bins for each analyzed roll.
Fig. 74 depicts the data of all rolls as histograms over time and instrumental azimuth bin as well as instrumental elevation (deflection) bin. Unfortunately, another consequence of the low count statistics is that during the period of a single roll for only He^+ PHAs the statistics is very low. However, through the combination of all rolls a larger number of counts can be achieved. To combine the data of several rolls, the superposed epoch method is employed. This means that all time stamps are related to the beginning of their respective roll. So the time axis is transformed into time since/before roll. While this superposition of different times has the disadvantage of mixing different solar wind conditions it allows for better statistics during the rolls and since the effect of the rolls is to be observed the mixing is justifiable.
Such a superposition of all the rolls is shown in Fig. 76. As expected, during the roll the counts change periodically as a function of the position bins. However, in the deflection bins no significant modification is directly visible, at least within the unnormalized counts. Outside the rolls, the distribution in the deflection bins appears as a profile centered around bin 16, which represents the in-ecliptic direction. The structure declines swiftly with increasing distance to the central bin symmetrically at an approximately constant width over time. The version of the deflection-bin-time histogram which is normalized to the maximum of each time-slice has enhanced contrast per time bin. This results in structures becoming visible during the roll. In the following it is assumed that the spacecraft is rolled continuously during the three hour period, by which is meant, that the spacecraft only accelerates at the beginning an the end of the roll to obtain the required angular velocity and to stop the roll, respectively. Unfortunately, the documentation about that topic is not clear. Officially, the rolls are called stepped calibration rolls [Kucera [2014]], which would suggest, that the spacecraft is not continuously rolled, but in incremental steps. This would require numerous acceleration and deceleration processes. In contrast for a continuous roll, only an initial acceleration and a final deceleration is required, as in between the angular velocity is constant angular velocity. To stop and resume the rolls would be less fuel efficient since each acceleration and deceleration requires a thruster burn. Also, each thruster burn requires delicate planning and validation, since erroneous burns can result in deviations from the planned velocity, course deviations and in the worst case contact loss if the spacecraft's antenna is pointed in the wrong direction or the spacecraft rotates such that the solar panels power output does not fulfill the spacecraft's power requirements. Under the assumption of the roll being commenced by two angular accelerations, the roll is at 180° at half of the rolls time (1.5 h). At quarter (0.75 h) and three quarters (2.25 h) of the time the spacecraft is then rolled 90° and 270°. This means, that if structures in the He^+ distribution are broader in horizontal than in vertical direction, the deflection bins are expected to observe broader structures at the quarter and three quarter points and in the normalized version, excursions in broadness of the symmetric distribution are seen. Mid-roll the distribution appears less broad again. An important conclusion from these observations is that the deflection system appears to not influence the detection efficiency as a function of vertical direction of incident. At least, the symmetric nature of the data suggests that. Still, the observations can not rule out so far that the detection efficiency depends on absolute distance from the central bin.

The interpretation of the observations of the azimuthal distribution during the roll is challenging. To form an expectation to compare with, the aberration of the measured azimuthal direction caused by the spacecraft's velocity has to be respected. Since the spacecraft's orbit is almost circular, for the following deliberations, the spacecraft's velocity is considered constant. On its 347 days orbit the spacecraft orbits the Sun at a $\sim$ 1 AU radius thereby covering a distance of $2\pi \cdot 1$ AU. So the spacecraft velocity is estimated as $v^* = 2\pi 1\text{AU}/347\text{d} \approx 31.35\text{km/s}$. This velocity points in tangential direction, while the central position bin of the SWS aperture points

in radial direction. So a particle with a completely radial velocity is expected to be detected at a position bin which is systematically shifted by the tangential velocity component introduced by the spacecraft's own velocity. From basic trigonometry the angle, by which the velocity is offset is computed as $\arctan(v^*/v)$, where v is the particle's velocity. This angle is plotted in Fig. 75 as a function of a particle's velocity for typical velocities of particles in the SW under the assumption, that the velocity is completely radial. With the approximation, that the position bins are evenly spaced, the resulting systematic error in terms of the position bins is then approximated as $32 \cdot \arctan(v^*/v)/45°$. The systematic error is shown in Fig. 75 as well. For a velocity of 200 km/s the aberration is 6 bins large. However, for PUIs this value is unlikely, since PUI velocities typically range at once to twice the bulk velocity of the SW and the aberration decreases with increasing particle velocity. For velocities more typical for PUIs, the aberration is ≤ 4 bins. Even though this is smaller than for 200 km/s, it is still a meaningful aberration.
The expectation which lead into the comparison of the azimuthal bins was that the half of the instrument with bin numbers below 32 measures events more efficiently than the other half. Under the assumption of a spatially symmetric distribution of He^+ PHAs still a density enhancement in the lower half would not be expected during the roll. However, taking into account, that the He^+ PHAs are also expected to follow the magnetic field direction in terms of their velocity distribution more than the bulk SW, and that the average magnetic field direction is expected to point in Parker direction, more particles in the direction, which is un-rolled above bins of 32, are a sensible assumption. Certainly, an investigation of the magnetic field vector data during the roll would help to further study this aspect. Yet, the rolls are commenced for calibration of the magnetometer. This means, the magnetic field data during the rolls can be affected by a modification of the magnetometer's calibration parameters.
The density of the PHA events, which are observed mid-roll by the positional bins below bin numbers of 32 is interesting, since it is increased w.r.t. the densities, which the opposite bins (bin numbers > 32) observe before and after roll. During the roll, also the bins with numbers > 32 have the least counts. This points towards the observed density trend during the roll being a product of the instrumental bins being asymmetric in detection efficiency on the one hand and the particle distribution being also asymmetric on the other hand.
It is interesting that if both preliminary conclusions were true, that then the instrument's efficiency is exactly the opposite of the direction in which He^+ densities are enhanced. If this were not only the case for He^+, but for a larger number of other SW ions, then maybe the asymmetries in the detection efficiencies were due to one half of the instrument aging faster, since it is in contact with a higher rate of particles than the other half. However, this assumption does not hold true to a consideration of Fig. 73: The time series of the ratio between left and right counts in both doubles and triples does not suggest, that the right half gradually counts less events in comparison to the left half over time. For a detailed review of 73, the beginning of this investigation of instrumental asymmetries (Chapter 5.4.1) is referred to.
Also, only He^+ events are involved into this analysis. The scheme that the instrument employs to select which events are sent to earth as PHAs is designed to select a fairly constant number of events per energy per charge step with the additional condition of selecting events out of pre-defined boxes, the coordinates of which are defined by time-of-flight, energy and energy-per-charge. The priority rates are tailored to restore the original rate through priority-weighting, at least on average. Since the He^+ PHAs contain events from different priorities as well as partly also events which are not triple but double coincidences, it can not be guaranteed that the priority weighting also restores the original azimuthal distribution. Interestingly, even the priority rates are not stored as a function of azimuthal position bin, they are provided as a function of deflection step (at least for counts within SWS), but as one rate per two bins. Hence, an inversion of systematic influences of the PHA selection is at least partly reversed by the priority weighting

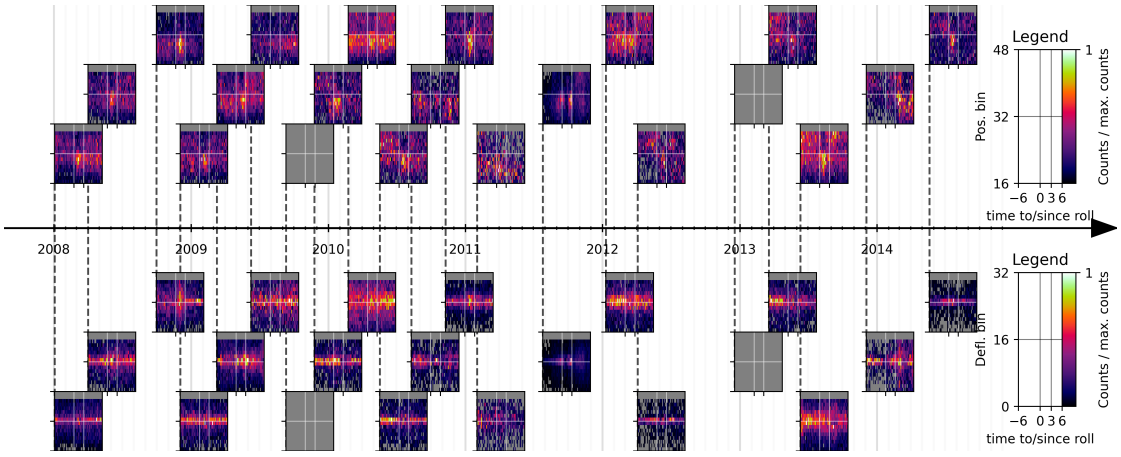

Figure 74: Collection of histograms of He^+ PHA events. The histograms show the time development of events per azimuthal position bin (above the central time axis) and latitudinal deflection bin (below the central time axis) during the rolls. Each pair of azimuthal position and latitudinal deflection histograms corresponds to one calibration roll. The dashed vertical lines connect the histograms to the central time axis which indicates year and month of the roll.

in terms of the distribution in deflection bins. This might also explain the qualitatively different and in total more plausible behavior of the deflection bins during the roll.
Performing this analysis for different ions might help to shed light on the plausibility of the proposed ideas of explaining the unexpected behavior of the positional bins. Especially the plausibility of the effect of PHA selection may be simpler to prove or disprove with different ions, especially when ions are employed, which reside in different priority boxes than He^+. However, further calibration is required for different ions and since ions like O^{6+} or the various charge states of Fe reside at more populated parts of energy-per-charge vs. time-of-flight vs. energy space, the disentanglement of the counts contributions of the different ions requires in parts different analysis techniques than those employed to separate He^+. Finally, also the assumption that the SW conditions remain similar, may be wrong. However, since Fig. 76 is a combination of all roll events, it is unlikely, that varying SW conditions have a systematic effect on the average, since the SW deviating from average in a similar way for each roll is improbable. Yet, one major problem concerning the variability of conditions remains, as Fig. 74 indicates: Even though low statistics also introduce a high noise factor into the data, it is visible that the directional distribution varies significantly from roll event to roll event. There are also roll events, where the distribution visually changes before or after the roll. So any efficiency factor derived from the rolls must be considered with a high statistical error.

5.4.2.i Comparison between He^+-PHAs and unfiltered PHAs The comparison of the data of different ions requires extensive data preparation which is beyond the scope of this work. Yet, at least one set of different data is available for comparison: Originally, the PHA data features a plethora of different ions, which first need to be carefully filtered in order to compare the directional distributions of different ions to each other. Still, to obtain a directional distribution, knowledge of the particles' mass and mass-per-charge is not necessary. So at least the directional distribution of unfiltered PHA events is readily available. Hereby, unfiltered means that no filtering for the particle species is applied.

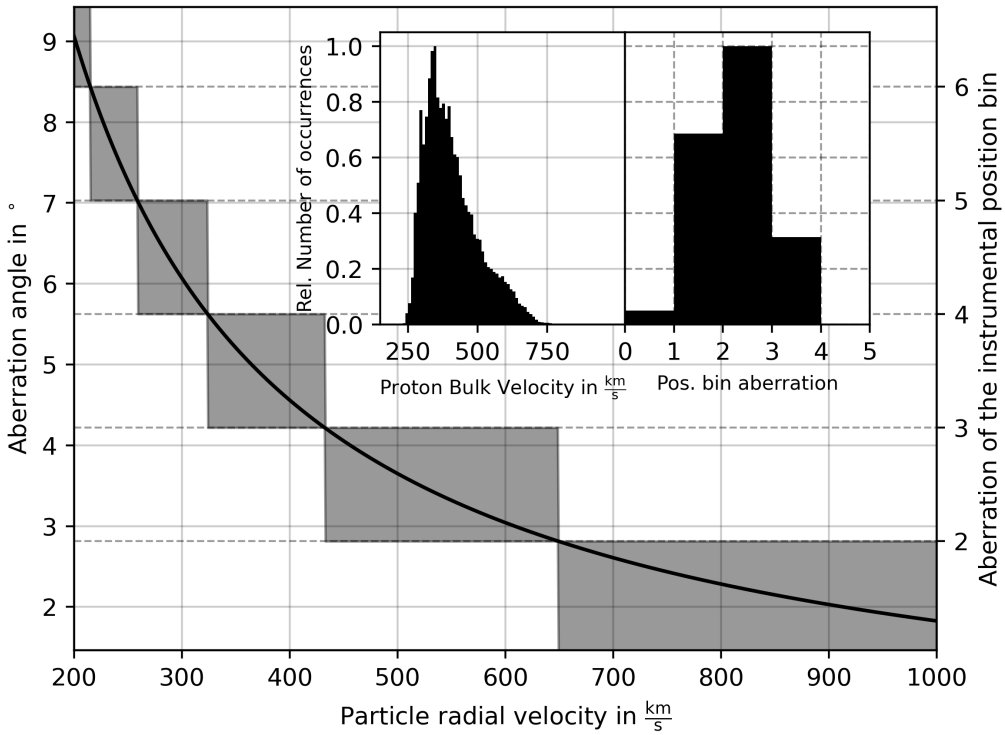

Figure 75: Model aberration angle (left y-axis) caused by the spacecraft's velocity of translation as a function particle radial velocity (x-axis). The gray shaded boxes in the background of the black lined plot indicate zones of velocity and angle, for which the aberration is discretized to a certain number of instrumental position bins (right y-axis). Inset into the plot are two histograms of SW proton observations for reference. Left, the proton bulk velocity is histogrammed and right the corresponding aberration in position bins as computed by the plotted model function. Both histograms are normalized to their respective maximum.

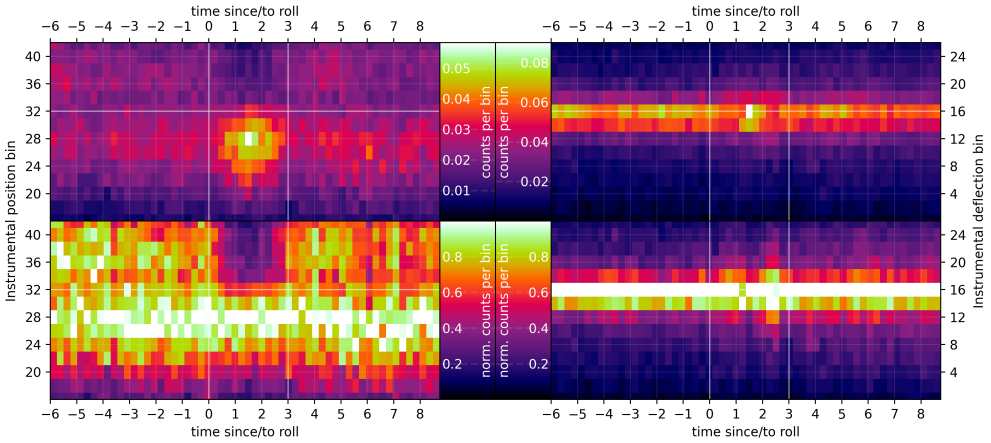

Figure 76: Histogram of He^+ PHA events accumulated over all rolls and histogrammed as a function of time since/to roll in hours ($x-axis$) in instrumental position bins (y-axis, left plots) and instrumental deflection bins (y-axis, right plots). The color scales of the top plots are normalized to the maximum of the respective histogram. In the bottom plots, each y-slice is normalized to its maximum.

In analogy to Fig. 74, Fig. 77 provides an overview over the data collected from all roll events. Especially in 2008 the histograms of single rolls behave similarly. Yet, with increasing time the accumulated data becomes more irregular. Whether this is due to underlying swift changes in the SW attributed to increasing solar activity from 2009 on with solar maximum conditions from 2012 on or due to irregularities introduced from instrumental aging is unknown. However, since irregularities are also seen in data before and after the rolls, it is likely, that swift changes in the SW conditions dominate.
Since the count statistics of unfiltered PHAs allow for lower noise than with He^+ PHAs only, in the following, only the first five rolls are analysed. Fig. 78 is a superposition of these. In comparison to He^+ PHAs only, in the distribution of all PHAs, a drastically larger fraction of the events is found in the half of the instrument with bin numbers > 32 before and after the roll. During the roll, most events are found in the half with bin numbers < 32. This may be due to the aberration of the azimuthal angles of incident caused by the spacecraft's own velocity is expected to shift the average angle of incident into a preferred direction. The expectation is a shift of ≤ 4 bins for He^+ and more for slower particles and indeed before and after a roll in the majority of azimuthal histograms shown in Fig. 76 the center of the center of the distribution of events is found at bin 36 (4 angular steps from the center). During a roll, in the majority of rolls the center is found at bin number 28. This fits the expectation of a preferred direction, since mid-roll the spacecraft is flipped, but maintains its translation velocity. It is interesting, that this effect is very prominent for unfiltered PHAs while almost not to be observed for He^+ PHAs only. This indicates a different incident angle distribution for He^+ PHAs. However, the observed shifts in incident angle can also coincidentally match expected aberration, since the resistive anode has a nonlinear response to the angle of incident (compare Fig. 32 of Chapter 3.2.1.v).
Seen from the instrumental perspective, the discrepancy of the fraction of counts in one half of the instrument w.r.t. the other before and after the roll between unfiltered PHAs and PHAs filtered for He^+ hint towards the directional deviations in the detection efficiency being caused

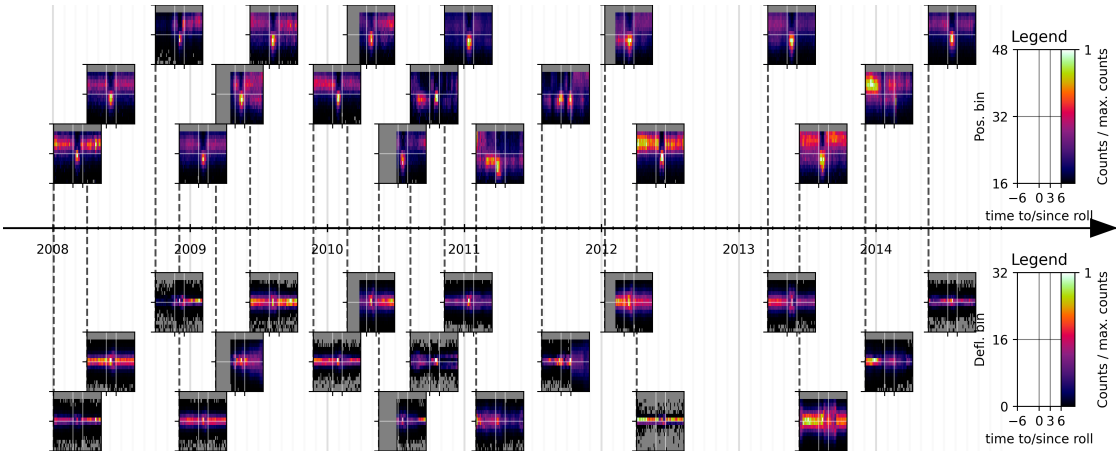

Figure 77: Analogous to Fig. 74, but for unfiltered PHAs instead of He^+ PHAs.

by processes, which depend on the incident particles' species. Since He^+ also on average reside at different energies than the bulk SW, the effect may also a function of energy or energy-per-charge. Of course, this also supports the theory that the deviations are partly or completely caused by the PHA down-selection process. So for a following study, further investigation of the down-selection process is indicated. For that investigation, a monte-carlo approach could be employed which simulates the selection processes by sampling from a random distribution of simulated particles and compares their directional distribution to a directional distribution which is obtained in the following way: A subset of the sampled particles is drawn randomly according to the instrument's PHA selection scheme. Base rates and priority rates can be computed from the particle sample and the subsets and enable the application of simulated priority weights. The second directional distribution to compare with is calculated from the subset, respecting priority weights. The comparison of both (provided, the process is repeated until statistical significance is reached) is expected to prove or disprove, whether the PHA down-selection process systematically influences the observation of directional distribution of particles. The challenges to such a study would be the seed population of particles. Since the process selects particles based on expected particle species and energies, it is necessary to sample a population of particles as observed in the SW (not just a single particle species). The energy ranges and initial directional distribution of the particles are also expected to significantly influence the result of the study.
For now, since the study is concerned with He^+, it seems most reasonable to continue with the analysis of the rolls with data limited to He^+ PHAs.

5.4.2.ii Methods to compute preliminary relative detection efficiencies Within limits of precision, the histograms of Fig. 76 obtained from He^+ PHAs allow to compare the counts in the instrument during twelve phases of the rotation (the twelve time bins) with the conditions before and after the roll. For this, an average histogram of counts as a function of positional bin is derived from the parts of the histogram, which are before and after rotation. Then the position histograms of the twelve time steps of rotation are divided by this average. This results in a comparison of the instrumental bin's counts during the rolls (compare Fig. 79). However, at the mid point of the roll, it is expected that a bin observes a part of the particle distribution, which previously a bin on the other side of the instrument has observed. To be precise: Since the SWS points with its central bin (bin number 32) in sunward direction, the i-th bin now observes

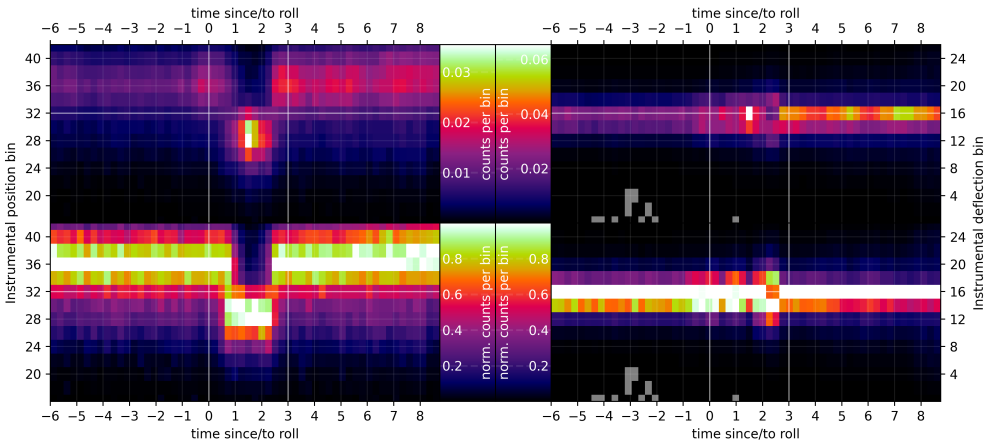

Figure 78: Analogous to Fig. 76, but for events accumulated over the first five rolls only and for unfiltered PHAs instead of He^+ PHAs.

particles from a direction, which before the $(32-(i-32))$-th bin has observed. So, a comparison of the positional histograms during rotations with an accordingly flipped version of the averaged positional histogram before and after the roll is necessary. Such a comparison is provided with Fig. 80. In general, the comparison reflects what has already been observed: For He^+ PHAs the left half of the instrument seems to observe the events more efficiently than for the right half. Hereby, the count comparison is lowest at beginning and end of the roll and reaches a maximum mid-part of the roll. Actually, since only at ~ 1.5 h from the beginning of a roll the instrument is flipped by 180°, only the curves from around this time can be taken into account as a meaningful comparison. The curves from other times are an indicator for the periodic nature of the roll. At maximum, the left half of the instrument observes particles ~ 2.5 times more efficiently than its right counterpart on average and the efficiency minimum is found at the right half with a factor of ~ 0.75. If the reciprocals of these were applied as weights to PHAs in order to mitigate the directional efficiencies, the resulting counts would still not reflect actual particle numbers, since the correction factors derived from this work's method are yet the product of a combination of the efficiency factors of both a bin and its opposing bin. However, employing these factors (and assuming their correctness), directional distributions are expected to be less affected by the different efficiencies. If these factors are interpreted as statistical weights, ideally they normalize the directionally dependent detection probabilities.
However, for this to apply not only the underlying conditions in the SW are required to remain mostly constant, but also the count statistics need to be reliable. For the results in Fig. 80 edge effects are visible, i.e. that the comparison of position bins becomes more unexpected, the closer the considered position bins are to the edge of the aperture. This make sense since it has also been observed that at these directions only a small number of counts is found (compare e.g. Fig. 76) and in general, the comparison between little numbers is statistically volatile.
Also, one effect that the comparison can not reflect is the scattering of particles close to the central direction (around bin 32), which lowers counts close to the center and scatters particles to different directions. Both the flipped and not flipped counts as a function of the position bin which is affected by that in the same way.

This effect can be further investigated by employing a comparison with observations from the electrostatic deflection system of the instrument: When the instrument is rolled 90° and 270°,

the elevation bins effectively observe the azimuthal angle distribution and the azimuthal bins observe the elevation angle distribution. Therefore, again under the assumption that the SW conditions remain similar during the roll, a comparison of both provides a second observation of the instrumental efficiencies. And since the axis observed by elevation bins is perpendicular to the axis observed by the position bins, the distributions of PHA counts as a function of deflection bin may provide a reference distribution which is unaffected by the instrumental effects of the azimuthal bins (or at least a distribution in which all bins are affected similarly). However, instrumental aberrations in the deflection bins are also unknown. So also here, only guideline values can be derived at best.
Also the angular resolution of the deflection bins deviates slightly from the angular resolution of the position bins. While the 32 bins of deflection cover a range of 40° (nominally 1.25° per bin, although the actual acceptance range of the bin is larger for the main channel, as explained in chapter 3.2.1.i), the 32 positional bins cover a range of 45° (nominally 1.40625° per bin). So, a direct comparison between deflection bins and position bins is less precise, the further the bins are away from the center. However, especially for the central bins a comparison between deflection and positional bins is of interest, so for the purpose of this work the bins are directly compared. Such a comparison is provided by Fig. 81. Since different kinds of bins of location are compared, the x-axis is labeled location bin here which represents both position and azimuthal bins. The location bins range from 0 to 32 and represent the positional bins 16 to 48 and the deflection bins 0 to 32. For both, a location bin of 16 is the center. Concerning the systematic error of both kinds of bins not referring to the same angular range, it can be stated, that for locations further away than 8 location bins from the center, the deviation is one bin or more.
In Fig. 81 four effects are superimposed. For one, it is unknown whether the instrument has been rotated clockwise or counterclockwise. For both cases different bins need to be compared (compare Tab. 7). Secondly, under the assumption that the azimuthal distribution is symmetrical, in the comparison flipped averages can be utilized, which increases statistical significance. The results of this are also shown for a clockwise or counterclockwise roll. Since all cases are fairly similar in their result, an average of all is also plotted, which is just intended as a guideline for the eye. In grayscale also the curves of Fig. 80 are plotted, but as a reciprocal, because in Fig. 80 momentary counts are compared to counts before and after the roll and in Fig. 81 the comparison is commenced in different directions. For the right side and partly the left side of the instrument both the position-position and the position-deflection comparison agree in their assessment, which side observes particles more efficiently. Also for location bins of $\tilde{}16 \pm 8$ bins, the values of the correction factor are similar. However, with increasing distance from the center, the deviation between both comparisons increases in the left half. Interestingly, at the right half the results remain fairly similar (considering, how noisy the data of both comparisons is). The interesting part is within 8 bins of the central location bin 16. Here, the correction factor increases to ~ 4 with decreasing distance to the center which is representation of the positional detection being inefficient close to the central bin due to scattering.

5.4.2.iii Conclusions from the analysis of the rolls The rolls of the spacecraft have provided direct insights into the detection efficiencies of the instrument as a function of position bin. However, exact correction factors could not be obtained.
The comparison between positional and positional bins in azimuth for He^+ PHAs showed that the left half of the instrument tends to observe particles more efficiently than the right half. From the comparison between positional and deflection bins a direct observation of the fact that the central position bins detect particles less efficiently has been made.
However, to obtain a meaningful comparison, all rolls which this work investigated, needed to be superimposed, since the He^+ PHAs are scarce in counts during a 3 h time interval. So, data

from considerably different times, solar wind and solar cycle conditions contributed to the comparison. Also, for the comparison of before and after the roll to during the roll the assumption needed to be made that during the roll the particle distributions and SW conditions change little. Particularly during solar maximum conditions the validity of this assumption is questionable.
To obtain a larger number of events, unfiltered PHAs (i.e. PHAs which have not been preselected for their species) have been analogously compared. These PHAs allowed for single rolls to be investigated and showed, that the distributions can change considerably during a roll and that the detection efficiencies yield contrary results for He^+ PHAs, than for unfiltered PHAs. This lead to the idea that the instrumental downselection process of PHAs which are sent to Earth, introduces systematic effects, which affect the directional distribution.
In future studies, the PHAs of different species should be investigated in a similar way to evaluate further by how much the directional dependence of the detection efficiency is affected by particle species. Also simulations of the down-selection process may gain insights about possible contributions to the directionality of the detection efficiency.
Still, within all these restrictions and caveats, the following statements can be made: At least for He^+ PHAs, the instrument observes particles with a strong asymmetry (factors of ~ 2 are probable between both sides of the instrument). The positional bins have a hole in detection efficiency, which is at the center of the instrument. The values found from this study are not certain, but provide a first guideline.

Official event number	Year	Day of year	time (UTC)
3	**2008**	3	07:10 UT
4	-	92	10:35 UT
6	-	274	06:55 UT
7	-	337	14:50 UT
8	**2009**	69	01:20 UT
9	-	160	09:50 UT
10	-	253	12:45 UT
11	-	328	14:15 UT
12	**2010**	54	02:10 UT
13	-	138	00:25 UT
14	-	222	08:10 UT
15	-	313	08:30 UT
16	**2011**	32	13:15 UT
18	-	207	07:15 UT
20	**2012**	10	02:40 UT
21	-	94	14:15 UT
24	-	353	10:15 UT
25	**2013**	78	10:10 UT
26	-	162	08:35 UT
28	-	337	14:30 UT
30	**2014**	140	14:45 UT

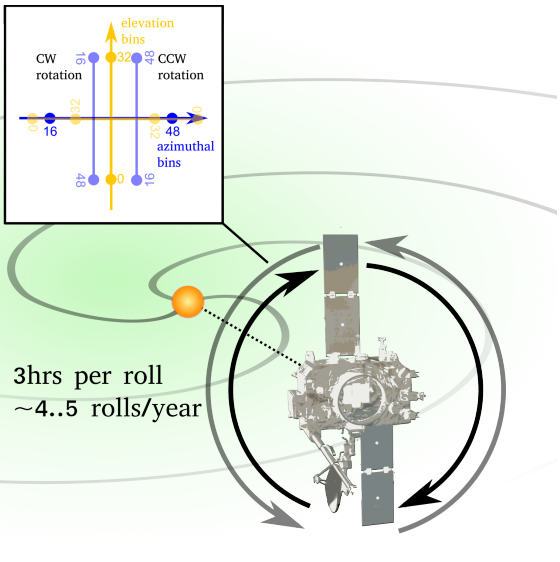

Table 7: Left: List of SECCHI Stepped Calibration Rolls employed in this works analysis. The roll events have been documented in publicly available planning and weekly meeting notes. However, for some events the exact time of day has not been documented. For this works analysis only events since 2008 have been respected, which were fully documented. Only these are listed in the table. Right: Artistic illustration of the STEREO spacecraft and its roll axis. Unfortunately, it is unknown, whether the spacecraft is rotated clockwise (CW) or anticlockwise (CCW). Hence, the inserted panel describes the orientation of SWS azimuthal (blue) bins and elevation (yellow) bins during both cases. Hereby, the fully shaded lines represent un-rolled conditions and the more transparent shaded lines represent orientations during a 90° roll.

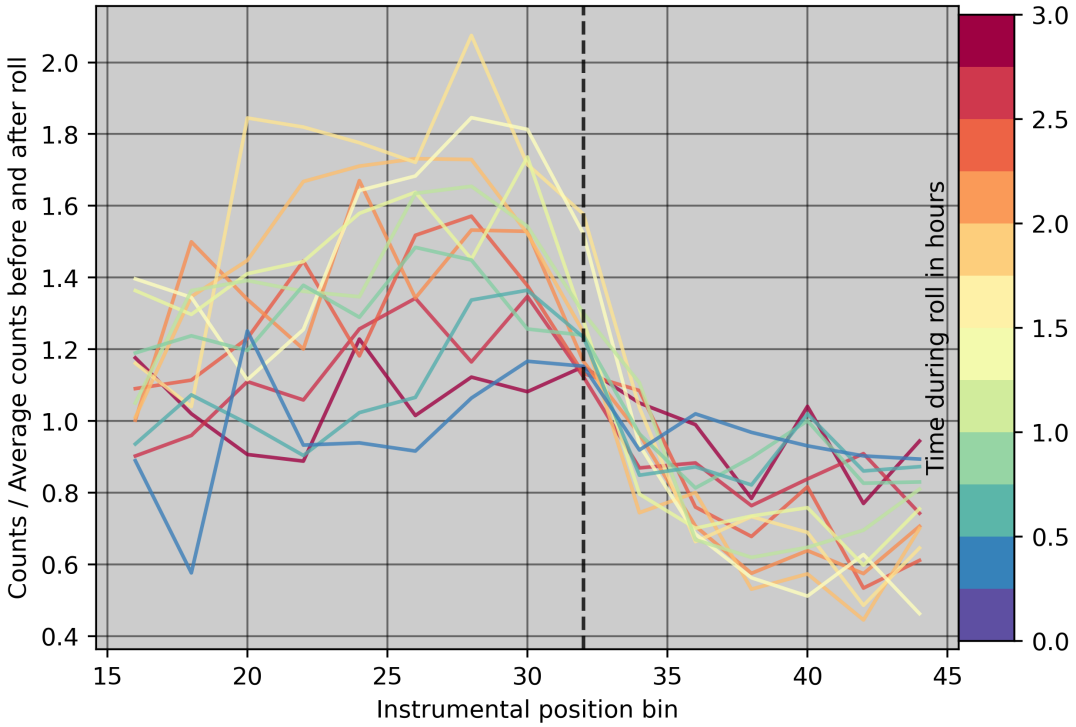

Figure 79: Fractions of counts during a period of a calibration roll (y-axis) vs. the average counts before and after a roll of the instrumental position bins (x-axis). Each curve represents a different time period during the rolls. The time period is color coded and the digitization into time periods indicated by the color bar on the right which plots time in hours from the start of a roll. For this plots, the data of all rolls was superimposed.

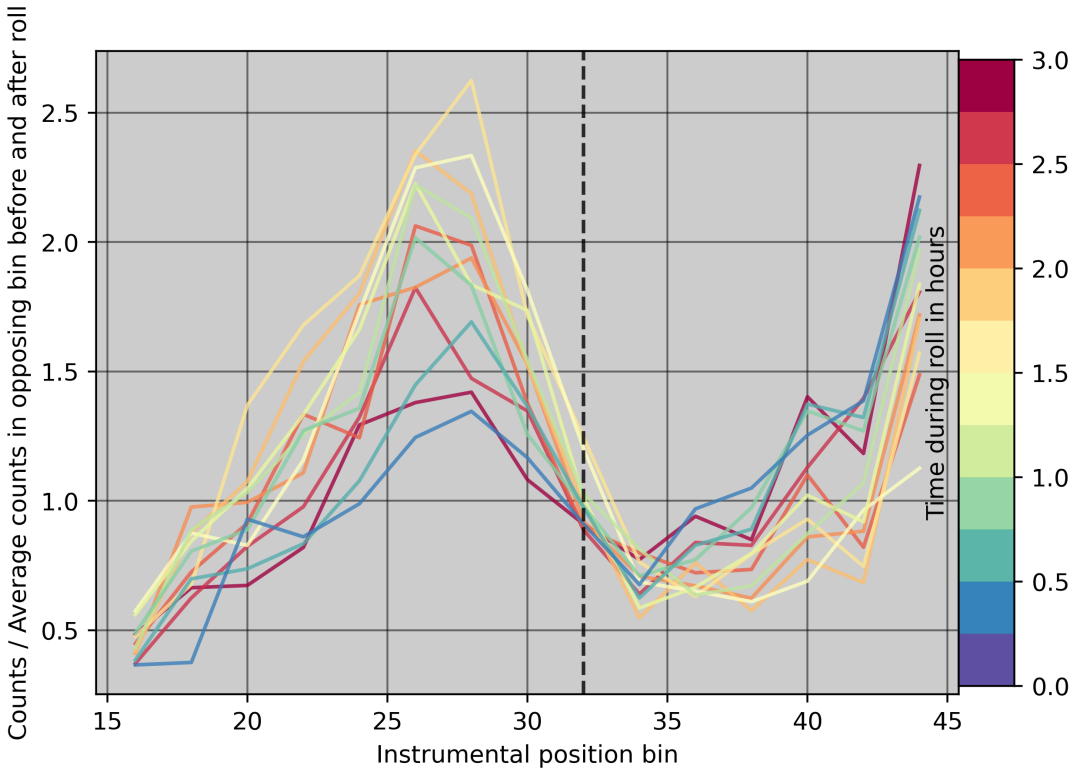

Figure 80: Analogous to Fig. 79, but the fraction of counts are counts of a bin during the roll vs. average counts of the opposing bin before and after roll. Here, the opposing bin of a bin is at the position which is obtained from flipping around bin number 32 (i.e. the opposing bin to bin number 24 is bin number 40).

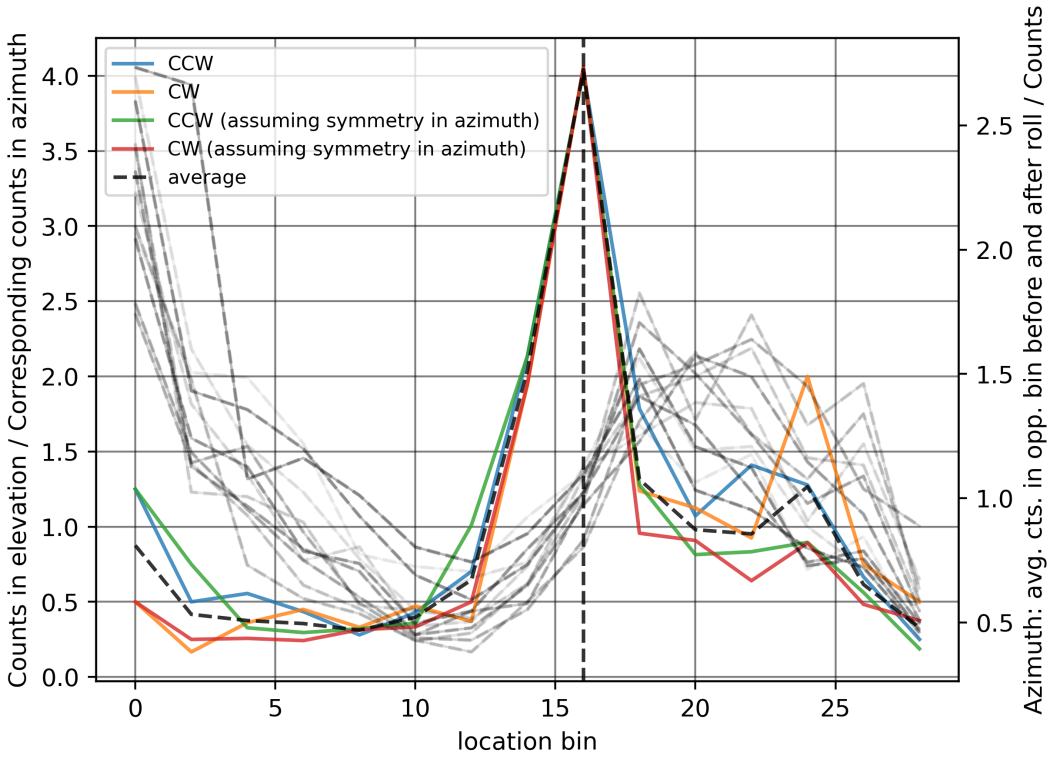

Figure 81: Comparison between counts in elevation bins during a roll w.r.t. their counterpart in azimuth before and after the roll (compare Tab. 7). On the left y-axis the fraction of these is plotted as a function of location bin (x-axis). The fractions are plotted for four different assumptions: For the blue curve, a counter-clockwise roll is assumed. For the orange curve, a clockwise roll is assumed. For the green curve, a counter-clockwise roll is assumed and the comparison in azimuth is obtained under the assumption of symmetry. This means, that an average of the azimuthal distribution and the same distribution but flipped is made for comparison. The red curve is the analogous, but under the assumption of a clockwise roll. In gray shades in the background of the plot the data of Fig. 80 is plotted (right y-axis) in a version which is transformed into the coordinate system of the location bins.

6 Pitch angle distributions of He^+ pickup ions observed with STEREO / PLASTIC

Chapter 5 presents 3d observations of He^+ PUI VDFs. This chapter presents findings similar to Drews et al. [2015] who also found density enhancements at parts of velocity space perpendicular to the local magnetic field. Moreover, the observed signatures are strongest if the azimuthal magnetic field direction is approximately perpendicular to the center of the aperture of SWS.
Based on these findings this chapter revisits these findings and presents observed pitch angle distributions. While the underlying 3d distribution is partly obscured by a reduction of three dimensional velocities to this single quantity, the pitch angle, the observation of pitch angle distributions grants more oversight over observations of the multidimensional parameter space that observations of 3d VDFs as a function of solar wind conditions and magnetic field orientation are. Also, the focus on the pitch angle may lead to insights into underlying acceleration processes.

6.1 Introductory discussion of instrumental limitations

The limited field of view of PLASTIC's SWS aperture also creates limitations for the pitch angles of PUIs which are observable. The range of observable pitch angles depends on the configuration of the velocity $\vec{v}_a$[5] of the reference frame a, the local magnetic field vector $\vec{B}$ (primarily its direction) and the total particle velocity $\vec{v}$. This does not necessarily mean, that not all pitch angles in the range of 0° to 180° can be observed, but for the majority of configurations their observable range is limited. If different configurations are mixed in the accumulation of a pitch angle distribution, this may result in skewed distributions. Hence, it is necessary to know the limitations in terms of observable pitch angles.

Closely connected to the problem is, that not only the range of observable pitch angle, but also the measurement probability of a particle at a certain pitch angle varies in the outlined scenario. In the following, this issue is presented under the assumption of the following requirements:

- The particles gyrate around the local magnetic field.
- The phase space distribution of the observed particle population is gyrotropic.

While the first requirement naturally applies to PUIs, the second is a common assumption for PUIs and is at the current instrumental state of the art impossible to be either proven or disproven. The second requirement implies, that the phase of the gyration, at which the particle is found close to the instrument is a stochastic quantity. For some configurations it may be possible, that the particle's velocity is situated within the aperture for only a part of the gyro orbit (compare Fig. 82). A particle with such a configuration is less likely to be observed than a particle with an orbit fully situated within the instrument's aperture. The cause for this selection effect on configurations is the instrument's geometry. Hence, a systematic error emerges for observed distribution functions. In this section, an idea is presented how to mitigate that systematic error.
The goal of the following deliberations and calculations is to obtain a measure for the range of

[5] Not to be confused with the Alfvénic velocity v_A defined in Chapter 2.1.6.

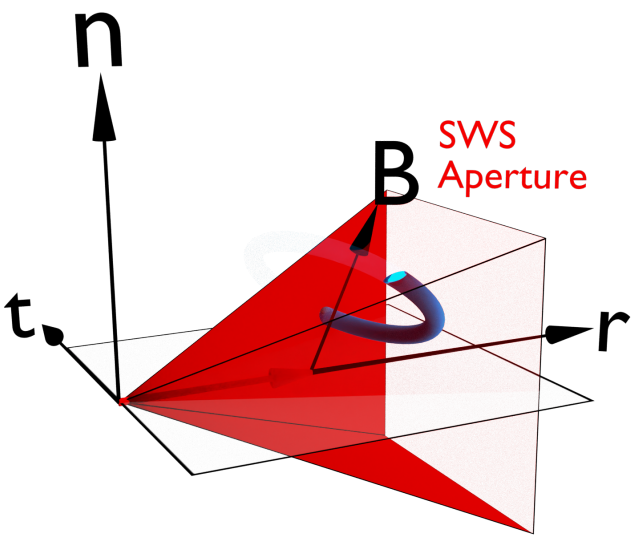

Figure 82: Artistic rendition of the aperture of PLASTIC's Solar Wind Sector in radial (r), tangential (t) and normal (n) velocity space. Through a red arrow the reference velocity is indicated, from which the magnetic field vector $\vec{B}$ starts. Centered around the local magnetic field a ring is found, which represents a sample particle's velocities at different gyration phases but same pitch angle. For visualization of the systematic error arising from the geometric limitations of the aperture only the part of the ring, which lies within the aperture is shown.

pitch angles covered by the instruments aperture (in radians). Via division by a full circle (2π) a factor is obtained which represents the probability of measurement emerging from the stochastic distribution of gyration phases. The reciprocal of which can be seen as a correction factor which is utilized analogously to a correction factor of the preceding chapter.

6.1.0.i Construction of a pitch-angle invariant ring To construct a ring which represents all gyro phases of a particle with the velocity $\vec{v}$, it is useful to split its reference-velocity transformed version $\vec{v} - \vec{v}_a$ into a field-parallel and a field-perpendicular component such as $\vec{v} - \vec{v}_a = \vec{v}_\parallel + \vec{v}_\perp$. Instead of expressing these velocities through vectors, in the following their absolute values are employed, i.e. $\vec{v}_\parallel =: v_\parallel \hat{e}_\parallel$ and $\vec{v}_\perp =: v_\perp \hat{e}_\perp$. Here, $\hat{e}_\parallel$ and $\hat{e}_\perp$ are unit vectors which point in parallel and in perpendicular direction. In the following, the magnetic field direction is expressed via the spherical coordinate angles φ_B and ϑ_B, where $\varphi_B \in [-\pi, \pi]$ and $\vartheta \in [-\pi/2, \pi/2]$. Then, a different representation of $\hat{e}_\parallel$ is

$$\hat{e}_\parallel = \begin{pmatrix} \cos(\varphi_B)\cos(\vartheta_B) \\ \sin(\varphi_B)\cos(\vartheta_B) \\ \sin(\vartheta_B) \end{pmatrix} \ . \tag{97}$$

The vector $\hat{e}_\perp$ may point into a variety of directions, which all are perpendicular to the magnetic field vector, but since $\vec{v}_\perp = v_\perp \hat{e}_\perp$ has to be fulfilled, it points into a direction associated with the particles gyration phase. If the gyration phase is defined as an angle ϕ, the construction $\hat{e}_\perp = \cos(\phi)\hat{e}_{\perp,1} + \sin(\phi)\hat{e}_{\perp,2}$ suffices. Here, $\hat{e}_{\perp,1}$ and $\hat{e}_{\perp,2}$ are defined by

$$\hat{e}_{\perp,1} = \begin{pmatrix} \cos(\varphi_B)\sin(\vartheta_B) \\ \sin(\varphi_B)\sin(\vartheta_B) \\ -\cos(\vartheta_B) \end{pmatrix} \tag{98}$$

and

$$\hat{e}_{\perp,2} = \begin{pmatrix} \sin(\varphi_B) \\ -\cos(\varphi_B) \\ 0 \end{pmatrix} \ . \tag{99}$$

With these, the ring of the particles gyro phases in velocity space is constructed under utilization of

$$\vec{v}_\phi = \vec{v}_a + v_\parallel \hat{e}_\parallel + v_\perp \left(\cos(\phi)\hat{e}_{\perp,1} + \sin(\phi)\hat{e}_{\perp,2}\right) \ . \tag{100}$$

6.1.0.ii Intersections of the ring and the aperture boundary The boundaries of the aperture's coverage in velocity space are described via four vectorial planes: Two for the boundaries in azimuthal direction and two for the elevation boundaries. Let $\varphi_{\min,\max} = \pm 22.5°$ define the minimum and maximum azimuthal acceptance angle of the instrument and $\vartheta_{\min,\max} = \pm 20°$ the analogous angle in elevation direction. Then, the unit vectors $(\cos(\varphi_{\min,\max}), \sin(\varphi_{\min,\max}), 0)$ and $(0, 0, 1)$ describe the azimuthal boundary layers' directions. The coordinate system for this description is in spacecraft frame RTN. Conveniently, the origin is set as the layers origin for construction. Hence, the boundary layers intersect with the coordinate origin. The unit vectors $(\cos(\vartheta_{\min,\max}), 0, \sin(\vartheta_{\min,\max}))$ and $(0, 1, 0)$ describe the directions of the elevation boundaries' layers. Via the vector product layer normals are computed and the boundary layers are defined

by

$$B_{az}: \left(\vec{X}_{B,az} \cdot \left(\begin{pmatrix} \sin(\varphi_{\min,\max}) \\ -\cos(\varphi_{\min,\max}) \\ 0 \end{pmatrix}\right)\right) = 0 \text{ for the azimuthal boundary, and} \tag{101}$$

$$B_{elev}: \left(\vec{X}_{B,elev} \cdot \left(\begin{pmatrix} -\sin(\vartheta_{\min,\max}) \\ 0 \\ \cos(\vartheta_{\min,\max}) \end{pmatrix}\right)\right) = 0 \text{ for the elevation boundary.} \tag{102}$$

The layer normals are unit vectors. For simplicity, the unit vector $\hat{e}_\varphi$ represents in the following the layers' normal vectors. From the replacement of $\vec{X}_{B,az}$ or $\vec{X}_{B,elev}$ with $\vec{v}_\phi$ from eq. 100 the condition

$$0 = \vec{v}_a \cdot \hat{e}_\varphi + v_\parallel \hat{e}_\parallel \cdot \hat{e}_\varphi + v_\perp \left(\cos(\phi)\hat{e}_{\perp,1} \cdot \hat{e}_\varphi + \sin(\phi)\hat{e}_{\perp,2} \cdot \hat{e}_\varphi\right) \tag{103}$$

for intersecting gyration phases is obtained. However, the trigonometrical functions make that equation tedious to treat. Instead, the trigonometrical functions are substituted by the variables $\chi := \cos(\phi)$ and $\xi := \sin(\phi)$ with the condition

$$\chi^2 + \xi^2 = 1 \ . \tag{104}$$

With this approach, information about the quadrant of ϕ is lost. Means to reconstruct that information are discussed after a an analytical solution for χ and ξ are found. To compute ξ, eq. 103 is transformed to

$$\chi = -\xi \frac{\hat{e}_{\perp,2} \cdot \hat{e}_\varphi}{\hat{e}_{\perp,1} \cdot \hat{e}_\varphi} - \frac{\left(\vec{v}_a + v_\parallel \hat{e}_\parallel\right) \cdot \hat{e}_\varphi}{v_\perp \hat{e}_{\perp,1} \cdot \hat{e}_\varphi} \text{ , which} \tag{105}$$

is inserted into eq. 104 to obtain

$$1 = \xi^2 + \left(\xi \frac{\hat{e}_{\perp,2} \cdot \hat{e}_\varphi}{\hat{e}_{\perp,1} \cdot \hat{e}_\varphi} + \frac{\left(\vec{v}_a + v_\parallel \hat{e}_\parallel\right) \cdot \hat{e}_\varphi}{v_\perp \hat{e}_{\perp,1} \cdot \hat{e}_\varphi}\right)^2 \ . \tag{106}$$

This transforms into the quadratic equation

$$0 = \xi^2 \left(1 + \left(\frac{\hat{e}_{\perp,2} \cdot \hat{e}_\varphi}{\hat{e}_{\perp,1} \cdot \hat{e}_\varphi}\right)^2\right) + 2\xi \cdot \frac{\hat{e}_{\perp,2} \cdot \hat{e}_\varphi}{\left(\hat{e}_{\perp,1} \cdot \hat{e}_\varphi\right)^2} \cdot \frac{\left(\vec{v}_a + v_\parallel \hat{e}_\parallel\right) \cdot \hat{e}_\varphi}{v_\perp} + \left(\frac{\left(\vec{v}_a + v_\parallel \hat{e}_\parallel\right) \cdot \hat{e}_\varphi}{v_\perp \hat{e}_{\perp,1} \cdot \hat{e}_\varphi}\right)^2 - 1 \ . \tag{107}$$

For readability, the coefficients of the quadratic equation are substituted. The substitution variables are defined by

$$d_1 := \frac{\hat{e}_{\perp,2} \cdot \hat{e}_\varphi}{\hat{e}_{\perp,1} \cdot \hat{e}_\varphi} \tag{108}$$

$$d_2 := \frac{\left(\vec{v}_a + v_\parallel \hat{e}_\parallel\right) \cdot \hat{e}_\varphi}{v_\perp} \tag{109}$$

$$\bar{a} := 1 + d_2^2 \tag{110}$$

$$b := 2d_2 \frac{\hat{e}_{\perp,2} \cdot \hat{e}_\varphi}{\left(\hat{e}_{\perp,1} \cdot \hat{e}_\varphi\right)^2} \tag{111}$$

$$c := \frac{d_2^2}{\left(\hat{e}_{\perp,1} \cdot \hat{e}_\varphi\right)^2} - 1 \ . \tag{112}$$

This results in the simple quadratic equation

$$0 = \bar{a}\xi^2 + b\xi + c \text{ , which} \tag{113}$$

is solved by

$$\xi_{1|2} = -\frac{b}{2\bar{a}} \pm \sqrt{\left(\frac{b}{2\bar{a}}\right)^2 - c} \,. \tag{114}$$

To obtain solutions for χ from eq. 114, in the definition of the substitution variables $\hat{e}_{\perp,1}$ and $\hat{e}_{\perp,2}$ need to be interchanged. This is from a computational point of special importance for situations in which the scalar product of $\hat{e}_{\perp,1}$ and $\hat{e}_{\varphi}$ is zero. Since $\hat{e}_{\perp,1}$ and $\hat{e}_{\perp,2}$ are perpendicular to each other, it is unlikely that the scalar product of $\hat{e}_{\perp,2}$ and $\hat{e}_{\varphi}$ is zero as well and a solution for χ can be computed instead.

Another special case appears, if the content of the square root in eq. 114 is zero or smaller than zero. If zero, only one intersection point is obtained. In that case, only an infinitesimal fraction of the ring which represents the particles gyration is either inside or outside the aperture, while the rest of the ring has an opposite state. In that case, the ring is considered either fully inside or outside the aperture.
The ring is also either fully inside or outside the aperture if the square roots content is below zero, since then no real valued solutions for the intersections are found. In both cases it is checked, whether the vector $\vec{v}_{\phi}$ is inside or outside the space with the aperture boundary layer of consideration as boundary for an arbitrary ϕ. For this, e.g. the sign of the scalar product between the layer normal $\hat{e}_{\varphi}$ and $\vec{v}_{\phi}$ can be employed.
For the case, that two solutions are found, the issue remains, that from the solutions of ξ or χ the gyro phases ϕ need to be found where the ring intersects one of the layers with missing quadrant information of the phase ϕ. For the outline of a reconstruction of the missing information, it is assumed, that solutions for ξ are found, but similar deliberations apply, if a solution for χ is found instead. In that case, eq. 104 yields two values for χ per solution of ξ which are $\chi_{1|2} = (1-\xi_1^2)^{1/2}$ and $\chi_{3|4} = (1-\xi_2^2)^{1/2}$. The extra solutions correspond to the lost quadrant information. And one of each pair of solutions $\chi_{1|2}$ and $\chi_{3|4}$ corresponds to a wrong quadrant for ϕ and is therefore a virtual, but not a meaningful solution. ξ and χ are coordinates in a two dimensional cartesian coordinate system defined by the orthonormal base formed by $\hat{e}_{\perp,1}$ and $\hat{e}_{\perp,2}$. In this system, ϕ is the polar angle and therefore the equation $\phi = \arctan_2(\xi, \chi)$ yields ϕ from the discussed solutions. To find out, which of the four values of ϕ obtained from the pairs of solutions (ξ_1, χ_1),(ξ_1, χ_2),(ξ_2, χ_3) and (ξ_2, χ_4), the corresponding vectors $\vec{v}_{\phi}$ are computed and their scalar products with the layer normal $\hat{e}_{\varphi}$. Solutions, for which this scalar product is (sufficiently close to) zero, the vectors $\vec{v}_{\phi}$ are located within the layer and the values of ϕ, from which they are computed, corresponds to a point of intersection.

To determine, at which of the intersection points the ring leaves the aperture and at which it enters the aperture, the ring's tangent $\partial\vec{v}_{\phi}/\partial\phi$ is employed, which is computed by

$$\frac{\partial\vec{v}_{\phi}}{\partial\phi} = v_{\perp}\left(-\sin(\phi)\hat{e}_{\perp,1} + \cos(\phi)\hat{e}_{\perp,2}\right) \,. \tag{115}$$

6.1.0.iii Computed measurement probabilities for selected solar wind configurations and model PUI VDFs Of special interest for this work is, for which pitch angles and PUI velocities (relative to the transporting frame), the measurement probability differs from 1 and therefore influences observed pitch angle distributions. Also from the computation of the

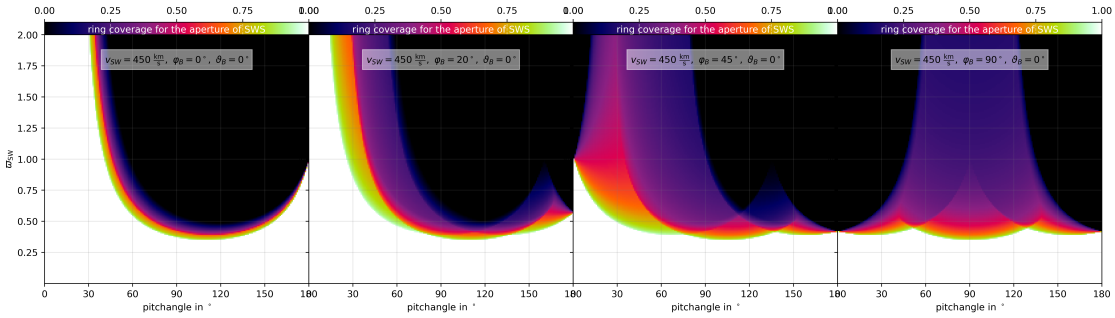

Figure 83: Computed measurement probabilities (ring coverages) as a function of pitch angle and transformed PUI velocity for different magnetic field azimuthal angles.

coverage of a ring within the aperture the limits of the instrument in terms of measurable pitch angles are found, since where the coverage (hence the measurement probability) is zero, a configuration is found for which no particles are expected.
Fig. 83 depicts an overview of ring coverages as a function of particle velocity and pitch angle for four different azimuthal magnetic field angles and a magnetic field pointing within the ecliptic layer and at a SW velocity of 450 km/s. Common for all depicted configurations is, that for $\varpi_{SW} < 0.4$ all pitch angles are covered by the instrument's aperture. Above, the measurement probability decreases for some pitch angles, whereas the areas of decrease change at different magnetic field angles. Depending on the magnetic field configuration, some pitch angles are not measurable at $\varpi_{SW} \sim 1$, which is expected to influence observed PUI pitch angle distributions. At radial magnetic field, pitch angles below 30° are observable throughout the plotted range of ϖ_{SW} with a probability of 1, whereas at Parker configuration at higher ϖ_{SW} two bands of observable pitch angles are found, which decrease in width with increasing ϖ_{SW}. One of which is found at pitch angles below 90° and one above 90°. The latter vanishes quickly with increasing ϖ_{SW}.

The computed measurement probabilities indicate, that the angular configuration of the magnetic field strongly influences the range of observable pitch angles as well as their probabilities of observation. Therefore, a VDF and its pitch angle distribution might appear to systematically change with magnetic field direction, when it is observed with an instrument which has a limited angular acceptance. To illustrate that further, simulated particles are sampled randomly from an isotropic PUI shell distribution at a SW velocity of 450 km/s and magnetic field angles within the ecliptic plane. An isotropic distribution is ideally suited for the purpose of illustration, since an ideal torus distribution would be a delta peak in pitch angle space.
Fig. 84 compares the resulting pitch angle distributions for ideal shell distributions, where for each plot a different value of ϖ_{SW} (no width in ϖ_{SW} space) is selected. Initial analysis showed that if the pitch angle distribution's shape is not modified by the simulated instrument's limited field of view, then it resembles a sine-like shape. From the measurement probabilities shown in Fig. 83 it is expected, that for $\varpi_{SW} < 0.5$ the measurement probabilities are 1 throughout pitch angle space regardless of the magnetic field azimuthal angle. The pitch angle distributions in the top left panel of Fig. 84 match that expectation: No visually detectable significant deviation from the grey-shaded pitch angle distribution of the sampled particles before the measurement probabilities were applied is found there. This changes in the top right panel ($\varpi_{SW} = 0.5$).
Firstly, the pitch angle distributions differ from each other as a function of the azimuthal mag-

netic field angle. Secondly, the pitch angle distribution for a magnetic field angle of φ_B matches the pitch angle distribution for an angle of $-\varphi_B$ flipped around a pitch angle of 90°. Hence, curves look symmetrical, since for each plotted positive angle also its negative equivalent is plotted.
For increased ϖ_{SW} the overall measurement probabilities are decreased further and another trend becomes evident: In pitch angle distributions filtered by the magnetic field azimuthal angle, pitch angle distributions which are observed at magnetic field angles close to (i.) 0° or (ii.) ±180° are favoured over those at angles in between these. The pitch angle distributions for these angles have ring-coverage based measurement probabilities of 1 at pitch angles close to (i.) 0° and (ii.) 180°, respectively. Thus, pitch angle distributions at these angles are measured with increased densities over the other distributions.

6.1.0.iv Implications for the derivation of pitch angle distributions from STEREO/PLASTIC PHAs Due to the limited angular acceptance of the instrument for each magnetic field orientation only parts of the pitch angle distribution are observable through the aperture. The range of observable pitch angles is a delicate function of the relative particle velocity (w.r.t the transport frame in the SW) and the orientation of the local magnetic field, whereas the range also depends on the orientation of the velocity of the transport frame in the SW.
Fig. 85 illustrates the dependence of observable pitch angles on the magnetic field azimuthal direction and compares with STEREO/PLASTIC observations of He^+ ions for selected values of ϖ_{SWp} and Fig. 86 shows modelled minimum and maximum pitch angles observable within the aperture as well as their difference for $\varpi_{\mathrm{SWp}} = 1$ as a function of φ_{B} and ϑ_{B}. For the next chapter, these plots serve as a guideline for the discussion of STEREO A/PLASTIC's measurements. From Fig. 86, a general rule of thumb for radial SW velocities and magnetic field configurations within the ecliptic plane can be seen, which states that the average observable pitch angle α_m at that configuration is estimated by $\alpha_m \approx 180° - |\varphi_{\mathrm{B}}|$.
The main implications for the derivation of pitch angle distributions are.

Implication 1 Only a part of the pitch angle distribution can be observed at once by the instrument.

Implication 2 A gyrating particle's probability to incident into the instrument's aperture scales with the fraction of the part of the gyro orbit,which is covered by the aperture in velocity space, as compared to the whole gyro orbit. So, pitch angle distributions derived from observation do not reflect the actual pitch angle distribution and need to be divided by that probability.

As a consequence of 6.1.0.iv, an additional challenge is introduced into the interpretation of derived pitch angle distributions: Since with a limited FOV it is impossible to observe all pitch angles for a selected magnetic field configuration, a full pitch angle distribution can only be derived from observations at multiple pitch angle distributions. However, for the validity of pitch angle distributions found from such a superposition of different magnetic field configurations the assumption is inherent that the pitch angle distribution does not change as a function of the magnetic field angle.
Yet, the possibility of a dependence of the pitch angle distribution of the magnetic field configuration can not be discounted: Initially, the pitch angle at which the PUIs are injected into the SW is a function of the angle between the magnetic field vector and the solar wind velocity (compare e.g. Fig. 17 of chapter 2.2.5). If not swiftly isotropized or even only partially, anisotropic features remain in the PUI VDF, which are then expected to manifest in a dependence of the pitch angle distribution of the magnetic field orientation. And, since to find new insights into whether anisotropic features exist and are observable within the VDF of PUIs is one of the main

topics of this work, neglecting changes of the pitch angle distributions with the magnetic field orientation would be to the detriment of this work's goals.

6.1.0.iv makes the observation of apparent systematic behavior of PUI VDFs more likely, if not accounted for. Also, the observations of chapter 5, which in agreement with Oka et al. [2002], Drews et al. [2015] indicated the existence of strong anisotropic signatures within He^+ PUI VDFs. A glance at corrected pitch angle distributions may also falsify or qualitatively verify these results.

To disentangle the pitch angle distributions from the ring coverage based measurement probabilities (6.1.0.iv), each contributing particle is assigned with a weight, which is derived from the reciprocal of the measurement probability derived from the fraction of the gyro orbit which is within the aperture based on its pitch angle as well as the local magnetic field and SW configuration at the time of observation. In the following, this type of correction is referred to as Ring Coverage corrected (RiCo corrected). If for a particle a weight already exists from other normalizations (e.g. base rate weighting), the weight is multiplied with the RiCo correction weight.

6.2 Pitch angle distributions for selected magnetic field and solar wind conditions

To study the modification of PUI VDFs during the transport in the SW, one would ideally start with observations of VDFs of freshly ionized PUIs and then observe the evolution of these distributions during transport. However, the observed VDFs always need to be considered a mixture of PUIs of different age. Simulations (compare e.g. chapter 2.2.4) suggest, that at locations closer to the Sun than 1 AU the fraction of freshly ionized PUIs is larger, so observations of PUIs at smaller distances than 1 AU would be best suited for a study of PUI transport. Therefore for future studies the data of Solar Orbiter or PSP has the potential to yield new insights into the transport of PUIs. However, for this study the data of STEREO PLASTIC is investigated which orbits the Sun at ~ 1 AU. Hence, the observed PUI VDF is to a large fraction of particles already affected by transport effects. Hence, with PLASTIC observations the results of transport rather than the initial conditions are observed.
So, this chapter aims to discuss transport affected PUI VDFs in different SW conditions. Also, the PUI density and the initial velocity of PUIs is expected to deviate as a function of ecliptic longitude (compare e.g. chapter 2.2.4). Hence, in this chapter the pitch angle distribution of He^+ PUIs is observed both as a function of SW condition and of ecliptic longitude. To this end, to derive a pitch angle distribution from the observations, time periods are selected for which the instrument is located within selected coordinates and the SW conditions that match the respective case of interest.
To select different conditions within the SW, the classification scheme of Xu and Borovsky [2015] (compare Chapter 2.1.4.iii) is employed to select SW streams with similar physical properties. The pitch angle distributions could also be observed as a function of different proton bulk velocities, yet that quantity is misleading: Both the velocity of the proton bulk and the physical properties of an SW stream during PUI injection can differ from those at the point of observation (compare e.g. Chapter 2.1).
The approach selected for this study mixes different time periods. Therefore further measures need to be considered to ensure comparability. Firstly, the time periods consist of mixed magnetic field directions. To simplify the analysis, therefore only time periods are selected when

the magnetic field elevation angle is within the interval of ±5° w.r.t. the ecliptic plane. Also, since the range of observable pitch angles depends on the magnetic field angle (compare Chapter 6.1) and the initial pitch angles of the PUI VDFs depend on the magnetic field angle during observation (compare Chapter 2.2.5) the pitch angle distributions are observed as a function of the azimuthal magnetic field angle. Naturally, the momentarily observed magnetic field direction at 1 AU does not necessarily represent the magnetic field direction at injection, yet the argument, that the range of observable pitch angles relates to the momentary pitch angle, makes this selection necessary. In addition, unless explicitly stated otherwise, each PHA word which contributes to a distribution is normalized by multiplication with the following factors:

- Priority weighting (compare Chapter 3.1.5.iii.a).
- Normalization to the total number of instrumental observation time periods, that the current magnetic field direction is observed (compare Chapter B.2.1).
- Ring Coverage (RiCo) correction, which is a division by the gyro orbit based probability, that the particle is within the aperture (compare Chapter 6.1).

To avoid contamination by SW particles, only He^+ PHAs are selected, for which $\varpi^{\pm}_{\mathrm{SWp}} > 0.75$ applies. The range of $0.75 < \varpi^{\pm}_{\mathrm{SWp}} < 1.0$ preferentially selects PUIs which are freshly created or have been decelerated. Unfortunately, for $\varpi^{\pm}_{\mathrm{SWp}} > 1.0$ for which accelerated PUIs are expected, not enough PHAs are available to observe the pitch angle distribution with a meaningful signal to noise ratio. So, the analysis is restricted to $0.75 < \varpi^{\pm}_{\mathrm{SWp}} < 1.0$.

6.2.1 Statistical considerations

Each combined selection of SW types and spacecraft position results in a different number of events which contribute to the resulting distribution. To visualize this and to provide an overview of the number of events which contribute to the selected conditions, in Fig. 87 time series are shown. In the top three panels, histograms of pitch angle, magnetic field elevation angle and magnetic field azimuthal angle are plotted over time, where the time resolution is five days. With the same time resolution in the fourth top panel the fraction of time during which a certain SW type is present within these five day intervals is plotted color coded, where the color represents the SW type. The fourth panel plots a time series of proton density and proton velocity and the fifth panel shows a time series of the priority weighted number of He^+ PHA events per 5 day interval. The Parker angle of $\sim 45°$ (compare chapter 2.1.3.i) is alongside its 180° flipped counterpart one of the most prominent angles in the third panel. As expected, the most He^+ PHAs are found at time intervals, when the instrument is close to the focusing cone. Naturally, close to the focusing cone not an evenly distributed mix of SW conditions is found. During the first two passes through the region the the majority of SW is categorized as sector reversal plasma. Afterwards, particularly streamer belt wind is found close to the focusing cone. With the exception of ICMEs and SIRs, the coronal hole wind has the smallest fraction of events during the passes through the focusing cone. This implies that in 2008 and 2009 in the majority of the focusing cone region sector reversal wind was observed, and in later time periods within the focusing cone the majority of samples is made up of streamer belt SW. Therefore, the following observations of pitch angle distributions in the focusing cone and the sector reversal wind sample most of their data from solar minimum conditions while the the same coordinates combined with streamer belt SW mostly coincide at increasing solar activity and solar maximum. For

coronal hole wind, the sample density in the time periods is equalized. Yet, the number of counts generally decreases with increasing mission time. All in all implications or conclusions found about the transport of PUIs from pitch angle distributions in the focusing cone during the different SW conditions may also partly be caused by different stages of the solar activity cycle. Similar deliberations apply to regions close to the crescent region. Also, since the number of counts close to the focusing cone region is considerably higher than in any other region, the pitch angle distributions are expected to be less statistically significant in the crescent region and even less in neither the focusing cone nor the crescent region. For this reason and in addition to increase the chance for a more diverse mix of different SW conditions in each observed region is increased, for the following analysis a $\pm 15^\circ$ tolerance is employed around the coordinate of $\lambda_{\mathrm{ecl}} = 75^\circ$ for PHAs to be considered within the focusing cone region and analogously for coordinates of $\lambda_{\mathrm{ecl}} = 255^\circ \pm 15^\circ$ are considered within the crescent region. Data within neither of these regions are labelled lateral. It is noteworthy that these values may differ from the physical width of the regions. However, with this selection, i.e. it might be possible that parts of the actual crescent region are also found in the coordinates considered lateral in this work. However, the majority of events is categorized correctly. This scheme is also sketched in a top down view of the heliosphere in Fig. 88.

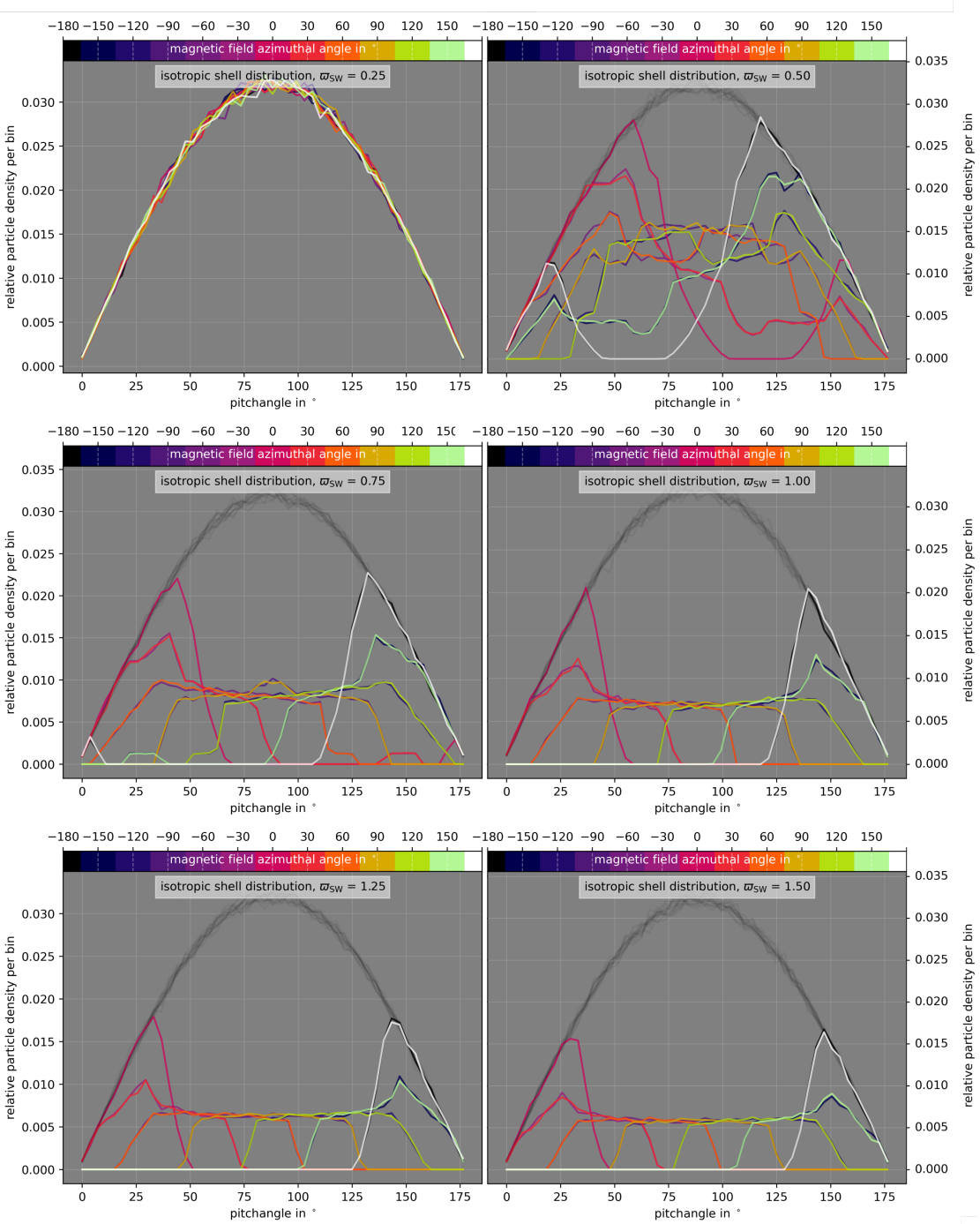

Figure 84: Pitch angle distributions of stochastically sampled particles from an isotropic shell model distribution. In each plot the raw pitch angle distribution is plotted grey shaded. In the foreground of these gray shaded distributions the pitch angle distribution is plotted with gyro orbit based measurement probability weight applied to it. For the measurement probability the orientation of the magnetic field is of importance, hence each probability affected distribution is color coded to reflect the magnetic field azimuthal angle. The magnetic field elevation angle is kept within the in-ecliptic plane for all distributions. Each of this figure's six plots displays the distributions corresponding to an isotropic shell distributions for different values of ϖ_{SW}.

Duncan Keilbach- Three dimensional Pickup Ion velocity distribution functions observed at 1 AU with STEREO/PLASTIC: Anisotropic features and density enhancements in pitch angle distributions as tools to investigate transport effects

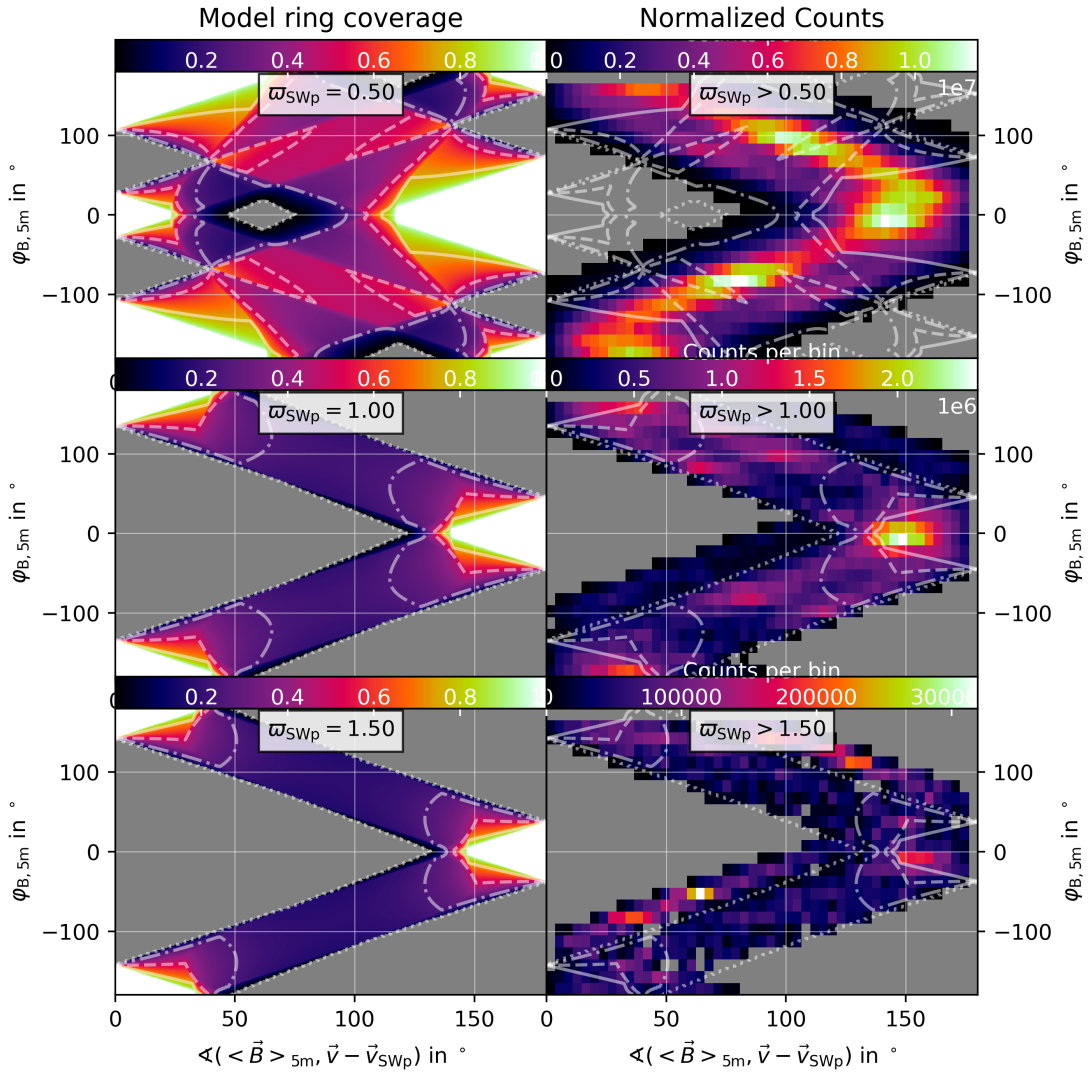

Figure 85: Comparison between model ring coverage (left plots) and ring coverage corrected STEREO PLASTIC He^+ PHA observations (right plots). All plots are displayed as two dimensional color coded probability (left) and ring coverage corrected individually normalized magnetic field angle time corrected counts per bin (right) and plot the pitch angle on the x-axis and the magnetic field azimuthal angle on the y-axis. Each row of plots corresponds to a different setting of ϖ_{SWp}. For overview, additionally a contour of the ring coverage based probabilities as according to the left plots is plotted in all plots.

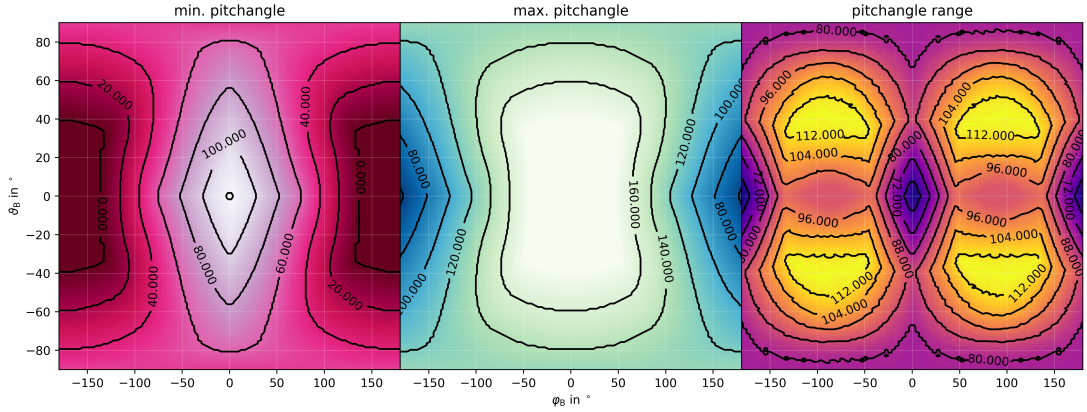

Figure 86: Maps of ranges of pitch angles as observable through the aperture of the solar wind sector of STEREO PLASTIC as a function of the magnetic field azimuthal angle (x-axis) and the magnetic field elevation angle (y-axis). The left panel displays the minimum observable pitch angle, the central panel the maximum observable pitch angle and the right panel the range of observable pitch angle as the difference between maximum and minimum.

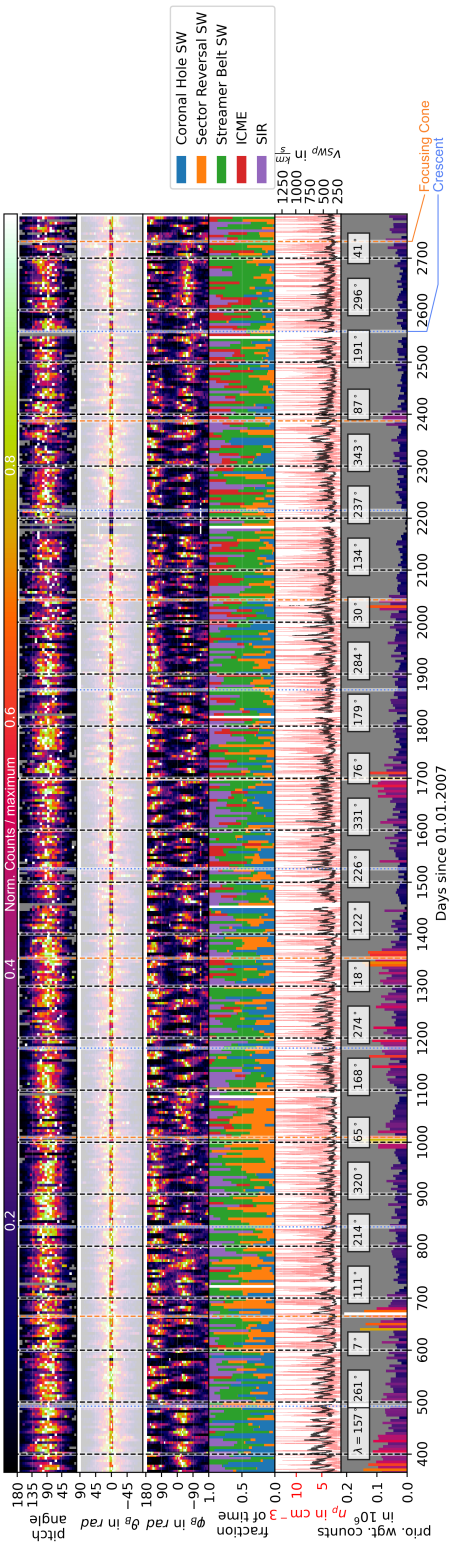

Figure 87: Timeseries over the complete time period to which the analyzed data is restricted to (01.01.2008 to 31.12.2014). Top axis: Histogram of the He^+ PHAs' pitch angle distribution as a function of time (with a 5 days time resolution). Second top axis: Histogram of magnetic field elevation angle as a function of time (same resolution). The superimposed white shading represents the limitation, that the analyzed data is restricted to $\pm 5°$ out of the ecliptic plane. Third top axis: Histogram of magnetic field azimuthal angle as a function of time (same resolution). Fourth top axis: Fraction of time of the top histograms' time bins, during which a certain SW type is observed. The different SW types are color coded and plotted as stacked bars wherein the length of a bar represents the fraction of time. A bar spanning over the complete y-axis means that the corresponding type is observed during the complete duration of the time bin. Fifth top plot: Time series of SW proton density (red line, left axis) and of the SW proton bulk velocity (black line, right axis) with a time resolution of 1 day. Sixth top plot: Priority weighted counts of He^+ PHAs as a bar plot per 5 days time interval. As time progresses, the spacecraft orbits to different coordinates. Therefore the spacecraft's ecliptic longitude is also indicated in degrees by black text in white boxes for each time bin. In addition at the times when the spacecraft passes the focusing cone, an orange dashed vertical line is drawn. analogously a blue dotted vertical line is drawn at times when the spacecraft passes the crescent's coordinates.

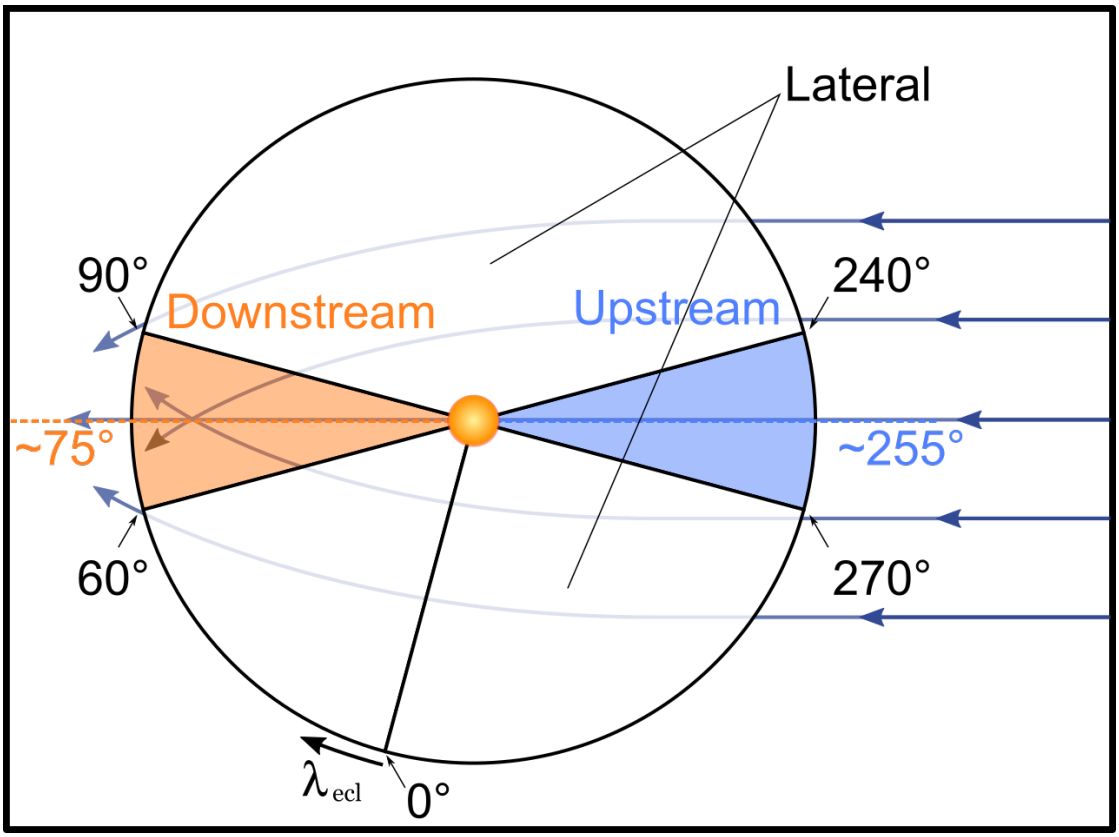

Figure 88: Sketched top down view of the ecliptic plane to visualize the analysis' selection of coordinates where the Sun is represented by a yellow dot in the center. For the downstream region (Focusing Cone) ecliptic longitudes between 60° and 90° are selected. For the upstream region (Crescent) ecliptic longitudes between 240° and 270° are selected. The remaining coordinates are labelled as lateral.

6.2.2 Observed pitch angle distributions

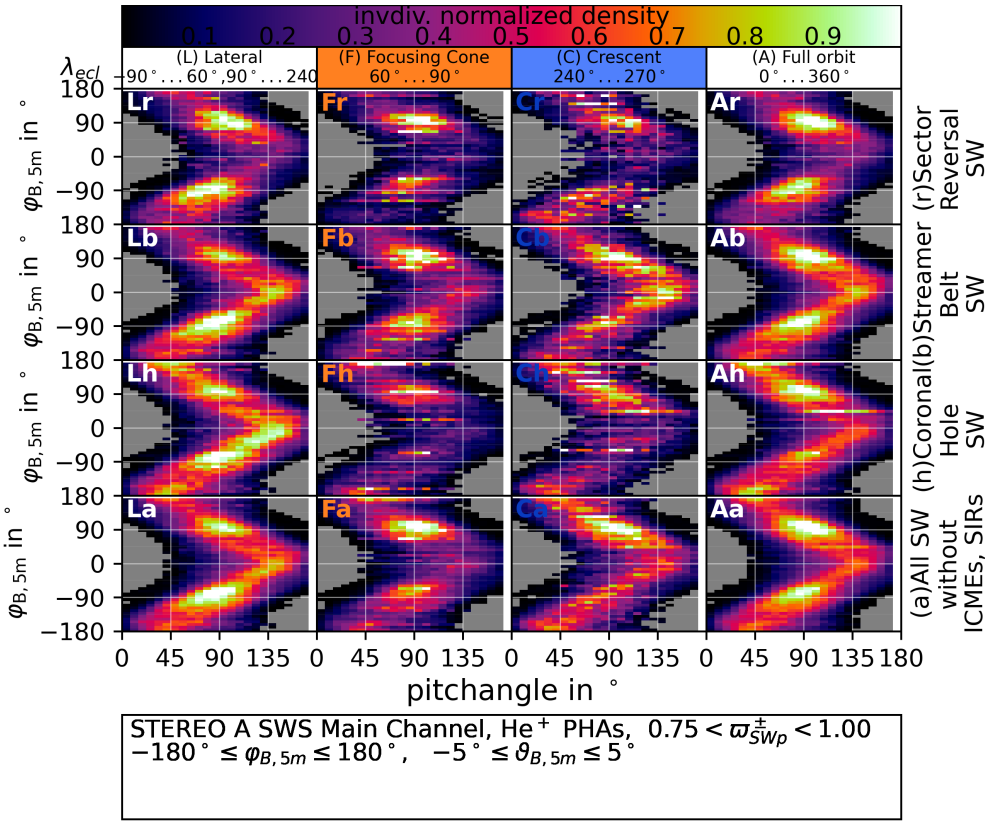

Figure 89: Pitch angle distributions as a function of magnetic field azimuthal angle with the elevation angle set to ±5° within the in-ecliptic plane. The x-axes correspond to pitch angle and the y-axes correspond to the magnetic field azimuthal angle. Each plot's color key is normalized to the respective 99-percentile of the histogram. Larger values are clipped to 1. The four columns correspond to different zones in the heliosphere to which the data is limited and the four rows correspond to different SW regimes to which the data is limited. Each panel corresponds to a combination of these two categories of limitations. The pitch angle distributions are corrected according to the total number of times, when a magnetic field direction is measured, but not RiCo corrected.

Figs. 89 and 90 each show 16 histograms which count PLASTIC SWS He^+ PHAs as a function of pitch angle (x-axis) and magnetic field azimuthal angle (y-axis). The histograms of each of the figures' panels are normalized by division by the histograms' individual 99-percentile. Values larger than 1 are clipped to 1. The histograms are arranged in a matrix and represent a different combination of ecliptical longitude coordinate ranges (columns) and solar wind conditions (rows). The difference between both figures is, that in contrast to Fig. 89, the events contributing to the histograms in Fig. 90 are RiCo corrected. In the following, the panels of the figures are referenced to by a combination of a capital abbreviating letter which indicates the column as read from left to right and a small letter which indicates the row as read from top to bottom. These letters are listed in Tab. 8. For example, panel **Fh** is the panel in the

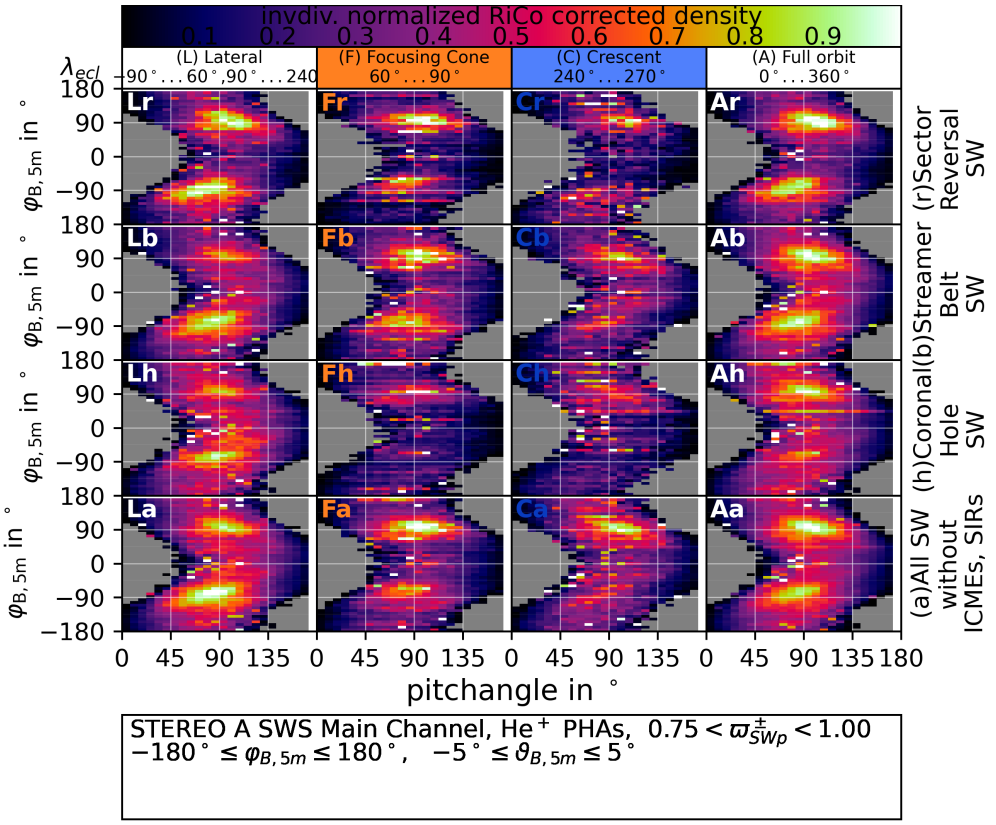

Figure 90: Analogous to Fig. 89, but with RiCo correction applied to the distributions.

Definition of plot labels

First label character: Coordinate selection

Label	L	F	C	A
Definition	Lateral	Focusing Cone	Crescent	Full Orbit

Example **Fh** Limit data to Focusing Cone coordinates, and only during coronal hole wind conditions.

Second label character: SW type selection

Label	r	b	h	a
Definition	Sector Reversal	Streamer Belt	Coronal Hole	All SW except ICMEs and SIRs

Table 8: Definition and construction of labels which reference panels or plots of pitch angle distributions.

second column (Focusing Cone coordinates) and the third row (Coronal Hole SW). Similar to the plots in Chapter 5 the histograms investigate the VDF as a function of azimuthal magnetic field direction, yet with the abstraction that instead of velocity coordinates the pitch angle is investigated. Therefore, for an agreement with the results of Chapter 5 at magnetic field angles of ±90° and a pitch angle of 90° density enhancements are expected. To be more precise, this

is the expectation for not RiCo corrected histograms, since in Chapter 5 the RiCo correction was not applied. In the not RiCo corrected histograms (Fig. 89) such localized increases in density are found at least at one of the magnetic field angles of ±90° in all panels. Hence, the uncorrected histograms match the previous observations well. Interestingly, the instrumental asymmetries discussed in Chapter 5.4.1 do not seem to dominate the plots, even though no correction for these have been applied. The reason for no application of such corrections is, that the investigations of Chapter 5.4.1 did not yield measures of instrumental efficiencies to determine limits for sufficient accuracy of the distributions. Strongly visible asymmetric behavior of the observed distributions are especially found in panels **Fh** and **Ch**. In these panels, also the most noise is visible in the data. That panels which only consider coronal hole wind conditions are the most affected by noise was expected since this type of SW had compared to the other two types considered in Fig. 89 the least amount of events in the overview timeseries of Fig. 87. In addition, in the crescent region less statistics are expected, since for He^+ counts in the focusing cone is more prominent than the crescent region (compare chapter 2.2.4) and even though per spatial volume more counts are expected in the crescent than in any other region which is not the focusing cone, the increased counts do not significantly make up for the coordinate selection of the crescent yielding a smaller region than the coordinate selection of the lateral regions.
It also needs mentioning that while the instrumental asymmetries directly affect the observation of symmetries or asymmetries in the pitch angle distribution, each of the panels of Figs. 89 and 90 are affected by the instrumental asymmetries in the same way. So, the panels are not accurate in shape of the distributions by themselves, but are comparable to each other.

With the RiCo correction applied in Fig. 90, the density enhancements at 90° pitch angles become more distinct. Interestingly, the least optical difference between corresponding panels of Fig. 89 (uncorrected) and Fig. 90 (RiCo corrected) is observed in the **F**-panels since a smaller amount of events is visible in the **F**-panels of Fig. 89 compared to their respective local maxima at pitch angles of 90°. So, the RiCo-corrected distributions deviate the least in their shape from the uncorrected distributions in the focusing cone region. So, there the RiCo correction weights are closer to 1 than in other regions. For a RiCo correction weight of 1, the particle's complete gyration trajectory is covered in the instrument's aperture. It is possible that the magnetic field and SW conditions might just randomly fit that criterion better in the **F**-panels. However, a systematic difference between the initial conditions during the pickup process between the **F**-region and others is the ISN velocity which in the focusing region is expected on average at radial direction (compare Chapter 2.2.2).
The distributions of the **L**-panels of Fig. 90 appear diminished in comparison to Fig. 89 in density especially for magnetic field angles in the area of ±45° around an angle of 0°. At ∼ 0° local maxima are observed in the panels **Lb** and **Lh** of the uncorrected distributions in Fig. 89. Since most of the time of the orbit is spent in the lateral region, analogous observations are found in the **A**-panels (full orbit) of both figures.
The observed shapes of the uncorrected distributions in the Crescent region are most distinct from each other compared to the Focusing Cone and the lateral regions. In panel **Cr**, a profile with maxima at magnetic field angles of ±90° and almost no events in the area of ±45° around 0° is observed. In panel **Cb**, almost all magnetic field angles between +90° and −90° have high densities. All panels are affected by noise. Panel **Ch**, as mentioned earlier seems dominated by effects of low statistics and is therefore disregarded. Panel **Ca** is asymmetric with a local maximum of density at a magnetic field angle of +90° on top of a background of medium densities over all angles.

These different behaviors are partly visible in the corrected distributions of Fig. 90. The profile

of the uncorrected distribution in panel **Cr** is still visible in the corrected version. The **Cb** panel has increases in local maxima at ±90° w.r.t. the uncorrected distribution and the asymmetric behavior of the panels **Ch** and **Ca** are also found in the RiCo corrected versions.

6.2.3 Density enhancements at azimuthal magnetic field angles of ±90°

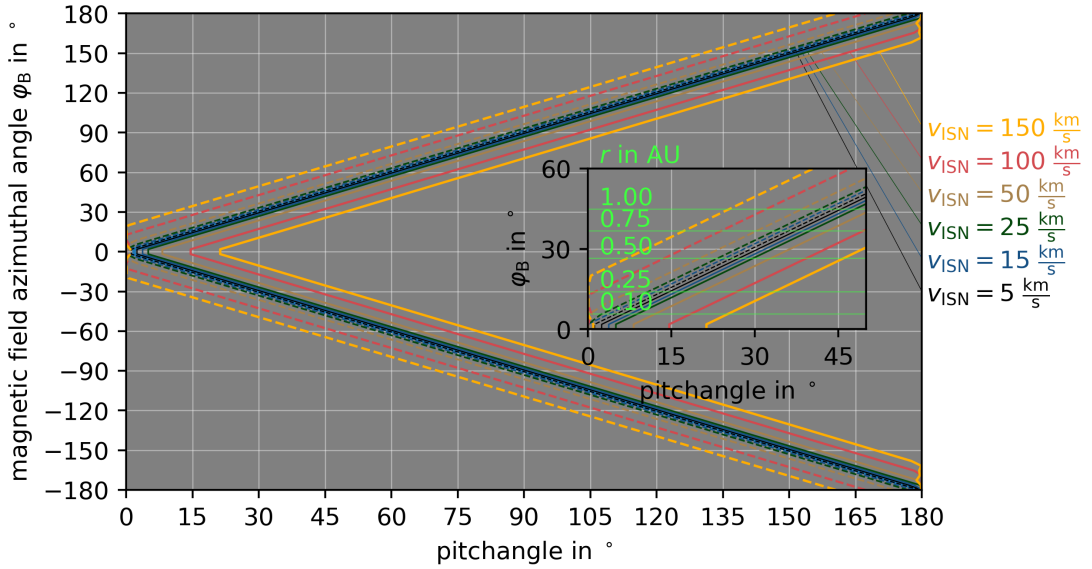

Figure 91: Expected initial pitch angle (x-axis) of freshly created PUIs as a function of the magnetic field azimuthal angle (y-axis) wherein the elevation angle is within the in-ecliptic plane. For the model, different ISN velocities are assumed and each line color corresponds to a different ISN velocity. The dashed lines correspond to the minimum and and dotted lines to the maximum. In addition, the same relation is plotted for a smaller range of magnetic field azimuthal angles in an insert plot. The magnetic field azimuthal angles in the insert plot correspond to average angles of the magnetic field at different distances from the Sun according to the model of Parker [1958] for a SW proton bulk velocity of 450 km/s. The corresponding distance is indicated by green horizontal lines and labels. Hence, the insert plot can also be read as a model expectation for pitch angles of fresh PUIs during quiet SW as a function distance from the Sun.

A common observation of Chapter 5 and 6.2.2 are density enhancements at pitch angles at ∼ 90° and magnetic field azimuthal angles around ±90° with the elevation angle limited to the ecliptic plane. Common to both chapters is the observation as a function of the magnetic field azimuthal angle and that the aperture of SWS is limited to incident angles of −45°...45°. The implication of the limited range of incident angles (compare Chapter 6.1) is that a limited range of pitch angles is observable and the magnetic field orientation controls that range. So, while the limitation of the data to different azimuthal magnetic field angles allows to observe different parts of the pitch angle distribution, it is not guaranteed that the pitch angle distribution does not change as a function of the azimuthal magnetic field angle. In fact, it is very likely that different magnetic field orientations correspond to different pitch angle distributions, since the initial pitch angle of freshly created pickup ions depends on the angle between SW velocity and

magnetic field vector (compare Chapter 2.2.5.i). However, this argument needs to be considered with the caveat, that not necessarily the magnetic field orientation is observed, at which a PUI has been created. That the observed in-situ magnetic field is similar to the magnetic field during creation of a PUI is more likely, the younger the PUI is.
The expected initial pitch angle of freshly created PUIs is plotted as a function of the magnetic field azimuthal angle in Fig. 91. To create Fig. 91, a set of ISN velocities is selected. Then, for each ISN velocity the direction of the velocity is permutated to infer a minimum and a maximum pitch angle. For Fig. 91 the elevation angle is limited to orientations within the ecliptic plane. Interestingly, the initial pitch angle intersects with the zone of pitch angles observable by the SWS aperture for azimuthal angles around ±90° which also coincides with a pitch angle around 90°. All in all the expected initial pitch angle is a zig-zag shaped function which resembles the shape of the zone of observable pitch angles, but mirrored along the pitch angle axis with a central point of 90°. Therefore, it is likely that PUIs at these pitch angles are freshly created or were only slightly modified by transport effects. The observations of torus-like structures at 90° of Chapter 5 also fit to this concept.

However, there are two caveats to this concept. Firstly, the velocity of the ISN the PUI originated from also influences the initial pitch angle. To estimate the extent to which the pitch angle might deviate from the idealized model, in Fig. 91 the maximum and minimum pitch angle are plotted as a function of the magnetic field azimuthal angle for different magnitudes of ISN velocity. Here, the maximum and minimum pitch angles are determined by varying the direction of the ISN velocity. Different relative average ISN velocity directions are expected as a function of the ecliptic longitude and these directions can be determined from expected ISN trajectories (compare Chapter 2.2.2). E.g. in the focusing cone region preferably outward pointing ISN velocity vectors are expected. However, since ISN velocities of more than 50 km/s are unlikely, the deviation in pitch angles is only in the magnitude of one or two histogram bins of Figs. 89 and 90 and the peaks and structures observed in these structures are broader than that, the deviations in pitch angle caused by different ISN velocities only plays a minor for this study. Secondly, the magnetic field is dynamic in its behavior during the expansion of the SW and therefore the magnetic field conditions during the creation of the observed PUIs are not necessarily similar to the magnetic field conditions during observation. Hence, to relate the momentary pitch angle distribution and magnetic field conditions to these at creation of the observed PUIs is a simplified way of interpreting the observations. If adiabatic cooling is considered the main process in the transport, PUIs with $\varpi_{SW} \sim 1$ are considered fresh PUIs, since they have not yet been cooled. Slower PUIs then have already undergone cooling and hence have been created further inside the heliosphere than at the point of observation. For this interpretation, also no significant acceleration is presumed, since otherwise PUIs with $\varphi_{SW} \sim 1$ could also be older PUIs which have been first accelerated and then cooled. Also, the time scales of adiabatic cooling are to be determined in future works.

6.2.4 Traces of fresh pickup ions and indications of transport as a function of the age of PUIs in the Focusing Cone region

The overview on pitch angle distributions for selected regions and solar wind conditions of Fig. 90 unfortunately shows, that since the distributions within the crescent regions are strongly affected by noise, a direct comparison between focusing cone and crescent region (upstream vs. downstream) is not possible. However, an investigation of the distributions observed within the focusing cone region might also yield interesting results.

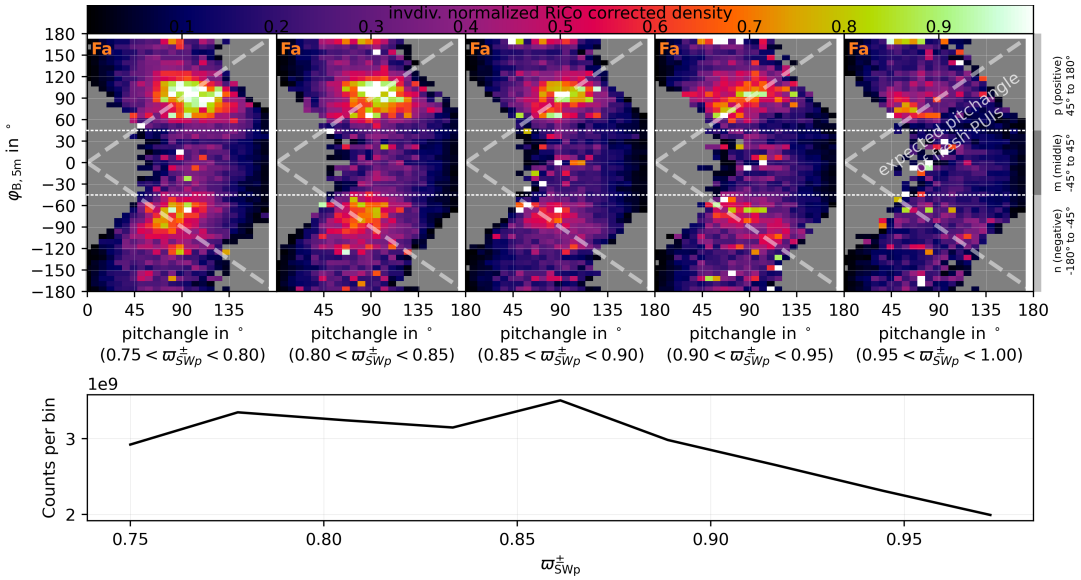

Figure 92: Top plots: RiCo corrected pitch angle distributions as a function of magnetic field azimuthal angle analogous to Fig. 90. Each of the top panels corresponds to a different selection of ϖ_{SWp}, where the selected ϖ_{SWp} increase for each panel as seen from left to right. The selection of ϖ_{SWp} is indicated below each of the top panels. Bottom plot: Histogram of ϖ_{SWp} where each contributing event is corrected by a factor which takes the total time into account when the magnetic field orientation which corresponds to the event is observed.

Compared to the lateral region, PUI densities are expected to be enhanced w.r.t. densities of other SW particles (compare e.g. Chapter 2.2.4). Hence, this region is ideally suited to investigate the behavior of the PUIs pitch angle distributions. If all SW conditions (except ICMEs and SIRs) are combined in an analogous way to the a-rows of Fig. 90, the number of events allows to observe the distributions with a narrower selection of $\varpi^{\pm}_{SWp}$. Fig. 92 displays pitch angle distributions as a function of magnetic field azimuthal angle observed in the Focusing cone region filtered by $\varpi^{\pm}_{SWp}$ with windows of 0.05 width which start at the lower boundary of 0.75. The lower and upper boundaries increase seen from left to right with each of the five panels of Fig. 92. The final panel observes pitch angles for $0.95 < \varpi^{\pm}_{SWp} < 1.0$. To provide a guide to the number of events which contribute to each panel below the panels a histogram of $\varpi^{\pm}_{SWp}$ is plotted where the events which contribute to the distributions are also RiCo corrected (as well as the depicted pitch angle distributions).

In all panels the distributions are asymmetric. Therefore, for the discussion of the distributions the following three regions in magnetic field azimuthal angle are defined:

- p (positive) : $180° < \varphi_{B,5m} \leq 45°$
- m (middle, in between) : $45° < \varphi_{B,5m} \leq -45°$
- n (negative) : $-45° < \varphi_{B,5m} \leq -180°$

In the p-range of magnetic field angles the dominating features are enhanced densities at magnetic field angles of $90° \pm 30°$ and pitch angles in a similar range around 90°. For $0.75 < \varpi_{SWp} < 0.8$,

enhanced densities are observed over almost all observable pitch angles. This might indicate the presence of a strongly isotropized pitch angle distribution. Similar observations are found for $0.8 < \varpi_{SWp} < 0.85$.
Yet, in the n-range also stronger densities are found than in the m-region. Yet, the pitch angle distributions are more shifted towards pitch angles below 90° and appear narrowly centered around pitch angles of $\alpha = 180° - |\varphi_{SWp}|$ which is opposite to the expected pitch angles as indicated by Fig. 91.
This behavior is not completely continued for $0.8 < \varpi_{SWp} < 0.85$. The behavior of the pitch angle distributions for $0.75 < \varpi_{SWp} < 0.8$ in the n-region might illustrate that the interpretation of the momentary magnetic field conditions as the magnetic field during creation of the PUIs is not meaningful, especially for PUIs which have undergone transport, since longer transported PUIs are further away from the point of their injection into the SW. The consideration of the age of transported PUIs is interesting in the discussion of the distributions. If adiabatic cooling applies, PUIs with $0 < \varpi^{\pm}_{SWp} \ll 1$ can be considered as PUIs, which have been transported during a significant time and PUIs with $\varpi^{\pm}_{SWp} = 1$ are freshly created. So, depending on whether transport effects instantaneously isotropize pitch angle distributions, Fig. 91 provides direct expectations for the profile of the pitch angle distributions at $\varpi^{\pm}_{SWp} = 1$. It needs to be added to this deliberation, that the average magnetic field angles expected from the model of Parker [1958] for distances from the Sun of 1 AU and lower are $\leq 45°$. Unfortunately, the combination of azimuthal magnetic field angles of 45° and pitch angles of 45° is not observable with the aperture of SWS. This argument is also interesting for the consideration of the magnetic field direction present when the PUIs are created: If the PUIs observed at the angles of enhanced densities have been created at similar or comparable magnetic field angles, the magnetic field angle at the point of creation deviates from the average angles expected from the model of Parker [1958]. Since it is likely, that such angles are the result of a disturbed or turbulent magnetic field, it is more unlikely, that observed magnetic field direction resembles the magnetic field angle at observation.

Yet, pitch angles which feature enhanced densities in the p-region seem to resemble the profile of expected pitch angles from Fig. 91 more, the more $\varpi^{\pm}_{SWp}$ increases towards 1.0. In the rightmost panel of Fig. 92 close to the lower-pitch angle boundary of observable pitch angles a feature is observed close to pitch angles of 45°, which may originate from freshly created PUIs within the expected average magnetic field azimuthal angle at 1 AU. Yet, since the rightmost panel also has a low signal-to-noise ratio it needs to be mentioned, that without the expectation of a feature for that pitch angle, the feature would probably be treated as part of the noise which governs the plot.
Enhanced densities in the n-region are observed for $0.8 < \varpi^{\pm}_{SWp} < 0.85$, but decrease in prominence with increasing $\varpi^{\pm}_{SWp}$ and for $0.95 < \varpi^{\pm}_{SWp} < 1.0$ no significant densities are found in the n-region. Therefore, for all considered ranges of $\varpi^{\pm}_{SWp}$ the observed densities are asymmetric in magnetic field angles. This is consistent with observations of PUI VDFs in Chapter 5 and with the instrumental asymmetries.

The densities in the m-region are enhanced for $0.95 < \varpi^{\pm}_{SWp} < 1.0$ w.r.t. to the other regions and the observed pitch angle distributions feature an increasing profile with increasing pitch angle and a maximum close to 180°. Since 180° is an attractor in quasi-linear-theory of the interaction between gyrating particles and cyclotron waves (compare Chapter 2.1.7.i) this may be an indication of wave activity and a strong scattering of the particles. Yet, again the high signal-to-noise ratio does not allow to attribute a high degree of significance to the distributions. So, more observations are necessary to verify or falsify this.

What these distributions demonstrate, is that there are visible differences between the pitch angle distributions of PUIs which have been transported w.r.t. fresh PUIs. The pitch angle, at which the distributions peak as a function of magnetic field azimuthal angle is not significant, since with increasing age of a PUI the momentary magnetic field does not necessarily reflect the magnetic field during creation. Still, the width of the pitch angle distributions indicates different extents of isotropization. Also, the principles of this study can be applied to the data of future and newer ongoing missions. Especially a similar study which employs data from the Heavy Ion Sensor of Solar Orbiter or instruments with a directional resolution at least comparable to PLASTIC might yield more insights into the transport of PUIs. Also, this study stresses the importance to build instruments which have as much field of view as possible alongside a decent directional resolution.

6.2.5 Traces of fresh pickup ions and transport effects in different regions and solar wind conditions

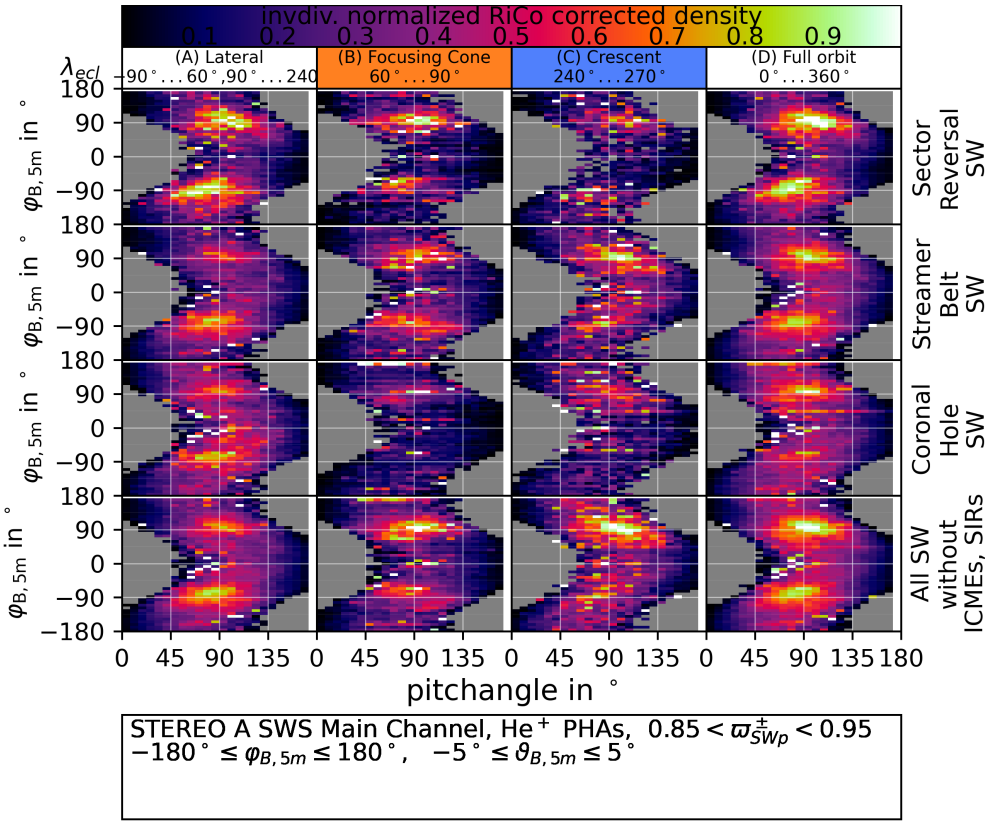

Figure 93: Analogous figure to Fig. 90, but with the limitation of $0.85 < \varpi^{\pm}_{SWp} < 0.95$.

Since the study of pitch angle distributions for varied values of $\varpi^{\pm}_{SWp}$ demonstrates different extents of PUI transport, Figs. 93 and 94 display pitch angle distributions as a function of magnetic field angle analogously to Fig. 90 for two different ranges of $\varpi^{\pm}_{SWp}$. In Fig. 93 the data is

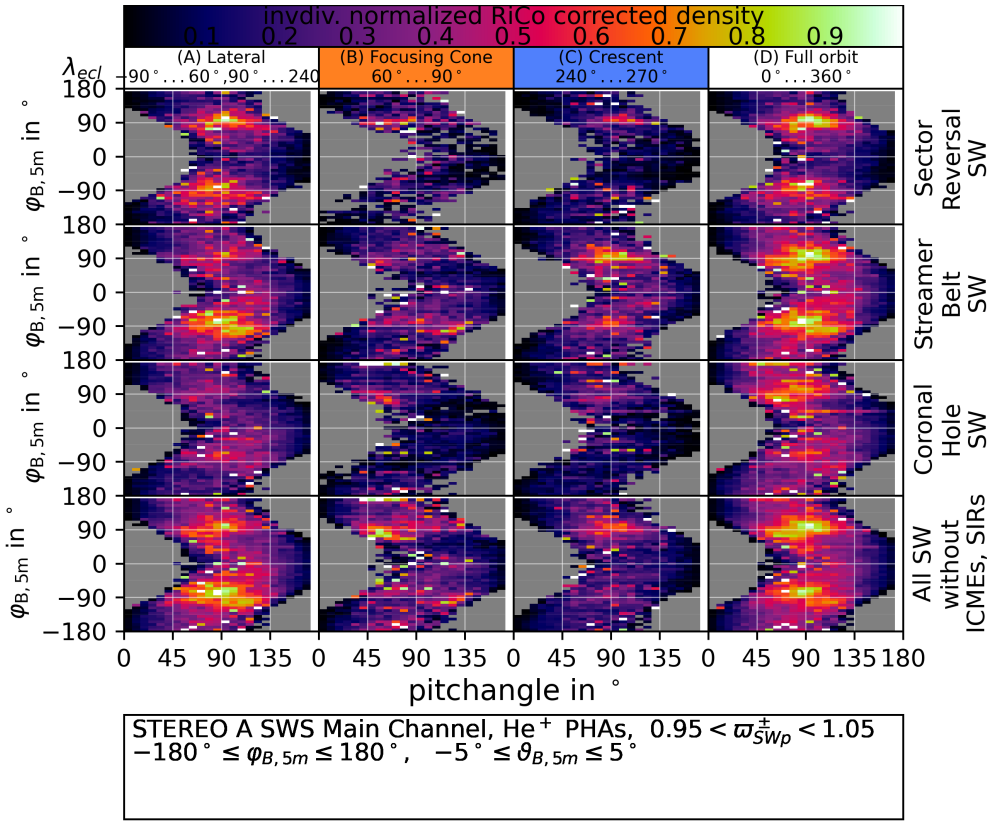

Figure 94: Analogous figure to Fig. 90, but with the limitation of $0.95 < \varpi^{\pm}_{SWp} < 1.05$.

limited to $0.85 < \varpi^{\pm}_{SWp} < 0.95$ and in Fig. 93 the data is limited to $0.95 < \varpi^{\pm}_{SWp} < 1.05$. The panels are labelled analogously to Fig. 90.
In these distributions, it is more clearly visible than in Fig. 92, that the pitch angle distribution is differently shaped for different values of $\varpi^{\pm}_{SWp}$. In the **L**-Panels the profile of the enhanced densities at magnetic field angles close to $\pm 90°$ resemble the expectations of Fig. 91 for $0.95 < \varpi^{\pm}_{SWp} < 1.05$. For $0.85 < \varpi^{\pm}_{SWp} < 0.95$ this is not the case. Interestingly, in the F-panels the distributions resemble the expectations of Fig. 91 for both ranges of $\varpi^{\pm}_{SWp}$. In the **C**-panels again the signal-to-noise ratio is strong, so these are excluded from the discussion.

Overall, the observed distributions hint, that if a filter in $\varpi^{\pm}_{SWp}$ is applied, transport effects can be observed in the pitch angle distributions. Also, the presence of density enhancements at pitch angles close to 90° and a narrower density profile of the magnetic field angle dependent pitch angle distributions which also resembles the expected PUI injection angles as a function of magnetic field direction indicates, that at $\varpi^{\pm}_{SWp} \sim 1$ the isotropic distribution of fresh PUIs is (at least partly) observable, but only traces of it for $\varpi_{SWp} < 1$.
Since the density increases in the pitch angle distributions have been observed for both positive and negative magnetic field angles, it can also be discounted, that the phenomenology of the increases is strongly affected by the yet uncorrected instrumental asymmetries which are investigated in Chapter 5.4.1.

7 Conclusions and Outlook

In this work the Velocity distribution Functions (VDFs) of interstellar Pickup Ions (PUIs) have been investigated with data of the PLAsma and SupraThermal Ion Composition (PLASTIC) instrument [Galvin et al. [2008]] onboard of the Solar Terrestrial RElations Observatory (STEREO) [Kaiser et al. [2008]]. Even though they are found in the solar wind (SW), a continuos stream of charged particles emanating from the Sun [Biermann [1951]], interstellar PUIs are of non solar origin (e.g. Axford [1972]). They originate from the Local Interstellar Medium (LISM), which is the medium which surrounds the Heliosphere [Spitzer [1942], Axford et al. [1963], Crutcher [1982], Lallement and Bertin [1992], Frisch et al. [2011]], the region governed by the SW. Charged particles from the LISM can not enter the Heliosphere (e.g. Axford et al. [1963]). This limits the direct observations of particles in the local interstellar medium to (initially) neutral particles and in-situ observation of the LISM by spacecraft. The latter is challenging, since the boundary to the LISM is at a distance of more than 100 AU from the Sun (e.g. Stone et al. [2013], Gurnett et al. [2013], Richardson et al. [2019a,b]).
The trajectory of a neutral particle which enters the heliosphere is the trajectory of a particle in a central gravitational potential where the Sun is the central mass which exerts the gravitational pull (e.g. Lee et al. [2015]).
This way, interstellar neutral particles are also found at 1 AU and are detected by e.g. the instruments onboard of the Interstellar Boundary EXplorer (IBEX) [McComas et al. [2005]]. However, the majority of spacecraft observations of particles is focused on charged particles. Hence, more observations of the interstellar particles are available if an interstellar neutral is ionized. After ionization, the former neutrals are subjected to the Lorentz force from the local magnetic field which is carried by the SW and gyrate around the magnetic field lines embedded into the SW. This makes the initial VDF of the particles torus-shaped where the torus is perpendicular to the local magnetic field (e.g. Axford [1972], Vasyliunas and Siscoe [1976]). Since the particles are forced to co-move with the local magnetic field, they are picked up by the SW and fittingly they are called PUIs. The exact position and width of the torus distribution is a measure for parameters of the local interstellar medium. E.g. from the maximum absolute velocity of the PUI VDF the inflow direction of the LISM has been inferred [Möbius et al. [2015], Taut et al. [2018]]. However, the modification of the PUI VDF during transport in the SW complicates the interpretation of PUI measurements.
The theoretical concepts of the transport of PUIs in the SW have undergone many iterations for which the main driver have been observations which did not agree with the previous models. An example for these concepts is the isotropization of the VDFs, for which in general swift time scales are assumed w.r.t. the time scale of transport from ionization to observation (e.g. Vasyliunas and Siscoe [1976]). Yet, anisotropic features have been observed in PUI VDFs [Oka et al. [2002], Drews et al. [2015]] which can be seen as an indicator that the time scale of isotropization is longer than assumed. In addition, the observations of PUI VDFs were instrumentally limited to one dimension with the exception of data from STEREO/PLASTIC and probably at the time of writing only partly released data of Solar Orbiter/SWA/HIS. The anisotropic features observed by Drews et al. [2015] were based on data from STEREO/PLASTIC to derive two-dimensional VDFs. However, PLASTIC is designed to provide observations of three dimensional (3d) VDFs and this work focuses on the full 3d information that the instrument provides.
So, for this work the Pulse Height Analysis (PHA) data of STEREO/PLASTIC was re-calibrated to identify He^+ PUIs and to derive 3d VDFs. To that end, the data products which provide directional information have been investigated. STEREO/PLASTIC is a top-hat time-of-flight mass spectrometer. Time-of-flight mass spectrometers such as PLASTIC [Galvin et al. [2008]],

Ulysses/SWICS [Gloeckler et al. [1992]], ACE/SWICS [Gloeckler et al. [1998]] or Solar Orbiter/SWA/HIS [Owen et al. [2020]] detect particles in three (or two, depending on the implementation) consecutive steps: Firstly, particles pass an electrostatic analyzer. The electrostatic analyzer filters particles by energy per charge by application of an electric field. For PLASTIC, the electrostatic analyzer is a dome shaped parallel-plate condensator. This way, theoretically particles from all horizontal directions can enter and pass the analyzer [Galvin et al. [2008]]. Secondly, a two-point measurement in a time-of-flight chamber is employed to determine a particle's velocity. For this, particles pass a thin carbon foil. This releases electrons and these trigger a start signal for a timer. In PLASTIC the stop signal for a timer is triggered by either of two mechanisms depending on where the particle is located in the instrument. The instrument is divided into mainly three different sections: The solar wind sector (SWS), the wide angle partition (WAP) with SSDs (WAPSSD) and the WAP without SSDs (WAPNOSSD) [Galvin et al. [2008]]. In sections with SSD, the particles release the secondary electrons on impact on the SSD. Also, by stopping the particle in the SSD, the third stage of measurement is completed, which is measurement of total energy. Since then three data products are available for a particle, these are called triple coincidences (TCRs). Contrarily, particles without a measurement of total energy are called double coincidences (DCRs). In the sections without SSDs, only double coincidences are measured. The stop signal for the time-of-flight chamber is directly triggered by impact of the particle on a discrete anode at the end of the time-of-flight chamber. To process events from different horizontal directions, the trigger logic of PLASTIC's time-of-flight chamber is segmented. Hence, in segments without SSD the segmentation of the resistive anodes provides information of the horizontal angle of incident.
In SWS and WAPSSD two systems provide information about the horizontal angle of incident. Firstly, the number of the SSD which has been hit by a particle is stored. Secondly, the secondary electrons released by the impact into the SSD are amplified with micro channel plates and hit a resistive anode. The segmentation of discrete anodes is more coarse than the digital resolution of the resistive anode. However, the resistive anode has a nonlinear response to the angle of incident and therefore more challenging to read out [Galvin et al. [2008]].
Information about the latitudinal angle of incident is provided by an electrostatic deflection system which is found at the entrance of the instrument [Galvin et al. [2008]].
Originally, this work aimed to employ PLASTIC's nearly full 360° field of view in azimuth. This made a calibration of all the instrument's segments necessary and a thorough investigation of differences in detection efficiencies which emerge from the different systems of measurement in different sections. The density of He^+ PUIs is for WAPSSD and WAPNOSSD affected by patterns, which are unexpected and unphysical. In some of the instrumental longitudinal position bins, the He^+ density systematically changes w.r.t. the magnetic field orientation, but in others not and the count rates in those bins, where the densities do not follow the magnetic field orientation systematically, the number of counts per measurement interval is low. In the other bins, the counts are comparable to observations in SWS. We considered the possibility that in bins of Quadrant 1 these count rates are at least partially caused by particles which are deflected at the spacecraft's solar panels, but this still remains open. Also scattering of particles within the instrument or issues with the signalling electronics of the instruments can not be ruled out. A defect within the discrete anodes where the counts are low is also a probable cause, since the densities as a function of positional bin do not follow a regular pattern, but the bins where the counts are very low maintain their very low count rates. Since the SW is variable and the local magnetic field changes direction over time, it would be unphysical for incidenting particles to create such a time constant pattern. Because of the problematic nature of the data in WAPSSD and WAPNOSSD data from these sections has been disregarded and the focus is put on data in SWS.

For plausibility, in the SWS the directional information inferred from the number of the triggered SSD and the resistive anode have been compared. Since the SSDs are broader than a bin of the anode, a profile which reflects at least that broadness was expected. Also, as described in Galvin et al. [2008] the directional information from the resistive anode is affected by scattering of particles at a support structure which is fitted in the center of the instrument and ground calibration of the flight spare instrument showed a nonlinear response of the resistive anodes position indication. With these results in mind it is not surprising that the distribution of discrete anode position measurements of events which incident into a single SSD is a broad distribution. The distributions for the SSDs which are not close to the aperture's boundary have a maximum at the position bin which corresponds to the lateral position of the SSD. The Full Width at Half Maximum (FWHM) is at least 7 bins, which corresponds to an angular spread of $\sim 10°$ (twice the lateral width of an SSD). All distributions showed a significantly lower number of counts than expected close to the left boundary of the aperture (bin number 16), but not at the right boundary (bin number 48). At the right boundary the distributions also show a peak in density. We interpret these observations as likely scattering of the particles at the edges of the boundary. Further observations showed that density profiles observed over long times (e.g. the time needed for one orbit) are asymmetric. In the following, all position bins with numbers ≤ 32 are considered the left half of SWS and conversely all bins > 32 the right half with the exclusion of bins < 16 and ≥ 48 which are not part of SWS. Initially (from 2008 on) the more density is observed in the left half of the instrument w.r.t. the right half of the instrument regardless of the magnetic field direction, the solar wind conditions or the position of the spacecraft. Until 2015 for both DCRs and TCRs this asymmetric behavior continues. However, for DCRs, the ratio between left and right average densities gradually decreases to almost 1. For TCRs the ratio remains almost constant at ~ 2. During parts of 2015, the spacecraft was in solar conjunction, so that contact was temporarily lost. During that period, the spacecraft was flipped around the sunpointing axis. Interestingly after the conjunction period the former right side observed more particles than the former left side with an initial ratio of ~ 5 for the DCRs and ~ 3.5 for the TCRs. Yet, that trend quickly reversed and from 2017 on the former left side again systematically observed more counts. As of yet it is not completely understood, why the asymmetries evolved in this way. A combination of nonlinear aging effects, initial asymmetries and differences in the underlying physical distribution of the SW could at least partially explain the behavior. However, with long-term measurements there was no success with regard to a meaningful quantification of the instrument's nonlinear and asymmetric behavior.

An opportunity for a short-term investigation of asymmetries in the detection efficiency and maybe even correction factors are provided by short-term rolls of the spacecraft. These rolls were commenced regularly in order to obtain calibration data for the spacecraft's magnetometer (they are also called Sun Earth Connection Coronal and Heliospheric Investigation (SECCHI) calibration rolls) and take a time interval of ~ 3 h. Under the condition that the SW does not change too drastically during the rolls' time intervals, it is reasonable to assume, that an ideal instrument observes the same lateral distribution when it is rotated by 180° as before and after the roll, but flipped around the central axis. Then, discrepancies between the flipped lateral distribution at 180° rotation and the lateral distributions before and after the roll ideally reflect asymmetries in the detection efficiency of the instrument. With that approach, lateral distributions were compared for He^+ events. In particular for rolls during 2008, a discrepancy in the detection efficiency was found: The instrument's left half systematically observes more events than the right half. Yet, for following time periods, the comparisons show no clear systematic pattern. For one, the number of observed events per year is drastically reduced for years following 2008 which is either due to the distance between STEREO A and the Earth which allows

less bandwidth for data transfer or due to an aging of the instrument which causes fewer events to be observed. For another, the activity of the Sun increased so that also the SW was more dynamic. This increases the uncertainty of the analysis from 2008 to 2015 over time, because with increasing solar activity also the stability of the SW conditions during the rolls decreased. As a consequence of these, data from the rolls needed to be combined by a superposition of different time periods with regard to the time until/from the beginning of the roll. Yet, also the increased number of events gained from the superposition did not yield clear systematic trends with regard to detection efficiency. Also, for most of the rolls the parameters of the SW changed so much, that the assumption of similar SW conditions during a roll is an oversimplification. This introduces an additional systematic error into the comparison analysis.
Even though it is unknown whether the instrumental detection efficiency also varies in latitudinal angle, for data from 2008 another approach was employed to obtain a trend of the instrument's detection efficiency as a function of longitudinal angle of incident. When the spacecraft is rolled by 90° or 270°, the instrument's latitudinal angle detection system effectively detects the longitudinal distribution during un-rolled conditions. A comparison between these distributions showed similar detection efficiencies as before with regard to that the left half of the instrument observes by a factor of ~ 2 more events than the right half. Also, a strong dip in detection efficiency was observed in the center, which is a signature of the particles being scattered at the center of the instrument.

Unfortunately, the investigations of the SECCHI rolls did not yield reliable values for relative detection efficiencies or correction factors for the positional bins obtained from the instrument's resistive anode. This is mainly due to a strong variability of the SW during the rolls. Also the small number of PHA events during the 3 h of a single roll introduces another degree of uncertainty. However, asymmetries in the detection efficiency were found and it was directly shown, that due to scattering at the center of the instrument, in the center of the instrument the detection efficiency is low compared to the rest of the instrument. Hence, lateral distributions observed by the instrument's resistive anode resemble two islands of increased density. Probably, on the outer edges (towards bin 16 at the left edge and towards bin 48 at the right edge) scattering at the instrument's aperture decreases the count rates. In the instrument's center (~ 8 bins around bin 32) scattering at a support structure decreases the count rates. Overall, in the left half the counts are systematically increased w.r.t. the right half. Since on Solar Orbiter both a triaxial magnetometer which requires calibration rolls and a time of flight mass spectrometer (HIS) similar to PLASTIC are fitted, the method of this work to detect asymmetries in the instrument's detection efficiencies are also suitable for Solar Orbiter observations and might lead to correction factors for suprathermal particle observations from Solar Orbiter/HIS.

Since the available calibration opportunities were insufficient to derive reliable, time-dependent correction factors for the instrument's asymmetric behavior, following observations of particles are still affected by that behavior. However, it is still possible to make qualitative observations about the VDFs of He^+ PUIs. As a first approach to 3d VDFs, this work presents 3d histograms of He^+ PUI velocities. Yet, the observed distributions were strongly influenced by the asymmetries and nonlinearities of the instrument's azimuthal angle of incident detection. To at least partially counteract these, each velocity bin is divided by a global average of its density, so that relative distributions are derived. These enabled the observation of features within the 3d He^+ PUI VDFs, which resembled those observed by Drews et al. [2015] in 2d He^+ PUI VDFs. For the observation of anisotropic features it was imperative to limit data to time periods when a pre-defined magnetic field direction is found. In this study, the VDFs were thus observed as a function of the magnetic field azimuthal angle and the magnetic field elevation angle was kept

within the ecliptic plane to simplify the geometry. In future studies with this work's method VDFs can also be observed as a function of elevation angle. Yet, with increasing deviation from the ecliptic plane the number of events coinciding with that magnetic field angle decrease, so that considerations of statistical significance and the signal to noise ratio are of priority for such a study. Interestingly, strong enhancements in the PUI density were only found for magnetic field azimuthal angles close to $\pm 90°$.
In addition to the direction of the magnetic field, the VDFs were observed as a function of SW condition. To that end, the classification scheme of Xu and Borovsky [2015] was adapted to PLASTIC SW observations. In this scheme, the SW is classified into the categories ejecta, coronal hole wind, sector reversal wind and streamer belt wind. In this work, the classification is modified by a replacement of the ejecta category. As a first step also wind of the ejecta category is categorized into the other categories. In a second step the ICME and SIR list from the STEREO level 3 data [Jian et al. [2013, 2018, 2019], Kucera [2022]] is employed to mask for time periods of these events in the SW. This is important for the discussion of 3d VDFs, since these are expected to be regions of strong acceleration of PUIs (e.g. Bower et al. [2019]) and in the following, time periods of ICMEs and SIRs are not considered for contribution to the 3d VDFs. In all wind types similar anisotropic features were found, but with different relative clarity of manifestation. The strongest pronunciation of the anisotropies was found in the sector reversal wind. In streamer belt and coronal hole wind anisotropies were also found. These were similar to the aforementioned anisotropies in the sector reversal wind, but less pronounced in the coronal hole wind. Since sector reversal wind conditions tend to be found close to SIRs, which are regions of strong acceleration (e.g. Bower et al. [2019]), this result is unexpected. However, that fewer anisotropies are found in the coronal hole wind than in the streamer belt wind was expected, since more wave perturbations are expected in that wind type and interaction with waves is considered to isotropize PUI VDFs (e.g. Jokipii [1966], Fisk et al. [1997]). However, it should be denoted, that parts of the anisotropies observed in coronal hole and streamer belt wind could actually be connected to acceleration regions in the SW. This possibility exists, since in the classification scheme of Xu and Borovsky [2015] is unable to perfectly distinguish between these regions and the different types of SW. Thus, some acceleration regions might be classified as coronal hole or streamer belt wind. This can only partly be corrected by the consideration of the ICME and SIR lists, since these also not include all acceleration regions.
All in all due to instrumental detection efficiency problems and an often low signal to noise ratio, these findings merely hint towards tendencies. Yet, it can be noted that anisotropic features have been found in the VDF of PUIs which suggests that the process of PUI isotropization during transport is slower or less efficient than previously assumed.

With data of Solar Orbiter/SWA/HIS, which is not yet available, but promises better statistics and resolution than PLASTIC, different studies employing this work's methods may be possible. Since the interstellar neutrals (ISNs) velocity and ionization rate depend on the position in the heliosphere, with better statistics than from PLASTIC a comparison between PUI VDFs at different positions (e.g. focusing cone vs. crescent) might show how PUI transport is affected by changes of the initial conditions.
The elliptical orbit of Solar Orbiter also potentially allows to observe PUI VDFs as a function of distance from the Sun and therefore might contribute to the derivation of time scales of isotropization during PUI transport in the SW. In addition, from the observation of PUIs from further inside the heliosphere than 1 AU a higher fraction of inner source PUIs are expected. 3d VDFs might provide a tool to distinguish these from interstellar source PUIs.
Also, with the method of Němeček et al. [2020] to derive the de-Hoffmann-Teller (dHT) velocity from plasma data, which in this work was applied to PLASTIC data and simulations of PUI

transport presented in this work, a future study is enabled, which assesses features observed within the 3d VDFs with regard to simulation expectations and aims to find hints towards the question of whether the dHT frame is better suited to describe PUI transport than the SW frame.

For 3d velocity vectors in the context of charged particles in a magnetic field, the pitch angle is a useful abstraction. Before pitch angle distributions were derived from PLASTIC He^+ PUI observations, another look is taken on the detection efficiency of the instrument. This lead to a theoretical consideration of the effects of a geometrically limited instrumental aperture to the probability of a particle which gyrates sufficiently close to the instrument to also enter the instrumental aperture. The probability is based on the fraction of the particle's gyro orbit, which in velocity space is situated within the boundaries of the aperture. Hence, depending on the location of the transporting frame, the direction of the magnetic field and the pitch angle, the Ring Coverage (RiCo) results in a different measurement probability of particles which gyrate around the magnetic field and are transported by said transporting frame. Employing an isotropic model distribution, it was shown that if the RiCo based measurement probability is applied to the model test particles, the range of observable pitch angles is a function of the magnetic field direction, since the instrument's aperture is limited. It was also found that the probability of a pitch angle to be observed also depends on the magnetic field direction. This lead to a modification of the isotropic distribution's pitch angle distribution which lead even under integration over all magnetic field angles to a different shape of the distribution. Implications from this pre-study for the observed pitch angle distributions are:

- Per magnetic field direction, the range of observable pitch angles is limited. Since it can not be known whether the underlying pitch angle distribution changes when the magnetic field angle changes an integration over all pitch angles can not mitigate the limited range and would at least still need to be corrected by the RiCo probabilities. As a consequence, the observations should always be conducted as a function of the magnetic field direction and per magnetic field direction. This way, distributions are obtained, which are snapshots of the distributions which would be obtained with a full Field Of View (FOV).
- To obtain pitch angle distributions, the contribution of each event should be corrected to reflect the RiCo based measurement probability. For a statistically sufficiently large number of events this can be achieved by division by the RiCo.
- Even though it is not possible to directly observe an isotropic background under these limitations, anisotropic features are still visible in both RiCo corrected and RiCo uncorrected data. Yet, the RiCo also leads to an apparent systematic behavior of PUI densities as a function of the magnetic field direction.

Hence, a study of RiCo corrected and RiCo uncorrected pitch angle distribution can show whether the density enhancements which have been observed by Drews et al. [2015] and this work in 3d PUI VDFs and rotated similarly to the magnetic field direction are mainly a consequence of the RiCo based detection probabilities or are still observed if RiCo correction is applied. Particularly the strong density enhancements at $\pm 90°$ magnetic field azimuthal angles fit under the assumption of the geometry of the SWS to magnetic field directions of large RiCo based probabilities.

In uncorrected pitch angle distributions, these density enhancements are visible as well and are interestingly even more pronounced in RiCo corrected distributions. Even if the RiCo correction is applied, most density enhancements were only observed for magnetic field azimuthal angles of $\pm 90°$ and corresponding pitch angles of $90°$.

Similarly to the 3d VDFs, the pitch angle distributions were then investigated as a function not only of magnetic field direction but only of the SW condition according to the classification scheme of Xu and Borovsky [2015]. In addition, the distributions were observed as a function of the spacecraft's position within the heliosphere. However, the statistics was too small in the crescent region, so that a direct comparison of the distributions in the focusing cone and the crescent region is not feasible. Yet, a comparison of distributions in focusing cone and lateral regions (neither crescent nor focusing cone) was conducted.
Anisotropies or in that regard density enhancements at $\pm 90°$ are present in both zones, but more pronounced in the focusing cone region which may hint towards that a larger fraction of fresher PUIs is observed in the focusing cone region. This would fit to simulations which show that the spatial maximum of PUI production is closer to 1 AU in the focusing cone region than in the lateral zones. However, since it is yet unknown why the density enhancements are only seen at $\pm 90°$, it can not be discounted that the PUIs which contribute to these enhancements are not fresh. E.g. a pitch angle of $90°$ is an attractor in phase space under transport in a stochastic magnetic field in quasi-linear-theory (e.g. Jokipii [1966]).
Another approach to explain the specific observed pattern of enhanced densities actually assumes that these PUIs are (sufficiently) freshly created. In that case, their pitch angle resembles the initial pitch angle which correlates to the magnetic field direction. If the magnetic field is limited to be located within the ecliptic plane, the line which models expected pitch angles under the assumption that the momentary magnetic field azimuthal angle is similar to the magnetic field angle during creation of the observed PUIs intersects the zone of observable pitch angles at azimuthal magnetic field angles of $\pm 90°$. Yet, this approach has the caveat that the magnetic field changes dynamically and the magnetic field during PUI creation may deviate further from the observed magnetic field the longer the creation of the PUI occurred.
To investigate this further, the pitch angle distributions were observed for different values of $|\vec{\varpi}_{SWp}|$, since under the assumption of adiabatic cooling older PUIs are located at smaller values of $|\vec{\varpi}_{SWp}|$ [Moebius et al. [1988]]. In these distributions it was observed, that for $|\vec{\varpi}_{SWp}| \sim 1$ enhanced densities are located on a line which resembles the expected pitch angles of fresh PUIs. If $|\vec{\varpi}_{SWp}|$ is decreased, the line vanishes. This not only hints at the observation that the density enhancements are indeed created by freshly ionized or weakly transported PUIs, but also shows that theoretically, with this work's analysis direct observations of PUI transport affected pitch angle distributions can be made and maybe also time scales for the transport can be estimated. However, within the limitations of the instruments this can not be achieved with PLASTIC data. Maybe the data from Solar Orbiter/SWA/HIS will provide better statistics and therefore more robust results. Also, this work's analysis can derive parameters of adiabatic cooling, since Solar Orbiter's elliptical orbit allows for observation of PUIs at different distances from the Sun. Also the effect of RiCo based measurement probability for which this work provided a method to infer correction factors might play an important role for observations with HIS: The longitudinal FOV of SWA-HIS is $96°$ [Owen et al. [2020]].

With the knowledge that this work has gained with regard to instrumental asymmetries and with regard to the method of RiCo correction, it is conceivable, that the signatures of a torus distribution in PUI VDFs observed by Drews et al. [2015] are systematically too strong. However, this work observed similar traces of anisotropies in PUI VDFs. So the observations of Drews et al. [2015] are not disproven by this works' results. Yet, the amount of anisotropies were judging from this works' observations systematically overestimated by Drews et al. [2015].
This work provides the foundation for interesting future studies of PUI VDFs not only with the PLASTIC instrument which on STEREO A is still in operation, but also with the state-of-the-art Heavy Ion Sensor on board Solar Orbiter which also observes further inside the heliosphere

than STEREO so that the likelihood to also observe inner source PUIs is increased. In addition, recently data from the SWICS instruments were employed to derive long-term 3d PUI VDFs [Berger [2018], Fischer [2019]]. Hence, in the future new insights into the transport of PUIs can be expected as the set of observational data from which 3d PUI VDFs can be inferred is expanding.

The problems which this work encountered with the analysis of the data from STEREO/PLASTIC are also a feedback to the design of the instrument. If in the future an instrument were built which is specifically designed to observe 3d VDFs of suprathermal particles, the design should firstly focus on an improvement of the instruments FOV, since the FOV not only determines the range of observable pitch angles as a function of the magnetic field direction but also introduces a systematic error into the observed particle densities. The larger the FOV, the larger the range of observable pitch angles. Even though a full longitudinal and latitudinal FOV would be optimal, it is conceivable, that this can not be achieved since the instrument and the spacecraft are of finite size and always block portions of the FOV. But with a design similar to PLASTIC at least a full longitudinal FOV might be achievable for future instruments.
Yet, with a larger FOV another challenge arises which was also encountered with PLASTIC: Different detection efficiencies and different geometry factors for different angles of incident create a systematic error which is challenging to determine and reverse as the efforts of this work to determine this kind of systematic error with PLASTIC showed. So also attention should be put to design the instrument such that for each direction the probability of measurement is the same. However, this provides its own challenges and problems. E.g. it is expected that most particle flux comes from the direction of the SW. If all parts of the instrument had the same detection efficiencies, then the parts pointing in average SW direction would wear out quicker. Also, between all fitted components small differences and tolerances exist on too small scales to be mitigated during construction within a reasonable amount of effort. So even though if e.g. solid state detectors (SSDs) were fitted at the end of each direction's particle trajectory, their output would systematically differ. The same applies to the time of flight chambers which utilize foils which are no thicker than several layers of atoms.
But concerning the time of flight chambers, the signal from PLASTIC would probably be more improved, if the time of flight chambers' geometry would be simplified. The design of PLASTIC as compared to the design of e.g. SWICS involves more complicated trajectories of secondary electrons which trigger the start and stop signals for the time measurements. This created a signal which is overlayed by a large number of chance coincidence measurements. Despite the problematic and not yet fully understood behavior of the PLASTIC instrument, this work has for the first time observed 3d PUI VDFs and pitch angle distributions and investigated them for traces of phase space transport effects.

Glossary

CIR corotating interaction region. 16, 18

CME coronal mass ejection. 17

DC double coincidence. 63

FOV Field Of View. 4, 183, 185

ISN interstellar neutral. 1, 2, 40–49, 51, 55–57, 171–173, 182

MDNVDF Magnetic field Direction Normalized velocity distribution function. 120, 121, 123–129, 131–133, 135–137, 212–217

PUI Pickup Ion. i, ii, 1–7, 18, 27–31, 33, 37, 40–43, 45–61, 85, 92, 97, 99, 105, 106, 109, 114, 119, 120, 123, 126–128, 131, 133, 135, 143, 154, 158–163, 172–179, 181–185, 209

QLT Quasi Linear Theory. 34

SIR stream interaction region. 16, 18

SSD solid state detector. 4, 5, 81, 91, 92, 102, 139, 185

SW solar wind. i, ii, 1–3, 6–23, 25, 27, 33, 35–38, 40, 42, 43, 47–56, 58, 60, 61, 63, 67, 69, 70, 75, 79, 81, 85, 88, 92, 96–99, 105, 106, 110, 112, 113, 115, 119–121, 123, 125–129, 131–135, 137, 139, 140, 143–150, 159–163, 167, 169–175, 178–185, 211, 212

TC triple coincidence. 63

UV ultraviolet. 1

VDF Velocity Distribution Function. i, ii, 1–6, 11, 18, 27, 28, 33, 35, 36, 40, 42, 43, 47, 48, 51–61, 69, 85, 96, 105, 109, 112, 113, 120, 122, 123, 127, 128, 131, 133, 135, 139, 140, 154, 159–162, 170, 175, 178, 181–185, 209, 210

Acronyms

3d three dimensional. i, ii, 4, 5, 36, 45, 47, 178, 181–185

dHT de-Hoffmann-Teller. 3, 5, 37, 50, 56, 58, 60, 97–100, 102, 182, 183

DPU Data Processing Unit. 69–71

DSN Deep Space Network. 69

ESA electrostatic analyser. 63, 64, 71, 75–77

LIC Local Interstellar Cloud. 38

LISM Local Interstellar Medium. i, 38–40, 43, 45, 178

PHA Pulse Height Analysis. 4, 5, 70, 71, 96, 99, 109, 143, 162, 178, 181

SWS Solar Wind Sector. 109, 123, 131, 139–141, 154, 172, 173, 175

References

L. Biermann. Kometenschweife und solare Korpuskularstrahlung. *ZAp*, 29:274, January 1951.

E. N. Parker. Dynamics of the Interplanetary Gas and Magnetic Fields. *ApJ*, 128:664, November 1958. doi: 10.1086/146579.

Jr. Spitzer, Lyman. The Dynamics of the Interstellar Medium. III. Galactic Distribution. *ApJ*, 95:329, May 1942. doi: 10.1086/144407.

W. I. Axford, A. J. Dessler, and B. Gottlieb. Termination of Solar Wind and Solar Magnetic Field. *ApJ*, 137:1268, May 1963. doi: 10.1086/147602.

Priscilla C. Frisch, Seth Redfield, and Jonathan D. Slavin. The Interstellar Medium Surrounding the Sun. *ARA&A*, 49(1):237–279, September 2011. doi: 10.1146/annurev-astro-081710-102613.

W. I. Axford. *The Interaction of the Solar Wind With the Interstellar Medium*, volume 308, page 609. 1972.

J. Geiss, G. Gloeckler, L. A. Fisk, and R. von Steiger. C^+ pickup ions in the heliosphere and their origin. *J. Geophys. Res.*, 100(A12):23373–23378, January 1995a. doi: 10.1029/95JA03051.

George Gloeckler and Johannes Geiss. Interstellar and Inner Source Pickup Ions Observed with SWICS on ULYSSES. *Space Sci. Rev.*, 86:127–159, July 1998. doi: 10.1023/A:1005019628054.

P. R. Quinn, N. A. Schwadron, E. Möbius, A. Taut, and L. Berger. Inner Source C^+/O^+ Pickup Ions Produced by Solar Wind Recycling, Neutralization, Backscattering, Sputtering, and Sputtering-induced Recycling. *ApJ*, 861(2):98, July 2018. doi: 10.3847/1538-4357/aac6ca.

E. Möbius, D. Hovestadt, B. Klecker, M. Scholer, G. Gloeckler, and F. M. Ipavich. Direct observation of He^+ pick-up ions of interstellar origin in the solar wind. *Nature*, 318(6045):426–429, December 1985. doi: 10.1038/318426a0.

J. R. Jokipii. Cosmic-Ray Propagation. I. Charged Particles in a Random Magnetic Field. *ApJ*, 146:480, November 1966. doi: 10.1086/148912.

V. M. Vasyliunas and G. L. Siscoe. On the flux and the energy spectrum of interstellar ions in the solar system. *J. Geophys. Res.*, 81(7):1247, March 1976. doi: 10.1029/JA081i007p01247.

E. Moebius, D. Rucinski, D. Hovestadt, and B. Klecker. The helium parameters of the very local interstellar medium as derived from the distribution of He$\hat{+}$p̂ickup ions in the solar wind. *A&A*, 304:505, December 1995.

Philip A. Isenberg. A hemispherical model of anisotropic interstellar pickup ions. *J. Geophys. Res.*, 102(A3):4719–4724, March 1997. doi: 10.1029/96JA03671.

C. Drews, L. Berger, A. Taut, T. Peleikis, and R. F. Wimmer-Schweingruber. 2D He^+ pickup ion velocity distribution functions: STEREO PLASTIC observations. *A&A*, 575:A97, March 2015. doi: 10.1051/0004-6361/201425271.

Christian Drews, Lars Berger, Robert F. Wimmer-Schweingruber, Peter Bochsler, Antoinette B. Galvin, Berndt Klecker, and Eberhard Möbius. Inflow direction of interstellar neutrals deduced from pickup ion measurements at 1 AU. *Journal of Geophysical Research (Space Physics)*, 117 (A9):A09106, September 2012. doi: 10.1029/2012JA017746.

E. Möbius, M. A. Lee, and C. Drews. Interstellar Flow Longitude from the Symmetry of the Pickup Ion Cut-off at 1 AU. *ApJ*, 815(1):20, December 2015. doi: 10.1088/0004-637X/815/1/20.

A. Taut, L. Berger, E. Möbius, C. Drews, V. Heidrich-Meisner, D. Keilbach, M. A. Lee, and R. F. Wimmer-Schweingruber. Challenges in the determination of the interstellar flow longitude from the pickup ion cutoff. *A&A*, 611:A61, March 2018. doi: 10.1051/0004-6361/201731796.

L. Berger. 3D Pickup He^+ Spectra at 1 AU Observed by the Solar Wind Ion Composition Spectrometer on the Advanced Composition Explorer. In *AGU Fall Meeting Abstracts*, volume 2018, pages SH12B–06, December 2018.

Anne Fischer, Lars Berger, Verena Heidrich-Meisner, Duncan Keilbach, Martin Kruse, and Robert Wimmer-Schweingruber. 3D Velocity Distribution Functions of Pickup Ions with Ulysses/SWICS. In *AGU Fall Meeting Abstracts*, volume 2021, pages SH22A–06, December 2021.

R. M. Crutcher. The local interstellar medium. *ApJ*, 254:82–87, March 1982. doi: 10.1086/159707.

R. Lallement and P. Bertin. Northern-hemisphere observations of nearby interstellar gas : possible detection of the local cloud. *A&A*, 266:479–485, December 1992.

D. A. Gurnett, W. S. Kurth, L. F. Burlaga, and N. F. Ness. In Situ Observations of Interstellar Plasma with Voyager 1. *Science*, 341(6153):1489–1492, September 2013. doi: 10.1126/science.1241681.

E. C. Stone, A. C. Cummings, F. B. McDonald, B. C. Heikkila, N. Lal, and W. R. Webber. Voyager 1 Observes Low-Energy Galactic Cosmic Rays in a Region Depleted of Heliospheric Ions. *Science*, 341(6142):150–153, July 2013. doi: 10.1126/science.1236408.

D McComas, F Allegrini, L Bartolone, P Bochsler, M Bzowski, M Collier, H Fahr, H Fichtner, P Frisch, H Funsten, et al. The interstellar boundary explorer (ibex) mission. In *Solar Wind 11/SOHO 16, Connecting Sun and Heliosphere*, volume 592, page 689, 2005.

D. J. McComas, F. Allegrini, P. Bochsler, M. Bzowski, E. R. Christian, G. B. Crew, R. DeMajistre, H. Fahr, H. Fichtner, P. C. Frisch, H. O. Funsten, S. A. Fuselier, G. Gloeckler, M. Gruntman, J. Heerikhuisen, V. Izmodenov, P. Janzen, P. Knappenberger, S. Krimigis, H. Kucharek, M. Lee, G. Livadiotis, S. Livi, R. J. MacDowall, D. Mitchell, E. Möbius, T. Moore, N. V. Pogorelov, D. Reisenfeld, E. Roelof, L. Saul, N. A. Schwadron, P. W. Valek, R. Vanderspek, P. Wurz, and G. P. Zank. Global Observations of the Interstellar Interaction from the Interstellar Boundary Explorer (IBEX). *Science*, 326(5955):959, November 2009. doi: 10.1126/science.1180906.

J. Heerikhuisen, N. V. Pogorelov, G. P. Zank, G. B. Crew, P. C. Frisch, H. O. Funsten, P. H. Janzen, D. J. McComas, D. B. Reisenfeld, and N. A. Schwadron. Pick-Up Ions in the Outer Heliosheath: A Possible Mechanism for the Interstellar Boundary EXplorer Ribbon. *ApJ*, 708 (2):L126–L130, January 2010. doi: 10.1088/2041-8205/708/2/L126.

D. J. McComas, W. S. Lewis, and N. A. Schwadron. IBEX's Enigmatic Ribbon in the sky and its many possible sources. *Reviews of Geophysics*, 52(1):118–155, March 2014. doi: 10.1002/2013RG000438.

E. J. Zirnstein, J. Heerikhuisen, and D. J. McComas. Structure of the Interstellar Boundary Explorer Ribbon from Secondary Charge-exchange at the Solar-Interstellar Interface. *ApJ*, 804(1):L22, May 2015. doi: 10.1088/2041-8205/804/1/L22.

E. J. Zirnstein, J. Heerikhuisen, G. P. Zank, N. V. Pogorelov, H. O. Funsten, D. J. McComas, D. B. Reisenfeld, and N. A. Schwadron. Structure of the Heliotail from Interstellar Boundary Explorer Observations: Implications for the 11-year Solar Cycle and Pickup Ions in the Heliosheath. *ApJ*, 836(2):238, February 2017. doi: 10.3847/1538-4357/aa5cb2.

L. A. Fisk, N. A. Schwadron, and G. Gloeckler. Implications of fluctuations in the distribution functions of interstellar pick-up ions for the scattering of low rigidity particles. *Geophys. Res. Lett.*, 24(1):93–96, January 1997. doi: 10.1029/96GL03752.

Lukas Saul, Eberhard Möbius, Philip Isenberg, and Peter Bochsler. On Pitch-Angle Scattering Rates of Interstellar Pickup Ions as Determined by in Situ Measurement of Velocity Distributions. *ApJ*, 655(1):672–677, January 2007. doi: 10.1086/509732.

M. Oka, T. Terasawa, H. Noda, Y. Saito, and T. Mukai. 'Torus' distribution of interstellar helium pickup ions: Direct observation. *Geophys. Res. Lett.*, 29(12):1612, June 2002. doi: 10.1029/2002GL015111.

E. Moebius, B. Klecker, D. Hovestadt, and M. Scholer. Interaction of Interstellar Pick-Up Ions with the Solar Wind. *Ap&SS*, 144(1-2):487–505, May 1988. doi: 10.1007/BF00793200.

D. Keilbach, C. Drews, L. Berger, E. Marsch, and R. F. Wimmer-Schweingruber. Qualitative numerical studies of the modification of the pitch angle distribution of test particles by alfvènic wave activity. In *AGU Fall Meeting Abstracts*, volume 2017, pages SH33B–2768, December 2017a.

D. Keilbach, L. Berger, C. Drews, E. Marsch, and R. F. Wimmer-Schweingruber. Numerical study of alfvénic wave activity in the solar wind as a cause for pitch angle scattering with focus on kinetic processes. In *AGU Fall Meeting Abstracts*, volume 2017, pages SH33B–2785, December 2017b.

D. Keilbach, L. Berger, V. Heidrich-Meisner, and R. F. Wimmer-Schweingruber. Qualitative test particle simulations of pitch angle modifications due to Alfvénic waves. In *AGU Fall Meeting Abstracts*, volume 2018, pages SH12B–08, December 2018.

Liu Yang, Lars Berger, Robert F. Wimmer-Schweingruber, Linghua Wang, Jia Yu, Antoinette B. Galvin, and Eberhard Möbius. The Pitch-angle Distributions of Suprathermal Ions near an Interplanetary Shock. *ApJ*, 888(2):L22, January 2020. doi: 10.3847/2041-8213/ab629d.

E. Moebius, J. Bower, A. Aly, L. Berger, C. J. Farrugia, A. B. Galvin, D. Keilbach, B. Klecker, M. A. Lee, and N. Schwadron. He^+ Pickup Ion Tail Variations with Location across Solar Wind Compressions and Interplanetary Conditions. In *AGU Fall Meeting Abstracts*, volume 2019, pages SH53C–3352, December 2019.

J. S. Bower, E. Moebius, L. Berger, C. Farrugia, D. Keilbach, M. A. Lee, P. R. Quinn, N. Schwadron, and A. Taut. Effect of Rapid Changes of Solar Wind Conditions on the Pickup Ion Velocity Distribution. *Journal of Geophysical Research (Space Physics)*, 124(8):6418–6437, August 2019. doi: 10.1029/2019JA026781.

Zdeněk Němeček, Tereza Ďurovcová, Jana Šafránková, František Němec, Lorenzo Matteini, David Stansby, Nils Janitzek, Lars Berger, and Robert F. Wimmer-Schweingruber. What is the Solar Wind Frame of Reference? *ApJ*, 889(2):163, February 2020. doi: 10.3847/1538-4357/ab65f7.

A. B. Galvin, L. M. Kistler, M. A. Popecki, C. J. Farrugia, K. D. C. Simunac, L. Ellis, E. Möbius, M. A. Lee, M. Boehm, J. Carroll, A. Crawshaw, M. Conti, P. Demaine, S. Ellis, J. A. Gaidos, J. Googins, M. Granoff, A. Gustafson, D. Heirtzler, B. King, U. Knauss, J. Levasseur, S. Longworth, K. Singer, S. Turco, P. Vachon, M. Vosbury, M. Widholm, L. M. Blush, R. Karrer, P. Bochsler, H. Daoudi, A. Etter, J. Fischer, J. Jost, A. Opitz, M. Sigrist, P. Wurz, B. Klecker, M. Ertl, E. Seidenschwang, R. F. Wimmer-Schweingruber, M. Koeten, B. Thompson, and D. Steinfeld. The Plasma and Suprathermal Ion Composition (PLASTIC) Investigation on the STEREO Observatories. *Space Sci. Rev.*, 136(1-4):437–486, April 2008. doi: 10.1007/s11214-007-9296-x.

CJ Owen, R Bruno, S Livi, P Louarn, K Al Janabi, F Allegrini, C Amoros, R Baruah, A Barthe, M Berthomier, et al. The solar orbiter solar wind analyser (swa) suite. *Astronomy & Astrophysics*, 642:A16, 2020.

D. Müller, O. C. St. Cyr, I. Zouganelis, H. R. Gilbert, R. Marsden, T. Nieves-Chinchilla, E. Antonucci, F. Auchère, D. Berghmans, T. Horbury, R. A. Howard, S. Krucker, M. Maksimovic, C. J. Owen, P. Rochus, J. Rodriguez-Pacheco, M. Romoli, S. K. Solanki, R. Bruno, M. Carlsson, A. Fludra, L. Harra, D. M. Hassler, S. Livi, P. Louarn, H. Peter, U. Schühle, L. Teriaca, J. C. del Toro Iniesta, R. F. Wimmer-Schweingruber, E. Marsch, M. Velli, A. De Groof, A. Walsh, and D. Williams. The Solar Orbiter mission – Science overview. *arXiv e-prints*, art. arXiv:2009.00861, September 2020.

A. J. Hundhausen. Interplanetary neutral hydrogen and the radius of the heliosphere. *Planet. Space Sci.*, 16(6):783–793, June 1968. doi: 10.1016/0032-0633(68)90082-2.

G. Prölss. *Physik des erdnahen Weltraums: Eine Einführung*. Physics and astronomy online library. Springer Berlin Heidelberg, 2013. ISBN 9783642188077. URL `https://books.google.de/books?id=IgH2BQAAQBAJ`.

ISO 3529-1:2019. Vacuum technology — Vocabulary — Part 1: General terms. Standard, International Organization for Standardization, Geneva, CH, July 2019.

R. C. Carrington. Description of a Singular Appearance seen in the Sun on September 1, 1859. *MNRAS*, 20:13–15, November 1859. doi: 10.1093/mnras/20.1.13.

R. Hodgson. On a curious Appearance seen in the Sun. *MNRAS*, 20:15–16, November 1859. doi: 10.1093/mnras/20.1.15.

N.U. Crooker. Solar and heliospheric geoeffective disturbances. *Journal of Atmospheric and Solar-Terrestrial Physics*, 62(12):1071–1085, 2000. ISSN 1364-6826. doi: https://doi.org/10.1016/S1364-6826(00)00098-5. URL `https://www.sciencedirect.com/science/article/pii/S1364682600000985`.

DN Baker. What is space weather? *Advances in Space Research*, 22(1):7–16, 1998.

L. Biermann. Solar corpuscular radiation and the interplanetary gas. *The Observatory*, 77: 109–110, June 1957.

K. I. Gringauz, V. V. Bezrokikh, V. D. Ozerov, and R. E. Rybchinskii. A Study of the Interplanetary Ionized Gas, High-Energy Electrons and Corpuscular Radiation from the Sun by Means of the Three-Electrode Trap for Charged Particles on the Second Soviet Cosmic Rocket. *Soviet Physics Doklady*, 5:361, September 1960.

VN Obridko and OL Vaisberg. On the history of the solar wind discovery. *Solar System Research*, 51(2):165–169, 2017.

David R. Williams. Sun Fact Sheet, 2016a. `https://nssdc.gsfc.nasa.gov/planetary/factsheet/sunfact.html` (Website accessed at 9. August 2021).

NJ Fox, MC Velli, SD Bale, R Decker, A Driesman, RA Howard, Justin C Kasper, J Kinnison, M Kusterer, D Lario, et al. The solar probe plus mission: Humanity's first visit to our star. *Space Science Reviews*, 204(1):7–48, 2016.

JHU APL. STEREO Science operations plan, 2019. `http://parkersolarprobe.jhuapl.edu/The-Mission/index.php#Where-Is-PSP` (Website accessed at 21. October 2022).

William Hyde Wollaston. Xii. a method of examining refractive and dispersive powers, by prismatic reflection. *Philosophical Transactions of the Royal Society of London*, (92):365–380, 1802.

Joseph Fraunhofer. Bestimmung des brechungs-und des farbenzerstreungs-vermögens verschiedener glasarten, in bezug auf die vervollkommnung achromatischer fernröhre. *Annalen der Physik*, 56(7):264–313, 1817.

Henry Norris Russell. On the Composition of the Sun's Atmosphere. *ApJ*, 70:11, July 1929. doi: 10.1086/143197.

Martin Asplund, Nicolas Grevesse, A. Jacques Sauval, and Pat Scott. The Chemical Composition of the Sun. *ARA&A*, 47(1):481–522, September 2009. doi: 10.1146/annurev.astro.46.060407.145222.

Alfred Weigert, Heinrich J Wendker, and Lutz Wisotzki. *Astronomie und Astrophysik: Ein Grundkurs*. John Wiley & Sons, 2012.

Dieter (Hrsg.) Meschede and Christian Gerthsen. *Gerthsen Physik*. Springer-Verlag, 2015. ISBN 978-3-662-45976-8. doi: 10.1007/978-3-662-45977-5.

J. Schou, P. H. Scherrer, R. I. Bush, R. Wachter, S. Couvidat, M. C. Rabello-Soares, R. S. Bogart, J. T. Hoeksema, Y. Liu, T. L. Duvall, D. J. Akin, B. A. Allard, J. W. Miles, R. Rairden, R. A. Shine, T. D. Tarbell, A. M. Title, C. J. Wolfson, D. F. Elmore, A. A. Norton, and S. Tomczyk. Design and Ground Calibration of the Helioseismic and Magnetic Imager (HMI) Instrument on the Solar Dynamics Observatory (SDO). *Sol. Phys.*, 275(1-2):229–259, January 2012. doi: 10.1007/s11207-011-9842-2.

Julius Bartels. Twenty-seven day recurrences in terrestrial-magnetic and solar activity, 1923–1933. *Terrestrial Magnetism and Atmospheric Electricity*, 39(3):201–202a, 1934.

John M Wilcox and Robert Howard. Differential rotation of the photospheric magnetic field. *Solar Physics*, 13(2):251–260, 1970.

Herschel B. Snodgrass and Roger K. Ulrich. Rotation of Doppler Features in the Solar Photosphere. *ApJ*, 351:309, March 1990. doi: 10.1086/168467.

Jeffrey W. Brosius, Joseph M. Davila, Roger J. Thomas, and Brunella C. Monsignori-Fossi. Measuring Active and Quiet-Sun Coronal Plasma Properties with Extreme-Ultraviolet Spectra from SERTS. *ApJS*, 106:143, September 1996. doi: 10.1086/192332.

J. P. Delaboudinière, G. E. Artzner, J. Brunaud, A. H. Gabriel, J. F. Hochedez, F. Millier, X. Y. Song, B. Au, K. P. Dere, R. A. Howard, R. Kreplin, D. J. Michels, J. D. Moses, J. M. Defise, C. Jamar, P. Rochus, J. P. Chauvineau, J. P. Marioge, R. C. Catura, J. R. Lemen, L. Shing, R. A. Stern, J. B. Gurman, W. M. Neupert, A. Maucherat, F. Clette, P. Cugnon, and E. L. van Dessel. EIT: Extreme-Ultraviolet Imaging Telescope for the SOHO Mission. *Sol. Phys.*, 162(1-2):291–312, December 1995. doi: 10.1007/BF00733432.

M. Aschwanden. *Physics of the Solar Corona: An Introduction with Problems and Solutions*. Springer Praxis Books. Springer Berlin Heidelberg, 2006. ISBN 9783540307655. URL `https://books.google.de/books?id=W7FE5_aowEQC`.

George Gloeckler and Johannes Geiss. The abundances of elements and isotopes in the solar wind. In C. Jake Waddington, editor, *Cosmic Abundances of Matter*, volume 183 of *American Institute of Physics Conference Series*, pages 49–71, January 1989. doi: 10.1063/1.37985.

T. H. Zurbuchen, L. A. Fisk, G. Gloeckler, and R. von Steiger. The solar wind composition throughout the solar cycle: A continuum of dynamic states. *Geophys. Res. Lett.*, 29(9):1352, May 2002. doi: 10.1029/2001GL013946.

Michael R Collier, Thomas E Moore, Keith W Ogilvie, Dennis Chornay, JW Keller, S Boardsen, James Burch, B El Marji, M-C Fok, SA Fuselier, et al. Observations of neutral atoms from the solar wind. *Journal of Geophysical Research: Space Physics*, 106(A11):24893–24906, 2001.

S. J. Bame, J. R. Asbridge, W. C. Feldman, M. D. Montgomery, and P. D. Kearney. Solar Wind Heavy Ion Abundances. *Sol. Phys.*, 43(2):463–473, August 1975. doi: 10.1007/BF00152368.

R. von Steiger, N. A. Schwadron, L. A. Fisk, J. Geiss, G. Gloeckler, S. Hefti, B. Wilken, R. F. Wimmer-Schweingruber, and T. H. Zurbuchen. Composition of quasi-stationary solar wind flows from Ulysses/Solar Wind Ion Composition Spectrometer. *J. Geophys. Res.*, 105(A12): 27217–27238, December 2000. doi: 10.1029/1999JA000358.

K. P. Wenzel, R. G. Marsden, D. E. Page, and E. J. Smith. Ulysses: The first high-latitude heliospheric mission. *Advances in Space Research*, 9(4):25–29, January 1989. doi: 10.1016/0273-1177(89)90089-6.

D. S. Burnett, B. L. Barraclough, R. Bennett, M. Neugebauer, L. P. Oldham, C. N. Sasaki, D. Sevilla, N. Smith, E. Stansbery, D. Sweetnam, and R. C. Wiens. The Genesis Discovery Mission: Return of Solar Matter to Earth. *Space Sci. Rev.*, 105(3):509–534, January 2003. doi: 10.1023/A:1024425810605.

D. B. Reisenfeld, D. S. Burnett, R. H. Becker, A. G. Grimberg, V. S. Heber, C. M. Hohenberg, A. J. G. Jurewicz, A. Meshik, R. O. Pepin, J. M. Raines, D. J. Schlutter, R. Wieler, R. C. Wiens, and T. H. Zurbuchen. *Elemental Abundances of the Bulk Solar Wind: Analyses from Genesis and ACE*, volume 130, page 79. 2007. doi: 10.1007/978-0-387-74184-0_9.

Nadia Vogel, Veronika S. Heber, Heinrich Baur, Donald S. Burnett, and Rainer Wieler. Argon, krypton, and xenon in the bulk solar wind as collected by the Genesis mission. *Geochim. Cosmochim. Acta*, 75(11):3057–3071, June 2011. doi: 10.1016/j.gca.2011.02.039.

Robert O. Pepin, Dennis J. Schlutter, Richard H. Becker, and Daniel B. Reisenfeld. Helium, neon, and argon composition of the solar wind as recorded in gold and other Genesis collector materials. *Geochim. Cosmochim. Acta*, 89:62–80, July 2012. doi: 10.1016/j.gca.2012.04.024.

A. J. Hundhausen, H. E. Gilbert, and S. J. Bame. Ionization state of the interplanetary plasma. *J. Geophys. Res.*, 73(17):5485–5493, September 1968. doi: 10.1029/JA073i017p05485.

S. P. Owocki, T. E. Holzer, and A. J. Hundhausen. The solar wind ionization state as a coronal temperature diagnostic. *ApJ*, 275:354–366, December 1983. doi: 10.1086/161538.

MR Aellig, H Grünwaldt, P Bochsler, S Hefti, P Wurz, R Kallenbach, FM Ipavich, D Hovestadt, M Hilchenbach, CELIAS Team, et al. Solar wind minor ion charge states observed with high time resolution with soho/celias/ctof. In *Correlated Phenomena at the Sun, in the Heliosphere and in Geospace*, volume 415, page 27, 1997.

D. J. McComas, B. L. Barraclough, H. O. Funsten, J. T. Gosling, E. Santiago-Muñoz, R. M. Skoug, B. E. Goldstein, M. Neugebauer, P. Riley, and A. Balogh. Solar wind observations over Ulysses' first full polar orbit. *J. Geophys. Res.*, 105(A5):10419–10434, May 2000. doi: 10.1029/1999JA000383.

Joseph E. Borovsky. Flux tube texture of the solar wind: Strands of the magnetic carpet at 1 AU? *Journal of Geophysical Research (Space Physics)*, 113(A8):A08110, August 2008. doi: 10.1029/2007JA012684.

L. A. Fisk. Motion of the footpoints of heliospheric magnetic field lines at the Sun: Implications for recurrent energetic particle events at high heliographic latitudes. *J. Geophys. Res.*, 101 (A7):15547–15554, July 1996. doi: 10.1029/96JA01005.

L. A. Fisk, T. H. Zurbuchen, and N. A. Schwadron. On the Coronal Magnetic Field: Consequences of Large-Scale Motions. *ApJ*, 521(2):868–877, August 1999. doi: 10.1086/307556.

A. Balogh, E. J. Smith, B. T. Tsurutani, D. J. Southwood, R. J. Forsyth, and T. S. Horbury. The Heliospheric Magnetic Field Over the South Polar Region of the Sun. *Science*, 268(5213): 1007–1010, May 1995. doi: 10.1126/science.268.5213.1007.

T. H. Zurbuchen, N. A. Schwadron, and L. A. Fisk. Direct observational evidence for a heliospheric magnetic field with large excursions in latitude. *J. Geophys. Res.*, 102(A11):24175–24182, October 1997. doi: 10.1029/97JA02194.

R. A. Burger and M. Hitge. The Effect of a Fisk-Type Heliospheric Magnetic Field on Cosmic-Ray Modulation. *ApJ*, 617(1):L73–L76, December 2004. doi: 10.1086/427076.

P. H. Scherrer, J. Schou, R. I. Bush, A. G. Kosovichev, R. S. Bogart, J. T. Hoeksema, Y. Liu, T. L. Duvall, J. Zhao, A. M. Title, C. J. Schrijver, T. D. Tarbell, and S. Tomczyk. The Helioseismic and Magnetic Imager (HMI) Investigation for the Solar Dynamics Observatory (SDO). *Sol. Phys.*, 275(1-2):207–227, January 2012. doi: 10.1007/s11207-011-9834-2.

W. Dean Pesnell, B. J. Thompson, and P. C. Chamberlin. The Solar Dynamics Observatory (SDO). *Sol. Phys.*, 275(1-2):3–15, January 2012. doi: 10.1007/s11207-011-9841-3.

Martin D. Altschuler and Gordon Newkirk. Magnetic Fields and the Structure of the Solar Corona. I: Methods of Calculating Coronal Fields. *Sol. Phys.*, 9(1):131–149, September 1969. doi: 10.1007/BF00145734.

BJ Sams III, L Golub, and NO Weiss. X-ray observations of sunspot penumbral structure. *The Astrophysical Journal*, 399:313–317, 1992.

Thies Peleikis, Martin Kruse, Lars Berger, and Robert Wimmer-Schweingruber. Origin of the solar wind: A novel approach to link in situ and remote observations. A study for SPICE and SWA on the upcoming Solar Orbiter mission. *A&A*, 602:A24, June 2017. doi: 10.1051/0004-6361/201629727.

M. Kruse, V. Heidrich-Meisner, and R. F. Wimmer-Schweingruber. Evaluation of a potential field source surface model with elliptical source surfaces via ballistic back mapping of in situ spacecraft data. *A&A*, 645:A83, January 2021. doi: 10.1051/0004-6361/202039120.

M. Kruse, V. Heidrich-Meisner, R. F. Wimmer-Schweingruber, and M. Hauptmann. An elliptic expansion of the potential field source surface model. *A&A*, 638:A109, June 2020. doi: 10.1051/0004-6361/202037734.

Tamas I. Gombosi, Bart van der Holst, Ward B. Manchester, and Igor V. Sokolov. Extended MHD modeling of the steady solar corona and the solar wind. *Living Reviews in Solar Physics*, 15(1):4, July 2018. doi: 10.1007/s41116-018-0014-4.

Daniel Verscharen, Kristopher G. Klein, and Bennett A. Maruca. The multi-scale nature of the solar wind. *Living Reviews in Solar Physics*, 16(1):5, December 2019. doi: 10.1007/s41116-019-0021-0.

J. Geiss, G. Gloeckler, and R. von Steiger. Origin of the Solar Wind From Composition Data. *Space Sci. Rev.*, 72(1-2):49–60, April 1995b. doi: 10.1007/BF00768753.

M. R. Aellig, H. Holweger, P. Bochsler, P. Wurz, H. Grünwaldt, S. Hefti, F. M. Ipavich, and B. Klecker. The Fe/O elemental abundance ratio in the solar wind. In Shadia Rifai Habbal, Ruth Esser, Joseph V. Hollweg, and Philip A. Isenberg, editors, *Solar Wind Nine*, volume 471 of *American Institute of Physics Conference Series*, pages 255–258, June 1999. doi: 10.1063/1.58756.

E. Marsch, R. Schwenn, H. Rosenbauer, K. H. Muehlhaeuser, W. Pilipp, and F. M. Neubauer. Solar wind protons: Three-dimensional velocity distributions and derived plasma parameters measured between 0.3 and 1 AU. *J. Geophys. Res.*, 87(A1):52–72, January 1982. doi: 10.1029/JA087iA01p00052.

D. J. McComas, H. A. Elliott, N. A. Schwadron, J. T. Gosling, R. M. Skoug, and B. E. Goldstein. The three-dimensional solar wind around solar maximum. *Geophys. Res. Lett.*, 30(10):1517, May 2003. doi: 10.1029/2003GL017136.

U. Feldman, E. Landi, and N. A. Schwadron. On the sources of fast and slow solar wind. *Journal of Geophysical Research (Space Physics)*, 110(A7):A07109, July 2005. doi: 10.1029/2004JA010918.

Justin C Kasper, Michael L Stevens, Alan J Lazarus, John T Steinberg, and Keith W Ogilvie. Solar wind helium abundance as a function of speed and heliographic latitude: Variation through a solar cycle. *The Astrophysical Journal*, 660(1):901, 2007.

Fei Xu and Joseph E. Borovsky. A new four-plasma categorization scheme for the solar wind. *Journal of Geophysical Research (Space Physics)*, 120(1):70–100, January 2015. doi: 10.1002/2014JA020412.

L. K. Jian, C. T. Russell, J. G. Luhmann, A. B. Galvin, and K. D. C. Simunac. Solar wind observations at STEREO: 2007 - 2011. In Gary P. Zank, Joe Borovsky, Roberto Bruno, Jonathan Cirtain, Steve Cranmer, Heather Elliott, Joe Giacalone, Walter Gonzalez, Gang Li, Eckart Marsch, Ebehard Moebius, Nick Pogorelov, Jim Spann, and Olga Verkhoglyadova, editors, *Solar Wind 13*, volume 1539 of *American Institute of Physics Conference Series*, pages 191–194, June 2013. doi: 10.1063/1.4811020.

L. K. Jian, C. T. Russell, J. G. Luhmann, and A. B. Galvin. STEREO Observations of Interplanetary Coronal Mass Ejections in 2007-2016. *ApJ*, 855(2):114, March 2018. doi: 10.3847/1538-4357/aab189.

L. K. Jian, J. G. Luhmann, C. T. Russell, and A. B. Galvin. Solar Terrestrial Relations Observatory (STEREO) Observations of Stream Interaction Regions in 2007 - 2016: Relationship with Heliospheric Current Sheets, Solar Cycle Variations, and Dual Observations. *Sol. Phys.*, 294(3):31, March 2019. doi: 10.1007/s11207-019-1416-8.

T. Kucera. Stereo science center - impact/level3, 2022. `https://stereo-ssc.nascom.nasa.gov/pub/ins_data/impact/level3/` (Website accessed at 26. January 2022 - 19:56).

A. S. Krieger, A. F. Timothy, and E. C. Roelof. A Coronal Hole and Its Identification as the Source of a High Velocity Solar Wind Stream. *Sol. Phys.*, 29(2):505–525, April 1973. doi: 10.1007/BF00150828.

SK Antiochos, Z. Mikić, VS Titov, R. Lionello, and JA Linker. A model for the sources of the slow solar wind. *The Astrophysical Journal*, 731(2):112, 2011.

Roberto Bruno and Vincenzo Carbone. The solar wind as a turbulence laboratory. *Living Reviews in Solar Physics*, 10(1):1–208, 2013.

W. C. Bartley, R. P. Bukata, K. G. McCracken, and U. R. Rao. Anisotropic cosmic radiation fluxes of solar origin. *J. Geophys. Res.*, 71(13):3297–3304, July 1966. doi: 10.1029/JZ071i013p03297.

R. Bruno, V. Carbone, P. Veltri, E. Pietropaolo, and B. Bavassano. Identifying intermittency events in the solar wind. *Planet. Space Sci.*, 49(12):1201–1210, October 2001. doi: 10.1016/S0032-0633(01)00061-7.

David F. Webb and Timothy A. Howard. Coronal Mass Ejections: Observations. *Living Reviews in Solar Physics*, 9(1):3, June 2012. doi: 10.12942/lrsp-2012-3.

H. V. Cane and I. G. Richardson. Interplanetary coronal mass ejections in the near-Earth solar wind during 1996-2002. *Journal of Geophysical Research (Space Physics)*, 108(A4):1156, April 2003. doi: 10.1029/2002JA009817.

I. G. Richardson and H. V. Cane. Near-Earth Interplanetary Coronal Mass Ejections During Solar Cycle 23 (1996 - 2009): Catalog and Summary of Properties. *Sol. Phys.*, 264(1):189–237, June 2010. doi: 10.1007/s11207-010-9568-6.

L. Jian, C. T. Russell, J. G. Luhmann, and R. M. Skoug. Properties of Stream Interactions at One AU During 1995 2004. *Sol. Phys.*, 239(1-2):337–392, December 2006. doi: 10.1007/s11207-006-0132-3.

Bruce T. Tsurutani and Gurbax S. Lakhina. Some basic concepts of wave-particle interactions in collisionless plasmas. *Reviews of Geophysics*, 35(4):491–501, January 1997. doi: 10.1029/97RG02200.

H. Alfvén. Existence of Electromagnetic-Hydrodynamic Waves. *Nature*, 150(3805):405–406, October 1942. doi: 10.1038/150405d0.

Thomas H. Stix. Oscillations of a Cylindrical Plasma. *Physical Review*, 106(6):1146–1150, June 1957. doi: 10.1103/PhysRev.106.1146.

Thomas Howard Stix. *Waves in plasmas*. American Inst. of Physics, 1992. ISBN 9780883188590.

Wolfgang Baumjohann and Rudolf A Treumann. *Basic space plasma physics (revised edition)*. World Scientific Publishing Company, 2012.

D. Verscharen and E. Marsch. Apparent temperature anisotropies due to wave activity in the solar wind. *Annales Geophysicae*, 29(5):909–917, May 2011. doi: 10.5194/angeo-29-909-2011.

D. Keilbach, L. Berger, V. Heidrich-Meisner, and R. F. Wimmer-Schweingruber. Qualitative test particle simulations of pitch angle modifications due to Alfvénic waves. In *DPG-Verhandlungen: München 19*, 2019.

Tilman Butz. *Fouriertransformation für Fußgänger*, volume 6. Springer, 2009.

I. Daubechies. *Ten Lectures on Wavelets*. CBMS-NSF Regional Conference Series in Applied Mathematics. Society for Industrial and Applied Mathematics, 1992. ISBN 9780898712742. URL `https://books.google.de/books?id=B3C5aG4OboIC`.

J. Köhler and R. F. Wimmer-Schweingruber. Wave amplitudes in the solar wind at 1 AU: Implications for energetic particle transport. In *AGU Fall Meeting Abstracts*, volume 2010, pages SH41B–1805, December 2010.

Erik Jentsch. Three-Dimensional Structures in Solar Wind. Bachelor's thesis, Mathematisch-Naturwissenschaftliche Fakultät,Christian-Albrechts-Universität zu Kiel, 2021.

Duncan Keilbach. Numerical study of alfvénic wave activity in the solar wind as a cause for pitch angle scattering with focus on kinetic processes. Master's thesis, Christian-Albrechts-Universität zu Kiel, Institut für Experimentelle und Angewandte Physik, 2017.

Rémi Lehe, Ian J. Parrish, and Eliot Quataert. The Heating of Test Particles in Numerical Simulations of Alfvénic Turbulence. *ApJ*, 707(1):404–419, December 2009. doi: 10.1088/0004-637X/707/1/404.

Wolfgang Baumjohann and Rudolf A Treumann. *Advanced space plasma physics*. World Scientific, 1997.

Reinhard Schlickeiser. Cosmic-Ray Transport and Acceleration. *ApJS*, 90:929, February 1994. doi: 10.1086/191927.

K. Hasselmann and G. Wibberenz. A Note on the Parallel Diffusion Coefficient. *ApJ*, 162:1049, December 1970. doi: 10.1086/150736.

Charles F. Kennel and John M. Greene. Finite Larmor radius hydromagnetics. *Annals of Physics*, 38(1):63–94, June 1966. doi: 10.1016/0003-4916(66)90251-X.

C. F. Kennel and F. Engelmann. Velocity Space Diffusion from Weak Plasma Turbulence in a Magnetic Field. *Physics of Fluids*, 9(12):2377–2388, December 1966. doi: 10.1063/1.1761629.

J. Beeck and G. Wibberenz. Pitch Angle Distributions of Solar Energetic Particles and the Local Scattering Properties of the Interplanetary Medium. *ApJ*, 311:437, December 1986. doi: 10.1086/164784.

Eckart Marsch. Kinetic Physics of the Solar Corona and Solar Wind. *Living Reviews in Solar Physics*, 3(1):1, July 2006. doi: 10.12942/lrsp-2006-1.

Alexander Piel. *Plasma physics: an introduction to laboratory, space, and fusion plasmas*. Springer, 2017.

E Marsch, X-Z Ao, and C-Y Tu. On the temperature anisotropy of the core part of the proton velocity distribution function in the solar wind. *Journal of Geophysical Research: Space Physics*, 109(A4), 2004.

Justin C. Kasper, Robert Abiad, Gerry Austin, Marianne Balat-Pichelin, Stuart D. Bale, John W. Belcher, Peter Berg, Henry Bergner, Matthieu Berthomier, Jay Bookbinder, Etienne Brodu, David Caldwell, Anthony W. Case, Benjamin D. G. Chandran, Peter Cheimets, Jonathan W. Cirtain, Steven R. Cranmer, David W. Curtis, Peter Daigneau, Greg Dalton, Brahmananda Dasgupta, David DeTomaso, Millan Diaz-Aguado, Blagoje Djordjevic, Bill Donaskowski, Michael Effinger, Vladimir Florinski, Nichola Fox, Mark Freeman, Dennis Gallagher, S. Peter Gary, Tom Gauron, Richard Gates, Melvin Goldstein, Leon Golub, Dorothy A. Gordon, Reid Gurnee, Giora Guth, Jasper Halekas, Ken Hatch, Jacob Heerikuisen, George Ho, Qiang Hu, Greg Johnson, Steven P. Jordan, Kelly E. Korreck, Davin Larson, Alan J. Lazarus, Gang Li, Roberto Livi, Michael Ludlam, Milan Maksimovic, James P. McFadden, William Marchant, Bennet A. Maruca, David J. McComas, Luciana Messina, Tony Mercer, Sang Park, Andrew M. Peddie, Nikolai Pogorelov, Matthew J. Reinhart, John D. Richardson, Miles Robinson, Irene Rosen, Ruth M. Skoug, Amanda Slagle, John T. Steinberg, Michael L. Stevens, Adam Szabo, Ellen R. Taylor, Chris Tiu, Paul Turin, Marco Velli, Gary Webb, Phyllis Whittlesey, Ken Wright, S. T. Wu, and Gary Zank. Solar Wind Electrons Alphas and Protons (SWEAP) Investigation: Design of the Solar Wind and Coronal Plasma Instrument Suite for Solar Probe Plus. *Space Sci. Rev.*, 204(1-4):131–186, December 2016. doi: 10.1007/s11214-015-0206-3.

L. Berger, R. F. Wimmer-Schweingruber, and G. Gloeckler. Systematic Measurements of Ion-Proton Differential Streaming in the Solar Wind. *Phys. Rev. Lett.*, 106(15):151103, April 2011. doi: 10.1103/PhysRevLett.106.151103.

N. P. Janitzek, L. Berger, C. Drews, and R. F. Wimmer-Schweingruber. Differential Streaming at 1 AU observed with SOHO/CELIAS/CTOF and ACE/SWICS. In *AGU Fall Meeting Abstracts*, pages SH51B–2586, December 2016.

F. de Hoffmann and E. Teller. Magneto-Hydrodynamic Shocks. *Physical Review*, 80(4):692–703, November 1950. doi: 10.1103/PhysRev.80.692.

D. E. Innes and T. W. Hartquist. Are we in an old superbubble? *MNRAS*, 209:7–13, July 1984. doi: 10.1093/mnras/209.1.7.

Nikolai G. Bochkarev. Local Interstellar Medium. *Ap&SS*, 138(2):229–302, November 1987. doi: 10.1007/BF00637850.

Donald D. Clayton, Donald P. Cox, and Curtis F. Michel. A local recent supernova: evidence from X rays, ^{26}Al radioactivity and cosmic rays. In Roman Smoluchowski, John M. Bahcall, and Mildred S. Matthews, editors, *The Galaxy and the Solar System*, pages 129–144, January 1986.

Donald P. Cox and Ronald J. Reynolds. The local interstellar medium. *ARA&A*, 25:303–344, January 1987. doi: 10.1146/annurev.aa.25.090187.001511.

Seth Redfield and Jeffrey L. Linsky. The Structure of the Local Interstellar Medium IV: Dynamics, Morphology, Physical Properties, and Implications of Cloud-Cloud Interactions. *arXiv e-prints*, art. arXiv:0709.4480, September 2007.

Jeffrey L. Linsky, Seth Redfield, and Dennis Tilipman. The Interface between the Outer Heliosphere and the Inner Local ISM: Morphology of the Local Interstellar Cloud, Its Hydrogen Hole, Strömgren Shells, and ^{60}Fe Accretion. *ApJ*, 886(1):41, November 2019. doi: 10.3847/1538-4357/ab498a.

Thomas E. Holzer. Interaction between the solar wind and the interstellar medium. *ARA&A*, 27:199–234, January 1989. doi: 10.1146/annurev.aa.27.090189.001215.

EC Stone, AC Cummings, FB McDonald, BC Heikkila, N Lal, and WR Webber. Voyager 1 explores the termination shock region and the heliosheath beyond. *Science*, 309(5743):2017–2020, 2005.

Edward C Stone, Alan C Cummings, Frank B McDonald, Bryant C Heikkila, Nand Lal, and William R Webber. An asymmetric solar wind termination shock. *Nature*, 454(7200):71–74, 2008.

John Richardson, John W. Belcher, Edward C. Stone, Alan C. Cummings, and the Voyager Team. Voyager 2 Crosses the Heliopause. In *EGU General Assembly Conference Abstracts*, EGU General Assembly Conference Abstracts, page 18817, April 2019a.

John D. Richardson, John W. Belcher, Paula Garcia-Galindo, and Leonard F. Burlaga. Voyager 2 plasma observations of the heliopause and interstellar medium. *Nature Astronomy*, 3:1019–1023, November 2019b. doi: 10.1038/s41550-019-0929-2.

E. N. Parker. The Stellar-Wind Regions. *ApJ*, 134:20, July 1961. doi: 10.1086/147124.

V. B. Baranov and Yu. G. Malama. Model of the solar wind interaction with the local interstellar medium numerical solution of self-consistent problem. *J. Geophys. Res.*, 98(A9):15157–15164, September 1993. doi: 10.1029/93JA01171.

N. A. Schwadron and M. Bzowski. The Heliosphere Is Not Round. *ApJ*, 862(1):11, July 2018. doi: 10.3847/1538-4357/aacbcf.

M. Opher, J. F. Drake, B. Zieger, and T. I. Gombosi. Magnetized Jets Driven By the Sun: the Structure of the Heliosphere Revisited. *ApJ*, 800(2):L28, February 2015. doi: 10.1088/2041-8205/800/2/L28.

Jeffrey L. Linsky and Brian E. Wood. The α Centauri line of sight: D/H ratio, physical properties of local interstellar gas, and measurement of heated hydrogen (the "hydrogen wall") near the heliopause. *ApJ*, 463:254–270, May 1996. doi: 10.1086/177238.

Brian E. Wood and Jeffrey L. Linsky. The Winds of Solar-like Stars and Their Interactions with the ISM. In Robert A. Donahue and Jay A. Bookbinder, editors, *Cool Stars, Stellar Systems, and the Sun*, volume 154 of *Astronomical Society of the Pacific Conference Series*, page 1652, January 1998.

Dave van Buren and Richard McCray. Bow Shocks and Bubbles Are Seen around Hot Stars by IRAS. *ApJ*, 329:L93, June 1988. doi: 10.1086/185184.

Dave van Buren, Alberto Noriega-Crespo, and Ruth Dgani. An IRAS/ISSA Survey of Bow Shocks Around Runaway Stars. *AJ*, 110:2914, December 1995. doi: 10.1086/117739.

J. L. Bertaux and J. E. Blamont. Evidence for a Source of an Extraterrestrial Hydrogen Lyman-alpha Emission. *A&A*, 11:200, March 1971.

G. E. Thomas and R. F. Krassa. OGO 5 Measurements of the Lyman Alpha Sky Background. *A&A*, 11:218, March 1971.

H. J. Fahr. The Extraterrestrial UV-Background and the Nearby Interstellar Medium. *Space Sci. Rev.*, 15(4):483–540, February 1974. doi: 10.1007/BF00178217.

C. S. Weller and R. R. Meier. Observations of helium in the interplanetary/interstellar wind: the solar-wake effect. *ApJ*, 193:471–476, October 1974. doi: 10.1086/153182.

R. Kallenbach, J. Geiss, G. Gloeckler, and R. von Steiger. Pick-up Ion Measurements in the Heliosphere - A Review. *Ap&SS*, 274:97–114, October 2000. doi: 10.1023/A:1026587620772.

DJ McComas, D Alexashov, M Bzowski, H Fahr, J Heerikhuisen, V Izmodenov, MA Lee, E Möbius, N Pogorelov, NA Schwadron, et al. The heliosphere's interstellar interaction: No bow shock. *Science*, 336(6086):1291–1293, 2012.

G. P. Zank, J. Heerikhuisen, B. E. Wood, N. V. Pogorelov, E. Zirnstein, and D. J. McComas. Heliospheric Structure: The Bow Wave and the Hydrogen Wall. *ApJ*, 763(1):20, January 2013. doi: 10.1088/0004-637X/763/1/20.

Klaus Scherer and Horst Fichtner. The return of the bow shock. *The Astrophysical Journal*, 782 (1):25, 2014.

E. Möbius, D. Hovestadt, B. Klecker, M. Scholer, G. Gloeckler, F. M. Ipavich, and H. Lühr. Observation of lithium pick-up ions in the 5- to 20-keV energy range following the AMPTE solar wind releases. *J. Geophys. Res.*, 91(A2):1325–1332, February 1986. doi: 10.1029/JA091iA02p01325.

F. Allegrini, N. A. Schwadron, D. J. McComas, G. Gloeckler, and J. Geiss. Stability of the inner source pickup ions over the solar cycle. *Journal of Geophysical Research (Space Physics)*, 110 (A5):A05105, May 2005. doi: 10.1029/2004JA010847.

A. Taut, L. Berger, C. Drews, and R. F. Wimmer-Schweingruber. Composition of inner-source heavy pickup ions at 1 AU: SOHO/CELIAS/CTOF observations. Implications for the production mechanisms. *A&A*, 576:A55, April 2015. doi: 10.1051/0004-6361/201425139.

L. Berger, C. Drews, A. Taut, and R. F. Wimmer-Schweingruber. Short-term variability of inner-source pickup ions at 1 AU. SOHO/CELIAS observations. *A&A*, 576:A54, April 2015. doi: 10.1051/0004-6361/201425116.

LI Shestakova. Solar radiation pressure as a mechanism of acceleration of atoms and first ions with low ionization potentials. *Solar System Research*, 49(2):139–145, 2015.

David R. Williams. Planetary Fact Sheet - metric, 2016b. `https://nssdc.gsfc.nasa.gov/planetary/factsheet/index.html` (Website accessed at 9. August 2021).

Torsten Fließbach. *Lehrbuch zur theoretischen Physik*. Springer, 2003.

H. J. Fahr. Charge-transfer Interactions between Solar Wind Protons and Neutral Particles in the Vicinity of the Sun. *Nature*, 219(5153):473–474, August 1968a. doi: 10.1038/219473a0.

H. J. Fahr. Neutral Corpuscular Energy Flux by Charge-Transfer Collisions in the Vicinity of the Sun. *Ap&SS*, 2(4):496–503, December 1968b. doi: 10.1007/BF02175924.

Martin A. Lee, Eberhard Möbius, and Trevor W. Leonard. The Analytical Structure of the Primary Interstellar Helium Distribution Function in the Heliosphere. *ApJS*, 220(2):23, October 2015. doi: 10.1088/0067-0049/220/2/23.

G. Gloeckler, E. Möbius, J. Geiss, M. Bzowski, S. Chalov, H. Fahr, D. R. McMullin, H. Noda, M. Oka, D. Ruciński, R. Skoug, T. Terasawa, R. von Steiger, A. Yamazaki, and T. Zurbuchen. Observations of the helium focusing cone with pickup ions. *A&A*, 426:845–854, November 2004. doi: 10.1051/0004-6361:20035768.

E. Möbius, M. A. Lee, G. Gloeckler, C. Drews, and D. Keilbach. Interstellar flow longitude from pickup ion cut-off observations at 1 AU with STEREO and ACE. In *Journal of Physics Conference Series*, volume 767 of *Journal of Physics Conference Series*, page 012017, November 2016. doi: 10.1088/1742-6596/767/1/012017.

D. J. McComas, N. A. Schwadron, F. J. Crary, H. A. Elliott, D. T. Young, J. T. Gosling, M. F. Thomsen, E. Sittler, J. J. Berthelier, K. Szego, and A. J. Coates. The interstellar hydrogen shadow: Observations of interstellar pickup ions beyond Jupiter. *Journal of Geophysical Research (Space Physics)*, 109(A2):A02104, February 2004. doi: 10.1029/2003JA010217.

M Bzowski, E Möbius, S Tarnopolski, V Izmodenov, and G Gloeckler. Density of neutral interstellar hydrogen at the termination shock from ulysses pickup ion observations. *Astronomy & Astrophysics*, 491(1):7–19, 2008.

S Tarnopolski and M Bzowski. Neutral interstellar hydrogen in the inner heliosphere under the influence of wavelength-dependent solar radiation pressure. *Astronomy & Astrophysics*, 493 (1):207–216, 2009.

A. Kramida, Yu. Ralchenko, J. Reader, and and NIST ASD Team. NIST Atomic Spectra Database (ver. 5.9), [Online]. Available: `https://physics.nist.gov/asd` [2022, May 4]. National Institute of Standards and Technology, Gaithersburg, MD., 2021.

G. Gloeckler, J. Geiss, H. Balsiger, L. A. Fisk, A. B. Galvin, F. M. Ipavich, K. W. Ogilvie, R. von Steiger, and B. Wilken. Detection of Interstellar Pick-Up Hydrogen in the Solar System. *Science*, 261(5117):70–73, July 1993. doi: 10.1126/science.261.5117.70.

G. Gloeckler, N. A. Schwadron, L. A. Fisk, and J. Geiss. Weak pitch angle scattering of few MV rigidity ions from measurements of anisotropies in the distribution function of interstellar pickup H^+. *Geophys. Res. Lett.*, 22(19):2665–2668, October 1995. doi: 10.1029/95GL02480.

G. Gloeckler, L. A. Fisk, J. Geiss, N. A. Schwadron, and T. H. Zurbuchen. Elemental composition of the inner source pickup ions. *J. Geophys. Res.*, 105(A4):7459–7464, April 2000a. doi: 10.1029/1999JA000224.

J. Geiss, G. Gloeckler, U. Mall, R. von Steiger, A. B. Galvin, and K. W. Ogilvie. Interstellar oxygen, nitrogen and neon in the heliosphere. *A&A*, 282(3):924–933, February 1994a.

J. Geiss, G. Gloeckler, and U. Mall. Origin of the O$\hat{+}$pick-up ions in the heliosphere. *A&A*, 289: 933–936, September 1994b.

G. Gloeckler, L. A. Fisk, J. Geiss, N. A. Schwadron, and T. H. Zurbuchen. Elemental composition of the inner source pickup ions. *J. Geophys. Res.*, 105(A4):7459–7464, April 2000b. doi: 10.1029/1999JA000224.

D. Keilbach, C. Drews, A. Taut, and R. F. Wimmer-Schweingruber. Modelling injection rates of PUIs from photoionization using kinetic simulations of interstellar neutrals traversing the heliosphere. In *AGU Fall Meeting Abstracts*, pages SH21B–2520, December 2016.

A. C. Cummings, E. C. Stone, and C. D. Steenberg. Composition of Anomalous Cosmic Rays and Other Heliospheric Ions. *ApJ*, 578(1):194–210, October 2002. doi: 10.1086/342427.

D. Rucinski and H. J. Fahr. The influence of electron impact ionization on the distribution of interstellar helium in the inner heliosphere - Possible consequences for determination of interstellar helium parameters. *A&A*, 224(1-2):290–298, October 1989.

H. J. Fahr. The Interplanetary Hydrogen Cone and its Solar Cycle Variations. *A&A*, 14:263, September 1971.

D. Rucinski, M. Bzowski, and H. J. Fahr. Imprints from the solar cycle on the helium atom and helium pickup ion distributions. *Annales Geophysicae*, 21(6):1315–1330, June 2003. doi: 10.5194/angeo-21-1315-2003.

Maciej Bzowski. A model of Charge Exchange of Interstellar Hydrogen on a Time-Dependent, 2D Solar Wind. *Space Sci. Rev.*, 97:379–383, May 2001. doi: 10.1023/A:1011814125384.

William H Press, Brian P Flannery, Saul A Teukolsky, William T Vetterling, et al. Numerical recipes, 1989.

Charles K Birdsall and A Bruce Langdon. *Plasma physics via computer simulation*. CRC press, 2018.

Wolfgang Demtröder. *Experimentalphysik 1 - Mechanik und Wärme*. Springer-Lehrbuch, 2018. ISBN 978-3-662-54846-2. doi: 10.1007/978-3-662-54847-9.

Justyna M. Sokół, Maciej Bzowski, Marzena A. Kubiak, and Eberhard Möbius. Solar cycle variation of interstellar neutral He, Ne, O density and pick-up ions along the Earth's orbit. *MNRAS*, 458(4):3691–3704, June 2016. doi: 10.1093/mnras/stw515.

D. Keilbach, V. Heidrich-Meisner, L. Berger, and R. F. Wimmer-Schweingruber. Three dimensional He^+ pickup ion velocity distributions observed by STEREO/PLASTIC. In *AGU Fall Meeting Abstracts (submitted)*, 2021.

P. N. Bernasconi, N. E. Raouafi, R. B. Decker, S. Bale, R. Howard, J. C. Kasper, D. J. McComas, M. Velli, and A. Posner. Parker Solar Probe: A NASA Mission to Touch the Sun - Mission Status Update. In *AGU Fall Meeting Abstracts*, volume 2018, pages SH43A–01, December 2018.

G. Gloeckler, J. Geiss, H. Balsiger, P. Bedini, J. C. Cain, J. Fischer, L. A. Fisk, A. B. Galvin, F. Gliem, D. C. Hamilton, J. V. Hollweg, F. M. Ipavich, R. Joos, S. Livi, R. A. Lundgren, U. Mall, J. F. McKenzie, K. W. Ogilvie, F. Ottens, W. Rieck, E. O. Tums, R. von Steiger, W. Weiss, and B. Wilken. The Solar Wind Ion Composition Spectrometer. *A&AS*, 92(2): 267–289, January 1992.

D. McComas, F. Allegrini, F. Bagenal, P. Casey, P. Delamere, D. Demkee, G. Dunn, H. Elliott, J. Hanley, K. Johnson, J. Langle, G. Miller, S. Pope, M. Reno, B. Rodriguez, N. Schwadron, P. Valek, and S. Weidner. The Solar Wind Around Pluto (SWAP) Instrument Aboard New Horizons. *Space Sci. Rev.*, 140(1-4):261–313, October 2008. doi: 10.1007/s11214-007-9205-3.

Anne Fischer. Velocity Distribution Functions of Pickup Ions with Ulysses/SWICS. Master's thesis, Christian-Albrechts-Universität zu Kiel, Institut für Experimentelle und Angewandte Physik, 2019.

Jun Hong Chen, Eberhard Möbius, George Gloeckler, Peter Bochsler, Maciej Bzowski, Philip A. Isenberg, and Justyna M. Sokół. Observational study of the cooling behavior of interstellar helium pickup ions in the inner heliosphere. *Journal of Geophysical Research (Space Physics)*, 118(7):3946–3953, July 2013. doi: 10.1002/jgra.50391.

D. Keilbach, L. Berger, V. Heidrich-Meisner, and R. F. Wimmer-Schweingruber. The Solar Wind Frame of STEREO/PLASTIC: Contributions of the de-Hoffmann-Teller Frame. In *AGU Fall Meeting Abstracts*, volume 2020, pages SH009–0020, December 2020.

D Hovestadt, M Hilchenbach, A Bürgi, B Klecker, P Laeverenz, M Scholer, H Grünwaldt, WI Axford, S Livi, E Marsch, et al. Celias-charge, element and isotope analysis system for soho. *Solar Physics*, 162(1):441–481, 1995.

E. C. Stone, A. M. Frandsen, R. A. Mewaldt, E. R. Christian, D. Margolies, J. F. Ormes, and F. Snow. The Advanced Composition Explorer. *Space Sci. Rev.*, 86:1–22, July 1998. doi: 10.1023/A:1005082526237.

G. Gloeckler, J. Cain, F. M. Ipavich, E. O. Tums, P. Bedini, L. A. Fisk, T. H. Zurbuchen, P. Bochsler, J. Fischer, R. F. Wimmer-Schweingruber, J. Geiss, and R. Kallenbach. Investigation of the composition of solar and interstellar matter using solar wind and pickup ion measurements with SWICS and SWIMS on the ACE spacecraft. *Space Sci. Rev.*, 86:497–539, July 1998. doi: 10.1023/A:1005036131689.

Michael L Kaiser, TA Kucera, JM Davila, OC St Cyr, Madhulika Guhathakurta, and Eric Christian. The stereo mission: An introduction. *Space Science Reviews*, 136(1):5–16, 2008.

Marc Gonin. *Ein semiempirisches Modell des Ladungsaustausches von niederenergetischen Ionen beim Durchgang durch dünne Folien, zur Eichung von isochronen Flugzeit-Massenspektrometern.* PhD thesis, Philosophisch-Naturwissenschaftliche Fakultät der Universität Bern, 1995.

Markus J. Aschwanden, Jean-Pierre Wülser, Nariaki V. Nitta, and James R. Lemen. First Three-Dimensional Reconstructions of Coronal Loops with the STEREO A and B Spacecraft. I. Geometry. *ApJ*, 679(1):827–842, May 2008. doi: 10.1086/529542.

Goddard Space flight center NASA. STEREO Science operations plan, 2021. `https://stereo.gsfc.nasa.gov/img/STEREObooklet.pdf` (Website accessed at 23. September 2021).

William Thompson, Joseph B. Gurman, Therese Kucera, Russell Howard, Bougeret Jean Louis H., Janet G. Luhmann, Galvin Antoinette, and Ron Dennisen. STEREO Science operations plan, 2009. `https://stereo-ssc.nascom.nasa.gov/publications/stereo_sop.pdf` (Website accessed at 23. September 2021).

Therese Kucera. STEREO-B status update, 2018a. `https://stereo-ssc.nascom.nasa.gov/behind_status.shtml` (Website accessed at 23. September 2021).

Therese Kucera. STEREO-B status update, 2018b. https://stereo-ssc.nascom.nasa.gov/status.shtml (Website accessed at 23. September 2022).

SILSO World Data Center. The International Sunspot Number. *International Sunspot Number Monthly Bulletin and online catalogue*, 2007-2019.

Robert F. Wimmer-Schweingruber. We reviewed original blueprints of plastic stored at the institute. (priv. comm.). Priv. Comm., 2022.

Lynn Kistler and Lorna Ellis. PLASTIC Level 1 Data Document Version G, 2007. http://stereo.sr.unh.edu/data/PLASTIC_Resources/Level1Data_verG.pdf (Website accessed at 19. October 2021).

MH Acuña, D Curtis, JL Scheifele, CT Russell, P Schroeder, A Szabo, and JG Luhmann. The stereo/impact magnetic field experiment. *Space Science Reviews*, 136(1):203–226, 2008.

J. G. Luhmann, D. W. Curtis, P. Schroeder, J. McCauley, R. P. Lin, D. E. Larson, S. D. Bale, J. A. Sauvaud, C. Aoustin, R. A. Mewaldt, A. C. Cummings, E. C. Stone, A. J. Davis, W. R. Cook, B. Kecman, M. E. Wiedenbeck, T. von Rosenvinge, M. H. Acuna, L. S. Reichenthal, S. Shuman, K. A. Wortman, D. V. Reames, R. Mueller-Mellin, H. Kunow, G. M. Mason, P. Walpole, A. Korth, T. R. Sanderson, C. T. Russell, and J. T. Gosling. STEREO IMPACT Investigation Goals, Measurements, and Data Products Overview. *Space Sci. Rev.*, 136(1-4): 117–184, April 2008. doi: 10.1007/s11214-007-9170-x.

M. Acuna. Fluxgate magnetometers for outer planets exploration. *IEEE Transactions on Magnetics*, 10(3):519–523, September 1974. doi: 10.1109/TMAG.1974.1058457.

Mario H Acuna. Space-based magnetometers. *Review of scientific instruments*, 73(11):3717–3736, 2002.

B. Semenov. The navigation and ancillary information facility - the spice concept, July 2021. https://naif.jpl.nasa.gov/naif/spiceconcept.html (Website accessed at 22. January 2022 - 20:12).

J. von Forstner. Et spice - gitlab page, January 2021. https://gitlab.physik.uni-kiel.de/ET/et_spice (Website accessed at 22. January 2022 - 20:17).

CA Murray. The transformation of coordinates between the systems of b1950. 0 and j2000. 0, and the principal galactic axes referred to j2000. 0. *Astronomy and Astrophysics*, 218:325–329, 1989.

P Kenneth Seidelmann. *Explanatory supplement to the astronomical almanac*. University Science Books, 2006.

UCLA. Stereo data server at ucla, January 2022. https://stereo-dev.epss.ucla.edu (Website accessed at 22. January 2022 - 21:16).

A. Galvin, L. Ellis, and K. Simunac. Readme for stereo plastic proton validated data files, March 2017. https://stereo-ssc.nascom.nasa.gov/data/ins_data/plastic/level2/Protons/Derived_from_1D_Maxwellian/READ_ME_PLASTIC_Protons_1DMax_v11.pdf (Website accessed at 22. January 2022 - 21:30).

Ole Rasmus Becker. Schwere Sonnenwindionen mit STEREO PLASTIC Untersuchung der Differenzgeschwindigkeit verschiedener Eisenionen mit STEREO PLASTIC. Master's thesis, Christian-Albrechts-Universität zu Kiel, Institut für Experimentelle und Angewandte Physik, 2020.

Dong C Liu and Jorge Nocedal. On the limited memory bfgs method for large scale optimization. *Mathematical programming*, 45(1):503–528, 1989.

Pauli Virtanen, Ralf Gommers, Travis E. Oliphant, Matt Haberland, Tyler Reddy, David Cournapeau, Evgeni Burovski, Pearu Peterson, Warren Weckesser, Jonathan Bright, Stéfan J. van der Walt, Matthew Brett, Joshua Wilson, K. Jarrod Millman, Nikolay Mayorov, Andrew R. J. Nelson, Eric Jones, Robert Kern, Eric Larson, C J Carey, İlhan Polat, Yu Feng, Eric W. Moore, Jake VanderPlas, Denis Laxalde, Josef Perktold, Robert Cimrman, Ian Henriksen, E. A. Quintero, Charles R. Harris, Anne M. Archibald, Antônio H. Ribeiro, Fabian Pedregosa, Paul van Mulbregt, and SciPy 1.0 Contributors. SciPy 1.0: Fundamental Algorithms for Scientific Computing in Python. *Nature Methods*, 17:261–272, 2020. doi: 10.1038/s41592-019-0686-2.

Therese Kucera. Planned Science Data during reduced stereo science operations, 2015. `https://stereo-ssc.nascom.nasa.gov/solar_conjunction_science.shtml` (Website accessed at 9. December 2022).

J. Yu, L. Berger, C. Drews, R. Wimmer-Schweingruber, and A. Taut. Spectral variation of suprathermal protons associated with stream interaction regions: STEREO A/PLASTIC observations. *A&A*, 615:A126, July 2018. doi: 10.1051/0004-6361/201732444.

Therese Kucera. STEREO MOC operations schedule, 2014. `https://stereo-ssc.nascom.nasa.gov/plans/ops_schedules/Operations_Schedule_140604.xlsx` (Website accessed at 23. December 2022).

A Probability distribution of chance coincidences in case A

This appendix analyses one of the two cases for chance coincidences in time-of-flight mass spectrometers that are defined in Chapter 3.1.2.i. Also, the same notation and definitions as in Chapter 3.1.2.i apply.
While scenario A leads to systematically shorter observed times of flight, scenario B leads to longer observed times of flight. Here, as an example for both, the probability of case A is derived.
From Fig. 25 it is evident, that a chance coincidence of case A is triggered with the probability of

$$P_{\mathrm{CC,A}} = (1 - P_{\mathrm{start}}) \cdot P_{\mathrm{stop}} \cdot P_{\mathrm{start,II}} \ . \tag{116}$$

Hereby, the probability for the second particle to trigger a start signal before the second particle triggers a stop signal, is denoted by $P_{\mathrm{start,II}}$. And it is dependent on time - or to be more precise: the time since the first particle entered the time of flight chamber. For this section, that time is referred to as t and the time dependence is denoted by replacing $P_{\mathrm{start,II}}$ with $P_{\mathrm{start,II}}(t)$. We only consider the time before the first particle triggers a stop signal, since trivially $P_{\mathrm{start,II}}(t) = 0$ applies after the first particle has triggered a stop signal.
To derive an expression for $P_{\mathrm{start,II}}(t)$, we consider a small fraction of time $[t, t + \Delta t]$. The probability of a start signal to be triggered during that time (denoted by $p_{\mathrm{start,II}}(\Delta t)$) is given by the product of the probability that a particle enters the chamber ($P_{\mathrm{enter}}(\Delta t)$) and the probability that this particle triggers a start signal P_{start}. The probability, that a particle enters the chamber, is computed by

$$P_{\mathrm{enter}}(\Delta t) = \Gamma A \Delta t \ , \text{ where} \tag{117}$$

Γ is the particle flux in the instrument and A the chamber's cross section. The expression for $P_{\mathrm{enter}}(\Delta t)$ might be larger than 1 in the momentary configuration. So Δt is to be chosen in such a way that $P_{\mathrm{enter}}(\Delta t)$ is smaller than 1. This does not constrain this derivation, since later Δt will approach 0 in a limit process. Assuming Δt is chosen such that the elapsed time t is an integer multiple of Δt, the probability that a start pulse has not been triggered $p_{\mathrm{nst,II}}(\Delta t, t)$ is in discrete approximation geometrically distributed and therefore expressed by

$$\begin{aligned} p_{\mathrm{nst,II}}(\Delta t, t) &= (1 - p_{\mathrm{start,II}}(\Delta t))^{\frac{t}{\Delta t}} & (118)\\ &= (1 - \Gamma A P_{\mathrm{start}} \Delta t)^{\frac{t}{\Delta t}} \ . & (119) \end{aligned}$$

To obtain the latter equation, $p_{\mathrm{start,II}}(\Delta t) = P_{\mathrm{enter}}(\Delta t) \cdot P_{\mathrm{start}}$ has been inserted. The approximation becomes more precise, the closer Δt is to zero. So we denote for the probability $P_{\mathrm{nst,II}}(t)$, that no start signal has been triggered during the time until t

$$\begin{aligned} P_{\mathrm{nst,II}}(t) &= \lim_{\Delta t \to 0} (1 - \Gamma A P_{\mathrm{start}} \Delta t)^{\frac{t}{\Delta t}} & (120)\\ &= \left(\lim_{\Delta t \to 0} (1 - \Gamma A P_{\mathrm{start}} \Delta t)^{\frac{1}{\Delta t}} \right)^{t} \ . & (121) \end{aligned}$$

Substituting $1/\Delta t$ by x we find that the limit process is equivalent to

$$P_{\mathrm{nst,II}}(t) = \left(\lim_{x \to \infty} \left(1 - \frac{\Gamma A}{x} \right)^{x} \right)^{t} \ . \tag{122}$$

With the well-known limit representation of the exponential function, namely

$$\lim_{x\to\infty}\left(1-\frac{a}{x}\right)^{x}=e^{-a} \tag{123}$$

for any real a we find

$$P_{\mathrm{nst,II}}(t)=e^{-\Gamma A P_{\mathrm{start}} t}\ . \tag{124}$$

The probability $P_{\mathrm{start,II}}$, that a particle triggers a start signal at the time t is the complement probability to $P_{\mathrm{nst,II}}(t)$. So the time dependent probability of a chance coincidence is given by

$$\begin{aligned} P_{\mathrm{CC,A}}(t) &= (1-P_{\mathrm{start}})\cdot P_{\mathrm{stop}}\cdot(1-P_{\mathrm{nst,II}}(t)) && (125)\\ &= (1-P_{\mathrm{start}})\cdot P_{\mathrm{stop}}\cdot\left(1-e^{-\Gamma A P_{\mathrm{start}} t}\right). && (126)\end{aligned}$$

This function is plotted for different rates of incidenting particles in Fig. 95. It is noteworthy that the maximum probability of a chance coincidence directly scales with $1-P_{\mathrm{start}}$. So, the more efficient the detection of a particle entering the chamber is, the unlikelier is a chance coincidence at maximum probability. Finally, it is noteworthy that the probability distribution functions $P_{\mathrm{CC}}(t)$ variable t is not the measured time of the chance coincidence, but the time between the first particle entering the chamber and the second triggering a start signal. It is evident from the time line in the right panel of Fig. 25, that the distribution of measured time of flight is simply acquired by substituting t for $\tau_{\mathrm{cc}} := \tau_{\mathrm{ion}} - t$, where τ_{ion} is the ions actual time of flight and τ_{cc} is the time of flight acquired because of chance coincidence.

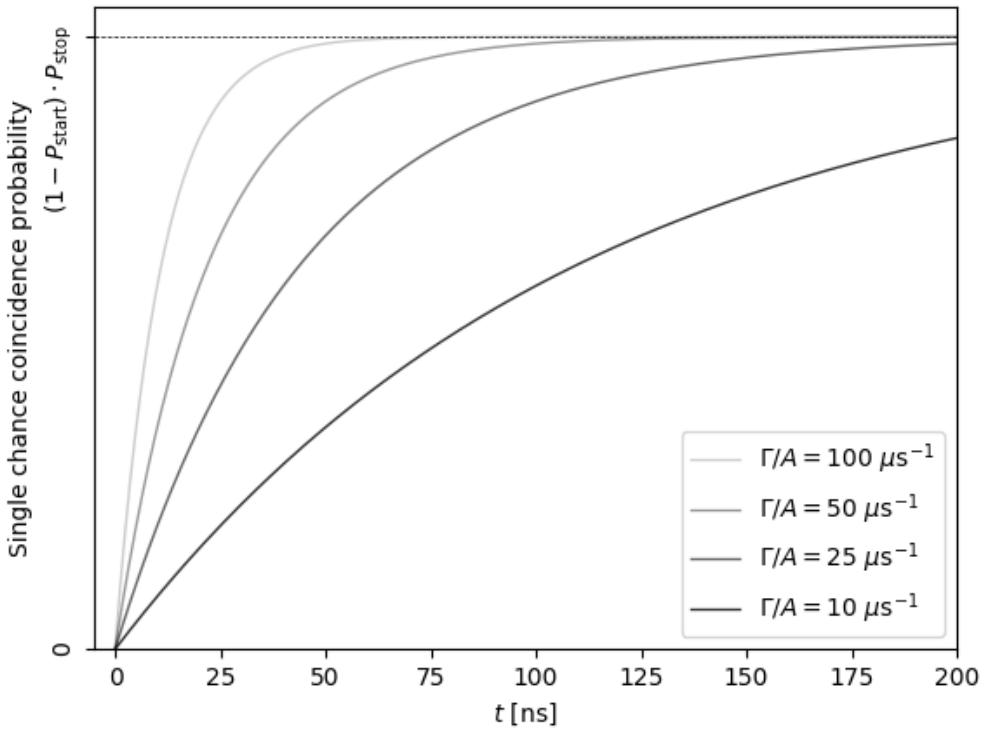

Figure 95: Chance coincidence probability according to Eq. 126 plotted over time, since the first particle (which missed to trigger a start signal) entered the chamber. The chance coincidence has been plotted for four different values of incoming particle rates.

B Description of algorithms and computational schemes

This chapter is deemed to describe some of the algorithms employed in this thesis.

B.1 Noise reduction

Many algorithmic techniques work best on data which has a low signal-to-noise ratio. Unfortunately such a situation is not always achievable albeit many algorithms lack in reliability, if applied to noisy data. Noise reduction is generally an attempt to reconstruct the hypothetical trend of measured data, which would be obtained, if it was not affected by statistical errors. Hence, noise reduced data is always an estimation and might also be data affect by loss of detail, if the noise reduction method is too aggressive.
A typical approach to reduce noise is to convolve the data with a kernel. If the kernel is shaped like a gaussian function, this method is often referred to as gaussian blur (in picture processing)

or more general as a gaussian filter. The underlying assumption for this filter is, that the noise affecting the data is gaussian distributed. For differently distributed deviations, this approach may introduce a systematic error into the analysis.
Also a convolution filter introduces a relatively high loss of detail while reducing noise. To (partially) circumvent the loss of detail while still reducing noise, this work employs a method based on the prevalence of original features. The pseudo code of Algorithm 3 describes this algorithm. With this method, the prevalence of features in the data is controlled by the parameter f. By

Algorithm 3 Noise reduction with feature prevalence

Input:data D, level l, feature prevalence f
Require an odd integer number for $l > 0$
Require $0 \leq f \leq 1$
$r \leftarrow \text{copy}(D)$
for i in $[0, l[\cap\mathbb{Z}$ **do**
    if i is even **then**
        continue to next iteration
    else
        Build a symmetric kernel K, which is shaped analogous to a pyramid and has a length of i in each dimension of the data D
        $C \leftarrow \text{convolve}(D, K)$
        $r \leftarrow r^f \cdot C^{1-f}$
Output:r

iteratively looping over different kernel sizes, a higher noise reduction is achieved. With the value l the number of iterations of noise reduction is selected. As a guideline for the adjustment of f and l a compromise between computational time, noise reduction and prevalence of features should be found. For this work, the algorithm has been implemented in *python3* using *numpy* and can be employed for an arbitrary number of dimensions of input data.

B.2 Normalizations and weights

In addition to the weights obtained from priority weighting, some of the analyses of this work require special weights or normalizations for the PHA events. In the following, these are represented.

B.2.1 Normalization to the occurrences of magnetic field directions

The VDFs of PUIs are expected to strongly depend on the orientation of the local magnetic field. At the same time the aperture of the instrument only allows for a limited set of incoming velocity directions to be observed. This has the consequence that parts of the VDF which are found within the apertures boundaries when a the magnetic field points in a direction which is frequently observed are more likely for observation than parts of the VDFs which combine in the same way to less frequent magnetic field direction. This pre-selection effect might skew the inter-comparability of 3D VDFs, if observed at different magnetic field directions, 3D VDFs integrated over a broad range of magnetic field directions, and also pitch angle distributions.

Since this effect is irreversible in total, the next best approximation to reversion is to introduce a normalization factor based on the frequency a magnetic field direction has been observed.

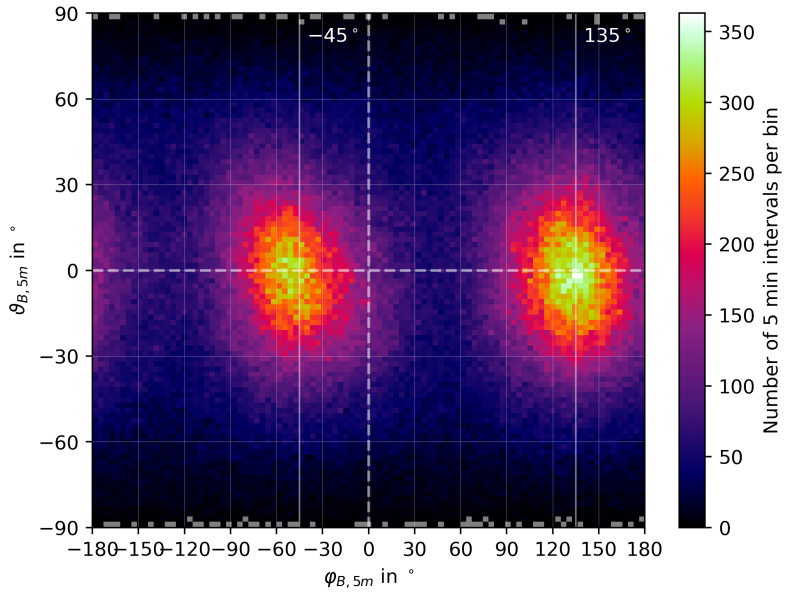

Figure 96: Histogram of magnetic field directions accumulated from 2008 until 2019. As expected, the magnetic field directions are most probable within the plane and at the Parker angle of $\sim 45°$ and 180° of it.

For this, all magnetic field data of the 5 min averaged STEREO/MAG data set (compare chapter 4.2.2) is transformed into spherical coordinates and the azimuthal and elevation angles histogrammed. This results in the distribution of angles displayed in Fig. 96.
The resulting normalization for histograms then works in the following way: Before histogramming each particle obtains a weight. Usually, already a weight exists per particle (e.g. priority weight) in this case, the weight resulting from this method is multiplied to that weight. The weight is computed by the reciprocal fraction of 5 min intervals (compare Fig. 96), that the magnetic field direction which was observed when the particle was observed was observed globally. Or in other words: First, identify the histogram bin which belongs to the magnetic field direction corresponding to the particle. Then compute the weight by dividing the sum of the histogram by the value within the bin. With this method, events belonging to less probable magnetic field directions obtain a larger weight than those with more probable magnetic field direction.

B.2.2 Normalization to the coverage of a particles gyro orbit within the aperture.

In addition, normalization factors are sometimes employed which take into account that due to the limited field of view of STEREO/PLASTIC/SWS under certain magnetic field conditions the gyro orbit of a particle is not fully covered by the instrument. This has the effect, that parts of the VDF are more likely to be observed than others. The observations corrected for this effect are labelled Ring-Coverage (RiCo) corrected. The derivation and application of the correction factors is described in Chapter 6.1.

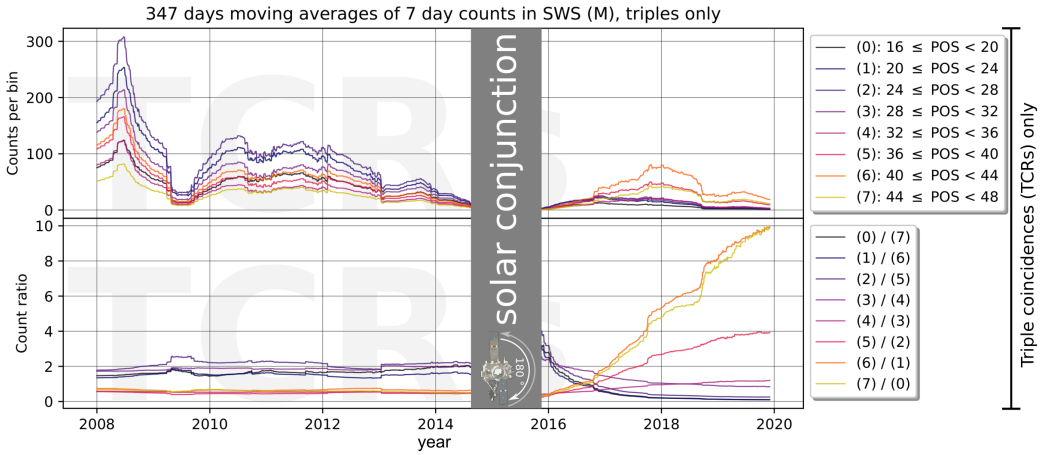

Figure 97: 347 days moving averages of time series of He$^+$ PHA counts in different groups of position bins of the resistive anode of STEREO/PLASTIC SWS. In the top combined counts of eight groups of bins are plotted over time and in the bottom plot the ratio of a group's counts to its counterpart on the other side of the instrument are plotted over time. During a perriod of solar conjunction between Earth and the spacecraft, there was a data outtage. This period is shaded in gray. For this figure, only triple coincidences are considered.

C Overview of moving averages of TCR counts in the Solar Wind Sector of STEREO A / PLASTIC for groups of azimuthal position bins

In Chapter 5.4.1 a time series of moving averages of counts in two halves of the Solar Wind Sector of STEREO A/PLASTIC are displayed in Fig. 73. In figure 97, for completeness an analogous figure is displayed, but instead of only two groups of azimuthal position bins (the two halves), 8 groups of bins are employed where 4 consecutive position bins form a group.

D Full overview of slices through the 3d He$^+$ PUI VDFs

For increased readability, Chapter 5.3.3 moderated through the velocity slices at different magnetic field directions. Here, a complete overview of slices in velocity space with each magnetic field direction and SW conditions is provided in an analogous way to Fig. 64 of Chapter 5.3.3, where slices were shown for time periods when no ICMEs or SIRs were observed. The following is deemed as an uncommented supplementary catalogue of the plots not shown in Chapter 5.3.3.

Figure 98: Collection of diff. Magnetic field Direction Normalized velocity distribution functions (MDNVDFs) analogous to Fig. 64. For this plot, no filtering for SW condition is made.

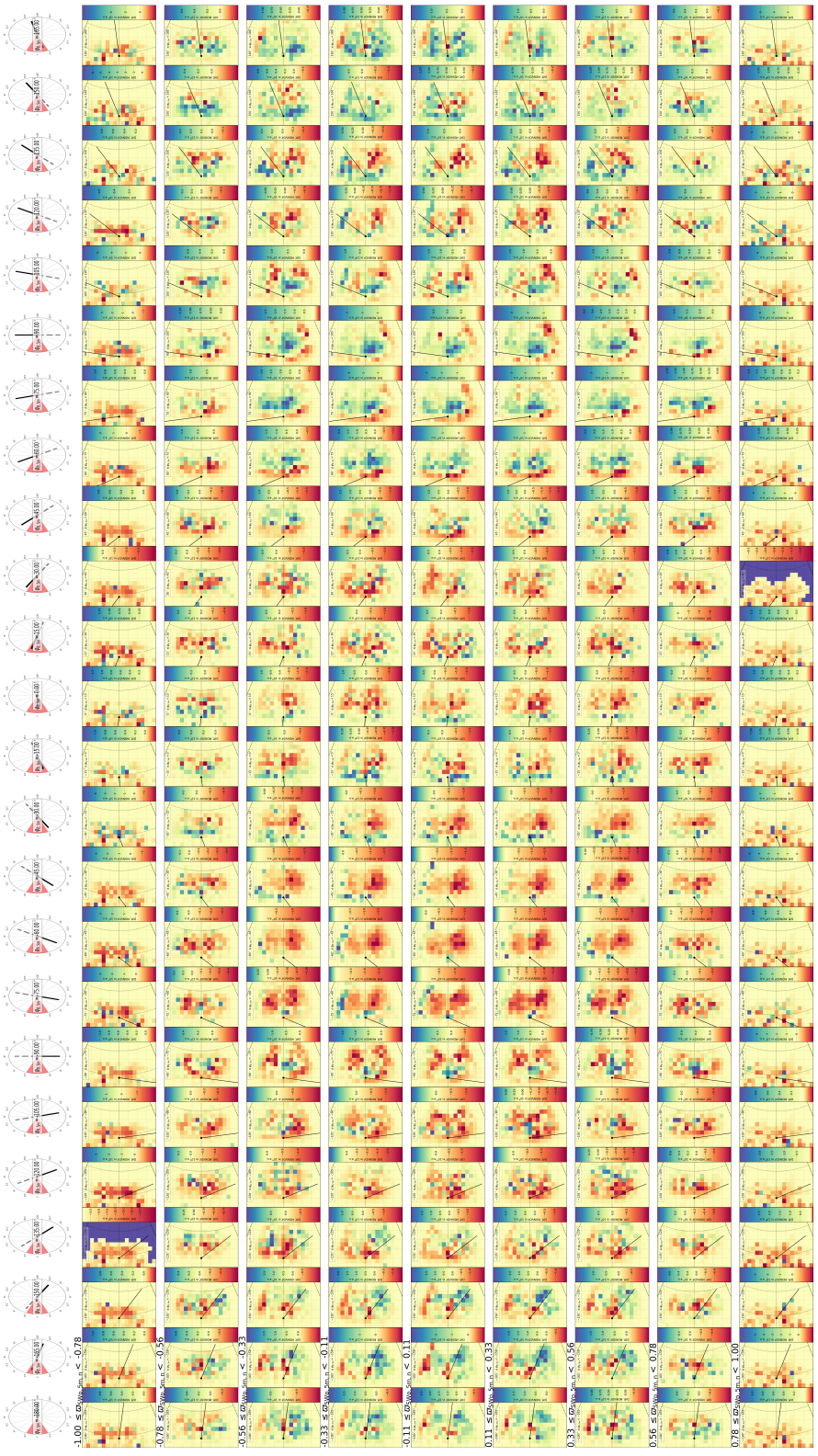

Figure 99: Collection of diff. MDNVDFs analogous to Fig. 64. For this plot, only events during coronal hole wind conditions were considered.

Duncan Keilbach- Three dimensional Pickup Ion velocity distribution functions observed at 1 AU with STEREO/PLASTIC: Anisotropic features and density enhancements in pitch angle distributions as tools to investigate transport effects

Figure 100: Collection of diff. MDNVDFs analogous to Fig. 64. For this plot, only events during sector reversal wind conditions were considered.

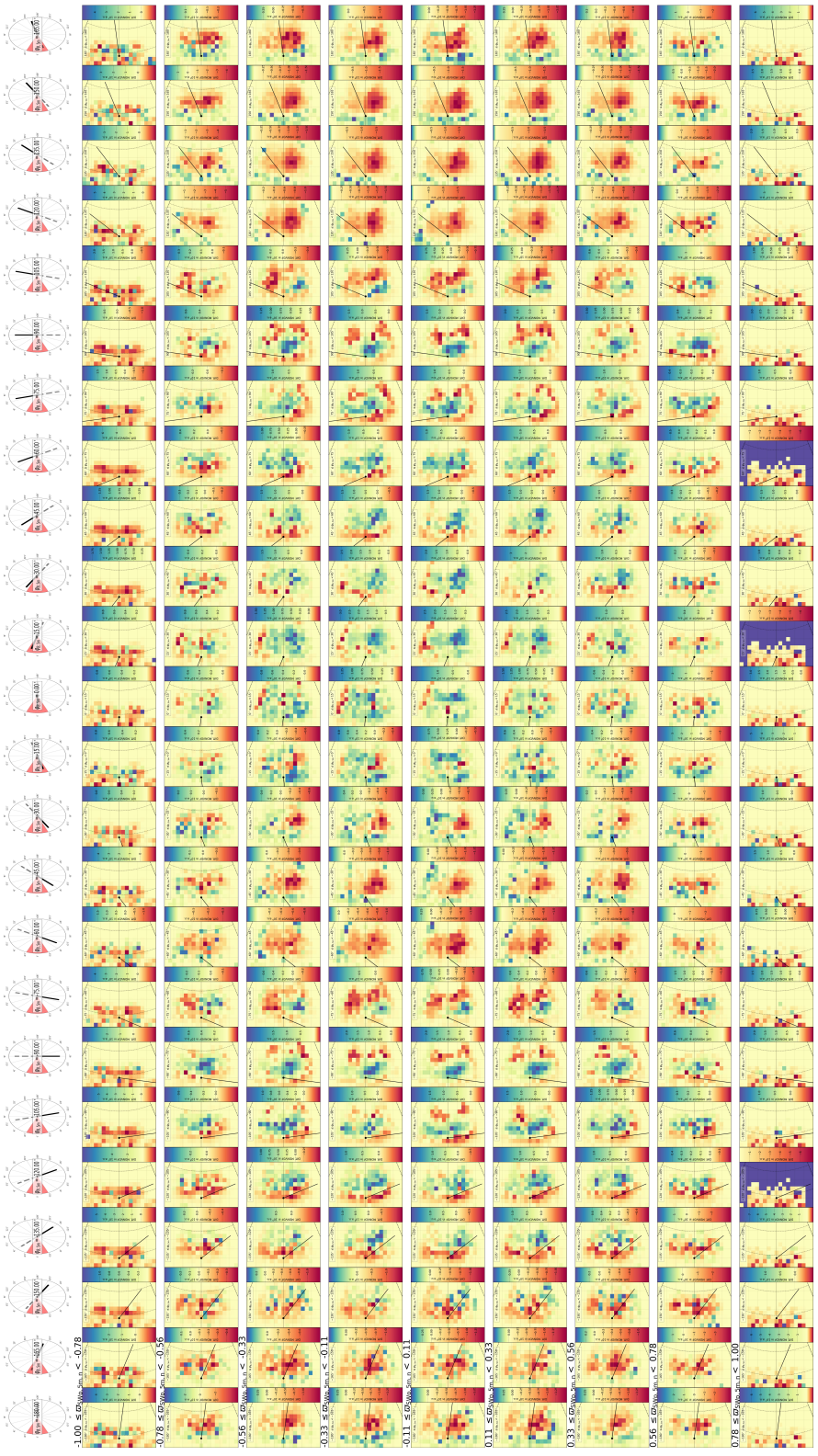

Figure 101: Collection of diff. MDNVDFs analogous to Fig. 64. For this plot, only events during streamer belt wind conditions were considered.

Duncan Keilbach- Three dimensional Pickup Ion velocity distribution functions observed at 1 AU with STEREO/PLASTIC: Anisotropic features and density enhancements in pitch angle distributions as tools to investigate transport effects

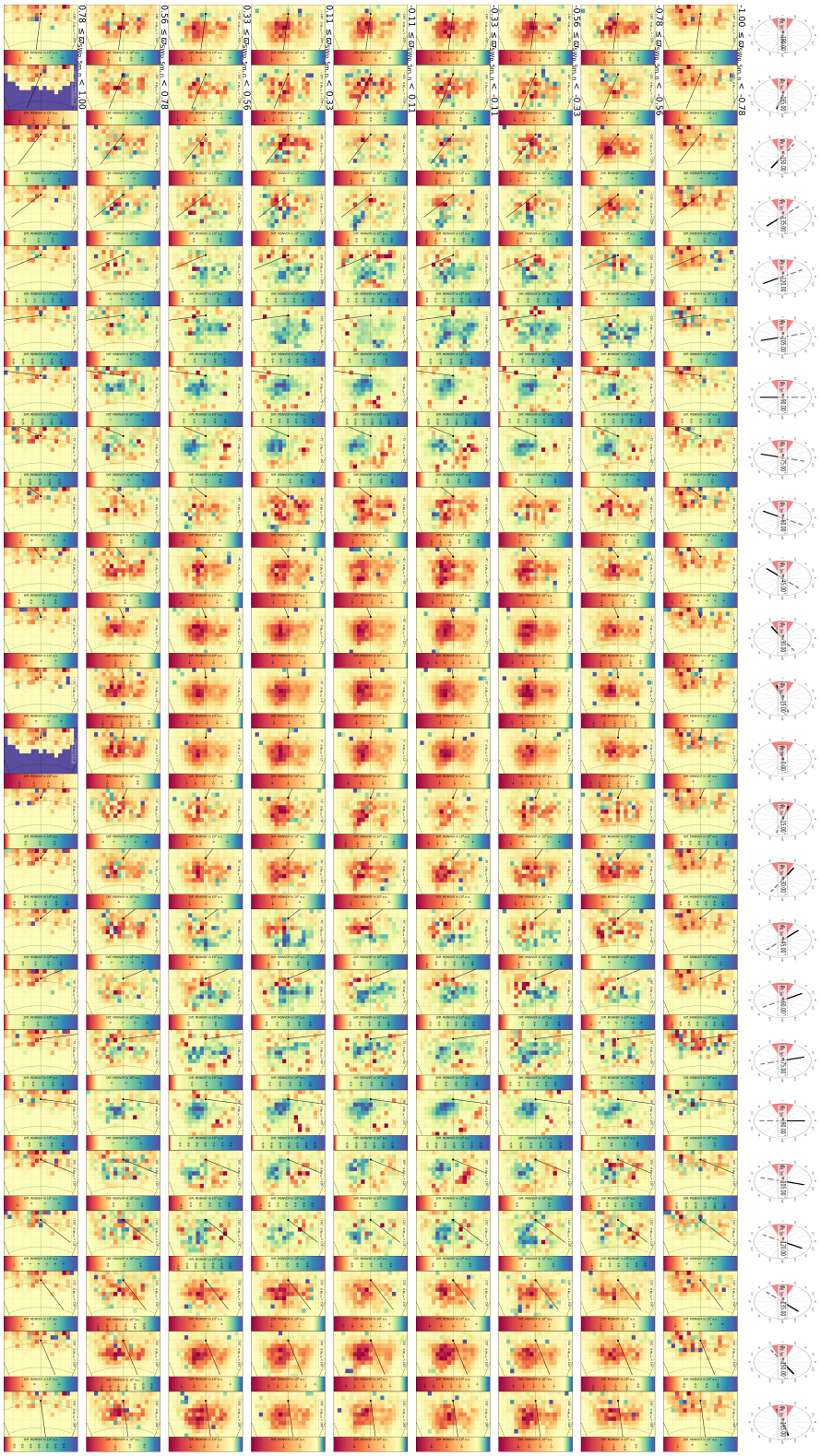

Figure 102: Collection of diff. MDNVDFs analogous to Fig. 64. For this plot, only events during ICME conditions were considered.

Figure 103: Collection of diff. MDNVDFs analogous to Fig. 64. For this plot, only events during SIR conditions were considered.

Duncan Keilbach- Three dimensional Pickup Ion velocity distribution functions observed at 1 AU with STEREO/PLASTIC: Anisotropic features and density enhancements in pitch angle distributions as tools to investigate transport effects

Danksagung

"Space, the final frontier..." mit diesen berühmten Worten hat die Fernsehserie angefangen, die mich als Kind an die Mattscheibe fesselte. Seitdem beschäftigten und faszinierten mich Fragen danach, wie die Welt, das Universum und eigentlich alles funktioniert, welche Geheimnisse dahinter stecken und natürlich, was sich im Weltall alles finden lässt. Schon seit ich denken kann, war ich eigentlich immer Forscher. Als Kleinkind krabbelte ich durch Schränke, kletterte auf Bäume und versuchte, die Kindersicherung an Schubladen zu knacken - mit Erfolg und zum Leidwesen meiner sehr geduldigen Eltern. Bei beiden möchte ich mich an dieser Stelle einmal ganz riesig bedanken. Ohne ihre Unterstützung wäre ich sicherlich nie bis zur Doktorarbeit gekommen.
Ein weiteres berühmtes Fernsehzitat aus einer anderen Serie ist "Die Wahrheit ist irgendwo da draußen." Und so ließich mir ein Spiegelteleskop schenken und die faszinierenden Formationen im Weltall rückten alle ein wenig näher.
Doch so richtig wusste ich manchmal auch nicht, wohin mit meiner Neugier. Aber zum Glück verstand mein Physikleher, Andre Streicher, diese Neugier zu fördern und zu fordern. An dieser Stelle einen riesen Dank an ihn und für sein Engagement. Ohne ihn hätte ich vielleicht nie Physik studiert.

Aus heutiger Sicht fühlt sich das Physikstudium an, wie eine Reise, deren ultimatives Ziel die Doktorarbeit ist. Doch das ist nicht wirklich der Fall. Eigentlich war es viel mehr ein schwerer, ständig bergauf ansteigender Pfad. Aber wie lautet nochmal der Spruch: "Mit seinen Aufgaben wächst man." Direkt nach dem Abitur fühlt man sich so erwachsen, so sehr wie eine vollständige Person. Ich bin dankbar für die Erfahrung, dass dieses Gefühl nicht trügerischer hätte sein können und was sich aus dieser Zeit wirklich abseits des fachlichen lernen lässt ist, dass man nie vollständig ausgelernt hat und dass es immer etwas Neues gibt, das man noch nicht kennt. Insofern ist man eigentlich nie in dem Sinne vollständig oder fertig. Ist das frustrierend? Natürlich nicht. Im Gegenteil, denn ohne etwas Neues, das man entdecken kann, wäre es auch langweilig. So habe ich vielleicht auch die letzten Jahre auf ein Ziel hingearbeitet, um letztlich festzustellen, dass nicht wirklich das Ziel wichtig ist, sondern der Weg dorthin. Und ja, das klingt wie ein abgedroschener Standardspruch von einem Motivationsposter, aber auf der Meta-Ebene heißt es auch, dass man sich mehr Gedanken darüber machen sollte, was man tun möchte als was man erreicht haben möchte. Und ich bin dankbar für die Gelegenheit und die Zeit, die mir während des Promotionsstudiums eingeräumt wurde, nicht nur um fachlich zu wachsen, sondern auch mich selbst kennen zu lernen und nicht nur als Physiker sondern auch als Person zu wachsen.

Eigentlich bin ich schon einen Schritt zu weit gegangen. Denn die Voraussetzung für das Promotionsstudium ist der Master und die Voraussetzung dafür ist der Bachelor und gerade bei Letzterem bin ich dankbar dafür, die richtigen Menschen kennen gelernt zu haben. Danke an Andreas Taut, dass er mich durch die extraterrestrische Arbeitsgruppe geführt hat und mir direkt das Gefühl gegeben hat, willkommen zu sein. Ein noch riesigeres Dankeschön an Christian Drews, der mit viel Engagement und Enthusiasmus meine Bachelorarbeit und Masterarbeit betreut hat. Selbstverständlich auch ein riesiges Dankeschön an Robert Wimmer-Schweingruber für den Vertrauensvorschuss in meine Fähigkeiten, als er mich als Doktorand aufgenommen hat und für die scheinbar unermüdliche Geduld, wenn etwas nicht so läuft wie geplant - ebenso für die angenehme Arbeitsatmosphäre in der Arbeitsgruppe.
Mit Beginn der Doktorarbeit kam auch der eigene Platz in einem Büro und ich hätte vielleicht keine bessere Bürogenossin finden können als Verena Heidrich-Meisner. Vielen Dank an sie für die Unterstützung, das offene Ohr, die vielen Tipps und Hinweise und das Korrekturlesen dieser

Arbeit.

Ich wäre nicht der, der ich bin ohne meine Verlobte. Worte können nicht ausdrücken, wie dankbar ich ihr bin. Deswegen auch nur dieser viel zu kurze und wortkarge Absatz für sie. Auch möchte ich mich hier bei meinem besten Freund bedanken. Auch für ihn gilt, dass Worte definitiv nicht reichen.

Schließlich ein großes Danke an alle, die jemals im Kaffeeraum den Geschirrspüler ausgeräumt, sauber gemacht, die Post sortiert, oder Ordnung gemacht haben. Vor allem, wenn ich es mal vergessen habe. Noch mehr ein Dankeschön an alle, die Kaffee gekocht haben oder dafür gesorgt haben, dass Kaffe verfügbar war.

Eidesstattliche Versicherung

Hiermit versichere ich an Eides Statt, dass diese Dissertation - abgesehen von der Beratung durch meine akademischen Lehrer - nach Inhalt und Form eine eigenständige und nur mit den angegebenen Hilfsmitteln und der angegebenen Literatur von mir verfasste Arbeit ist.
Diese Arbeit wurde nicht, auch nicht zum Teil, schon einer anderen Stelle im Rahmen eines Prüfungsverfahrens vorgelegt, veröffentlicht oder zur Veröffentlichung eingereicht.
Ferner versichere ich, dass diese Arbeit unter Einhaltung der Regeln guter wissenschaftlicher Praxis der Deutschen Forschungsgemeinschaft entstanden ist und dass mir bislang kein akademischer Grad entzogen worden ist.

Kiel, den _____

Duncan Keilbach